# DESIGN AND CHARACTERISATION OF MILLIMETRE-WAVE PLANAR GUNN DIODES AND INTEGRATED CIRCUITS

**Chong Li**

(BEng, MSc)

A THESIS SUBMITTED TO

SCHOOL OF ENGINEERING

COLLEDGE OF SCIENCE AND ENGINEERING

UNIVERSITY OF GLASGOW

IN FULFILMENT OF THE REQUIREMENTS

FOR THE DEGREE OF

DOCTOR OF PHILOSOPHY

January 2012

***To my beloved wife Rui and our daughter Lily***

献给我的爱妻—金锐和我们的宝贝女儿李跺廷

# ABSTRACT

Heterojunction planar Gunn devices were first demonstrated by Khalid et al in 2007. This new design of Gunn device, or transferred electron device, was based on the well-established material system of GaAs as the oscillation media. The design did not only breakthrough the frequency record of GaAs for conventional Gunn devices, but also has several advantages over conventional Gunn devices, such as the possibility of making multiple oscillators on a single chip and compatibility with monolithic integrated circuits. However, these devices faced the challenge of producing high enough RF power for practical applications and circuit technology for integration.

This thesis describes systematic work on the design and characterisations of planar Gunn diodes and the associated millimetre-wave circuits for RF signal power enhancement. Focus has been put on improving the design of planar Gunn diodes and developing high performance integrated millimetre-wave circuits for combining multiple Gunn diodes.

Improvement of device design has been proved to be one of the key methods to increase the signal power. By introducing additional δ-doping layers, electron concentration in the channel increases and better Gunn domain formation is achieved, therefore higher RF power and frequency are produced. Combining multiple channels in the vertical direction within devices is another effective way to increase the output signal power as well as DC-to-RF conversion efficiency. In addition, an alternative material system, i.e. $In_{0.23}Ga_{0.77}As$, has also been studied for this purpose.

Planar passive components, such as resonators, couplers, low pass filters (LPFs), and power combiners with high performance over 100 GHz have been developed. These components can be smoothly integrated with planar Gunn diodes for compact planar Gunn oscillators, and therefore contribute to RF power enhancement.

In addition, several new measurement techniques for characterising oscillators and passive devices have also been developed during this work and will be included in this thesis.

# List of publications

## 2011

## Journals

[1] Chong Li, Lai Bun Lok, Ata Khalid, and David R. S. Cumming, "An ultra wideband planar ring combiner/divider with high isolation for V and W-band applications," *(Submitted to IEEE Microwave and Wireless Component Letters).*

[2] Chong Li, Lai Bun Lok, Ata Khalid, Bruno Romeira, Charlie N. Ironside, Iain G. Thayne, and David R. S. Cumming, "Analysis of oscillation detection technique by using vector network analyser," *(Submitted to IEEE Transactions on Microwave Theory and Techniques).*

[3] M. Montes, G. Dunn, A. Stephen, A. Khalid, C. Li, D. Cumming, C. H. Oxley, R. H. Hopper, and M. Kuball, "Reduction of impact ionisation in GaAs-based planar Gunn diodes by anode contact design" (*Accepted by IEEE Transactions on Electron Devices, in press).*

[4] Chong Li, Lai Bun Lok, Ata Khalid, Iain G. Thayne and David R. S. Cumming, "Investigation of loading effect on power performance for planar Gunn diodes using load-pull measurement technique," *IEEE Microwave and Wireless Components Letters,* vol. 21, no.10, pp. 556-558, October 2011.

[5] Chong Li, Ata Khalid, Sonia H. Paluchowski Caldwell, Martin C. Holland, Geoff M. Dunn, Iain G. Thayne, and David R. S. Cumming, "Design, fabrication and characterization of $In_{0.23}Ga_{0.77}As$-channel planar Gunn diodes for millimeter wave applications", *Solid State Electronics,* vol. 64, no. 1, pp. 67-72, October 2011.

[6] Chong Li, A. Khalid, Sonia H. Paluchowski Caldwell, N. J. Pilgrim, M. C. Holland, G. M. Dunn, and D. R. S. Cumming, "Enhancement of power and frequency in HEMT-like planar Gunn diodes by introducing extra delta-doping layers," *Microwave and Optical Component Letters,* vol. 53, no.7, pp. 1624-1626, July 2011.

[7] Chong Li, Lai Bun Lok, Ata Khalid, and David R. S. Cumming, "Coplanar ring divider with wideband high isolation performance", *Progress in Electromagnetics Research Letters,* vol. 25, pp.1-10, June 2011.

[8] L. P. Hou, M. Haji, Chong Li, and A. C. Bryce, "80-GHz AlGaInAs/InP 1.55μm colliding-pulse mode-locked laser with low divergence angle and timing jitter", *Laser Physics Letters,* vol. 8, no. 7, pp. 535-540, March 2011.

[9] A. Khalid, Chong Li, N. J. Pilgrim, M. C. Holland, G. M. Dunn, and D. R. S. Cumming, "Novel composite contact design and fabrication for planar Gunn devices for millimeter-wave and terahertz frequencies," *physica status solidi (c*), vol. 8, no. 2, pp. 316-318, February 2011.

[10] N. J. Pilgrim, A. Khalid, Chong Li, G. M. Dunn, and D. R. S. Cumming, "Contact shaping in planar Gunn diodes," *physica status solidi (c),* vol. 8, no. 2, pp. 313-315, February 2011.

# Conferences

[11] Ata Khalid, Chong Li, James Grant, Shimul Saha, Susan Ferguson and David R. S. Cumming, "A Simple Air Bridge Technology for mm-Wave Applications", in Proceedings of 37th International Conference on Micro and Nano Engineering, Berlin, Germany, 19-23 September 2011.

[12] L. Hou, M. Haji, C. Li, J. Akbar, J. Marsh, and A. Bryce, "80-GHz AlGaInAs/InP 1.55 μm colliding-pulse mode-locked laser with low divergence angle and timing jitter", *European Conference on Lasers and Electro-Optics and the XIIth European Quantum Electronics Conference*, Munich, Germany, 22 May 2011.

[13] Chong Li, Lai Bun Lok, Ata Khalid, and David R. S. Cumming, "A broadband circular combiner/divider for planar Gunn oscillators," in *Proceedings of 2nd Annual Passive RF and Microwave Components Seminar*, Glasgow, 30 March 2011.

[14] Chong Li, Ata Khalid, Lai Bun Lok, and David R. S. Cumming, "Novel on-wafer measurement technique for passive multiport devices in millimetre wave frequency range," *9th Millimetre-wave User Group Meeting*, Glasgow, 31 March 2011.

## 2010

[1] N. J. Pilgrim, A. Khalid, Chong Li, G. M. Dunn, and D. R. S. Cumming, "Vertical scaling of multi-stack planar Gunn diodes," *International Semiconductor Conference*, Sinaia, Romania, 11th Oct-13th Oct 2010.

[2] Chong Li, Ata Khalid, Lai Bun Lok, and David R. S. Cumming, "Low power signal detection in emerging transferred electron devices using vector network analyser above 100 GHz," *8th NPL Millimeter-wave Users' Group meeting*, London, UK, 1st October 2010.

[3] Chong Li, A. Khalid, L. B. Lok, N. J. Pilgrim, M. C. Holland, G. M. Dunn, and D. R. S. Cumming, "An $In_{0.23}Ga_{0.77}As$-based pHEMT-like planar Gunn diode operating at 116 GHz," *The 35th International Conference on Infrared, Millimeter and THz Waves*, Rome, Italy, 5th -10th September 2010.

[4] L. B. Lok, Chong Li, A. Khalid, N. J. Pilgrim, G. M. Dunn, and D. R. S. Cumming, "Demonstration of the self-mixing effect with a planar Gunn diode at millimeter-wave frequency ," *The 35th International Conference on Infrared, Millimeter and THz Waves*, Rome, Italy, 5th - 10th September 2010.

[5] Chong Li, A. Khalid, Lai Bun Lok, Neil J. Pilgrim, Martin C. Holland, Geoff M. Dunn, and David R. S. Cumming, "Millimeter-wave Planar Gunn diodes," *UK Semiconductor conference 2010,* University of Sheffield, 7-8 July 2010.

## 2009

[1] Chong Li, A. Khalid, N. Pilgrim, M. C. Holland, G. Dunn, and D. R. S. Cumming, "Novel planar Gunn diode operating in fundamental mode up to 158 GHz," *J. Phys.:Conf. Ser.*, vol. 193, no. 1, 012029, 2009.

[2] A. Khalid, Chong Li, G. Dunn, N. Pilgrim, and D. R. S. Cumming, "Observation of Multiple Domains in a Planar Gunn Diode," in *Proceedings of the 4th European Microwave Integrated Circuits Conference*, Rome, Italy, September 2009.

# ACKNOWLEDGEMENTS

In the past three years, I have received help from a number of people around me. Without their assistance it would have been impossible for me to complete this work in such a short time.

I express my sincere appreciation and gratitude to the following people:

***Professor David R. S. Cumming***, my principal supervisor, for trusting me and offering me the opportunity to carry out my PhD study on this project. He has been constantly encouraging and guiding me throughout the last three years. In particular he has spent massive efforts helping me solve my financial difficulties.

***Dr. Ata Khalid***, my second supervisor, for helping me to develop and improve my expertise in semiconductor devices on a daily basis as well as his top-class electron beam lithography fabrication skills that made the project so fruitful.

***Dr. Lai Bun Lok*** for his expertise in millimetre-wave engineering that has helped me on the circuit development and characterisation throughout this project. Furthermore, his critical and advisable reviews on my thesis were extremely helpful in building a final solid body of work.

***Dr. Neil Pilgrim*** and ***Dr. Geoff Dunn***, the project collaborators, for their expertise on Monte-Carlo simulations and wonderful ideas in developing planar Gunn diodes.

***Dr. Martin Holland*** for wafer growth using molecular beam epitaxy.

***Dr. James Grant***, ***Dr. James Beeley***, ***Ms. Kirsty Walls***, and ***Mr. Peter MacPherson*** for proof-reading this thesis.

I have received a lot of additional assistance from ***Professor Iain Thayne, Dr. Qin Chen, Dr. Shimul Saha, Dr. Bingjie Cheng, Dr. Lianping Hou, Dr. Sonia Caldwell, Dr. Karol Kalna, Dr. Steven Bentley, Mr. Tom O'Hara, Mr. Liquan Wang, Mr. Bruno Romeira, Dr. Horacio Cantu, Mr. Feng Hong, Mr. Vasilleos Papageorge*** and many more.

I wish to express my sincere appreciation to my financial sponsors EPSRC and e2v Technology as well as ***Mr. Nigel Priestley*** and ***Mr. Michael Carr*** for their helpful discussions and advice on the project.

Last but not least I deeply thank my beautiful and smart beloved wife **Rui (金锐)**. She has been constantly supporting and encouraging me from every aspect of my life through my Master's and PhD's studies in the past five years. Importantly, she gave us wonderful gifts- our beautiful, adorable, and clever daughter **Lily and unborn son**. **My parents (李明武 and 赵淑华), parents-in-law** （金永厚 **and** 魏玉娟）**, sister (李妮), sister-in-law** （刘阳） and **brother-in-laws** （侯英林 **and** 金鑫） have also been supporting me to achieve the final completion of the PhD.

# CONTENTS

# LIST OF FIGURES

# LIST OF TABLES

# CHAPTER 1

# INTRODUCTION

## 1.1 Background

Gunn devices or transferred electron devices (TEDs) have been known as excellent microwave and lower millimetre-wave (e.g. 30 GH-100 GHz) signal sources since they were first demonstrated by J. B. Gunn in 1963 [1]. Compared to conventional signal sources, such as klystrons, magnetrons, and backward-wave oscillators, Gunn devices are smaller, simpler and have lower power consumption. After almost 50 years of development, Gunn devices have been established as one of the most widely used microwave signal sources in the industrial, scientific, medical, and military fields.

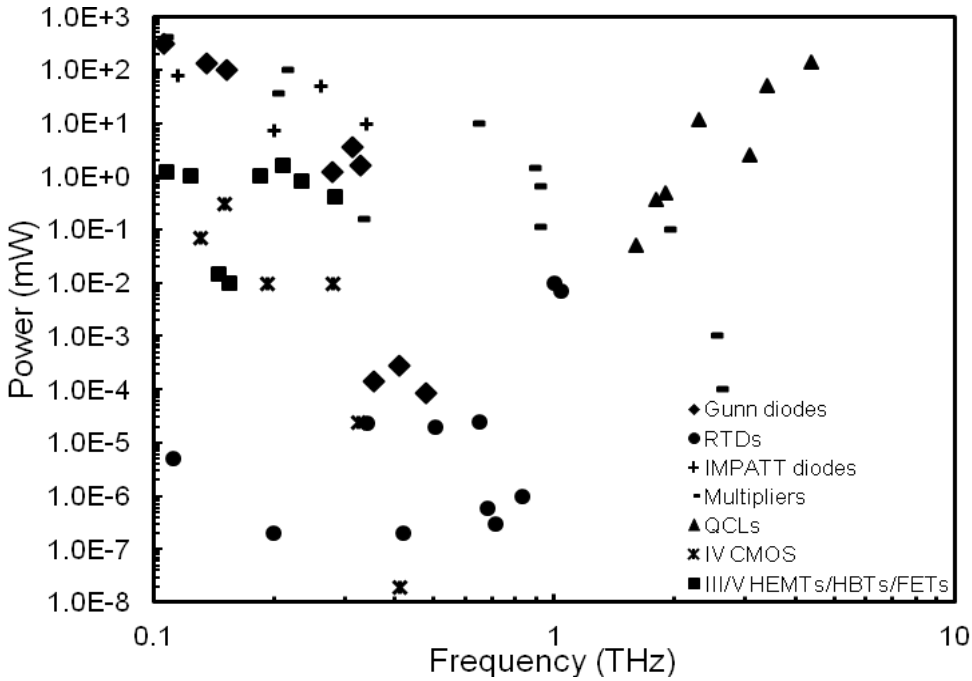


**Figure 1-1** Performance of selected solid state electronic and photonic millimetre-wave and terahertz signal sources, such as Gunn diodes [2-6], resonant tunnelling diodes (RTDs) [7-13], impact ionisation avalanche transit-time (IMPATT) diodes [3, 5, 14, 15], oscillators/amplifiers/multiplier chains [5, 16-19], quantum cascade lasers (QCLs) [20-26], Si/SiGe CMOS [5, 27-30], and III/V HEMTs/HBTs/FETs [5, 18, 31-33].

However, the conventional Gunn devices, compared with other solid state electronic and photonic sources as shown in Figure 1-1, have recently been challenged to meet the requirements as signal sources for upper millimetre-wave (typically defined between 100 GHz and 300 GHz) and terahertz (typically defined between 0.3 THz and 30 THz) applications, such as communications, radar, imaging, spectroscopy, and security screening [3, 34, 35].

Several theoretical and experimental attempts have been made to improve the Gunn devices to meet the growing demand including new material [36, 37], harmonic power extraction [6, 38], and new physical mechanisms [39-41] in order to improve the device frequency and power performance. One solution, using the well-established material system (e.g. GaAs), but with new designs, was proved to be successful at the University of Glasgow and the University of Aberdeen [42]. Advantages of these planar Gunn devices over the conventional Gunn devices include the ability to control the oscillation frequency of a planar Gunn diode by selecting the lithographic dimension, therefore multiple frequency sources can be made on a single chip. In addition, by reducing the anode and cathode separation ($L_{ac}$), sub-terahertz or even terahertz oscillation might be achieved. Furthermore, simple two-terminal planar structures do not need a complicated gate process like transistors [19, 43] but still have the capability to be integrated with other devices on the same chip using monolithic microwave integrated circuit (MMIC) techniques.

However, the first devices have shown weak RF power and low DC-to-RF efficiency. Therefore, it is the aim of this project to improve the power performance of such devices. In this thesis, the design, modelling, and characterisation of improved planar Gunn diodes and the related millimetre-wave components and circuits are described.

## 1.2 Organisation of the Thesis

The thesis is divided into seven chapters. The first chapter presents the background and motivation of this work. Highlights are given to the existing technologies for generation of millimetre-wave signal radiations. The advantages and challenges of planar Gunn diodes compared with other technologies are also included.

Chapter 2 is a literature review of Gunn devices. The general development of Gunn devices is first outlined. A more specific overview on the progress of planar types of Gunn devices or Gunn-like devices is included. Chapter 2 also presents the physical mechanism of operation of Gunn devices.

Chapter 3 describes the device characterisation methodologies that have been used to characterise millimetre-wave planar Gunn diodes and passive components and circuits in this work. The general principles of semiconductor material and contact characterisation methods are first given. A detailed discussion is presented on vector network analysers, and their application to characterising passive devices. The spectrum and power measurement systems are also included in this chapter. Finally, particular attention is given to the analysis of oscillation detection technique using vector network analysers.

Chapter 4 shows the improved and new design, modelling, and characterisation of planar Gunn diodes. Firstly, the fundamentals of material growth, device fabrication, and contact design are discussed. Then the modified and (or) new design of device layers is presented. The design is assisted by using a two-dimensional modelling tool (Medici). Experimental results confirm simulation and the improvement of RF power from the new design is achieved. Finally, another material system i.e. $In_{0.23}Ga_{0.77}As$ for heterojuncture planar Gunn devices is introduced.

Chapter 5 describes some special characteristics of planar Gunn diodes. Multiple domain-oscillations are demonstrated and discussed in Section 5.1. This discussion is then followed by an experimental illustration of self-mixing effect of planar Gunn diodes in Section 5.2. Investigations on the effect of heat and illumination on the power and frequency of planar Gunn diodes are shown in Sections 5.3 and 5.4, respectively. Finally a brief discussion on the drift of current, frequency, and power of the oscillations is summarised in Section 5.5.

Chapter 6 concentrates on the development of millimetre-wave planar passive components and circuits, such as thin-film resistor, airbridges, waveguides, resonators, low pass filters, couplers, and power combiners/dividers that play a significant role in constructing highly integrated planar Gunn oscillator circuits. The basic principles and design rules are given

along with the simulation and experimental results of the proposed devices. Where appropriate, some fabrication techniques and measurement methods are also included.

Chapter 7 concludes the results that have been achieved so far and summarises some future work.

# CHAPTER 2

# OVERVIEW OF GUNN DEVICES

In 1963 J. B. Gunn reported an important discovery relating to the effect of high electric fields on bulk semiconductor materials. He observed current instability at microwave frequency ranges on a short slab of n-type GaAs when the electric field exceeded a critical threshold value [1]. Similar current instability was also found in n-type InP. Later it was Kroemer [44] who successfully explained Gunn's discovery using the transferred-electron effect theory which had been theoretically studied by Hilsum [45] and Ridley and Watkins [46] before Gunn's discovery.

> With this discovery a new era of development of semiconductor devices was born. Suddenly the possibility existed of replacing the existing microwave vacuum tube sources and their bulky, high voltage power supplies with much simpler, low voltage solid state oscillators. This possibility loomed large and provided the target for intense activity on the new effect in laboratories all over the world [47].

In this chapter, a brief review on the development Gunn devices in general is first given in Section 2.1. A special type of Gunn devices named planar Gunn devices that directly relate to this project will be summarised in Section 2.2. Finally, theories of Gunn effect and modes of Gunn oscillations will be discussed in Section 2.3.

## 2.1 Introduction to the Development of Gunn Devices

Gunn's discovery has triggered intensive research on many aspects of this subject that include theories, materials, circuits, experimental methodologies, applications and so on. Incomplete statistics based on the collection of ISI Web of Knowledge$^{SM}$ indicate that there have been more than 1600 published journal and conference papers that are related to

Gunn devices or transferred electron devices since 1963. This means it is unrealistic to include all aspects of Gunn devices in this short literature review chapter. However, significant efforts have been made to put all major works into appropriate categories so that one can understand how the progress of research in each category has been made and maybe one can predict any future development.

### 2.1.1 In Search of Theories behind Gunn's Discovery

In 1963, Gunn reported current oscillations at microwave frequencies by simply applying several volts of voltage onto a piece of n-type bulk semiconductor. Figure 2-1 shows the current waveform generated by a 25 μm n-type GaAs when it was biased by a pulse with amplitude of 16 V. The frequency of the current oscillation was 4.5 GHz that was approximately the electron transit time in the sample.

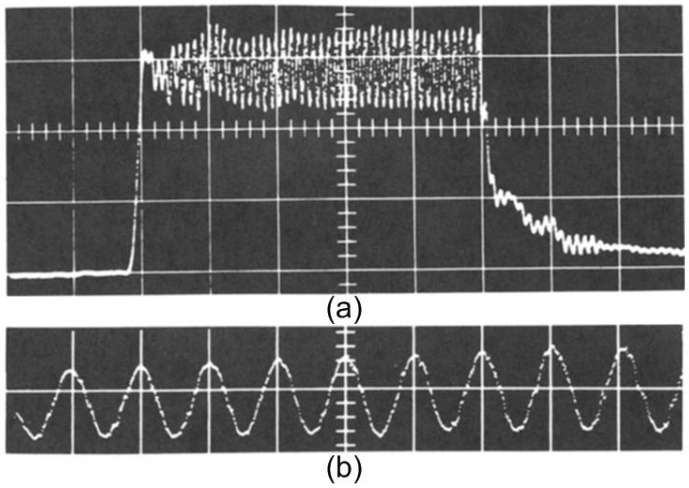


**Figure 2-1** Current waveform reported in Gunn's paper [1]. (a) Pulsed current with instability and (b) its waveform detail.

It was a revolutionary discovery because not only it has established solid state electronic devices as a novel type of signal generation source that has small size, low power consumption and simple structure, but also it also proved that theoretical studies are consistent with experimental results in this area. However, he could not explain the true mechanism of the oscillations he observed. In 1964 Kromer pointed out that Gunn's experimental results were the consequence of transferred electron effect that leaded to the current instability and negative differential resistance (NDR) [44].

In fact, before 1963 many researchers had been working on the possibility of obtaining negative differential resistance from bulk semiconductors for generating power at high frequencies both in theory [48, 49] and in experiments [50]. One of the theoretical works was from Hilsum [45] who predicted that materials such as GaSb and n-type GaAs exhibited negative conductance due to the transferred electron effect at high electric field and that could lead to amplifiers and oscillators devices. Alloying GaAs with GaP is potentially even better because this ternary material may have lower energy gap between conduction band minima Γ valley and *L* valley, thus electrons find it easier to "jump" into the high effective electron mass valley under a moderate electric field. He also derived closed form equations for current density and mobility against electric fields for both GaSb and GaAs.

Another promising theoretical work was from Ridley and Watkins [46] and Ridley [51] who predicted the existence of electrical domains in the crystal and the negative resistance behaviour of the device's IV characteristics. However, the NDR behaviour might not be easily observed because the current instability could overwhelm it. Ridley [51] concluded that for some materials the impact ionisation and electron injection from the contacts may have occurred before the negative resistance region was reached.

Although Gunn dismissed the transferred electron effect theory as the physical mechanism of the observed current oscillations in the paper [1] because of his miscalculation of the electron temperatures, Kroemer [44] believed that it was the transferred electron effect that made the oscillations occur. Meanwhile he suggested that high electric field domains ought to be observed along with the transit-time related current oscillations that had been already experimentally observed by Gunn [52]. Heeks' measurements on electric field domains further proved Kroemer's suggestion [53]. By then the transferred electron effect theory had been widely accepted as the theory of Gunn's NDR and current oscillations.

As more and more research interest focused on this subject, more current oscillation phenomena other than transit-time related oscillations from the transferred electron devices were observed. Carroll demonstrated a quenched domain mode of oscillation whose frequencies and DC-RF conversion efficiency were significantly higher than the transit-time mode of oscillation [54]. Copeland also reported another mode of oscillation called

limited space-charge accumulation (LSA) mode in which only the NDR characteristics of a transferred electron device was used for an oscillator and the current oscillation frequencies were circuit controlled [55, 56]. Other modes of oscillations were also reported but were only a combination of one or the other [57].

### 2.1.2 In Search of Materials, Circuits and Applications of Gunn Devices

The late 60s and the entire 70s there was a major increase in interest in Gunn devices. Many aspects of Gunn devices have been extensively explored and investigated. These included alternative materials for Gunn oscillations, circuits, numerical and analytical investigations on Gunn effect theories, applications and other phenomena in Gunn devices.

In addition to the n-GaAs and n-InP results reported by Gunn, researchers also investigated other semiconductor materials for Gunn effect. They include n-Ge [58], n-CdTe, n-InSb [59], n-InAs, GaSb, ternary compounds $GaAs_xP_{1-x}$ ($x<0.5$) [60], $In_xGa_{1-x}Sb$ [61, 62], $In_xGa_{1-x}As$ [63] and even the quaternary compound $Ga_{0.13}In_{0.87}Ga_{0.37}P_{0.63}$ [64]. The general requirements of any candidate semiconductor materials for generating Gunn oscillations are summarised as follow:

- The band gap $\Delta E_g$ must be rather greater than the intervalley band discontinuity $\Delta E$ between the minimum central conduction band and the minimum of next higher satellite conduction band so that avalanche breakdown will not occur before onset of NDRs [46].

- The intervalley band discontinuity $\Delta E$ must be several times greater than the lattice temperature $kT$ (approximately 0.027 eV) so that the electron intervalley transfer is not due to the heat effect.

- The electron effective mass in the satellite valley must be heavier than that in the central valley so that the electron mobility in the satellite valley is lower than that in the central valley.

Although other materials have been demonstrated showing the Gunn effect, due to their poorer RF performance, device stability, complex fabrication process and high cost etc.

GaAs is the most extensively studied. Thus, the detailed theories of Gunn effect in GaAs will be treated in Section 2.3.

Except investigations on alternative semiconductors for the Gunn effect, improving performance of Gunn devices from circuit point of view to meet the requirements for practical applications has also been deeply explored. Many important aspects of Gunn devices such as RF power level, DC-to-RF conversion efficiency, phase noise, frequency and power tuneability and stability, heat effect and so on need to be improved by applying appropriate circuits and other means. Gunn diodes have been deployed in various circuits, such as rectangular waveguide cavities [65, 66], coaxial waveguide cavities [67, 68], nonradiative dielectric (NRD) waveguides [69], substrate integrated waveguides (SIWs) [70], microstrip circuits [71, 72], coplanar waveguides (CPWs) [73, 74] and many more to make oscillators for different applications. However, the most widely used configuration is the rectangular waveguide and cavity as shown in Figure 2-2.

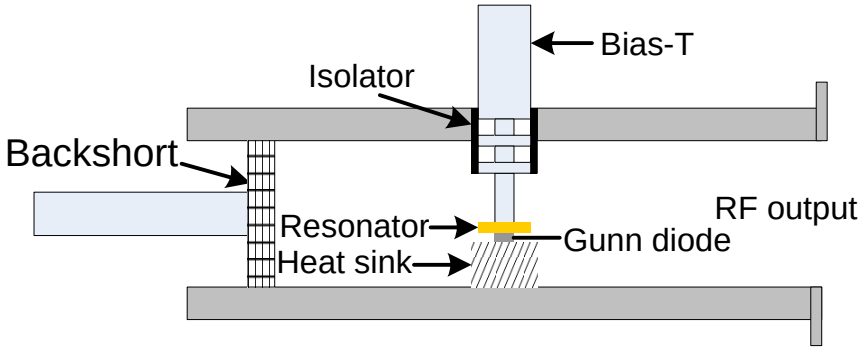


**Figure 2-2** Schematic circuit of a Gunn diode embedded in a rectangular waveguide cavity.

A Gunn diode is embedded into a metallic waveguide cavity with a disc resonator, radial line bias "T", a sliding backshort, and a heat sink. The Gunn diode has a cylindrical geometry. The anode and cathode are on the top and bottom, respectively. The disc resonator sitting on the top of the Gunn diode selects the oscillation frequency of the Gunn oscillator (the resonance frequency of the resonator determines the oscillation frequency). The radial line bias "T" allows DC bias to be applied on to the diode but prevents RF signals from leaking through. The heat sink beneath the Gunn diode helps dissipate heat generated as high current passes through the Gunn diode. The backshort serves as a tuner that improves circuit matching or frequency tuning by being manually moved forwards or backwards. The RF power is extracted from the rectangular waveguide. Gunn oscillators of

this type have advantages of low phase noise, high frequency stability and moderate power level. However, the frequency tuning range is usually limited.

Applications of Gunn devices have been extended to devices other than oscillators. With slightly lower doping level ( $NL < 10^{12}$ $cm^{-2}$), Gunn devices can be used as amplifiers. Detailed discussion can be found in Section 7-4 of [75], Chapter 7 in [47] and Chapter 6 in [76] and their references. Another proposed application of Gunn devices was for logic and functional circuits [77, 78]. It was believed that computing speed could be improved by a few orders if Gunn devices were used in the logic circuits [75].

Several phenomena have been found in Gunn devices, for example an acoustic wave can be generated along with RF oscillation in the crystal [79]. As a high electric field Gunn domain is formed within a device, the corresponding deformation of the semiconductor crystal is initiated due to the piezoelectric properties of the material i.e. GaAs [80]; once the Gunn domain dissipates in the anode region, the electric field decreases, and thus the semiconductor crystal returns its normal position. This periodic deformation and return process continues as the Gunn oscillation is generated and the corresponding acoustic wave can be coupled out by using a strong piezoelectric material such as $LiNbO_3$ [81]. The advantages of using Gunn diodes as acoustic sources are the small size and availability of high frequency.

In addition, it was also found that the high electric field Gunn domain could modulate light by either changing the refractive index of the material due to the electro-optical effect [82] or increasing absorption coefficient of light because of the Franz-Keldysh effect [83, 84]. The application of light modulation by Gunn domains in planar optical waveguide structures may be used for fast optical data processing [85]. On the other hand, light also affects the Gunn effect. The coherence and amplitudes of Gunn oscillations may be changed due to the alteration of uniformity of the electrons if the device is entirely exposed to light with different wavelength. Certainly, the illuminating position of the device has also an effect on the Gunn oscillations [86].

### 2.1.3 Commercialisation and Other Development of Gunn Devices

After more than ten years dramatic progress on theories, materials, devices, and circuits that made Gunn devices reach maturity in 1980s and 1990s. Commercial Gunn oscillators have shown excellent performance, such as low DC power consumption, moderate RF power, wide frequency tuning range, low phase noise, high temperature stability, and compact size. All these lead such devices to extensive applications in many fields, such as instrumentation, medical imaging, aerospace science, and defence. However, there was still much research going on in laboratories to explore any other potential of Gunn devices. Self-mixing, first reported in [87], is one of the many promising characteristics of Gunn devices. As is the case with other diode mixers (e.g. Schottky diodes), a Gunn diode has a nonlinear IV characteristics that allows an incident RF signal to mix with its own oscillation and produce a frequency difference and a sum. Thus, Gunn devices can potentially replace the separate oscillators and mixers in the transceiver frontend circuit of a conventional RF system because it can provide both local oscillator function and mixing function in a single device.

It has also been found that other semiconductor devices including metal semiconductor field effect transistors (MESFETs) [88, 89], heterojunction bipolar transistors (HBTs) [90, 91], and high electron mobility transistors (HEMTs) [92] may generate Gunn oscillations under certain circumstances. Certainly, such findings have pros and cons. On one hand, a variety of Gunn devices has been improved, therefore more choices are available for RF oscillator designs; on the other hand, the internal instability of Gunn oscillations made those devices difficult to use in building stable power amplifiers. In addition, the current instability in power HEMTs can also lead to unpredicted device failures [92]. Therefore appropriate techniques to suppress Gunn oscillations for their applications were required.

### 2.1.4 New Demands and Challenges for Gunn Devices

Since the new millennium, rapid growth in millimetre-wave and terahertz applications, such as high speed communications, anti-collision radar, medical and biological imaging, spectroscopy and security screening has attracted researchers to develop reliable sources from both the optical and electronic sides [3]. Although many such sources are available

from the optics side using quantum cascade lasers (QCLs) [93] or other technologies such as difference frequency generations [94, 95], the solid-state devices from the electronics side are still attractive due to their compact size and room temperature operation. These electronic millimetre-wave and terahertz sources include transistor based amplifiers and oscillators [19, 43], frequency multipliers [96], resonant tunnelling diode (RTD) oscillators [97], impact ionisation avalanche transit-time (IMPATT) diode oscillators [98, 99] and transferred electron (or Gunn) oscillators [6, 37]. Selective power and frequency performance of published signal sources was illustrated in Figure 1-1.

Early theoretical and numerical investigations showed that Gunn diodes are restricted to oscillation frequencies of approximately 100 GHz for GaAs, and 160 GHz for InP due to energy relaxation time and intervalley relaxation time [100]. Conventional vertical Gunn diodes are further limited to several tens of GHz by geometry, fabrication process, doping level and heating problems [100]. However, extraction of higher harmonic oscillations for sub-millimetre-wave and terahertz operation is possible if the output power at the fundamental frequency of oscillation is high enough [6]. Alternatively, using other materials that have lower relaxation time, higher mobility and higher energy bandgap, such as GaN, is another option to generate high power and high frequency Gunn oscillations [36]. Although theoretical and numerical investigations of such materials have shown great promise, experimental results are scarce except a report on the bias instability found in [37]. The lack of success in developing GaN Gunn diodes may come from the material problem, such as high level of defects. Nevertheless, new materials for high power and high frequency Gunn oscillation is still of interest to many researchers.

Apart from exploring new materials, there have been investigations on the well-established materials, such as GaAs and $In_xGa_{1-x}As$ for higher frequency operation. By reshaping or redesigning Gunn devices, experimental results have shown that oscillation frequencies over 100 GHz for the fundamental oscillation and 200 GHz for the second harmonic mode were possible [42, 101, 102]. Numerical investigations on Gunn-like oscillations in self-switching diodes [40] and nanowire diodes using InGaAs/InAlAs heterojunctures have shown such oscillations up to the terahertz frequency range [41]. However, the major challenge with these emerging devices is generating sufficient RF power. Nevertheless,

with continued advances in material growth and fabrication, Gunn devices for higher power and higher frequency applications are likely.

## 2.2 Historic Development of Planar Gunn Devices

In Section 2.1, the discussion has been concentrated on the development of Gunn devices in general. However, there have been two main types, namely vertical and planar Gunn devices. This classification of Gunn devices is based on the relationship between the direction of current flow (opposite to electron flow) and the epitaxial layers of the devices. For vertical Gunn devices the current flow is perpendicular to the epitaxial layers as shown in Figure 2-3a. On the contrary, the current flow is parallel to the epitaxial layers in planar devices as shown in Figure 2-3b. The initial interest in developing planar Gunn devices was the potential application for high speed logic devices as the planar geometry was ideal for mass production. However, the research on the Gunn devices for logic circuits was hindered in the 1970s by semiconductor material and device contact issues. Recently, the planar type Gunn devices have re-gained attention to the researchers due to high demand for millimetre-wave and terahertz sources. As will be discussed next, planar devices potentially meet the requirements and show advantages over vertical devices, especially as advances in wafer growth and fabrication technology make high quality semiconductor materials and nano-sized devices easily and reliably achievable.

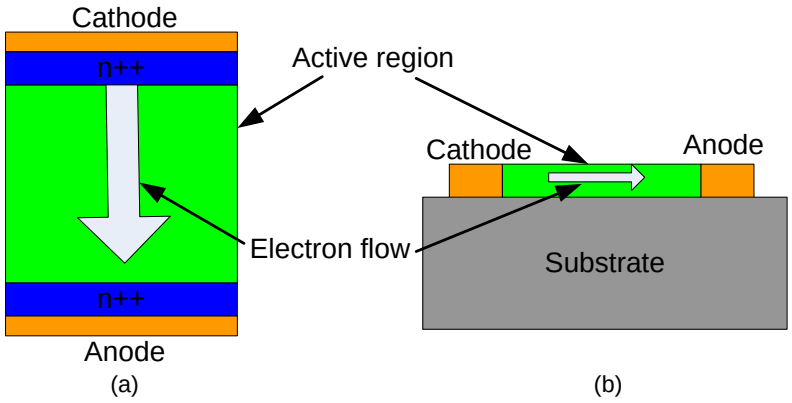


**Figure 2-3** Schematic view of electron flow in (a) a vertical Gunn diode and (b) a planar Gunn diode.

Compared with conventional vertical Gunn devices, planar Gunn diodes have several advantages since firstly they have lithographically controlled anode-cathode separation that determines the oscillation frequency of the device. This is not the case with conventional Gunn diodes because once the wafer of conventional Gunn diodes has been grown, the

anode-cathode separation is fixed. In other words, the transit-time oscillation frequency is fixed unless appropriate tuning circuits are applied. However, even then the circuit tuning is very limited. On the other hand, the planar structures allow great flexibility in adjusting the anode and cathode distance and therefore the oscillation frequencies. Potentially, such devices may oscillate at several hundreds of gigahertz or even terahertz frequencies once the distance is further reduced to submicron meters. Secondly, the planar structures are compatible with other planar circuitries, such as coplanar waveguide (CPW)-based components, so that complex circuits and systems, e.g. transceivers, can be fabricated on a single chip with a complete lithographic technology. Such seamless connection between signal sources and monolithic microwave integrated circuits (MMICs) will significantly improve the productivity and reproducibility, which is not achievable with conventional vertical Gunn devices because each individual device has to be cleaved and encapsulated in a cavity unless fabricated as per Figure 2-12. Certainly, the planar Gunn diodes may face challenges, such as low power or low phase noise compared to conventional Gunn diodes. However, planar structures allow combination of a large volume of devices to improve the power performance.

### 2.2.1 Planar Slab Type Gunn Diodes

The early planar Gunn diodes had very simple bar-like or “H” shaped structures as shown in Figure 2-4. A thin active layer (typically several tens of micrometers) of the n-doped material is grown directly onto a semi-insulating substrate. Metal alloys, such as Au/Ge and Ag/In/Ge [103, 104] are evaporated on the sides to form Ohmic contacts. The doping level and the thickness of the layer determine the device performance. However, it was found that such metallic contacts did not provide uniform electric field distribution underneath of the contact and high electric field was found near the edges of the channel so that early breakdown of the devices occurred [105].

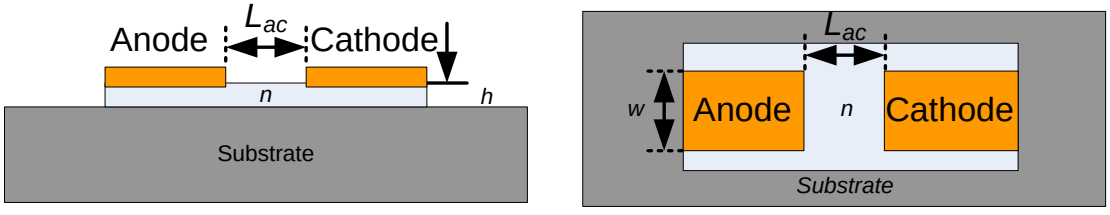


(a) (b)

**Figure 2-4** Planar type of Gunn diodes with metal alloyed Ohmic contacts. (a) Cross-sectional view, (b) Top view.

Several solutions have been reported to solve the contact problems. Figure 2-5 shows one of the solutions that was reported in [105] where an extra layer of highly doped material is grown. Another solution, as shown in Figure 2-6, is re-shaping the active region with the intention of improving the reproducibility for DC-biased operation due to the suppression of field-enhanced trapping of carriers in the channel [104]. A similar configuration has also been applied to investigate the Gunn effect in other materials, for example InP devices fabricated on a semi-insulating GaAs substrate [106, 107] or $In_{0.53}Ga_{0.47}As$ devices on a semi-insulating InP substrate [63, 108]. Alternatively, Figure 2-7 shows that complete side contacts were introduced by cleaving and isolating each individual device using a mechanical method and evaporating metal alloys on the sides to achieve uniform electric field at the edges using such an ideal contact [109].

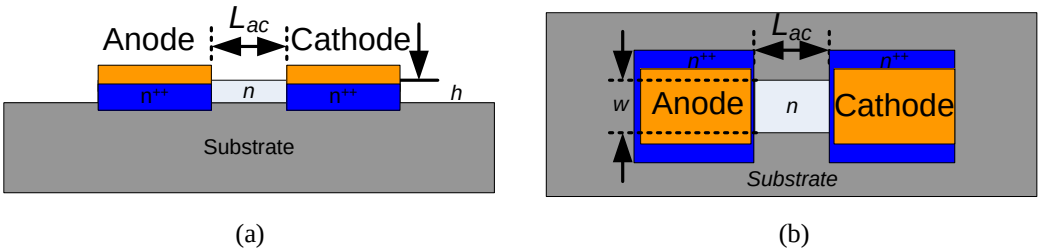


(a) (b)

**Figure 2-5** Planar type of Gunn diodes with re-grown highly doped material to improve contact performance. (a) Cross-sectional view, (b) Top view.

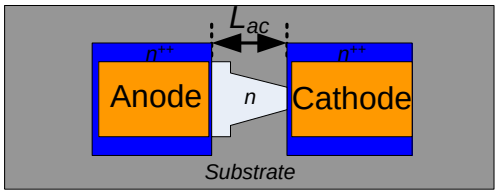


**Figure 2-6** Top view of a planar type Gunn device with tapered active region.

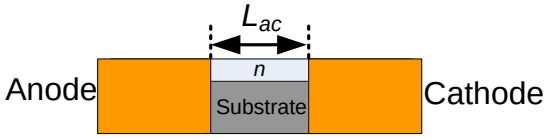


**Figure 2-7** Cross-sectional view of a planar Gunn diode with ideal contacts.

Figure 2-8 shows another type of planar type Gunn device that has concentric or semi-circular electrodes [110-113]. Due to the non-uniform distribution of the electric field, which has a radial line pattern, in between the two concentric contacts, the electric field is stronger near the central cathode electrode than that near the outer ring anode electrode. This means the electric field within the device induced by the external bias may exceed the threshold electric field of NDR at the near the cathode where Gunn domains nucleate and

lessen the threshold electric field at near the anode. In this case, the Gunn domains travel a shorter distance and recess before reaching the anode or even somewhere in the middle. Thus, the oscillation frequency is higher than usual transit-time mode of oscillation frequency. The characteristics of this type of planar Gunn devices is that it has a wide range of frequency tuning capability (i.e. from 1.5 GHz to 8.5 GHz for a 39 um device having geometry of Figure 2-8b [110]) because the higher the bias the longer the Gunn domains travel and the lower the oscillation frequencies. Certainly, the efficiency of such devices is low due to the existing positive resistance in the channel.

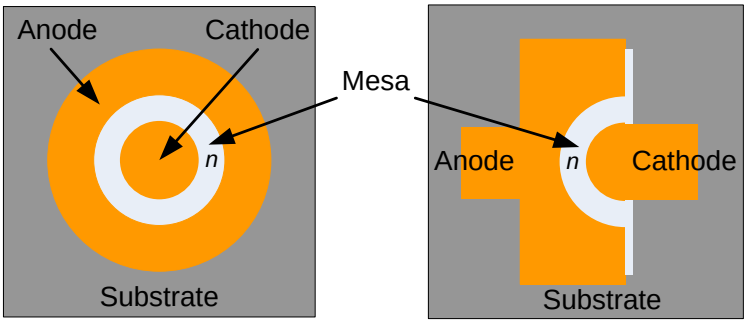


**Figure 2-8** Planar Gunn diodes having (a) concentric electrodes and (b) semi-circular electrodes.

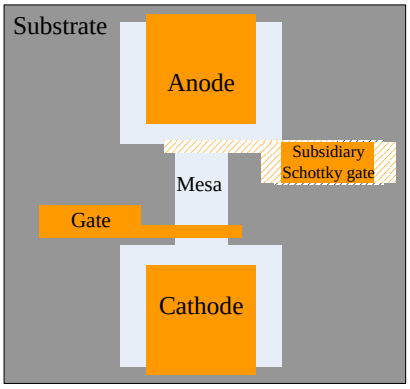


**Figure 2-9** A three-terminal Gunn device for logic circuit applications with a fourth subsidiary electrode.

Interest in using Gunn devices as high speed logic devices has led to the development of three terminal planar Gunn devices [114]. A third electrode (gate) is added near the Ohmic cathode of a normal two-terminal planar Gunn device to improve the input and output isolation and the triggering sensitivity. However, due to the existence of high electric field near the anode contact which causes device failure, a subsidiary Schottky gate may be added near the anode as shown in Figure 2-9 so that the high field layer is suppressed [115].

### 2.2.2 Field Effect Controlled Transferred Electron Device (FECTED) Oscillators

Field effect controlled (or cathode) transferred electron device (FECTED) oscillators have an MESFET-like structure that is planar and compatible with MMICs [116]. A schematic view of the device is shown in Figure 2-10. A moderately doped n-type GaAs or n-type InP layer is grown on the top of a semi-insulating substrate to form the active region. $In_{0.53}Ga_{0.47}As$ as an active layer for FECTED was investigated in [39]. The doping level is of the order of $10^{16}$ $cm^{-3}$. Three electrodes: Ohmic drain, Ohmic source and Schottky gate are fabricated on the top of the active region. The gate is extended onto the top of the source with an insulating layer to separate them.

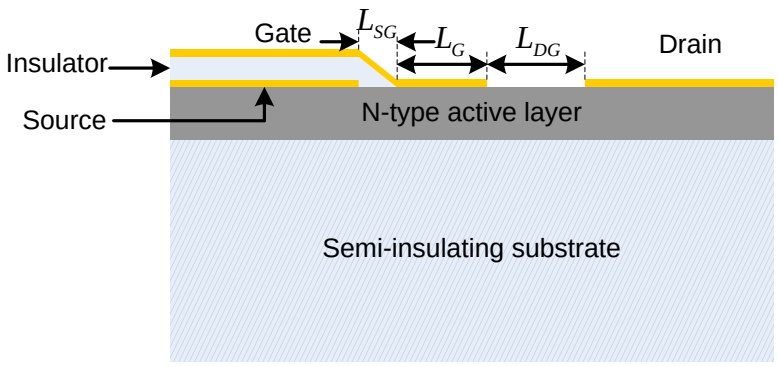


**Figure 2-10** Schematic cross-sectional view of a field effect controlled transferred electron device oscillator demonstrated in [116].

FECTEDs may have two operating modes depending on the relative values of the gate-source and drain-source voltages [39]. They are nontransit-time limited mode and dipolar-layer transit-time mode. The oscillation generated in nontransit-time limited mode is entirely from the negative differential resistance and the load circuits in the manner of the LSA mode of a transferred electron device demonstrated by Copeland [55]. However, the difference between these two modes is that while the LSA mode oscillation only uses the circuit to suppress Gunn domains; however for a FECTED oscillator the negatively biased Schottky gate injects current that avoids nucleation of Gunn domains. In the device a stationary high-field domain is formed between the gate and the drain and therefore a frequency-independent negative resistance is obtained. In addition, by tuning the Schottky gate bias voltage, the current injected from the gate changes therefore the device. The DC-RF conversion efficiency of this type of devices has been reported to be no more than 1.6% and the operating frequency ranges between 30 GHz and 60 GHz [116]. For the dipolar-layer transit-time mode, the resistive part of the device that contributes to additional loss in

the nontransist-time limited mode is suppressed. Therefore, the device efficiency will be enhanced. However, there has been no experimental evidence confirming this anticipated improvement so far [39].

### 2.2.3 Gunn or Gunn-like Oscillations in Heterojunction Devices

Investigations of transferred electron effects in heterojunction devices, which have a planar geometry, have been carried out [40, 41, 117-119]. A simplified view of heterojunction Gunn device epitaxial layers is shown in Figure 2-11. It has a channel sandwiched between two barrier layers. The channel layer could be one of those semiconductor materials having shown Gunn effect in the bulk form, such as GaAs and $In_xGa_{1-x}As$. The barrier layers have functions as found in HEMT devices: providing electrons for the channel, separating electrons from dopants, and preventing electrons from escaping from the channel. Thus, the barrier layers should have higher conduction band discontinuity as shown in Figure 2-11. The advantages of heterojunction Gunn devices over other planar Gunn devices are possible higher electron concentration in the active layer which is necessary for high frequency Gunn oscillations. The Monte Carlo simulation shows terahertz oscillations are achievable by reducing the electrode separation to submicron meters [41]. This may establish Gunn devices as potential sub-millimetre-wave and terahertz sources.

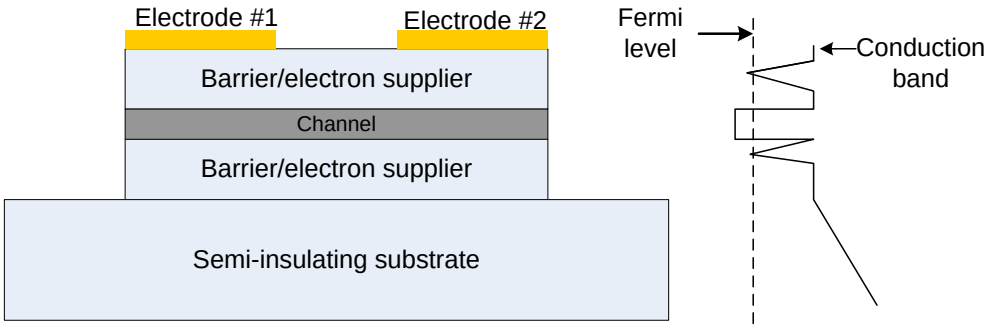


**Figure 2-11** Schematic view of the simplified epitaxial layers of a planar heterojunction Gunn device.

### 2.2.4 MMIC vertical Gunn oscillators

It should be mentioned here that MMIC-compatible vertical Gunn oscillators have been investigated recently in order to integrate the conventional bulky Gunn oscillators with planar MMIC technologies due to the high demand for the rapid growth of miniaturised circuits and systems [74, 120, 121]. Although the Gunn oscillators are called “planar”

Gunn diodes by those authors, they are still vertical devices having the direction of current flow normal to the epitaxial layers as shown in Figure 2-12. This structure allows the conventional Gunn diodes that are commonly packaged and constructed in bulky cavities to be smoothly integrated with other planar circuitries so that the entire system becomes highly compact. However, due to the limitations of intrinsic properties of the conventional Gunn diodes, such as doping level, mesa thickness and heat dissipation, the MMIC-compatible vertical Gunn diodes are not believed to operate at higher frequencies.

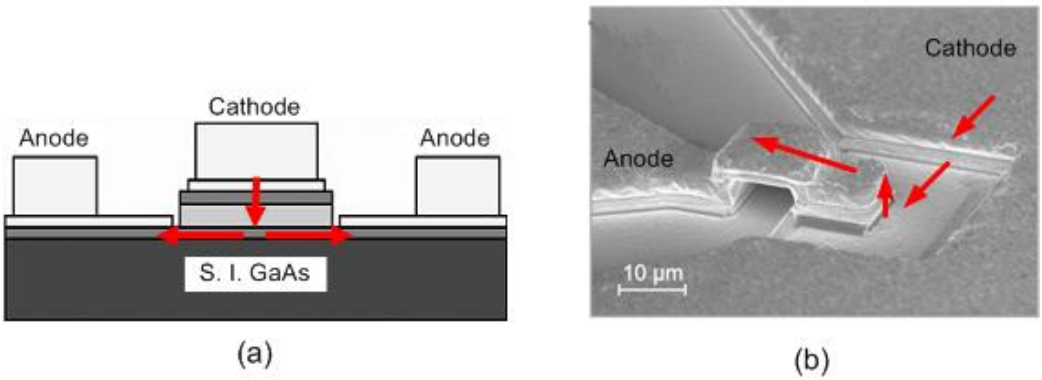


**Figure 2-12** MMIC-compatible vertical Gunn diodes. (a) Schematic view of current flow and epitaxial layers [120], (b) an SEM image shown in [74]. Arrows indicate electron flow direction.

## 2.3 Theory and Physics

### 2.3.1 Basic Properties of GaAs

N-type bulk GaAs has been the most widely studied semiconductor material for Gunn devices. Before introducing the transferred electron effect theory, a brief summary on the fundamental properties of GaAs materials (especially n-type GaAs where appropriate and applicable) is given.

#### *2.3.1.1 Basic Material Properties of GaAs*

Gallium arsenide is a compound semiconductor material consisting of 1:1 gallium (group III in the periodic table) and arsenic (group V in the periodic table). It has a zinc blende crystal structure that is commonly seen in other III-V compound semiconductor materials. Each cell of this structure consists of two sites of face-centred cubic lattices e.g. Ga and As for GaAs as shown in Figure 2-13 [76]. Material properties in different directions and planes of the cell in the microscopic scale or the entire crystal in the macroscopic scale are different. Using Miller indices is convenient to define the directions and planes in the

crystal. Some basic properties of GaAs are summarised in Table 2-I [122]. For comparison, basic properties of InP (the second most popular material for Gunn oscillations) and GaN (that is the most recently studied material for Gunn oscillations) are also summarised in the same table. Important parameters, such as band gap, energy separation between $L$ and Γ valleys and electron effective masses that are related to Gunn oscillation are highlighted in bold.

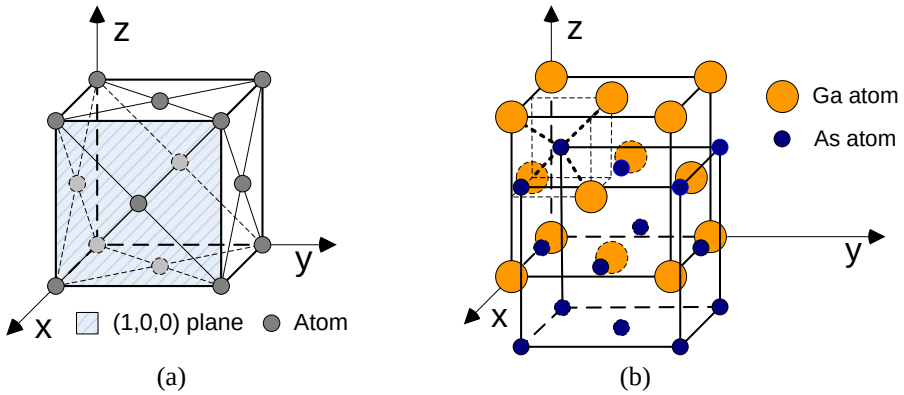


(a) (b)

**Figure 2-13** (a) A face-centred cubic lattice, and (b) a zinc blende crystal.

**Table 2-I** Basic properties of GaAs [122], InP [123] and GaN [124].

| Parameters | GaAs | InP | GaN | |
|---|---|---|---|---|
| Crystal structure | Zinc blende | Zinc blende | Wurtzite | Zinc blende |
| Lattice constant | 5.6532 | 5.8687 | 3.16-3.19(x)<br>5.12-5.19(z) | 4.52(x) |
| Thermal conductivity (W/cm•°C) | 0.55 | 0.68 | 1.3 | 1.3 |
| Breakdown field(V/cm) | $4\times10^5$ | $5\times10^5$ | $3.3\times10^6$ | $5\times10^6$ |
| Low field mobility ($cm^2/V\bullet s$) | 8500 | 5400 | 440 | 1000 |
| **Band gap at 300 K(eV)** | **1.424** | **1.344** | **3.39** | **3.2** |
| **Energy separation between *L* and *Γ* valleys** | **0.29** | **0.59** | **4.5-5.3** | **1.6-1.9** |
| Energy separation between *X* and *Γ* valleys | 0.48 | 0.85 | 4.7-5.5 | 1.4 |
| Dielectric constant (static) | 12.9 | 12.5 | 8.9 | 9.7 |
| Dielectric constant (high frequency) | 10.89 | 9.61 | 5.35 | 5.3 |
| **Effective electron mass in the central valley** | **$0.063m_0$** | **$0.08m_0$** | **$0.2m_0$** | **$0.13m_0$** |
| Electron affinity (eV) | 4.07 | 4.38 | 4.1 | 4.1 |
| Electron diffusion coefficient ($cm^2/s$) | ≤200 | 130 | 25 | 25 |
| Effective conduction band density of states ($cm^{-3}$) | $4.7\times10^{17}$ | $5.7\times10^{17}$ | $2.3\times10^{18}$ | $1.2\times10^{18}$ |

### *2.3.1.2 Band Structures and Electron Effective Mass*

The conduction band of GaAs has three main valleys in three different directions of the momentum as shown in Figure 2-14. The minimum conduction band (central valley or Γ

valley) is right above the maximum valence band at the centre of the Brillouin zone. The energy separation between them is known as band gap, in this case 1.42 eV for GaAs. The next higher conduction band minimum $L$ valley is located in (100) direction and the energy between $L$ valley and $\Gamma$ valley is 0.29 eV. The highest conduction band minimum is 0.48 eV higher than $L$ valley in the direction of (111).

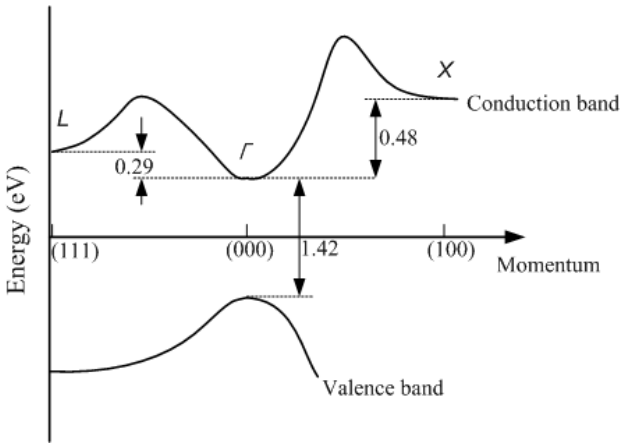


**Figure 2-14** Energy band structure of GaAs.

Since the electron effective mass $m_{eff}$ is determined by the electron energy $E_e$ and its momentum $p_e$ as

$$m_{eff} = \left( \frac{d^2 E_e}{dp_e^{\,2}} \right)^{-1} \tag{2.3.1}$$

and the conduction band in different valleys has different energy levels, therefore the electron effective masses are different in different valleys. For example, electrons are heavier in the $L$ valley ($m_{eff}^{L} = 0.85 m_0$, $m_0$ is the free-electron mass) than in the $\Gamma$ valley ($m_{eff}^{\Gamma} = 0.063 m_0$). It is worth mentioning that both energies of the conduction band minima and electron effective mass are dependent on temperature and pressure [76].

*2.3.1.3 Electron Transport*

Transport of carriers (electrons and holes) in semiconductors has several factors, such as drift, diffusion, recombination, generation, thermionic emission, tunnelling, and impact ionisation. Introductions to diffusion, drift and impact ionisation are only given here.

- **Diffusion**

Diffusion occurs when there is a carrier concentration gradient between two parts in the same semiconductor or between two different semiconductors when they are placed

together. Carriers continue to diffuse from one side where the concentration is high to the other side where the concentration is low until an equilibrium status is satisfied. The flux of carriers $F$ (i.e. $F_n$ for electrons) is related to the carrier concentration gradient, $dn/dx$ by the diffusion coefficient $D_n$, thus the electron diffusion current can be written as [76]

$$J_n = -qF_n = qD_n \frac{dn}{dx} \tag{2.3.2}$$

- **Drift**

At room temperature (i.e. 300 *K*), majority electrons residue in the Γ valley in n-type GaAs. Electrons gain kinetic energy from heat and scatter when colliding with atoms and impurities. The thermal velocity $v_{thermal}$ is given by [76]

$$v_{thermal} = \left( \frac{3kT}{m_{eff}} \right)^{\frac{1}{2}} \tag{2.3.3}$$

Under thermal equilibrium, electron movement is random in all directions. Therefore, the net velocity of electrons is zero and there is no net current flowing through the crystal.

However, once a small electric field $E$ is applied onto the crystal, the randomly scattered electrons are aligned along the electric field by the force $qE$ and travel at a combined thermal velocity $v_{thermal}$ and the electric field induced drift velocity $v_{drift}$ in the direction opposite to the electric field direction until they collide with other electrons. The drift velocity can be derived from the conservation of momentum [76]:

$$qE\tau_c = m_{eff} v_{drift} \tag{2.3.4}$$

where $\tau_c$ is the mean free time between collisions. Thus, the drift velocity is given by [76]

$$v_{drift} = \left( \frac{q\tau_c}{m_{eff}} \right) E \tag{2.3.5}$$

and the drift current density is given by [76]

$$J_{drift} = qnv_{drift} \tag{2.3.6}$$

where $n$ is the number of electrons within the crystal. It can be seen from Equation 2.3.5 that the drift velocity is proportional to the applied electric field by a constant $\mu$. This is known as mobility and defined as [76]:

$$\mu = \frac{q\tau_c}{m_{eff}} \tag{2.3.7}$$

Two factors, electron effective mass and mean free time, affect the mobility, therefore the drift velocity and the drift current. The electron effective mass is related to the energy level or the conduction band and has been discussed in Section 2.3.1.2. The mean free time is determined by various scattering mechanisms, such as lattice scattering, impurity scattering, polar optical scattering, acoustic scattering, and intervalley scatterings. However, the first two scattering mechanisms dominate. The lattice scattering results from thermal vibrations of the lattice atoms and it is sensitive to temperature. The higher the temperature the higher the scattering rate, and the lower the mean free time the lower the mobility. The impurity scattering comes from the deflection of an electron (or a hole) passing by an ionised dopant impurity (donor or acceptor). The higher the doping level the higher the impurity scattering and the lower the mobility. The impurity scattering becomes weaker when temperature increases because the rise of temperature increases the charge carrier's thermal velocity and thereafter reduces the possibility of Coulomb force effective onto the charge carrier.

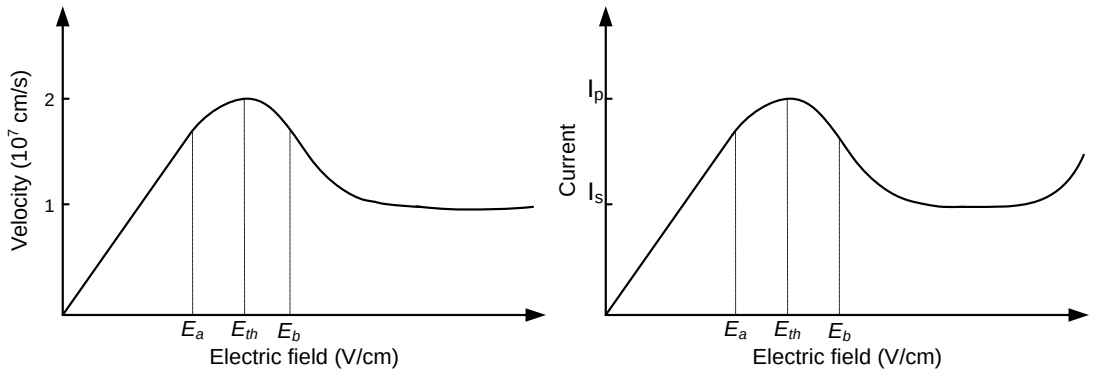


**Figure 2-15** Electron velocity and current versus electric field of GaAs.

The mobility remains constant at low electric fields (up to several hundred V/cm for GaAs) when other parameters, such as doping level, temperature and pressure are fixed. Therefore, a linear relationship between the applied field and the drift velocity and in turn the linear relationship between current and electric field is set up as shown in Figure 2-15. However, such a linear relationship is distorted as the applied electric field exceeds a critical value or threshold electric field $E_{th}$ (e.g. approximately 3.2 kV/cm for GaAs). The distortion comes from the change of mobility $\mu$. From Equation 2.3.7 one can see the change of electron effective mass leads to the change of mobility assuming the mean free time is fixed at high electric fields. The change of electron effective mass may be due to the relocation of electrons between the satellite $L$ valley and the central $\Gamma$ valley. Under low electric field, most electrons stay in the $\Gamma$ valley. However, when electric field increases higher and higher, electrons gain more and more energy and therefore become "hotter" and "hotter".

Once the electric field reaches the critical threshold value $E_{th}$ some electrons may have gained enough energy to conquer the intervalley barrier between $L$ valley and $\Gamma$ valley (0.29 eV for GaAs) and "jump" into the $L$ valley. Because electrons are heavier in the $L$ valley than in the $\Gamma$ valley as discussed in Section 2.3.1.2, the relocation of electrons leads to the change of the average electron effective mass and therefore the electron mobility. If we assume the total number of electrons in the conduction band is *n*, then the number of electrons in the $\Gamma$ valley and in the $L$ valley are $n_a(E)$ and $n_b(E)$, respectively that are electric field dependent. The electron motilities in the $\Gamma$ valley and $L$ valley are $\mu_a$ and $\mu_b$, respectively. Thus the average mobility $\bar{\mu}(E)$ is given by [76]

$$\bar{\mu}(E) = \frac{\mu_a n_a(E) + \mu_b n_b(E)}{n_a(E) + n_b(E)} \tag{2.3.8}$$

and the electron drift velocity is then

$$\begin{aligned} v_{drift}(E) &= \bar{\mu}(E) \cdot E = \frac{\mu_a n_a(E) + \mu_b n_b(E)}{n_a(E) + n_b(E)} \cdot E \\ &\approx \frac{\mu_a n_a(E) E + n_b(E) v_s}{n_a(E) + n_b(E)} \end{aligned} \tag{2.3.9}$$

where $v_s \approx \mu_b E$ at high electric fields. Defining the relative number of electron occupation in the $L$ valley as

$$\eta(E) = \frac{n_b(E)}{n_a(E) + n_b(E)} \tag{2.3.10}$$

Putting Equation 2.3.10 into Equation 2.3.9 and differentiating both sides with $E$, we have

$$\frac{dv_{drift}(E)}{dE} = \mu_a [1 - \eta(E)] + [v_s - \mu_a E] \frac{d\eta(E)}{dE} \tag{2.3.11}$$

From Equation 2.3.11 one can see that the differential mobility becomes negative when

$$\frac{d\eta(E)}{dE} > \frac{1 - \eta(E)}{E - v_s / \mu_a} \tag{2.3.12}$$

The drift velocity and electric field relationship at room temperature (300 $K$) can also be approximated using a numerical method as

$$v_{drift}(E) = \frac{\mu_a E + v_s (E/E_{th})^4}{1 + (E/E_{th})^4} \tag{2.3.13}$$

- **Impact Ionisation**

If the electric field continues increasing as can be seen in Figure 2-15b, the *I-E* curve starts rising again after reaching the minimum. The rise of current comes from another important high electric field phenomenon that is called impact ionisation. The impact ionisation process (also known as the avalanche process) takes place when electron-hole pairs are generated if some electrons have gained high enough kinetic energy to break the band gap $\Delta E_g$. The avalanche process is illustrated in Figure 2-16 [125]. Once a high energy electron (designated as 1 in Figure 2-16) collides with the lattice, a bond is broken and an electron-hole pair (designated 2 and 2') is generated. The electron (2) is also accelerated by the high electric force and trigger another pair of electron-hole (3 and 3') and the hole (2') also gains enough energy from the electric force and generate a third pair of electron-hole (4 and 4'). This process continues and the rate of generating electron-hole pairs $G_A$ is governed by [125]

$$G_A = \frac{1}{q}\left(\alpha_n |J_n| + \alpha_p |J_p|\right) \tag{2.3.14}$$

where $\alpha_n$ and $\alpha_p$ are electron and hole ionisation rate, respectively. They are defined by the number of electron-hole pairs generated by an electron or a hole per unit distance travelled. $J_n$ and $J_p$ are the electron and hole current densities, respectively.

The impact ionisation may lead to a breakdown for many devices including a PN junction. However, it can be used to make useful high frequency amplifier and oscillator devices, such as IMPATT diodes. For Gunn devices, when the domain electric field is high enough to break the energy band gap, impact ionisation also occurs. Not only is light with radiation wavelength of 0.9 μm emitted from the device but also the Gunn oscillations become incoherent [126].

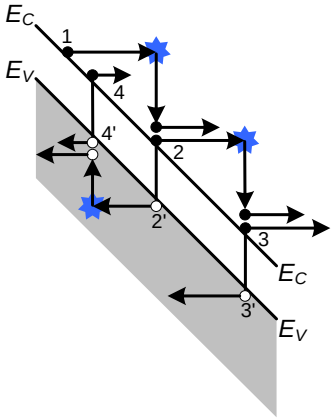


**Figure 2-16** Schematic view of avalanche process for showing the impact ionisation [125].

### 2.3.2 Gunn Domains and the Transit-time Mode of Oscillations

*2.3.2.1 Illustration of Domain Formation and Growth*

In the preceding section the transferred electron effect theory was briefly described. The transferred electron theory is the physical mechanism of the Gunn effect. It explains how the negative differential mobility (NDM) or NDR is generated. However, it does not explain how the continuous coherent current oscillations are produced. Kroemer pointed out the oscillations are due to the periodic nucleation and disappearance of travelling space-charge instability domains [44]. In fact, Gunn also conducted another important experiment in which he used a capacitive probe to measure the potential distribution across a long GaAs sample. He found high electric field domains (later called Gunn domains) being formed near the cathode accompanied by current reduction and travelling towards the anode where the domains disappear and the current returns to normal level. Once one domain disappears at the anode, another domain is nucleating near the cathode [52]. This cycling process of domain generation and disappearance is the origin of the current oscillation that is more vividly illustrated in Figure 2-17.

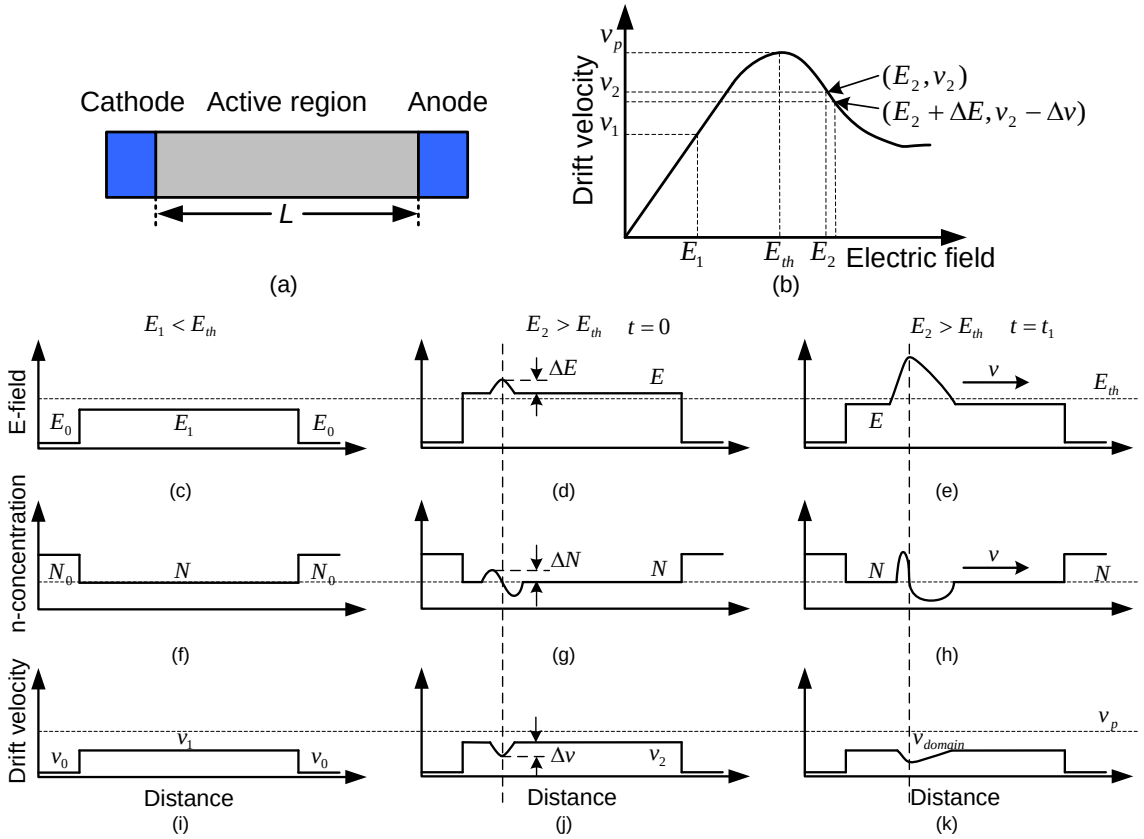


**Figure 2-17** Illustration of electron concentration and electron drift velocity variation in an n-type GaAs at low and high electric fields.

Assume a piece of n-doped bulk GaAs sample has a length of $L$ and a doping level of $N$ (Figure 2-17a). The anode and the cathode are Ohmic and have very high doping level $N_0$ ( $N_0 >> N$ ) as shown in Figure 2-17f. The electric field $E_0$ and drift velocity $v_0$ are minimal in the Ohmic contact regions (Figure 2-17c and i). When an external bias $V$ is applied onto the sample between anode and cathode, an electric field $E$ is induced within the sample. Ignoring the potential drops in Ohmic contact regions, the electric field is $E = V/L$. For $E = E_1 < E_{th}$ (Figure 2-17b and c), the electron drift velocity $v_1$ (Figure 2-17i) is proportional to the electric field $E_1$ (Equation 2.3.5).

If the applied electric field is greater than the threshold field e.g. $E = E_2 > E_{th}$ (Figure 2-17b and d), a small fluctuation of the electron concentration $\Delta N$ (Figure 2-17g), which may result from non-uniform doping or noise, would lead to an increase of electric field $\Delta E$ or an electric field domain (Figure 2-17d). As can be seen in Figure 2-17b, the increase in electric field therefore leads to a reduction in drift velocity of $\Delta v$ in Figure 2-17j. The total current through the sample drops too. At the same time, the electric field outside the domain drops because the total applied voltage between anode and cathode is fixed.

If the applied electric field remains unchanged, at the leading edge of the domain electrons within the domain travel more slowly than the electrons ahead and outside the domain that are accelerated at a lower electric field, thus the depletion region is widening (Figure 2-17h). On the other hand, at the trailing edge of the domain electrons which are behind and outside the domain travel faster than the electrons within the domain, therefore more and more electrons accumulate and the accumulation layer is enhanced (Figure 2-17h). As a consequence, the high field domain keeps growing while moving towards the anode and the space charge dipole also keeps developing. Meanwhile, both the electric field outside the domain and the electron drift velocity within domain keep reducing (Figure 2-17k).

After a short while, when the domain velocity is equal to the electron drift velocity outside the domain, then the domain stops growing but travels to the anode at a constant speed $v_{domain}$ until it disappears at the anode where the electric field is minimal. Meanwhile, the electric field within the sample is restored to its original format $E_2$ and a new domain

starts nucleating at near the cathode end of the sample again. This periodic cycle of domain nucleation and disappearance leads to the coherent current oscillation observed by Gunn. The oscillation frequency is approximately determined by the transit-time of the domain or the ratio of the domain velocity to the distance, $L$, that the domain travels. It is given by

$$f = \frac{v_{domain}}{L} \tag{2.3.15}$$

*2.3.2.2 Modelling the Domain Growth Using an Analytical Approach*

The domain growth process can be modelled by using an analytical approach. Assume the sample is biased at the unstable region (i.e. NDR region) with a constant value of electric field $E_2$, electron concentration of $N$ and drift velocity of $v_2$ are shown in Figure 2-17b. When small-signal components are superimposed onto the static parts, they become [47, 76]

$$E = E_2 + \Delta E \tag{2.3.16 a}$$

$$n = N + \Delta N \tag{2.3.16 b}$$

$$v = v_2 - \Delta v \tag{2.3.16 c}$$

$$J = J_2 + \Delta J \tag{2.3.16 d}$$

$$D = D_0 + \left(\frac{\partial D}{\partial E}\right)_0 \Delta E \tag{2.3.16 e}$$

The governing equations are one-dimensional (x-axis) current, continuity, and Poisson's equations as follows:

$$J = qnv - q\frac{\partial (Dn)}{\partial x} \tag{2.3.17 a}$$

$$\frac{\partial J}{\partial x} + \frac{\partial qn}{\partial t} = 0 \tag{2.3.17 b}$$

$$\frac{\partial E}{\partial x} = \frac{q}{\varepsilon_r \varepsilon_0}(n - N) \tag{2.3.17 c}$$

Substituting Equations 2.3.16 into Equations 2.3.17 and eliminating $\Delta E$ and $\Delta J$, we get

$$D_0 \frac{\partial^2 \Delta N}{\partial x^2} - v\frac{\partial \Delta N}{\partial x} + \frac{\Delta N}{\tau_n} = \frac{\partial \Delta N}{\partial t} \tag{2.3.18}$$

where $\tau_n = \dfrac{\varepsilon_r \varepsilon_0}{qN\, \partial v / \partial E}$ and $v = v_2 - \dfrac{qN}{\varepsilon_r \varepsilon_0}\left(\dfrac{\partial D}{\partial E}\right)_0$.

The solution to Equation 2.3.18 has the following form:

$$\Delta N \propto \exp\left[\left(\tau_n^{-1} - D_0 k^2\right)\cdot t\right]\exp\left[jk(x-vt)\right] \tag{2.3.19}$$

where $k$ is the wave number. As $\tau_n^{-1} >> D_0 k^2$ for most Gunn devices, so the growth exponent is dominated by $\tau_n$. Thus, the criterion for the growth of charge fluctuation in one transit (the transit–time is the inverse of Equation 2.3.15) is $\exp(t/\tau_n) > 1$, or $NL > \frac{\varepsilon_r \varepsilon_0 v}{q\, dv/dE}$, which is approximately $10^{12}$ cm$^{-2}$ for GaAs. The $NL$ product sets up a criterion for the operation mode of Gunn devices. Below this value, charge fluctuation is unlikely to grow, an amplifying mode is operational; an unstable oscillation mode is expected when the $NL$ value is exceeded.

*2.3.2.3 Analytical Method for Stable Domain Propagation and the Equal Area Rule*

As mentioned in Section 2.3.2.1, a domain does not grow indefinitely but saturates and travels at a constant speed of $v_{domain}$ to the anode. In this case, the following assumptions are valid for analysing the propagation of a stable domain in an analytical approach:

- The influence of anode and cathode on the domain motion is neglected.
- The shape of the domain does not change.
- The static doping level is $N$.

The electric field outside the domain is $E_R(t)$. The maximum electric field in the domain is $E_P$. The starting point of the domain is $x_0(x,t)$ that is space and time-dependant. The length of the domain is $x_L$. Therefore the electric field $E_D(y = x - v_{domain}\cdot t)$ at any point within the domain is a function of $y$ that is the relative distance to $x_0(x,t)$. The electron velocity outside the domain is $v_r$. Other parameters have been defined in Equation 2.3.16 or before. The Poisson equation 2.3.17c is rewritten for the domain as

$$\frac{\partial E_D(y)}{\partial y} = \frac{q}{\varepsilon_r \varepsilon_0}(n - N) \tag{2.3.20}$$

Put Equation 2.3.20 and Equation 2.3.17a into Equation 2.3.17b, and divide Equation 2.3.20, we get

$$\frac{q}{\varepsilon_r \varepsilon_0}\frac{\partial[Dn]}{\partial E} = \frac{n[v(E) - v_{domain}] - N(v_r - v_{domain})}{n - N} \tag{2.3.21}$$

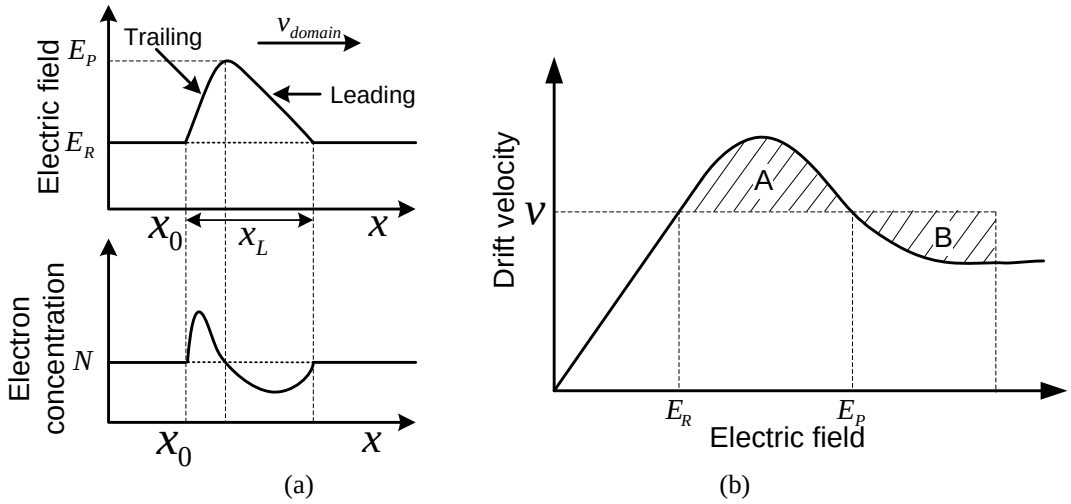


**Figure 2-18** Electric field and electron concentration for a fully grown domain.

Figure 2-18 a shows that $n$ is a double-valued function of $E$. The leading edge of the domain corresponds to the depletion region of the electron concentration and the trailing edge corresponds to the accumulation region. The electron concentration has the static value of $N$ at $x_0$, $x_0 + x_L$, and $x_{E_P}$ where the electric field of the domain is the maximum.

Now assume the diffusion coefficient is field-independent and solve Equation 2.3.21 by integrating with boundary conditions of $n = N$ at $E = E_R$ and $E = E_P$, we can get [47]

$$\frac{n}{N} - \ln\frac{n}{N} - 1 = \frac{\varepsilon_r \varepsilon_0}{qDN}\int_{E_R}^{E_P} dE\left\{\left[v(E) - v_{domain}\right] - \frac{N}{n}\left(v_r - v_{domain}\right)\right\} \tag{2.3.22}$$

Therefore Equation 2.3.20 yields

$$\int_{E_R}^{E_P} dE\left\{\left[v(E) - v_{domain}\right] - \frac{N}{n}\left(v_r - v_{domain}\right)\right\} = 0 \tag{2.3.23}$$

When the first term of Equation 2.3.23 vanishes, that is

$$\int_{E_R}^{E_P} v(E)dE = v_{domain}\left(E_P - E_R\right) \tag{2.3.24}$$

Equation 2.3.24 states the classic equal area rule that is the area under $v(E)$ curve from $E_r$ to $E_P$ (RHS of Equation 2.3.24) must be equal to the rectangle: LHS of Equation 2.3.24. This is illustrated in Figure 2-18b. The equal area rule indicates the condition of velocity for the stable domain propagation.

### 2.3.3 Other modes of Oscillation

In addition to the transit-time mode of oscillation, there are several other modes of oscillation that are related to the transferred electron effects. These oscillation modes include limited space-charge accumulation (LSA) mode, quenched domain mode and hybrid mode. All these oscillation modes use negative differential resistance that is the consequence of transferred electron effect to generate circuit-controlled oscillations. These oscillations are not restricted by the transit-time oscillation frequency, but on the other hand they could be a few times higher than the transit-time oscillation frequency. In this subsection, other modes of oscillation are briefly discussed.

#### *2.3.3.1 The Limited Space-charge Accumulation Mode of Oscillation*

The Limited Space-charge Accumulation (LSA) mode of oscillation was first investigated by Copeland [55, 56]. Important features of this type of oscillation include the frequency of operation, which is determined by the frequency of the circuit, is higher than the transit-time mode of oscillation and the power output and efficiency are higher than when the same device is operated in the transit-time mode [55].

The basic principle of this mode of oscillation is to prohibit Gunn domains from forming in the channel while the device is biased in the NDR region (unstable region) so that the transferred electron device can be used as a regular one-port NDR device, such as resonant tunnelling diodes and IMPATT diodes to build an oscillator. The necessary condition of suppressing the formation of Gunn domains is the new oscillation frequency must be higher than the transit-time mode oscillation frequency, thus the fast voltage swing makes Gunn domains not quick to form. The oscillator made using LSA mode of operation relies entirely on the negative differential resistance characteristics of a transferred electron device, and the oscillation frequency is determined by the entire circuit.

Figure 2-19a shows a canonical oscillator circuit using a one-port NDR device and Figure 2-19b shows a small-signal equivalent circuit of a Gunn diode. The diode has a frequency and bias-dependant negative resistance $R_{Source}$, an intrinsic capacitance $C$ and a small

inductance $L$ contributed by the electrode contacts. The inductance is negligible at lower microwave frequencies; however, it may affect the circuits at millimetre-wave frequencies. A more complicated small-signal equivalent circuit including parasitics from packaging is given in [47].

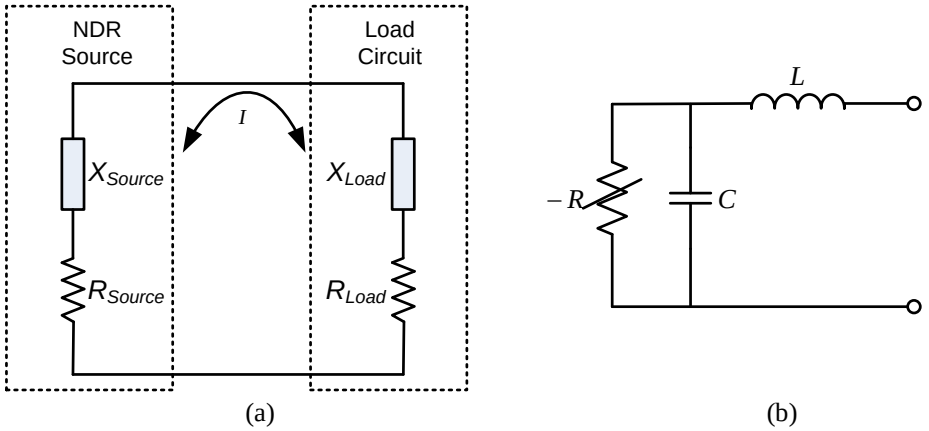


**Figure 2-19** (a) Schematic circuit for any one-port NDR oscillators, (b) Simplified small-signal equivalent circuit of a Gunn diode.

The basic condition of the oscillation is to satisfy

$$Z_{Source} + Z_{Load} = 0 \tag{2.3.25}$$

or

$$R_{Source} + R_{Load} = 0 \tag{2.3.26 a}$$

$$X_{Source} + X_{Load} = 0 \tag{2.3.26 b}$$

However, a more rigorous condition must be satisfied for stable oscillation [127]. This is often provided by a high-Q circuit. More detailed one-port NDR oscillator design rules can be found elsewhere [128].

*2.3.3.2 The Quenched Domain Mode of Oscillation*

Carroll described another mode of oscillation for a transferred electron device in which the oscillation frequency is also entirely determined by the resonant circuits [54]. Unlike the LSA mode of oscillation in which the Gunn domains are prohibited, in the quenched domain mode of oscillation, Gunn domains are allowed to be formed and travel towards the anode; however, they are "quenched" before reaching the anode. Thus, the total travel distance of a domain $L_{quenched}$ is shorter than that in transit-time mode $L$. According to

Equation 2.3.15, the oscillation frequency in this oscillation mode is higher than that in transit-time mode.

In Carroll's report, a Gunn diode operating at 2 GHz in its transit-time mode may have produced oscillation frequencies between 3.9 GHz and 31 GHz when placed in different resonant circuits. The oscillation frequencies and the corresponding power levels are summarised in Table 2-II.

**Table 2-II** Measured oscillation frequencies and power in different resonant cavities for a Gunn diode that has a transit-time mode of oscillation of 2 GHz [54].

| Frequency (GHz) | 2 | 3.9 | 8 | 9.4 | 22 | 31 |
|---|---|---|---|---|---|---|
| Power (mW) | NG | 150 | 50 | 12 | 1 | 0.1 |

## 2.4 Conclusion

In this chapter, the literature covering the development of Gunn devices has been reviewed. Special attention was given to the overall progress of development of planar Gunn devices which are directly related to the basis of this thesis. Brief, but focused, discussions on the theories and physics of the Gunn effect or transferred electron effect have also been included.

# CHAPTER 3

# DEVICE CHARACTERISATION METHODOLOGIES

In the previous chapter, an introduction to the development and physics of Gunn devices, and in particular *planar* Gunn devices, has been given. An important contribution of this PhD research concerns the characterisation of Gunn devices and passive components which will be discussed in this chapter. Since planar Gunn devices are semiconductor devices, electrical properties, such as material resistivity, carrier concentration and mobility, contact resistance, and current-voltage (IV) characteristics are important factors in determining devices' functionality, reliability, and reproducibility. Thus, appropriate procedures and methods of characterising these parameters are needed to assist in accurate design of planar Gunn oscillators. Furthermore, since planar Gunn devices are millimetre-wave signal sources, analysing their spectrum and power performance is another necessity. Therefore, accurate and reliable spectrum and power characterisation methodologies are essential.

Attention is also paid to measurement methodologies of passive components because the passive components are important building blocks of planar Gunn oscillators (a detailed discussion on passive components and integrated planar Gunn oscillators will be provided in Chapter 6). The commonly used instrument for characterising passive components is a vector network analyser (VNA); the basic principles and calibration methods of the VNA are given in this chapter. Since the passive components used in this work may operate in a very wide frequency range (e.g. from microwave to the upper end of millimetre-wave frequency), in different structures (e.g. rectangular or on-wafer planar waveguides) or even have various numbers of ports (e.g. one, two or three ports), the VNA setup and measurement methodologies are different. Hence, a discussion on the different applications of the VNA will also be included here. Moreover, VNAs have also been found to be capable of detecting the fundamental and harmonic oscillations of oscillators or signal

sources if certain care is taken. This feature of VNAs has been used in frequency identification or analysis in the development of planar Gunn devices, especially for identifying the devices' fundamental and harmonic oscillation frequencies. The VNA can therefore serve as a complementary tool to conventional spectrum analysers under certain circumstances. A detailed discussion on this topic is also included in this chapter.

The organisation of this chapter is as follows: Section 3.1 focuses on the basic characterisation methodologies of semiconductor materials and contacts. This is followed, in Section 3.2, by an introduction to the principles, calibration methods and procedures of vector network analysers, and their application to characterisation of passive networks. In Section 3.3 the spectrum and power measurement system setups and calibration techniques for characterising planar Gunn devices at millimetre-wave frequency range are described. Additionally, the one-port load-pull measurement technique, that has been devised to investigate the loading effects on the power and frequency performance of planar Gunn devices, is also included in this section. Finally, a discussion on the analysis of using VNAs to detect oscillator oscillation frequencies will be given in Section 3.4.

## 3.1 Basic Characterisation Methodologies for Semiconductor Materials and Contacts

There are a large number of parameters that need to be characterised to fully understand semiconductor materials so that they can be used for further applications. For example, basic physical properties include thermal, electrical, and mechanical properties. However, only some of these parameters, such as material resistivity, carrier concentration, and carrier mobility, may differ from one design to the other due to the change of doping level, dopant type, material growth method, procedure or recipe. Thus they should be accurately characterised once the wafer is grown in order to verify the design and assess the material's performance in further applications. As will be discussed, a general four-point probe measurement can derive the material resistivity; this can also be derived by using Van der Pauw method. The Van der Pauw method can also measure carrier concentration and mobility.

Apart from material properties of a semiconductor, Ohmic contact resistance is another important parameter that needs to be characterised. This is due to not only the variability of mobility and resistivity of the material, but also the fabrication method, process and environment of the contacts. Accurately determined contact resistances can help to verify if the contact is properly designed and can also be used to assess and optimise device performance. Although other methods are available in the literature, the method generally used for characterising Ohmic contact resistance is the transmission line model (TLM) method. In this section, both material and contact characterisation methodologies are described in detail.

### 3.1.1 Characterising Semiconductor Materials

Sheet resistance and Hall coefficients (i.e. the concentration and mobility of charge carriers) in epitaxial and thin films are important parameters in semiconductor materials. Resistivity measurement can be carried out using a four-point probe measurement method [129]. The Hall coefficients can be extracted using Van der Pauw method that was first introduced in [130] for isotropic materials and further extended for characterising anisotropic materials in [131]. An even simpler method was demonstrated in [132] where only three probes are needed.

#### *3.1.1.1 Resistivity, Sheet Resistance, and Four-point Probe Method*

When an external bias voltage ($V$) is applied to a bulk semiconductor sample that is majority carrier dominated (e.g. n-type GaAs) and has a length ($L$), an electric field ($E$) is induced within the sample. The drift current density ($J_{drift}$) as discussed in Section 2.3 was given as Equation 2.3.6 or re-written as [86]

$$J_{drift} = qnv_{drift} = qn\mu E \tag{3.1.1}$$

The proportional factor of $J_{drift}$ to $E$ is called conductivity $\sigma$ and is given as

$$\sigma = qn\mu \tag{3.1.2}$$

The resistivity, $\rho$, is the reciprocal of conductivity and is written as

$$\rho = \frac{1}{\sigma} = \frac{1}{qn\mu} \tag{3.1.3}$$

The most commonly used resistivity measurement method for a bulk material is the four-point probe method [129]. For a circular wafer with a diameter of $d$ and a finite thickness of $h$ (where $h << d$), as illustrated in Figure 3-1, four probes are equally placed in a line on the surface of the wafer with a separation distance of $s$. The current ($I$) is passed between the two outer probes and the two inner probes measure the potential ($V$).

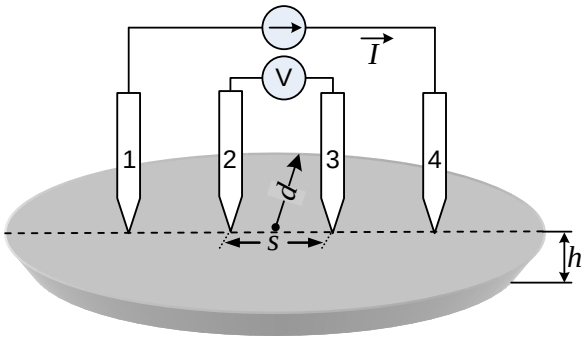


**Figure 3-1** Illustration of the four-point probe resistivity measurement setup.

The resistivity can be derived using the measurable parameters $V$ and $I$ by the following equation [133]

$$\rho = \frac{V}{I} \cdot \pi \cdot h \cdot f(d,s,h) \tag{3.1.4}$$

where $f(d,s,h)$ is a correction factor that is $\left\{\ln 2 + \ln\left[\left(d^2+3s^2\right)/\left(d^2-3s^2\right)\right]\right\}^{-1}$ for a circular thick bulk material and reduces to $(\ln 2)^{-1}$ for $d >> s$. When the wafer thickness approaches a very small value or becomes negligible, the material is considered as a thin film and its current is assumed to flow in the two horizontal directions. Thus, the resistivity that is defined for a bulk material is replaced by sheet resistance ($R_{sh}$) [133],

$$R_{sh} = \frac{V}{I} \cdot \pi \cdot f(d,s) \tag{3.1.5}$$

*3.1.1.2 Hall Effect and Van der Pauw Measurement*

When an n-type semiconductor sample, with dimensions $l \times b \times w$ (length × width × height), is exposed to an electric field $E$, electrons in the sample travel or "drift" parallel to the electric field but in the opposite direction. If a magnetic field is also applied to sample with its direction perpendicular to the electric field, Lorentz forces $F_L$ are exerted onto those drifting electrons. The Lorentz force on a drifting electron is defined as,

$$F_L = q\bar{v}_{drift} \times \bar{B} \tag{3.1.6}$$

where $\bar{v}_{drift}$ is the vector electron drift velocity and $\bar{B}$ is the vector magnetic field.

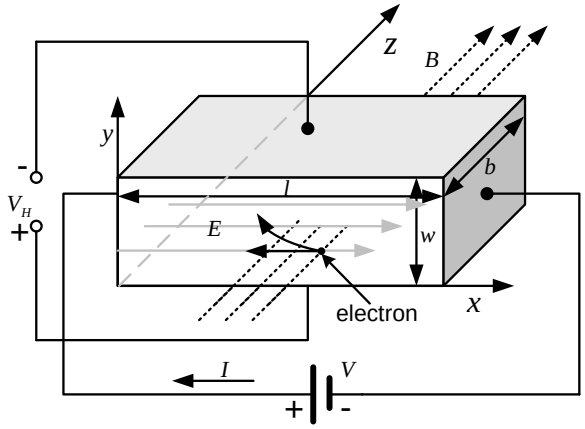


**Figure 3-2** Illustrations of the Hall effect and the experimental setup.

The Lorentz force diverts the electron movement direction away from its original straight route parallel to the electric field as shown in Figure 3-2. The electric field and magnetic field are applied along $x-$axis and $z-$axis directions, respectively. The electrons in the sample travel from the right to the left under the effect of electric field. The Lorentz forces bend the drifting route of the electrons upwards resulting in accumulation of the electrons at the top edge of the sample. The accumulated electrons create a vertical electric field or Hall field ($E_y$) which impedes electrons that have been diverted by the Lorentz force. Since there is no net current flowing vertically in the steady state, a balancing point is reached or the Hall effect is established when the vertical potential equals the Lorentz force. The equilibrium state is mathematically expressed as,

$$qE_y = qv_{drift}B \tag{3.1.7}$$

The Hall field is therefore given by

$$E_y = v_{drift}B \tag{3.1.8}$$

or

$$E_y = v_{drift}B = \frac{J_{drift}}{qn}B = J_{drift}R_H B \tag{3.1.9}$$

where $R_H = (qn)^{-1}$ that is the Hall coefficient. The Hall field can be derived from the externally measured Hall voltage $V_H$ that is given by

$$V_H = E_y w \tag{3.1.10}$$

The electron concentration $n$ can be expressed by rearranging Equation 3.1.9 as

$$n = \frac{1}{qR_H} = \frac{JB}{qE_y} = \frac{(I/wb)B}{q(V_H/w)} = \frac{IB}{qV_H b} \tag{3.1.11}$$

It can be seen all parameters on the right of Equation 3.1.11 are known or measurable.

The Hall effect is used not only to measure the actual concentration of the carriers but also to examine the polarity of the carrier. However, the accuracy of the conventional Hall effect measurement method is dependant on the sample dimension, for example the sample width *b* (see Equation 3.1.11). Yet, the method developed by Van der Pauw for measuring the resistivity and Hall measurement is suitable for material samples with arbitrary shapes [130]. The fundamental conditions to make the Van der Pauw method valid include that the contacts must be on the periphery of the sample and sufficiently small. In addition the sample must have uniform thickness and be free of physical defects, e.g. holes [134].

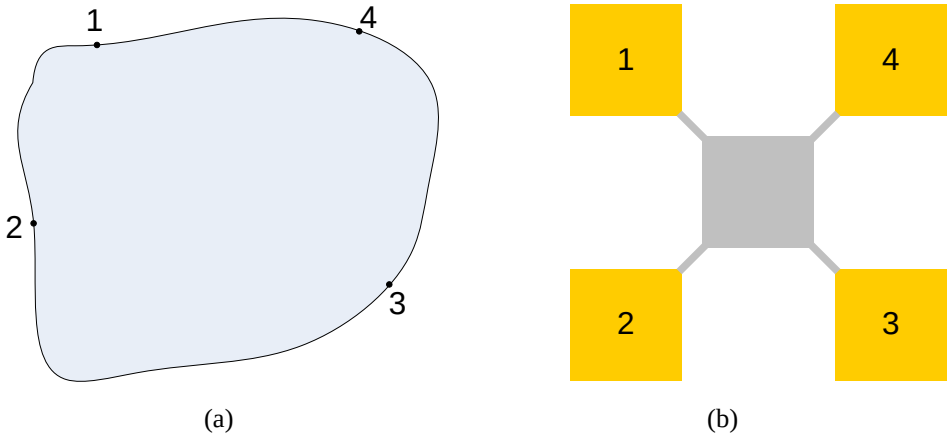


**Figure 3-3** Illustration of Van der Pauw method for resistivity and Hall measurements. (a) A sample with arbitrary shape; (b) The practical test structure used in this work.

Figure 3-3a shows the sample geometry demonstrated by Van der Pauw. Assuming the sample has a uniform doping, four contacts designated 1, 2, 3, and 4 are located randomly on the periphery of the sample (Figure 3-3a). When current is passed between any two contacts (e.g. 1 and 2), the potential difference ($V_{34}$) between the other two contacts (i.e. 3 and 4) is measurable. Thus the resistance between contacts 3 and 4 is derived from $R_{12-34} = V_{34}/I_{12}$. Similarly when the same current is passed between contacts 1 and 4, and the resistance between contact 2 and 3 is derived as $R_{14-23} = V_{23}/I_{14}$. The relationship between the two resistances, $R_{12-34}$ and $R_{14-23}$, is governed by the following equation [134],

$$\exp\left(-\pi w R_{12-34}/\rho\right) + \exp\left(-\pi w R_{14-23}/\rho\right) = 1 \qquad (3.1.12)$$

where $w$ and $\rho$ are the thickness and the resistivity of the sample, respectively. A more general situation was discussed in [131] where the sample is anisotropic and has resistivity tensors of $\rho_x$ and $\rho_y$ in $x$ and $y$ directions, respectively. For this condition the resistivity $\rho$ in Equation 3.1.12 is replaced by $\sqrt{\rho_x \rho_y}$.

A practical sample pattern for Van der Pauw's method is shown in Figure 3-3b in which there are five equally sized squares. The central square is the material to be tested and the four outer squares are contacts. This pattern leads Equation 3.1.12 to a simpler version because $R_{12-34}$ equals $R_{14-23}$. Thus the resistivity of the material is derived as [134]

$$\rho = \frac{\pi w R_{12-34}}{\ln 2} \tag{3.1.13}$$

When the Van der Pauw method is used to measure carrier concentration and mobility of the sample, a current is first applied between two opposite contacts, for example 1 and 3 in Figure 3-3a. The resistance between the other two opposite contacts, 2 and 4, is then measured. Once an additional magnetic field $B$ is applied vertically onto the sample a change to the resistance between contact 2 and 4 ($\Delta R$) that is measurable is induced. This resistance change is related to the Hall coefficient $R_H$ by [134]

$$R_H = \frac{w}{B}\Delta R \tag{3.1.14}$$

Thus, by putting the measured $\Delta R$ into Equation 3.1.14 to calculate the Hall Coefficient $R_H$, and then putting $R_H$ into Equation 3.1.11 the carrier concentration will be derived. The carrier mobility is derived by putting both the carrier concentration and the resistivity into Equation 3.1.3.

### 3.1.2 Characterising Ohmic Contacts

Semiconductor materials interface with other circuits via metal contacts. There are two types of metal-semiconductor interface, Schottky contact and Ohmic contact. The former is the fundamental contact between a metal and a semiconductor and forms elementary parts of many important electronic devices such as Schottky diodes and MESFETs. It is also the basis of Ohmic contacts. It is necessary to understand the Ohmic contacts as well as the Schottky contacts not only for characterising the Ohmic contacts, but also for designing appropriate contacts for different applications. More details about contact design for planar Gunn devices will be given in the next chapter.

#### *3.1.2.1 Introduction to Metal-semiconductor Contacts and Schottky Contacts*

Figure 3-4 shows the energy band structures before and after an isolated metal is placed within intimate contact next to an isolated n-type semiconductor. Several important phenomena occur:

- The Fermi levels of the metal and the n-type semiconductor are lined up at thermal equilibrium.
- Both valence and conduction bands of the semiconductor bend.
- Space charge is formed near the interface and a depletion region is generated in the semiconductor side with a distance of $w$.
- A metal-to-semiconductor barrier $\phi_{Bn}$ $(\phi_{Bn} = \phi_m - \chi_s)$ and semiconductor-to-metal barrier or built-in potential $V_{bi}$ $(V_{bi} = \phi_{Bn} - V_n)$ are formed at the interface. $\phi_m$ and $\phi_s$ are the metal and semiconductor work functions, respectively; $\chi_s$ is the electron affinity and $V_n = E_C - E_F$.

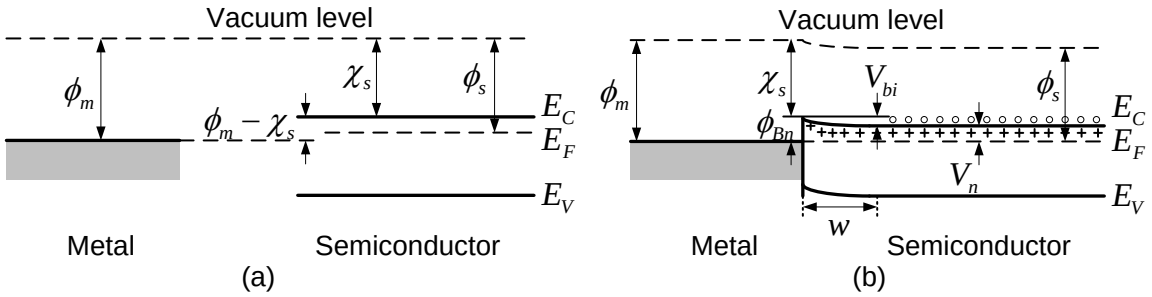


**Figure 3-4** Energy band diagrams of an isolated metal and isolated n-type semiconductor (a) when separated, and (b) when intimately attached at thermal equilibrium. The crosses indicate the positively charged donors and the circles indicate electrons.

The carrier transport mechanism across the metal-semiconductor interface is dominated by the thermionic emission. At thermal equilibrium, electrons travelling from the metal to the semiconductor are balanced by the electrons travelling from the semiconductor to the metal, therefore, there is no net current flow as shown in Figure 3-5c. However, once a positive bias voltage ($V_F$) is applied onto the metal, the conduction band will be re-aligned and the semiconductor-to-metal barrier decreases by $(V_{bi} - V_F)$. This allows more electrons from the semiconductor side to conquer the barrier than the electrons from the metal travelling to the semiconductor (Figure 3-5b) because the metal-to-semiconductor barrier does not change as external bias changes. The net current density is governed by [76]

$$J_F = A^* T^2 \exp\left(-\frac{q\phi_{Bn}}{kT}\right)\left[\exp\left(\frac{qV_F}{kT}\right) - 1\right] \tag{3.1.15}$$

where $A^*$ is the effective Richardson constant and $T$ is the absolute temperature.

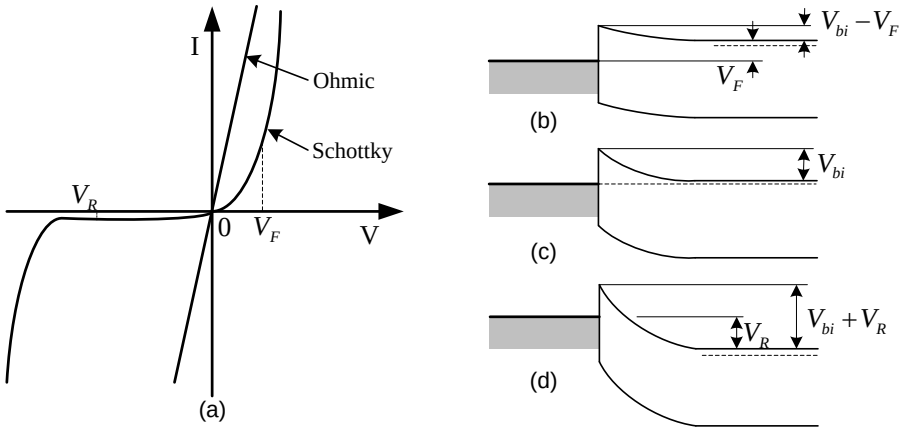


**Figure 3-5** (a) Current-voltage characteristics of Schottky and Ohmic contacts and energy band diagrams of Schottky contact under (b) a forward bias $V_F$, (c) zero bias, and (d) a reverse bias $V_R$.

On the other hand, if a positive bias voltage, $V_R$, is applied onto the semiconductor (Figure 3-5d), the semiconductor-to-metal barrier will rise to $V_{bi} + V_R$, and electrons from the semiconductor crossing over the barrier are impeded. There are only a small proportion of electrons that may still be able to cross the barrier due to the thermionic emission. The current density can still be written as Equation 3.1.15 except that $V_F$ is replaced by $V_R$.

Most metal-semiconductor contacts as previously mentioned are Schottky contacts if the barrier height is larger than *kT* and the semiconductor has a doping level less than its density of states in the energy bands. However, if either the barrier height is lower than *kT*, or the doping level is high enough, the metal-semiconductor contact may become Ohmic contacts. Figure 3-5a indicates the different current-voltage characteristics of an Ohmic contact and a Schottky contact.

### *3.1.2.2 Ohmic Contacts*

An Ohmic contact should have a linear current-voltage relationship as shown in Figure 3-5a as well as a negligible contact resistance relative to the bulk or series resistance of the semiconductor [135]. It should provide minimum perturbation to the semiconductor. There are two common methods to make a normal metal-semiconductor interface meet the requirements of an Ohmic contact. The first method is to reduce the height of the barrier, and this is mathematically confirmed below. Since the contact resistance ( $R_C$ ) is defined as [76]

$$R_C^{-1} = \left.\frac{\partial J}{\partial V}\right|_{V=0} \tag{3.1.16}$$

Thus the contact resistance for metal-semiconductor with the dominant thermionic emission current is derived by putting Equation 3.1.14 into Equation 3.1.16 as [76]

$$R_C = \frac{k}{qA^*T}\exp\left(\frac{q\phi_{Bn}}{kT}\right) \tag{3.1.17}$$

It can be seen in Equation 3.1.17 that the decrease of barrier height can lead to a reduction of the contact resistance. This method of achieving Ohmic contact can be practically realised by using a heterojunction contact with epitaxially grown graded gap materials between the metal and the semiconductor. For example, a non-alloyed Ohmic contact fabricated on n-type GaAs using InAs/$In_xGa_{1-x}As$/GaAs heterojunctions with graded composition of Indium from 0 to 0.8 (1.0) can make contact resistances between $5\times10^{-7}$ and $5\times10^{-6}$ Ω•cm$^2$ [136].

The second method to achieve an Ohmic contact from a normal metal-semiconductor contact is to increase the doping level of the semiconductor so that the barrier (or depletion) width is reduced, thus tunnelling current will replace the thermionic current to become dominate. The tunnelling current $I_{Tunnel}$ is approximated as [76]

$$I_{Tunnel} \propto \exp\left\{\frac{-4\sqrt{m_{eff}\varepsilon_r\varepsilon_0}\cdot(\phi_{Bn}-V_F)}{\hbar\sqrt{N_D}}\right\} \tag{3.1.18}$$

where $\hbar$ is the reduced Planck constant. By putting Equation 3.1.18 into Equation 3.1.16, one can derive the contact resistance for a metal-semiconductor interface with highly doped semiconductor as [76]

$$R_C \propto \exp\left(\frac{4\sqrt{m_{eff}\varepsilon_r\varepsilon_0}\cdot\phi_{Bn}}{\hbar\sqrt{N_D}}\right) \tag{3.1.19}$$

An increase of doping level, $N_D$, of the semiconductor can be practically achieved by alloying and implanting technologies. The alloyed Ohmic contacts are formed by evaporating metal alloys (e.g. Au/Ge/Ni/Au) at room temperature and then the sample is quickly brought to a high temperature (e.g. 450 ℃) for a short time, and then rapidly cooled to a low temperature. The contact resistance of n-type GaAs fabricated using this method is as low as $10^{-6}$ Ω•cm$^2$ [137]. The implantation or diffusion method to increase the doping level may be limited by the impurity solubility [86]. By applying a high-velocity ion beam to bombard the surface of a semiconductor defects are generated at the surface. The semiconductor is then annealed at a very high temperature (e.g. 800 ℃). The

advantage of this method is capable of providing a large degree of flexibility for contact locations and doping levels.

*3.1.2.3 Characterising Ohmic Contacts*

There are several techniques to characterise semiconductor Ohmic contacts including the Cox-Strack technique [138], the four-point probe method [139], and the transmission line model (TLM) measurements [140, 141]. The Cox-Strack technique was specially developed for characterising the contact resistance of thick (bulk) samples with contacts on the two opposite sides. The accuracy of applying this method to characterise contact resistance for n-type GaAs epitaxial layers is limited to 75% when the contact resistance is as small as $1\times10^{-6}\,\Omega\bullet\text{cm}^2$ [86]. The four-point probe method, as described in Section 3.1.1, for characterising material resistivity may be also suitable for characterising contact resistance for planar devices. However, the most commonly used contact resistance measurement technique is the TLM method. A simplified version of the TLM method, called circular TLM (CTLM), in which the mesa etching step used in the conventional TLM method is avoided, has also been demonstrated in [142-144].

For a planar device with two identical Ohmic contacts, separated by a distance of $L$ as illustrated in Figure 3-6a, the total resistance $R_{Total}$ of two Ohmic contacts is given as

$$R_{Total} = 2R_C + 2R_E + 2R_{AN} + R_{Sh}L/W \tag{3.1.20}$$

where $R_C$, $R_E$, $R_{AN}$, and $R_{Sh}$ are the contact resistance, the end resistance, the interface resistance between the alloyed region and the active region, and the sheet resistance of the active layer, respectively. $W$ is the width of the Ohmic contacts. The relationship between $R_{Total}$ and $L$, expressed in Equation 3.1.20, can be plotted as shown in Figure 3-6c. The alloyed regions under the metal contacts have higher doping levels than the active region therefore the sheet resistance of the alloyed regions is different from that of the active region. If no alloying technique is used to form Ohmic contacts they become equal. The interfaces between the alloyed region and the active region may contribute to some resistances that influence the measured Ohmic contact resistance [76].

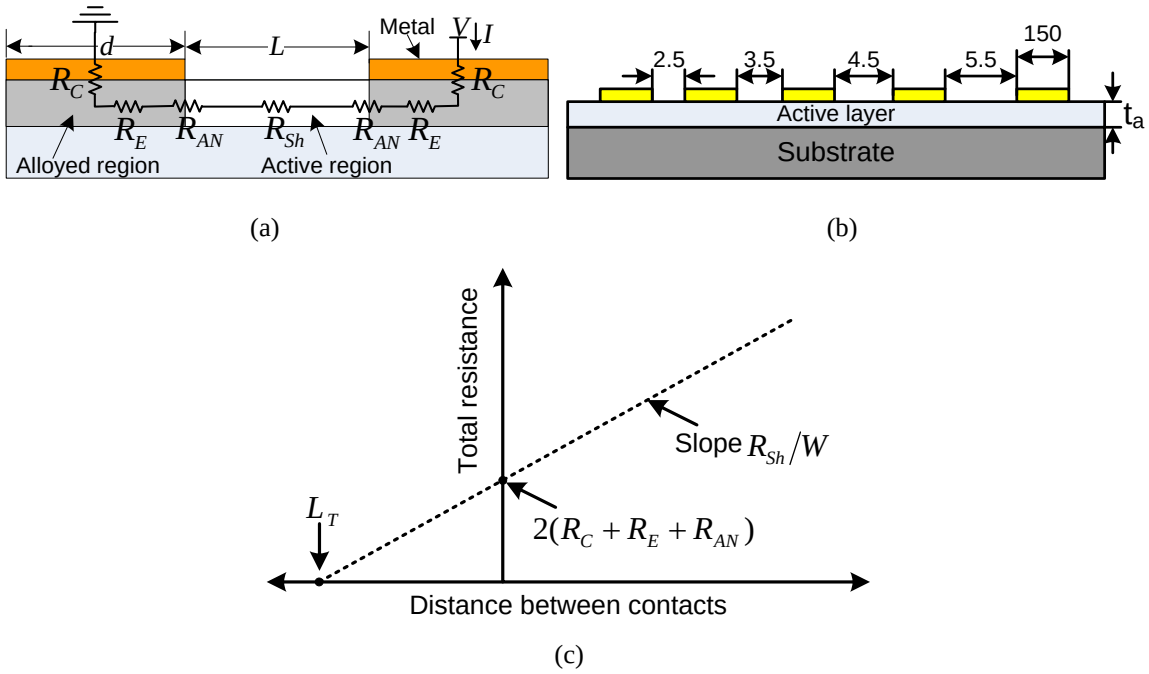


**Figure 3-6** (a) Illustration of a planar device having two identical Ohmic contacts for assisting analysis of alloyed contacts, (b) the actual TLM patterns used in the experiments for deriving the contact resistance, and (c) the relationship between the total resistance between two Ohmic contacts and their distance. The unit in (b) is micrometer.

It can be seen from Equation 3.1.20 that there are four unknown parameters, namely $R_C$, $R_E$, $R_{AN}$ and $R_{Sh}$. The former three items form the total Ohmic resistance which can be achieved by setting several different values of $L$ and measuring the corresponding resistances. Figure 3-6b shows the TLM patterns used in practice for measuring the contact resistance of the Ohmic contacts.

## 3.2 Characterising Passive Components Using Vector Network Analysers

The vector network analyser (VNA) is a well-recognised, sophisticated instrument that is used for characterising the frequency response of passive components and active devices [127, 128]. By measuring the scattering parameters (*S*-parameters) of a device-under-test (DUT) and extracting testing pads or parasitic circuits, important device parameters such as impedance, VSWR, gain or loss and group delay can be obtained [145, 146]. An introduction to the basic principles of the VNA, their calibration procedures and methods, and their applications to characterising passive components are given in this section.

### 3.2.1 Theory of Microwave and Millimetre-wave Networks

Before introducing the vector network analyser, some fundamental principles of microwave and millimetre-wave networks are provided. It is also useful to include an introduction to various parameters, such as impedance, scattering and transmission parameters, that are used to describe different networks according to their applications.

A microwave or millimetre-wave device or system can be treated as a network when interconnecting with other devices in a complex circuit or system. The network can be simply represented or characterised by the changes of voltage, current, and power at each individual port rather than inside the network. It is even convenient to use network theory to analyse a system if it consists of many such networks and they cascade by only investigating the change of transmissions and reflections at interconnections between networks.

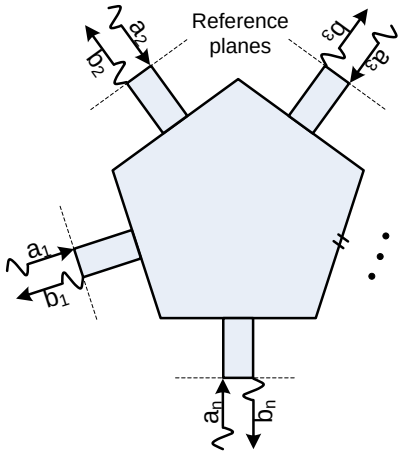


**Figure 3-7** Illustration of a microwave or millimetre-wave network having n ports.

Figure 3-7 shows a network having $n$ ports. At the reference plane of port $i$, $i \in (1,\cdots,n-1,n)$, there is an incident signal designated as $a_i$ that has a voltage of $V_i^+$ and a current of $I_i^+$ and a reflected wave designated as $b_i$ with a voltage of $V_i^-$ and a current of $I_i^-$. Using the equivalent voltages and currents of a transmission line, the total voltage and current at the $i^{th}$ port are [127]

$$V_i = V_i^+ + V_i^- \tag{3.2.1 a}$$

and

$$I_i = I_i^+ - I_i^- \tag{3.2.1 b}$$

The input impedance at $i^{th}$ port is defined by

$$Z_i = \frac{V_i}{I_i} = \frac{V_i^+ + V_i^-}{I_i^+ - I_i^-} \tag{3.2.1 c}$$

If the total voltages for each port of the network are listed on one side and all total currents on the other side, the matrix equation is as follows:

$$\begin{bmatrix} V_1 \\ V_2 \\ \vdots \\ V_n \end{bmatrix} = \begin{bmatrix} Z_{11} & Z_{12} & \cdot\cdot & Z_{1n} \\ Z_{21} & Z_{22} & \cdot\cdot & Z_{2n} \\ \vdots & \vdots & \vdots & \vdots \\ Z_{n1} & Z_{n2} & \cdot\cdot & Z_{nn} \end{bmatrix} \begin{bmatrix} I_1 \\ I_2 \\ \vdots \\ I_n \end{bmatrix} \tag{3.2.2}$$

The impedance matrix, $[Z]$, or Z-parameters of the multi-port network is formed. The element of the matrix is given as $Z_{ij} = \left.\frac{V_i}{I_j}\right|_{I_k=0, k\neq j}$. Occasionally, it is convenient to use the admittance matrix, $[Y]$, rather than impedance matrix to describe a network. The Y-parameters are defined as:

$$\begin{bmatrix} I_1 \\ I_2 \\ \vdots \\ I_n \end{bmatrix} = \begin{bmatrix} Y_{11} & Y_{12} & \cdot\cdot & Y_{1n} \\ Y_{21} & Y_{22} & \cdot\cdot & Y_{2n} \\ \vdots & \vdots & \vdots & \vdots \\ Y_{n1} & Y_{n2} & \cdot\cdot & Y_{nn} \end{bmatrix} \begin{bmatrix} V_1 \\ V_2 \\ \vdots \\ V_n \end{bmatrix} \tag{3.2.3}$$

Z or Y-parameters may become difficult to determine accurately due to the practical difficulties in measuring voltages and currents of a wave at microwave frequencies and above. It is more practical to use scattering parameters, $[S]$, that only relate the voltage vector of an incident wave and that of the reflected wave at a port to describe a network. This relationship for a multi-port network when written as a matrix is:

$$\begin{bmatrix} V_1^- \\ V_2^- \\ \vdots \\ V_n^- \end{bmatrix} = \begin{bmatrix} S_{11} & S_{12} & \cdot\cdot & S_{1n} \\ S_{21} & S_{22} & \cdot\cdot & S_{2n} \\ \vdots & \vdots & \vdots & \vdots \\ S_{n1} & S_{n2} & \cdot\cdot & S_{nn} \end{bmatrix} \begin{bmatrix} V_1^+ \\ V_2^+ \\ \vdots \\ V_n^+ \end{bmatrix} \tag{3.2.4}$$

The element of the matrix $[S]$ is defined as $S_{ij} = \left.\frac{V_i^-}{V_j^+}\right|_{V_k^+=0, k\neq j}$ that represents the ratio of reflected wave amplitude, $V_i^-$, at port $i$ to the incident wave amplitude, $V_j^+$, at port $j$.

When two or more networks are connected in series, the current flows from one to the next. It is convenient to use this property to define a transmission matrix $[T]$ (or *ABCD*-parameters for a two-port network) to characterise and analyse cascaded networks. For a two-port network $M$, its *ABCD*-parameters are defined as

$$\begin{bmatrix} V_1 \\ I_1 \end{bmatrix} = \begin{bmatrix} A_M & B_M \\ C_M & D_M \end{bmatrix} \begin{bmatrix} V_2 \\ I_2 \end{bmatrix} \tag{3.2.5}$$

If two two-port networks $M$ and $N$ cascade as shown in Figure 3-8, the relationship between the current and voltage at port 2 of network $N$ and those at port 1 of network $M$ is written as

$$\begin{bmatrix} V_1 \\ I_1 \end{bmatrix} = \begin{bmatrix} A_M & B_M \\ C_M & D_M \end{bmatrix} \begin{bmatrix} A_N & B_N \\ C_N & D_N \end{bmatrix} \begin{bmatrix} V_3 \\ I_3 \end{bmatrix} \tag{3.2.6 a}$$

or

$$\begin{bmatrix} V_1 \\ I_1 \end{bmatrix} = \begin{bmatrix} A_{MN} & B_{MN} \\ C_{MN} & D_{MN} \end{bmatrix} \begin{bmatrix} V_3 \\ I_3 \end{bmatrix} \tag{3.2.6 b}$$

where

$$\begin{bmatrix} A_{MN} & B_{MN} \\ C_{MN} & D_{MN} \end{bmatrix} = \begin{bmatrix} A_M & B_M \\ C_M & D_M \end{bmatrix} \begin{bmatrix} A_N & B_N \\ C_N & D_N \end{bmatrix}$$

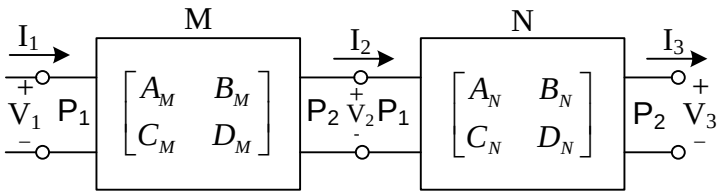


**Figure 3-8** Illustration of two cascaded networks using *ABCD*-parameters.

### 3.2.2 Vector Network Analysers

*3.2.1.1 Introduction to Vector Network Analysers*

Since it is relatively easier to measure the voltage vectors of the incident and reflected waves at the ports, most networks are represented and characterised using *S*-parameters that are measured by using a VNA. From these *S*-parameters, the *Z*, *Y*, and *ABCD*-parameters can all be easily derived [127]. Figure 3-9 shows a simplified block diagram of a typical two-port VNA system.

A VNA has two internal signal sources, RF and LO, that can sweep over the measurement frequencies of interest. Separate external sources may be needed for operation frequencies beyond the VNA. The RF and LO are commonly set to be equal or slightly different (e.g. 10 kHz) for measuring a linear network. This is governed by the setup of the IF bandpass filter or the IF bandwidth defined by the user, and is in the range of several tens of Hertz to several hundreds of kHz depending on the application [145]. An actual system will have two or more stages of down-conversion mixing for IF to achieve good accuracy. Each test port has a directional coupler for separating the RF signals sent out to the DUT and the reflected signals from the DUT. The directivity of the coupler limits the minimum detected power of the reflected signals and therefore the return loss of the DUT.

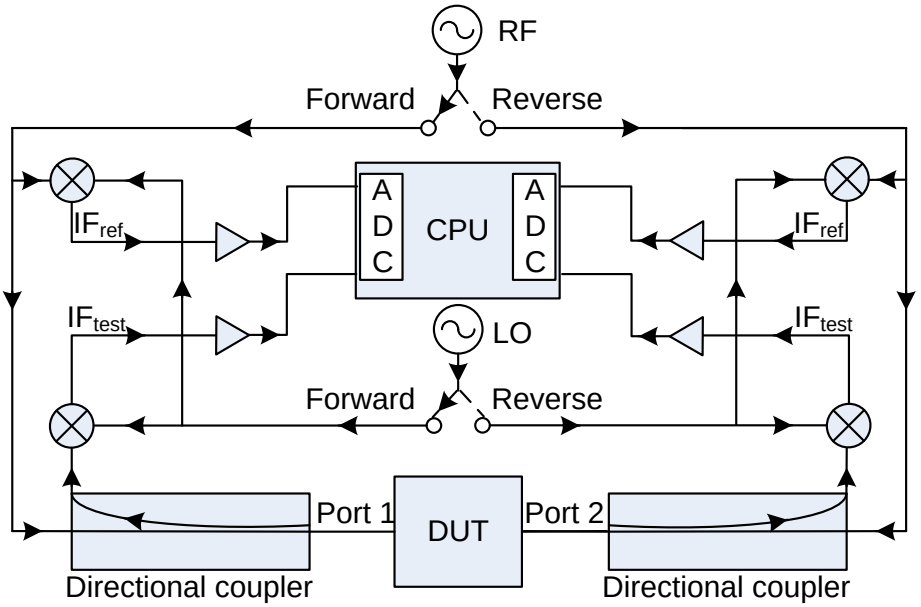


**Figure 3-9** A simplified block diagram of a two-port vector network analyser.

Taking a two-port network measurement as an example, when one-port reflection measurement (e.g. port 1) is in operation, the VNA terminates the other port (port 2 in this case) with a broadband matched load and sets its switch to the forward mode. The RF signal is split into two halves in terms of power. One goes into the mixer where it is mixed down by the LO to IF as a reference, the other goes into the DUT through the directional coupler. The reflected signal returns via the directional coupler to another mixer and is mixed with the LO to generate a test IF. The measured reflection coefficient, $S_{11}$, of the DUT is derived from the measured phase and magnitude difference of the test and reference IF signals. Similarly, the port 2 reflection coefficient, $S_{22}$, can be measured in this way.

When measuring the transmission coefficients of the two-port network, the RF source still sends a RF signal to the DUT via the directional coupler in its forward mode, the signal will pass through the DUT and is separated by the directional coupler at test port 2 of the VNA. It is then down-converted to an IF signal as a test result. The ratio of the power and phase of the measured signals gives the forward transmission coefficient or $S_{21}$ of the DUT. The reverse mode leads to the derivation of $S_{12}$. The final *S*-parameters of the DUT are then constructed by combining the measured two individual one-port reflections, $S_{11}$ and $S_{22}$, and the two transmissions, $S_{21}$ and $S_{12}$.

Some VNAs can provide additional functions, such as power sweep and frequency offset measurements. The former allows the output power of a VNA to change in a certain range, at a fixed frequency so that the power characterisation of a nonlinear network, such as power amplifiers, can be derived. The latter can set a frequency offset between sources and receivers so that devices, for example a mixer, which have different input and output frequencies can be characterised.

#### *3.2.1.2 VNA Calibration*

Properly calibrating a VNA is an important step to ensure that accurate, reliable and repeatable measurements are made. It is a process, using a mathematical method, to remove or minimise any systematic uncertainties caused by the imperfections of hardware in the measurement setup [147]. Unlike random uncertainties, such as system noise, that are unpredictable and irremovable, systematic errors, such as mismatch between connectors or imperfect components, can all be calculated and mathematically removed or minimised by measuring a group of known standards, such as opens, shorts, matched loads and lines, depending on the mathematical algorithms or calibration methods used. The commonly used calibration methods include Thru-Reflect-Line (TRL), Line-Reflect-Match (LRM), Line-Reflect-Reflect-Match (LRRM), Short-Open-Load-Thru (SOLT), and Short-Open-Load-Reciprocal (SOLR).

- **System Error Models**

The systematic errors can be modelled in several ways. The conventional 12-term error model was first introduced in the 1960s [148], and it has been simplified to an 8-term error model [149] or developed into the more complicated 16 term-error model [150]. Since

each error model has forward and reverse models that are a pair of opposite processes as discussed in Section 3.2.1.1, in order to simply the analysis only the forward model is discussed here.

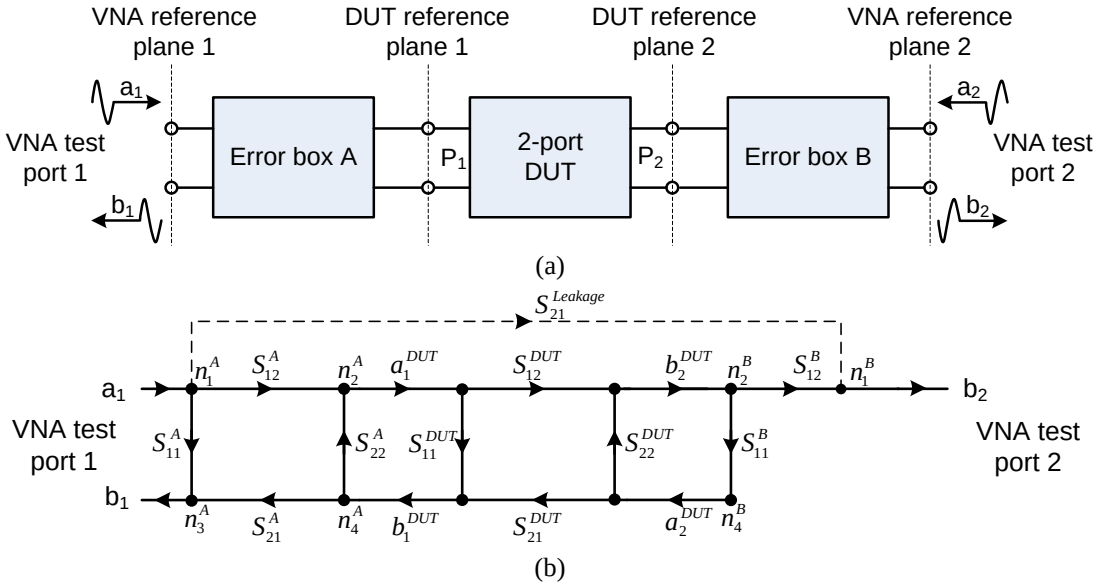


**Figure 3-10** (a) Block diagram of system errors and forward model of the 12-term error model for a two-port vector network analyser, and (b) its signal flow graph representation.

Figure 3-10 illustrates the block diagram of the systematic errors in a two-port VNA setup and the signal flow graph of the forward 6-term error mode operation of the classic 12-term error model. The six errors include Directivity ($S_{11}^A$), Leakage ($S_{21}^{Leakage}$), Reflection Tracking ($S_{12}^A \cdot S_{21}^A$), Transmission Tracking ($S_{12}^A \cdot S_{12}^B$), Port-1 Match ($S_{22}^A$) and Port-2 Match ($S_{11}^B$). In the forward mode the measured reflection, including the DUT at Port 1 (while Port 2 is terminated by a matched load), is given as [149]

$$S_{11}^M = \frac{b_1}{a_1} = S_{11}^A + S_{12}^A S_{21}^A \frac{S_{11}^A - S_{11}^B\left(S_{11}^{DUT} S_{11}^{DUT} - S_{12}^{DUT} S_{21}^{DUT}\right)}{1 - S_{22}^A S_{11}^{DUT} - S_{11}^B S_{22}^{DUT} + S_{22}^A S_{11}^B\left(S_{11}^{DUT} S_{11}^{DUT} - S_{12}^{DUT} S_{21}^{DUT}\right)} \quad (3.2.7)$$

and the transmission from Port 1 to Port 2 is given as [149]

$$S_{21}^M = \frac{b_2}{a_1} = S_{21}^{Leakage} + \frac{S_{12}^A S_{12}^B S_{21}^{DUT}}{1 - S_{22}^A S_{11}^{DUT} - S_{11}^B S_{22}^{DUT} + S_{22}^A S_{11}^B\left(S_{11}^{DUT} S_{11}^{DUT} - S_{12}^{DUT} S_{21}^{DUT}\right)} \quad (3.2.8)$$

The simplified 8-term error model, that is based on the 12-term error model, assumes there is no leakage error through the LO path of the mixers (i.e. $S_{21}^{Leakage} = 0$). In addition, the port match of the VNA is assumed to be constant by the perfect switch, which then can be

cancelled out by applying appropriate mathematical formulations [151, 152]. On the contrary, the 16-term error model adds 4 more leakage terms to the traditional 12-term error model. These additional error terms come from the switch leakage, signal reflecting from the DUT and leaking to the transmission port, and so on [150].

- **One-port Calibration Procedure and Method**

The systematic errors and corresponding error models of a two-port VNA setup have been described above. In order to remove these errors, appropriate calibration procedures and methods are required. The one-port calibration method is not only the calibration method of a VNA for one-port device measurements, but also the basis of two-port or multi-port calibration methods. The forward 6-term error model for a two-port VNA setup can be reduced to a 3-term error model for the one port calibration procedure as shown in Figure 3-11. They are Directivity ($S_{11}^A$), Reflection Tracking ($S_{12}^A \cdot S_{21}^A$), and Port-1 Match ($S_{22}^A$). Although four parameters appear in the three term errors only three equations, therefore three known standards, are required to derive the error terms because $S_{12}^A \cdot S_{21}^A$ can be treated as a single unknown parameter. Thus, the measured reflection coefficient (Equation 3.2.7) of a DUT at Port 1 of the VNA is simplified to

$$S_{11}^M = \frac{b_1}{a_1} = S_{11}^A + \frac{S_{12}^A S_{21}^A S_{11}^{DUT}}{1 - S_{22}^A S_{11}^{DUT}} \tag{3.2.9}$$

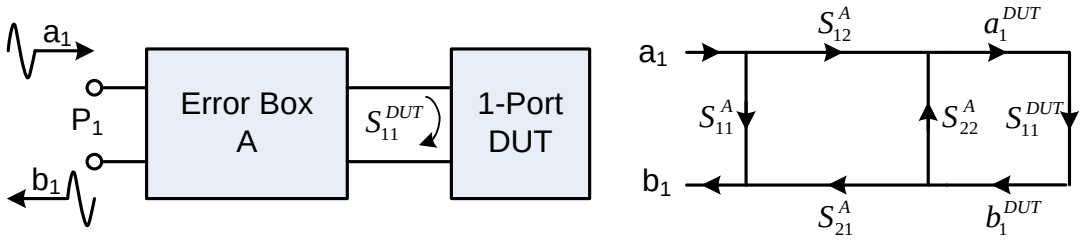


(a) (b)

**Figure 3-11** Illustrations of (a) 3-term error model of a one-port network and (b) its signal flow graph representation.

Once the three errors are derived by using three known standards, the system is calibrated and can be used to measure any one-port DUTs by re-writing Equation 3.2.9 as [149]

$$S_{11}^{DUT} = \frac{S_{11}^M - S_{11}^A}{S_{22}^A S_{11}^M - (S_{11}^A S_{22}^A - S_{12}^A S_{21}^A)} \tag{3.2.10}$$

The Short-Open-Load (SOL) on-wafer calibration method first introduced in [153] is a typical one-port calibration method, in which the three known standards are a short (a metallic bar), an open (probe in the air) and a matched load (50 Ω).

- **Two-port Calibration Procedures and Methods**

It has been shown that three errors namely Directivity ( $S_{11}^{A}$ ), Reflection Tracking ( $S_{12}^{A} \cdot S_{21}^{A}$ ), and Port-1 Match ( $S_{22}^{A}$ ) can be derived by solving three equations generated by the one-port SOL calibration method. For the remaining three errors, such as Leakage ( $S_{21}^{Leakage}$ ), Transmission Tracking ( $S_{12}^{A} \cdot S_{12}^{B}$ ), and Port-2 Match ( $S_{11}^{B}$ ) in the forward model for a two-port VNA calibration, additional calibration steps or standard(s) are needed.

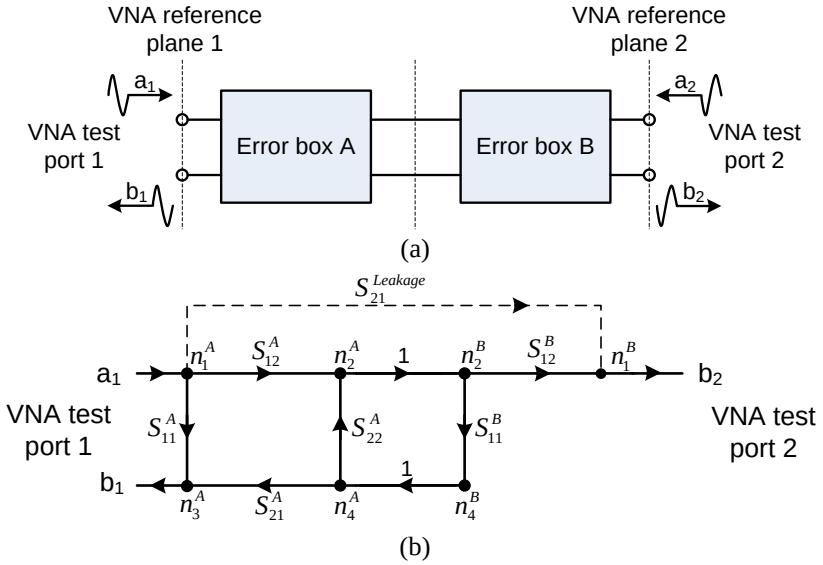


**Figure 3-12** Illustration of SOLT calibration method when two ports are connected directly.

The SOLT calibration method is probably the simplest two port calibration method. In this method an additional two steps are needed to remove the other three errors. By first measuring three known standards (short, open, and matched load) for each port, Directivity, Reflection Tracking and Port Match are derived as discussed before using the one-port SOL calibration method. Next, Port 1 and Port 2 are terminated with internal matched loads respectively so that Leakages can be derived. This can be observed for the forward model from Equation 3.2.8 in which $S_{21}^{DUT} = 0$ in this case. Finally, Port 1 and Port 2 are connected as shown in Figure 3-12 and Port 2 is switched to the termination load mode for the forward model so that Transmission Tracking and Port-2 Match can be derived as follows [149]

$$S_{11}^{B} = \frac{S_{11}^{M} - S_{11}^{A}}{S_{11}^{M} S_{22}^{A} - \left(S_{11}^{A} S_{22}^{A} - S_{12}^{A} S_{21}^{A}\right)} \tag{3.2.11}$$

$$S_{12}^{A} \cdot S_{12}^{B} = \left(S_{21}^{M} - S^{Leakage}\right)\left(1 - S_{22}^{A} S_{11}^{B}\right) \tag{3.2.12}$$

For on-wafer calibration, a standard Thru (a short line with characteristic impedance of 50 Ω and electrical length of $l$) is also required [154]. When putting the known S-parameters of the Thru into Equations 3.2.7 and 3.2.8, the Transmission Tracking and Port-2 Match are then derived.

Short-Open-Load-Reciprocal (SOLR) thru calibration method [151, 155-157] is based on SOLT with the assumption that the thru standard is reciprocal and less than 180 º. Thus the number of unknown parameters will be further reduced. The advantage of this calibration approach is that the detailed information about the thru is not needed as long as it is reciprocal. This is particularly useful when calibrating a VNA with orthogonal probe positions [155] or when two devices are far apart [151]. In the first case a right-angle thru is required during the calibration process however, at high frequencies, other modes of transmission are likely to be created due to the right angle bend. In the second case, a long thru is required for proper calibration however it becomes lossy at high frequencies.

In addition to these calibration methods, several other two-port calibration methods that may use fewer or simpler standards compared with SOLT and SOLR have also been developed. The TRL method [158] requires a thru standard, two reflect standards with high reflections (open or short) and a line standard with electrical length shorter than 180 º. This method is more suitable for high frequency operation where parasitics of the load match standards would significantly degrade the standard's performance. TRL also leads to the possibility of calibration using on-wafer standards and de-embedding any transitions for on-chip circuits.

On-wafer LRM method [159] requires a non-zero line, two preferable Opens as Reflects and two imperfectly Matched loads. The advantages of the LRM method include that no details about Opens are necessarily needed, plus long line standards are not needed so it is suitable for systems with fixed-position probes [160]. An improved version of LRM is called LRRM [161, 162] that uses two additional undefined Shorts. Only one matched load is required to be measured at either port. This calibration method minimises the inaccuracies that are caused by probing misalignments with Short and Matched Load standards [162]. However, this method is unable to define the reference impedance, and an improved LRRM method with four-standard self-calibration theory has been demonstrated with higher accuracy [161].

### 3.2.3 Using VNA to Measure Passive Networks

Having discussed the basic principles and calibration methods of VNAs, it is now necessary to mention the general procedures of using a VNA to measure any passive networks.

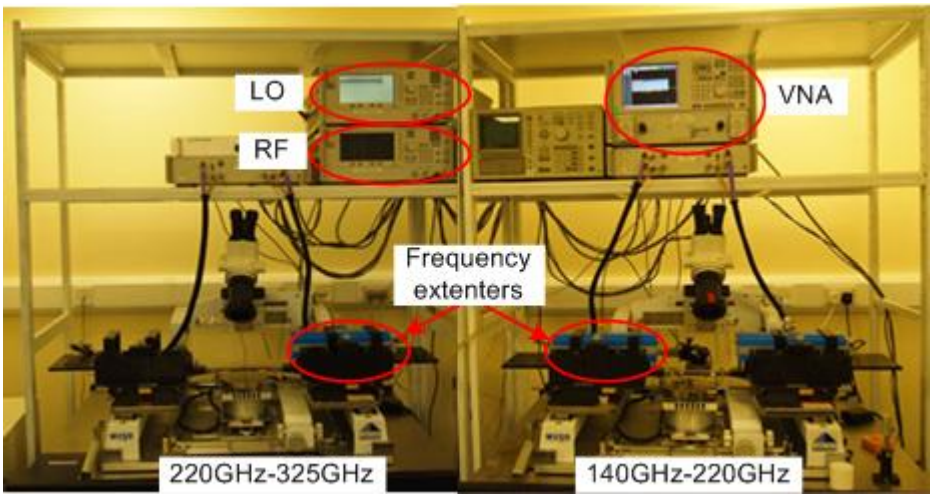


**Figure 3-13** Two *S*-parameter measurement setups using the same external signal sources ( Agilent E8257D 250 kHz-20 GHz) to extend the operation frequency of a VNA (Agilent E8364B 10 MHz-50 GHz) to upper millimetre-wave bands.

**Step 1: Choose the appropriate VNA for different applications**.

Several factors need to be considered when choosing an appropriate VNA for *S*-parameter measurements. These include availability, operation frequencies, and measurement port media: on-wafer or air-filled metallic waveguides. As mentioned in Section 3.3.1, external signal sources are needed to extend the operation frequency of a typical VNA. Figure 3-13 illustrates two VNA-based systems that use external RF and LO signal sources and a common VNA (whose operation frequency is between 10 MHz and 50 GHz) with frequency extenders for banded measurements at 140-220 GHz and 220-325 GHz.

**Step 2: Setup the VNA**. There are a number of things to be properly setup for different applications. These include the frequency span of interest, the number of points, the IF bandwidth and the power level.

**Step 3: Calibrate the System**. Different applications require different calibration methods and therefore different standards, especially for off-wafer calibrations. For example, if the DUT has orthogonal ports geometry, as will be shown in Chapter 6, the SOLR calibration method is most appropriate and accurate than other calibration methods. Apart from

accuracy, the availability of standards is another factor in determining what calibration methods should be used. If an on-wafer calibration or de-embedding transitions is involved, then TRL calibration method is recommended for avoiding the difficulties in fabricating accurate matched loads that are required by other calibration methods.

**Step 4: Verification/Validation**. Once the system is properly calibrated, it is necessary to verify the calibration. This is generally achieved by taking a measurement of known artefacts, such as a different line standard or different matched load. Apart from validating a calibration procedure, this process can also identify if the measurement data is well behaved, for example there are no glitches or resonances.

**Step 5: Measurements**. Proper alignment of the air-filled metallic waveguides or the probes is essential to ensure good reproducibility of the measurement results. When measuring on-chip DUTs alignment markers are generally recommended. These markers assist one to have the same travel distance for the probes and therefore the measuring planes are identically defined.

## 3.3 Spectrum and Power Measurement Systems

Since the planar Gunn diodes and oscillators developed in this thesis are signal sources, it is essential to characterise their spectral and power performance. A common spectral characterisation method is to use a spectrum analyser and other accessories, such as cables and probes if needed. The state-of-art stand-alone spectrum analysers have wide operating bands, for example, 3 Hz-50 GHz for the E4448A from Agilent Technologies. An external waveguide subharmonic mixer is needed to extend the spectrum analyser's operation range beyond 50 GHz. Since these mixers are normally band limited, such as *V*-band (50 GHz-75 GHz) or *W*-band (75 GHz-110 GHz), different measurement setups are required to characterise the same device across multiple banded frequency ranges. Detailed descriptions on the spectrum analyser measurement setup are given in Section 3.3.1.

An important measurement technique, called the one-port load-pull measurement, has been devised for investigating the load effect on power and frequency performance of oscillators, and will be discussed in Section 3.3.2. This measurement technique not only allows one to explore how the loadings influence the output oscillation frequency and power of a planar

Gunn diode or similar one-port oscillator devices, but also enables one to derive the optimum load impedance for the design of a matching circuit for maximum power output or operating frequency.

The power measurement at millimetre-wave frequency is challenging due to the shortage of reliable power sensors in this frequency range. An accurate and robust power measurement system for measuring planar Gunn oscillators will be discussed in Section 3.3.3.

### 3.3.1 Spectrum Analyser Measurement Setups

On-wafer spectrum measurement systems, as shown in Figure 3-14, have been used to characterise planar Gunn devices throughout this work. For devices operating up to 50 GHz, only a stand-alone spectrum analyser measurement, *V*-band cable and a DC-65 GHz probe are needed for a spectrum analyser based measurement (Figure 3-14a). If the DUTs operate beyond the frequency range of the stand alone spectrum analyser, an external mixer and a diplexer (sometimes they are combined) are required (Figure 3-14b). The diplexer functions as a circulator that separates the LO (higher harmonics) signal of the spectrum analyser from the mixing product (IF) of the LO and the RF. A practical *W*-band measurement setup is shown in Figure 3-14c. It can be seen that each measurement setup consists of several components. In order to achieve accurate measurement results, it is necessary to know the performance of each element in the setup. In the following sub-sections characterisation of the components in the setup is given.

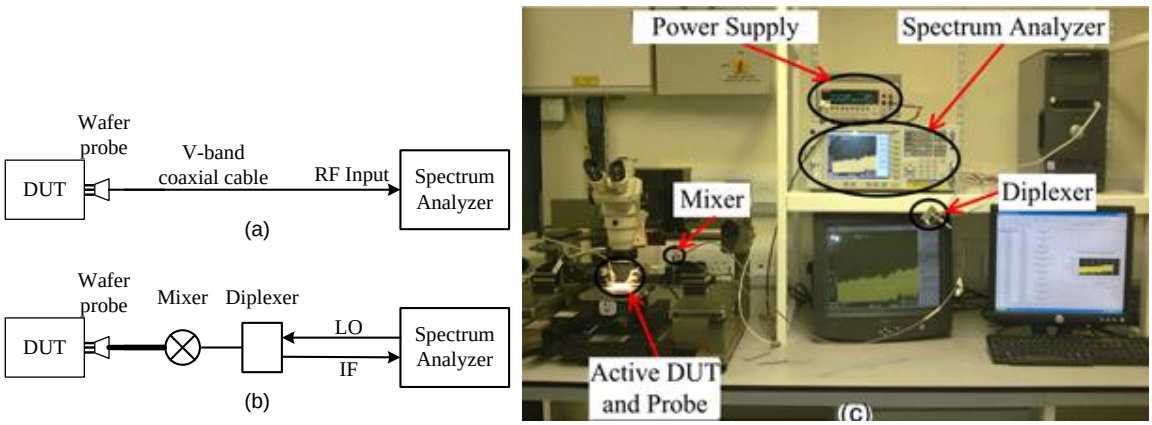


**Figure 3-14** Spectrum measurement setups (a) Canonical illustration of a spectrum measurement setup without using an external mixer; (b) Canonical illustration of a spectrum measurement setup using an external mixer; (c) an actual setup for a W-band spectrum measurement setup.

*3.3.1.1 Introduction to Spectrum Analysers*

A spectrum analyser is a precise instrument for signal spectrum characterisation. Figure 3-15 illustrates a simplified block diagram of a spectrum analyser [145]. The attenuator limits the input signal power to prevent the mixer from being overloaded. If the signal is weak, a low-noise power amplifier is used to boost the signal. A low pass filter performs as a pre-selector so that unwanted signals can be filtered out. The core component of the spectrum analyser is the mixer which down-converts the RF signal by mixing with the swept LO signal to IF. The IF will be further filtered by a resolution bandwidth filter in order to remove any intrinsic noise embedded in the signal, and then is amplified or compressed before being detected by a power detector. The measured power or amplitude of the signal is transferred to the microprocessor for display. The signal of interest continues through to the video filter where, unlike the resolution bandwidth filter, the system noise is removed. The signal finally reaches the analogue-to-digital converter (ADC) in which it is digitised for post-processing and displaying.

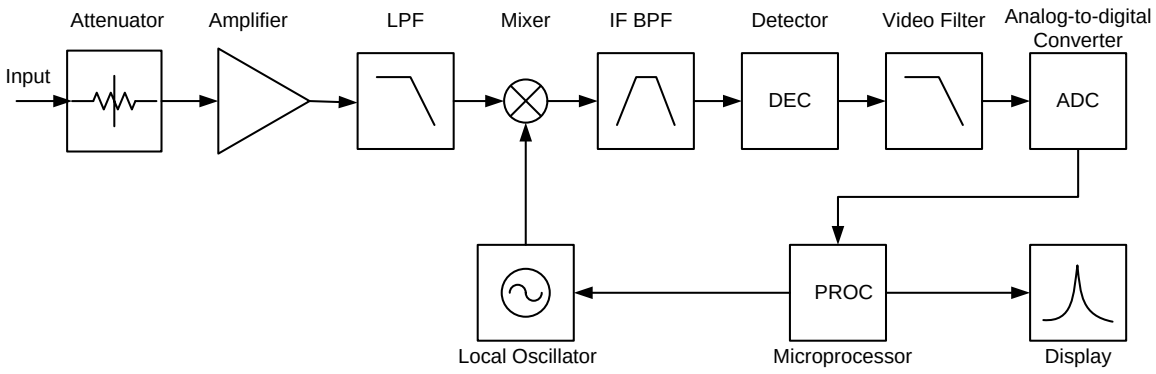


**Figure 3-15** A simplified block diagram of a spectrum analyser [145].

*3.3.1.2 Characterising GSG On-wafer Probes*

An on-wafer probe is a linear two-port network that has quasi-planar tips on one end for contacting an on-wafer DUT, and a coaxial or air-filled rectangular waveguide on the other end for connecting non-planar components or devices. The general method for characterising a probe is to use the one-port measurement technique to measure several calibration substrate standards on an impedance standard substrate (ISS) and therefore derive the *S*-parameters of the probe [163, 164]. The short-open-load (SOL) probe characterisation method is based on the cascade network theory [163]. A conventional

SOL calibration method, as described in Section 3.2.1, can be used to calibrate the VNA port 1 by the probe waveguide plane using known lumped open, short and load standards. Figure 3-16 shows the block diagram of the probe characterisation method. The probe and the calibration substrate are cascaded thus the reflection coefficient at the waveguide port of the probe, designated as $\Gamma_{in}$, can be written as [163]

$$\Gamma_{in} = S_{11}^{probe} + \frac{S_{12}^{probe} S_{21}^{probe} \Gamma_{load}}{1 - S_{22}^{probe} \Gamma_{load}} \tag{3.3.1}$$

when the probe tips port is terminated with various load standards. Assuming the probe is reciprocal, which is true in general, we have that $S_{12}^{probe} = S_{21}^{probe}$. Thus there are only three unknown parameters, $S_{11}^{probe}$, $S_{12}^{probe}$, and $S_{22}^{probe}$, to be determined in order to derive the S-parameters of the probe.

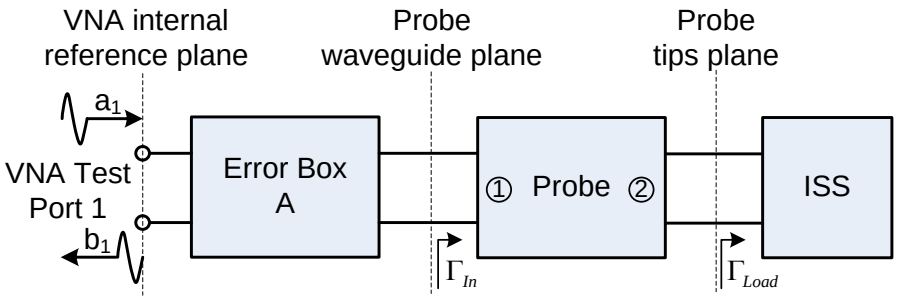


**Figure 3-16** Block diagram indicates the probe characterisation method using one-port measurement method and off-wafer calibration substrates.

Three load standards, namely open, short and match load, along with the three corresponding one-port measurements provide three equations. Equation 3.3.1 can be written as [163]

$$\Gamma_{in}^{open} = S_{11}^{probe} + \frac{S_{12}^{probe} S_{21}^{probe} \Gamma_{load}^{open}}{1 - S_{22}^{probe} \Gamma_{load}^{open}} \tag{3.3.2 a}$$

$$\Gamma_{in}^{short} = S_{11}^{probe} + \frac{S_{12}^{probe} S_{21}^{probe} \Gamma_{load}^{short}}{1 - S_{22}^{probe} \Gamma_{load}^{short}} \tag{3.3.2 b}$$

$$\Gamma_{in}^{match} = S_{11}^{probe} + \frac{S_{12}^{probe} S_{21}^{probe} \Gamma_{load}^{match}}{1 - S_{22}^{probe} \Gamma_{load}^{match}} \tag{3.3.2 c}$$

where $\Gamma_{in}^{open}$, $\Gamma_{in}^{short}$ and $\Gamma_{in}^{match}$ are the measured one-port reflection coefficients when the terminating load standard at the probe tips is open, short, and match load, respectively. $\Gamma_{load}^{match}$, $\Gamma_{load}^{open}$, and $\Gamma_{load}^{short}$ are the calculated reflection coefficients of the load, open and short of the calibration substrate, respectively.

If the above equations assume that the calibration standards are perfect and have negligible parasitic inductance or capacitance over the measurement frequency of interest as discussed in [163], the load reflection coefficients for open $\Gamma_{load}^{open}$, short $\Gamma_{load}^{short}$ and match load $\Gamma_{load}^{match}$ are 1, -1 and 0, respectively. The *S*-parameters of the probe can then be simplified and calculated by using Equations 3.3.3a-c:

$$S_{11}^{probe} = \Gamma_{in}^{match} \tag{3.3.3 a}$$

$$S_{12}^{probe} = S_{21}^{probe} = \sqrt{\frac{2(\Gamma_{in}^{open} - \Gamma_{in}^{match}) \cdot (\Gamma_{in}^{match} - \Gamma_{in}^{short})}{(\Gamma_{in}^{open} - \Gamma_{in}^{short})}} \tag{3.3.3 b}$$

$$S_{22}^{probe} = \frac{\Gamma_{in}^{short} + \Gamma_{in}^{open} - 2\Gamma_{in}^{match}}{\Gamma_{in}^{open} - \Gamma_{in}^{short}} \tag{3.3.3 c}$$

However, at high frequencies (e.g. 100 GHz or higher) the parasitics are no longer negligible, especially for the short standard that may contribute several Ohms of reactance that can not be ignored. When taking the parasitic elements into account the complete formula 3.3.3a-c for deriving the *S*-parameters of a two-port network by using a one-port measurement and a standard calibration substrate can be replaced by

$$S_{11}^{probe} = \frac{\Gamma_{in}^{match}\Gamma_{load}^{open}\Gamma_{load}^{short}(\Gamma_{in}^{open} - \Gamma_{in}^{short}) + \Gamma_{load}^{match}(\Gamma_{in}^{open}\Gamma_{in}^{short}(\Gamma_{load}^{short} - \Gamma_{load}^{open}) + \Gamma_{in}^{match}(\Gamma_{load}^{open}\Gamma_{in}^{short} - \Gamma_{load}^{short}\Gamma_{in}^{open})}{\Gamma_{load}^{open}\Gamma_{load}^{short}(\Gamma_{in}^{open} - \Gamma_{in}^{short}) + \Gamma_{load}^{match}(\Gamma_{in}^{match}(\Gamma_{load}^{open} - \Gamma_{load}^{short}) + \Gamma_{load}^{short}\Gamma_{in}^{short} - \Gamma_{load}^{open}\Gamma_{in}^{short})} \tag{3.3.4 a}$$

$$S_{12}^{probe} = S_{21}^{probe} = \sqrt{\frac{(\Gamma_{in}^{match} - \Gamma_{in}^{open})(\Gamma_{load}^{match} - \Gamma_{load}^{short})(\Gamma_{load}^{short} - \Gamma_{load}^{open})(\Gamma_{in}^{match} - \Gamma_{in}^{short})(\Gamma_{in}^{open} - \Gamma_{in}^{short})}{\left(\Gamma_{load}^{open}\Gamma_{load}^{short}(\Gamma_{in}^{open} - \Gamma_{in}^{short}) + \Gamma_{load}^{match}(\Gamma_{in}^{match}(\Gamma_{load}^{open} - \Gamma_{load}^{short}) + \Gamma_{load}^{short}\Gamma_{in}^{short} - \Gamma_{load}^{open}\Gamma_{in}^{short})\right)^2}} \tag{3.3.4 b}$$

$$S_{22}^{probe} = \frac{\Gamma_{in}^{match}(\Gamma_{load}^{open} - \Gamma_{load}^{short}) + \Gamma_{in}^{open}\Gamma_{load}^{short} - \Gamma_{in}^{short}\Gamma_{load}^{open} + \Gamma_{load}^{match}(\Gamma_{in}^{short} - \Gamma_{in}^{open})}{\Gamma_{load}^{open}\Gamma_{load}^{short}(\Gamma_{in}^{open} - \Gamma_{in}^{short}) + \Gamma_{load}^{match}(\Gamma_{in}^{match}(\Gamma_{load}^{open} - \Gamma_{load}^{short}) + \Gamma_{load}^{short}\Gamma_{in}^{short} - \Gamma_{load}^{open}\Gamma_{in}^{short})} \tag{3.3.4 c}$$

### *3.3.1.3 Characterising Mixers*

An external waveguide subharmonic mixer is needed for a spectrum analyser to characterise an oscillator device operating beyond 50 GHz. Generally speaking, if the output of a mixer is connected to a power amplifier that boosts the IF signal, the mixer is called an active mixer; otherwise it is a passive mixer. The simplest passive mixer can be made of a Schottky diode due to the nonlinear relationship between current and voltage at

its terminals. Other passive mixers may use various topologies, such as single or double-balanced mixers. In this work, passive mixers have been used for frequency bands at 50 GHz-75 GHz, 75 GHz-110 GHz, 90 GHz-140 GHz and 110 GHz-170 GHz. For frequency bands at 140 GHz-220 GHz and 220 GHz-325 GHz, active mixers were used to avoid excessive conversion losses at such high frequencies.

It is desirable to know the conversion loss performance of a mixer so that the power from the oscillator DUT can be approximately measured by using a spectrum analyser without resorting to a power meter. However, at high millimetre-wave frequencies, this critical data is surprisingly not always divulged by some manufacturers. Two mixers, at *V*-band and *W*-band, have therefore been characterised using known sources for this work.

- **Characterising a *V*-band Mixer and Measurement Setup**

The signal source was a synthesised sweep generator (68187B) from Wiltron Company. It provides a well-controlled output power level of signals from 10 MHz to 60 GHz. The *V*-band mixer was WHMP-15 from Farran Technology. Its RF input is a *V*-band rectangular waveguide, and its output is coaxial and connected to a diplexer that separates the IF from the LO of the spectrum analyser. A coaxial-rectangular adaptor (PTC-15VF-01 from Ducommun Incorporated) and a 36 inch long coaxial cable (V086MMHF-36D from RF Coax Inc.) with a core diameter of 1.85 mm are used for the interconnection. The same setup was used for *V*-band on-wafer spectrum analyser measurement setup. Due to the limited frequency range of the signal source only the frequency range between 50 GHz and 60 GHz was tested.

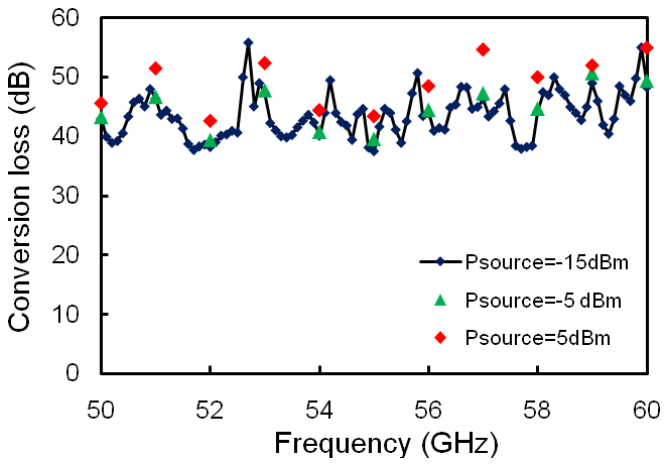


**Figure 3-17** System conversion loss of a *V*-band spectrum analyser measurement setup including conversion loss of a *V*-band mixer, a coaxial-to-rectangular waveguide transition and a 36-inch coaxial cable in the frequency range of 50 GHz-60 GHz.

The experiment started with a fixed output power of the signal source at three different levels: at -15 dBm, -5 dBm and 5 dBm, and the output frequency was varied from 50 GHz to 60 GHz. By reading the measured power level by the spectrum analyser and subtracting it from the signal source output power, the system loss is derived. The system loss includes the mixer conversion loss, the cable loss and the coaxial to rectangular transition loss. The calculated results are plotted in Figure 3-17. It is clearly seen that the system conversion loss has a wide variation, approximately 20 dB, ranging from 38 dB to 58 dB in the frequency range of 50 GHz-60 GHz. In addition, the system conversion loss was found to increase with signal source power output level due to the nonlinearity of the mixer. The conversion loss of the mixer can simply be calculated by subtracting the cable loss and the transition loss from the system conversion loss.

- **Characterising a *W*-band Mixer**

The *W*-band mixer was WHMP-10 from Farran Technology. It has a *W*-band rectangular waveguide input port and a coaxial IF/LO output port. Due to the lack of a reliable signal source at *W*-band in the laboratory, the system conversion loss or mixer conversion loss was not measured. Nevertheless, the reflection coefficient of the mixer could be measured using a VNA. The VNA having *W*-band rectangular waveguide was calibrated using the SOL method. The RF input port of the mixer was connected to the VNA waveguide test port, and the mixer output was loaded by the spectrum analyser while the frequency extension mode was activated. Figure 3-18 shows the measured magnitude of the reflection coefficients of the mixer. Note that this mixer's performance could be considered reasonably poor but the measurement was able to be performed anyway.

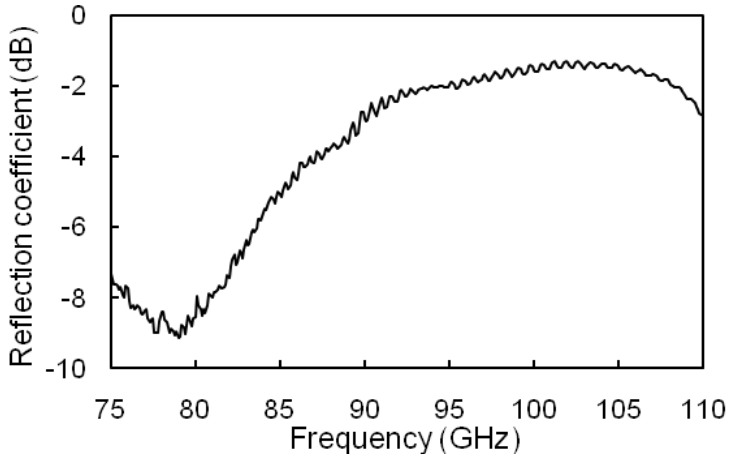


**Figure 3-18** Magnitude of the reflection coefficient of the RF port of the *W*-band mixer.

*3.3.1.4 System Loss*

The total system loss $P_{system}$ consists of all the losses contributed from all elements in the measurement setup. Thus, if using spectrum analyser measurement setup to measure the RF power of a signal source, the total system loss has to be excluded when reading the measured power level from the spectrum analyser. The total system loss can be derived by the following equation

$$P_{system} = P_{probe} + P_{cable} + P_{mixer} + P_{others} \tag{3.3.5}$$

where $P_{probe}$ is the insertion loss of the probe, $P_{probe} = 20\log|S_{21}|$. $P_{cable}$ is the transmission loss of any cables applied, $P_{mixer}$ is the conversion loss of the mixer, and $P_{others}$ is the losses from any other components such as diplexer and coaxial to rectangular transition.

### 3.3.2 Load-pull Measurement for Investigating Load Effect on Power and Frequency Performance of Planar Gunn Devices

The load-pull measurement technique is more commonly used in analysing the input and output impedances of two-port devices, or the influence of load mismatch on output power and frequency of one-port oscillators. In order to investigate the effect of load impedance on the output power for Gunn diodes, the one-port load pull measurement has been developed and applied. By using this technique, power and frequency variation can be easily observed as the E-H tuner is systematically adjusted. The load impedance is therefore derived by de-embedding the wafer probe, E-H tuner and mixer using a VNA.

*3.3.2.1 Measurement System Description*

Figure 3-19 shows a block diagram and a photograph of the on-wafer one-port load-pull measurement setup for *W*-band (75 GHz-110 GHz). It consists of a spectrum analyser (3 Hz-50 GHz), a diplexer, a *W*-band mixer and a *W*-band probe with integrated bias-tee. The DC bias is applied to the DUT through the bias-tee. It can be clearly seen from Figure 3-19 that the probe and the mixer make up the load circuit of the DUT ($Z_{system}$). Since they have fixed characteristics, a tuner, as shown in Figure 3-19, is needed between the mixer and the probe in order to vary the system load impedance and to investigate its effect on

the output power of the DUT. The major difference from a common spectrum measurement system, as discussed in the last section, is that the *S*-parameters of each component in the setup are required for determining the load impedance to the DUT.

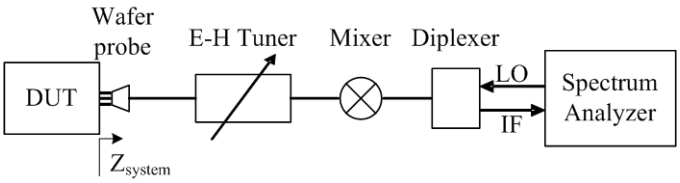


(a)

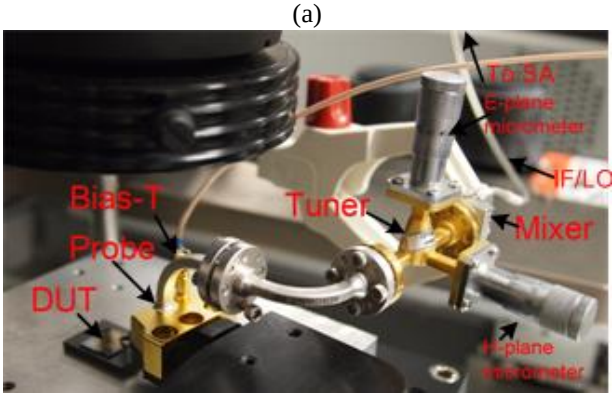


(b)

**Figure 3-19** Experimental setup for on-wafer load-pull measurements at *W*-band. (a) A block diagram, and (b) the actual setup.

### *3.3.2.2 Characterising the W-band Probe*

It was discussed that an improved SOL method can be used to characterise a millimetre-wave probe in Section 3.3.1.2. Putting three measured one-port reflection coefficients of the probe while terminated by three known standards along with the three known reflection coefficients of the loads into 3.3.4a-c, the *S*-parameters of the probe can be derived. The three known load standards from the calibration substrate (CS-15 from GGB Industries) are Matched load (50 Ω, 1.1 pH), open (3.25 fF) and short (7.2 pH), respectively.

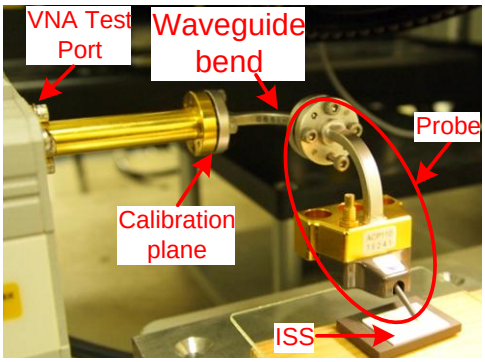


(a)

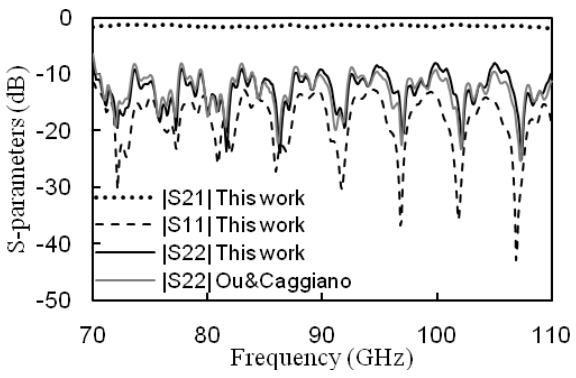


(b)

**Figure 3-20** (a) Measurement setup for deriving the *S*-parameters of a *W*-band probe, and (b) De-embedded *S*-parameters of the *W*-band probe. $|S_{11}|$ and $|S_{22}|$ are magnitudes of reflection coefficients at the rectangular waveguide port and GSG probe tips, respectively.

The *W*-band probe used in this experiment was an ACP110-100 series probe (Cascade MicroTech) that included 100 μm pitch GSG probe tips, a 90 °rectangular waveguide bend and a coax-rectangular waveguide transition. Figure 3-20a shows the measurement setup for deriving the *S*-parameters of the *W*-band probe. The de-embedded magnitudes of the *S*-parameters ($|S_{11}|$, $|S_{21}|$ and $|S_{22}|$) of the probe are shown in Figure 3-20b. The probe has a measured insertion loss of less than 2 dB in the frequency range of 70 GHz-110 GHz. For comparison the magnitude of reflection coefficient of the probe tip $|S_{22}|$ derived using Ou&Caggiano's method [163] is also plotted in Figure 3-20b. It can be clearly seen that the parasitics do make a difference when de-embedding the probe *S*-parameters using the one-port measurement technique.

### *3.3.2.3 Characterising the W-band E-H Tuner*

The waveguide tuner was characterised using the 2-port VNA that was calibrated between 70 GHz and 110 GHz using the TRL method with an Agilent W11644A calibration kit. The measurement setup is shown in Figure 3-21a. Each combination of E and H positions for the tuner, set by adjustable micrometers, corresponds to a different set of tuner S-parameters ( $S_{11}^{tuner}$ , $S_{12}^{tuner}$ , $S_{21}^{tuner}$ , and $S_{22}^{tuner}$ ). Figure 3-21b shows a linear relationship between the magnitude of $S_{21}^{tuner}$ and the E-plane micrometer of the tuner at 101.8 GHz while the H-plane micrometer position was fixed at 0.3 mm.

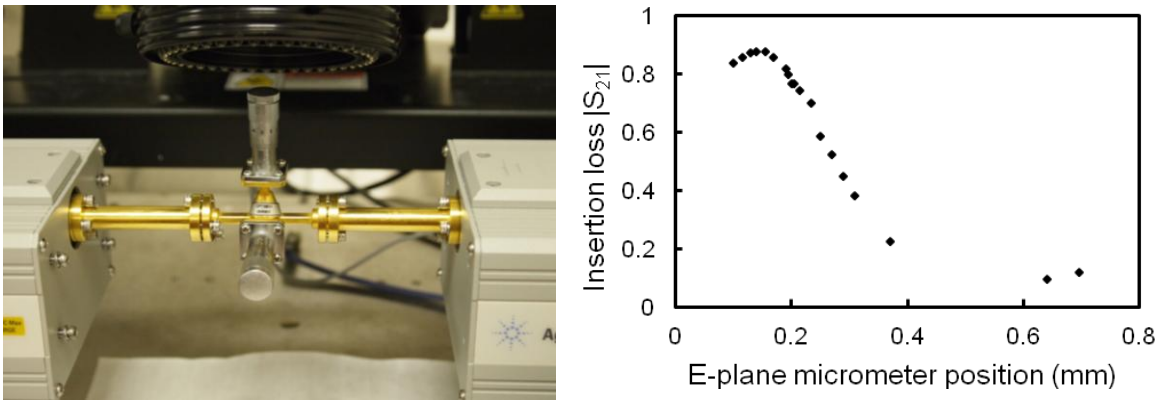


(a) (b)

**Figure 3-21** The measurement setup for characterising the *W*-band E-H tuner and its measured transmission characteristics at 101.8 GHz.

*3.3.2.3 Deriving Load Impedance*

Having determined the *S*-parameters of the wafer probe, the E-H tuner and the waveguide mixer, the system input impedance can be derived using the following equations,

$$Z_{system} = \frac{1-\Gamma_{system}}{1+\Gamma_{system}} \cdot Z_0 \tag{3.3.6}$$

$$\Gamma_{system} = S_{22}^{probe} + \frac{S_{12}^{probe} S_{21}^{probe} \Gamma_{tuner}}{1 - S_{11}^{probe} \Gamma_{tuner}} \tag{3.3.7}$$

$$\Gamma_{tuner} = S_{11}^{tuner} + \frac{S_{12}^{tuner} S_{21}^{tuner} \Gamma_{mixer}}{1 - S_{22}^{tuner} \Gamma_{mixer}} \tag{3.3.8}$$

where $Z_{system}$ and $\Gamma_{system}$ are the system input impedance and reflection coefficient, respectively, when the system consists only of the probe, tuner and mixer. $\Gamma_{tuner}$ is the reflection coefficient looking into the tuner when it is terminated by a mixer. $\Gamma_{mixer}$ is the measured input reflection coefficient of the mixer when it is terminated by the diplexer and the spectrum analyser.

### 3.3.3 Power Measurement Setup

In Section 3.2.1, it was discussed how the power of a signal can be approximately measured by a spectrum analyser if the system loss is available. However, it is only an approximate estimation because an accurate measurement on the conversion loss of mixers in the entire operation frequency range is impossible. A more commonly used RF power measurement method is based on a power meter. A power meter (e.g. PM4 from Erickson Instruments) has a sensor head and a processing and display unit. The sensor head uses the calorimetry method to measure millimetre-wave signal power. It has two broadband well matched absorbers that are embedded in two identical W-band waveguides. One is a test absorber which absorbs any incident millimetre-wave signals and converts it into heat resulting in an increase of temperature. The other is a reference absorber that is connected to the central control unit. A precisely controlled current leads to a temperature change of the reference absorber. A sensitive temperature comparator connects both absorbers and senses the temperature difference between them. Once a millimetre-wave signal is incident

on the test waveguide, and therefore the test absorber, the temperature rises. Meanwhile, the temperature comparator senses the difference in temperature between the two absorbers and sends a request to the central circuit control unit, which then increases the current for the reference absorber until the temperature in both absorbers are equal. By calculating the current applied to the reference absorber, the power the test absorber has absorbed from the incident signal is calculated.

Figure 3-22 illustrates an on-wafer power measurement setup for W-band application. Compared with the spectrum analyser measurement setup shown in Figure 3-16, the power measurement setup does not need an external mixer. Appropriate tapers can be used to measure frequencies higher than W-band. For example, a W-G band taper allows the power meter to measure a signal source operating in G-band. Theoretically speaking, this power meter may detect RF power up to 2 THz [165].

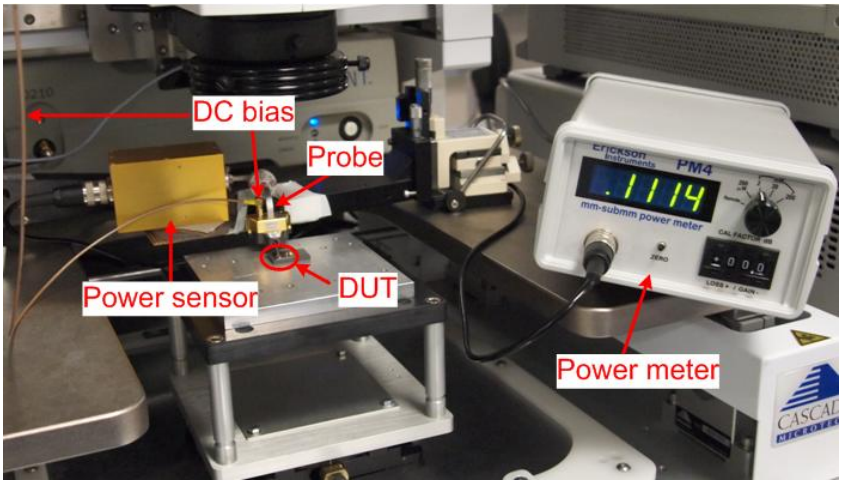


**Figure 3-22** An on-wafer W-band power measurement setup using a power sensor and a power meter.

The disadvantage of this type of power meter is that it has a broadband operating frequency range and uses the natural cut-off frequency of the rectangular waveguide as a lower operating frequency limit and there is no upper frequency limit on operating range. This means that the sensor absorbs the sum of all signals above the waveguide cut-off frequency. If a signal source generates harmonic oscillations at frequencies greater than the input waveguide cut-off frequency, then the measured power will include the sum of these harmonic signals. In this case, appropriate external filtering circuits are needed to ensure only the power of an individual frequency signal is detected.

## 3.4 Application of the VNA for Oscillation Detection

### 3.4.1 Introduction

It has been discussed in Section 3.2 that a calibrated VNA is commonly used for accurately characterising the frequency response of non-oscillating devices, such as passive networks and active amplifier components. In fact, every effort must be made to stabilise any active DUs before performing such measurements. It is also believed that the VNAs do not inherently have the ability to make spectral power measurements because the simpler receiving units of the VNAs, compared to the spectrum analysers, are not capable of rejecting image signals and other off-carrier frequency components [145]. Therefore, a possible application of the VNA technique for measuring oscillating devices does not seem immediately obvious and perhaps counter-intuitive. However, in the present work, theoretical analysis and a series of experiments have been conducted to show how a VNA can be used as a complementary tool to the spectrum analyser, to identify the oscillation frequency of a millimetre-wave signal source having a moderate or low output power, provided that certain care is taken.

The advantages of using the VNA to detect an oscillation are twofold. Firstly, VNAs have a comparatively simpler measurement setup than spectrum analyser. At present, the latest VNA instruments have a *single* setup for measurement frequencies from as low as 70 kHz to 110 GHz from Anritsu (ME7828A), or 10 MHz up to 110 GHz from Agilent (N5250C) and R&S (ZVA110). In contrast, as discussed in Section 3.3, three different setups are required for spectrum analyser-based measurements to cover the same frequency range e.g. 3Hz-50 GHz, 50 GHz-75 GHz and 75 GHz-110 GHz, because they are commonly band-limited by the additional external waveguide mixers and probes required. Figure 3-23 show the typical simplified block diagrams for an on-wafer spectrum analyser measurement setup and an on-wafer VNA measurement setup to 110 GHz. One can clearly see that for spectrum analyser based measurement, the probe and mixer need to be manually changed for measurements in different frequency bands below 110 GHz. In comparison, a VNA based setup is able to perform frequency measurements up to 110 GHz in a single sweep. Furthermore, important DC characteristics, such as current-voltage (IV) and capacitance-voltage (CV) measurements which are commonly needed for fully characterising active DUTs can be performed simultaneously using a semi-automated probe station. This simply

entails swapping the DC power supply with a semiconductor device analyser such as the Agilent B1500a for example. This integrated setup can dramatically reduce the time needed for accurately characterising the DC and RF performance of active devices. For frequencies above 110 GHz, both the spectrum analyser and VNA measurement methods require at least two separate setups (140 GHz-220 GHz and 220 GHz-325 GHz).

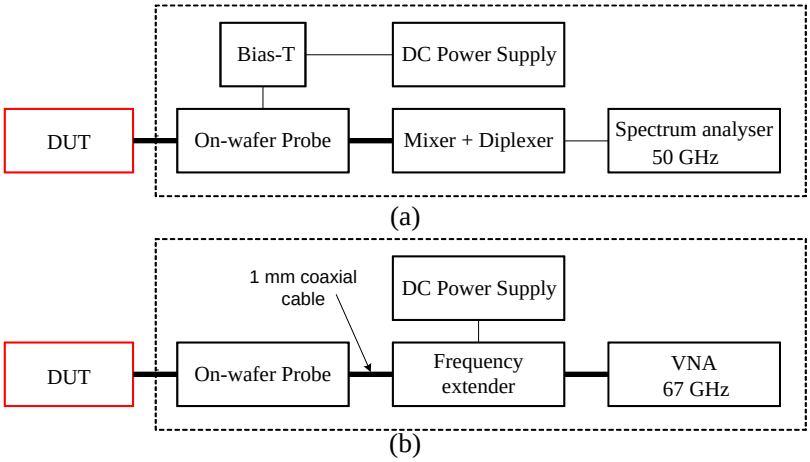


**Figure 3-23** Block diagrams showing (a) on-wafer spectrum analyser measurement setup and (b) on-wafer VNA measurement setup from near DC to 110 GHz. Note that the frequency extender enables the 67 GHz VNA to operate up to 110 GHz in this case.

Secondly, the VNA has another advantage in that it can measure low power oscillator devices at high frequencies (>140 GHz). In this frequency range, the spectrum analyser measurement technique needs an external mixer which has very high conversion loss (e.g. >50 dB typically). If a signal source has low output power, for example -40 dBm, it becomes difficult to use the spectrum analyser method to detect the signal due to the limit of internal noise floor, dynamic range and minimum detectable power etc, unless an amplifier is added immediately after the mixer. However, the VNA has the capability of detecting such low level signal. The theoretical discussion and experimental results will be given in the following sections.

### 3.4.2 Analysis of Characterising Oscillator Devices Using a VNA

#### *3.4.2.1 One-port Passive DUTs*

Taking one-port VNA measurement as an example, one-port DUTs can be classified into two categories. One category is passive DUTs such as antennas and resonators, and the second category is oscillating DUTs, such as oscillators. A schematic view of such test by

using a VNA is shown in Figure 3-24. For clarity, it is convenient to normalise the system impedance to unity.

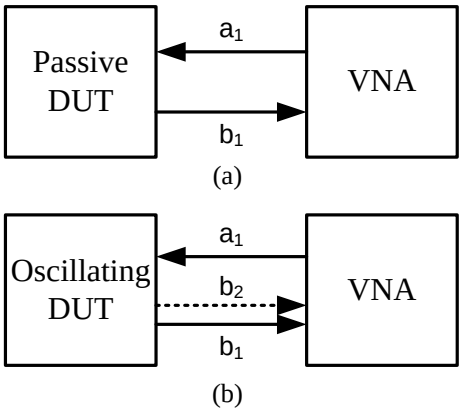


**Figure 3-24** Signal flow representation for testing a one-port (a) passive DUT and (b) oscillating active DUT by using a VNA.

As described in Section 3.2.2, the VNA sends a frequency-swept stimulus signal ($a_1$) to the DUT at each frequency sample point and measures the reflected signal ($b_1$). By comparing the amplitude and phase of the reflected signal with those of the stimulus signal, the reflection coefficients are derived [145, 146, 166]. In fact, both stimulus and reflected signals are down-converted to an IF and then the amplitude and phase are measured. In order to simplify the discussion, the down-mixing process is omitted.

Since the passive DUTs only change the stimulus signal of VNA by attenuating or phase-shifting depending on the reactance of the DUT, the reflection coefficient ($\Gamma_i$) of a one-port passive DUT measured by a VNA is written as

$$\Gamma_i = \frac{b_1}{a_1} = \frac{B_i \cos(\omega_i t + \theta_i)}{A_i \cos(\omega_i t)} \tag{3.4.1 a}$$

$$a_1 = A_i \cos(\omega_i t) \tag{3.4.1 b}$$

$$b_1 = B_i \cos(\omega_i t + \theta_i) \tag{3.4.1 c}$$

$$B_i = \alpha_i A_i \tag{3.4.1 d}$$

$i = 0,1,2 \cdots N$ where $N$ is the total number of sample points in the measurement frequency range of interests, and $i$ is the individual sample point. $A_i$ and $\omega_i$ are the amplitude and angular frequency of the stimulus at each sample point, respectively. $\alpha_i$ is the attenuation factor. $\theta_i$ is the phase change as the stimulus signal is reflected by the DUT. The DUT

does not change the stimulus frequency. Equation 3.4.1a can also be written in the decibel format as,

$$20\log|\Gamma_i| = 20\left(\log|b_1| - \log|a_1|\right) = 20\left(\log B_i - \log A_i\right) = P_2 - P_1 \qquad (3.4.2)$$

$P_1$ and $P_2$ are the power of the stimulus and the reflected stimulus normalised to the system impedance, respectively. Once the reflection coefficient is derived, the device impedance ( $Z_i^{DUT}$ ) can be calculated by using the following equation

$$Z_i^{DUT} = \frac{1+\Gamma_i}{1-\Gamma_i} \cdot Z_0 \qquad (3.4.3)$$

where $Z_0$ is the system impedance normally chosen as 50 Ω.

*3.4.2.2 One-port Oscillating DUTs-Theory*

Now consider the case when the one-port DUT is an active oscillating device. Assuming the device has frequency independent impedance except at the frequency where it outputs a signal. It is regardless of the device is on or off or any changes from biasing condition for voltage-controlled oscillators (VCOs). This assumption is valid for a commercial signal generator for example, as will be discussed in Section 3.4.2.3, or an oscillator that has a compensating output circuit (e.g. attenuators).

If the DUT does not generate a signal, its reflection coefficient, $\Gamma_i^{Off}$ , measured by a VNA can still be expressed using Equation 3.4.1a or Equation 3.4.2. However, if the DUT emits signals at a certain frequency $\omega_m$ or a certain range of frequencies $\omega_m \pm \Delta\omega$ as schematically depicted in Figure 3-24b, then apart from the reflected stimulus signal $b_1$ that goes back into the VNA test port (if the DUT has internal impedance other than 50 Ω), another signal $b_2$ generated by the DUT goes into the VNA test port, too. The DUT generated signal is mathematically represented here as

$$b_2 = B_m \cos(\omega_m t + \varphi) \qquad (3.4.4\ a)$$

and its power level, which is normalised to the system impedance, is represented as

$$P_3 = 20\log|b_2| = 20\log B_m \qquad (3.4.4\ b)$$

where $B_m$ and $\omega_m$ are the amplitude and angular frequency of the signal generated by the oscillating DUT, respectively. $\varphi$ is the phase difference between the stimulus signal and

the DUT generated signal. Phase noise of the signal is omitted here but discussion on it will be given later. Thus, the total signal detected by the VNA test port at the *k*-th sample point can be expressed as a sum of two signals

$$b_1 + b_2 = B_k \cos(\omega_k t + \theta_k) + B_m \cos(\omega_m t + \varphi) \tag{3.4.5}$$

This argument is valid when $\omega_k$ and $\omega_m$ are equal or very close because the default intermediate frequency (IF) filter of a VNA has a very narrow bandwidth (e.g. 100 kHz for an Agilent E5071 [167]). In practice it is normally set to be much lower than this in order to achieve higher accuracy. This means that the signal generated by the DUT can only be added to the reflected stimulus when the two frequencies are equal or very close, otherwise it will be rejected and cancelled. To simplify the discussion, it is assumed that the signals are equal in frequency. A more general case will be discussed in Section 3.4.3. Therefore, the reflection coefficient $\Gamma_i^{On}$ at the *k*-th sample point or frequency of $\omega_k$ becomes

$$\Gamma_k^{On} = \frac{b_1 + b_2}{a_1} = \frac{B_k \cos(\omega_k t + \theta_k) + B_m \cos(\omega_m t + \varphi)}{A_k \cos(\omega_k t)} \tag{3.4.6 a}$$

or in decibel as

$$\begin{aligned} 20\log\left|\Gamma_k^{On}\right| &= 20\left(\log|b_1 + b_2| - \log|a_1|\right) \\ &= 20\left(\log\left[B_k \cos(\omega_k t + \theta_k) + B_m \cos(\omega_m t + \varphi)\right] - \log A_i\right) \end{aligned} \tag{3.4.6 b}$$

where $k \in i$ and $\omega_k = \omega_m$. However, it remains unchanged as the device is off or Equation 3.4.2 at other frequencies where $\omega_i \neq \omega_m$. This indicates that when there is a signal generated by the DUT at a particular frequency, the measured reflection coefficient will show an abrupt change at that frequency and no change at any other frequencies, assuming that the device has a flat response to the stimulus at least in a small frequency range. Thus, by comparing any changes of the reflection coefficients of the DUT measured by a VNA when the device output is switched on or off, the oscillation frequency will be identified. Subtracting Equation 3.4.6b by Equation 3.4.2 results in the following equation,

$$20\left(\log\left|\Gamma_k^{On}\right| - \log|\Gamma_i|\right) = 20\left[\log\left|B_k \cos(\omega_k t + \theta_k) + B_m \cos(\omega_m t + \varphi)\right| - \log B_k\right] \tag{3.4.7}$$

The RHS of Equation 3.4.7 determines whether or not the oscillation can be identified by using the VNA measured reflection coefficients. If it is greater than zero, the subtraction leads to zero everywhere but a positive peak at frequency $\omega_k = \omega_m$. If the subtraction is

less than zero, it indicates zero everywhere else but a negative peak or a dip at frequency $\omega_k = \omega_m$. Finally if the RHS of Equation 3.4.7 is a zero, then it means that there is no change after the device is switched on. Therefore, with the exception of the third condition in which the right hand side of Equation 3.4.7 is zero, the former two situations will always give a definitive indication of an oscillation. In fact, the core of Equation 3.4.7 is the relationship between the sums of reflected signal from the DUT ( $B_k \cos(\omega_k t + \theta_k)$ ) and the output signal of DUT ( $B_m \cos(\omega_m t + \varphi)$ ) and the amplitude of the reflected signal from the DUT ( $B_k$ ). The detailed discussion is divided into three cases:

- **Case I**

When the amplitude of the DUT generated signal is much smaller than the amplitude of the reflected stimulus, that is $B_k >> B_m$, the influence of the $B_m$ on $B_k$ is small. The RHS of Equation 3.4.7 can thus be written as

$$20\left\{\log\left|B_k \cos(\omega_k t + \theta_k) + B_m \cos(\omega_m t + \varphi)\right| - \log B_k\right\} \approx 20\left[\log\left|B_k \cos(\omega_k t + \theta_k)\right| - \log B_k\right] = 0$$

This means although the DUT generates an oscillation at $\omega_m$, the measured total signal at the VNA test port has almost no change. Therefore, the VNA measured magnitudes of the reflection coefficient for the DUT with and without the oscillation shows little difference.

- **Case II**

When the amplitude of a generated signal is much greater than the amplitude of the reflected stimulus, that is $B_k << B_m$, then the reflected stimulus becomes negligible. Thus the total signal measured at the VNA test port will be dominated by the signal generated by the DUT at the frequency of $\omega_m$. The Equation 3.4.7 can be written as

$$20\left(\log\left|\Gamma_k^{On}\right| - \log\left|\Gamma_i\right|\right) = 20\left\{\log\left|B_k \cos(\omega_k t + \theta_k) + B_m \cos(\omega_m t + \varphi)\right| - \log B_k\right\}$$

$$\approx 20\left[\log\left|B_m \cos(\omega_m t + \varphi)\right| - \log B_k\right] = 20\left(\log B_m - \log B_k\right) \approx 20 \log B_m = P_3 \qquad (3.4.8)$$

where $P_3$ is the power of the DUT generated signal that is normalised to the system impedance. In this case, a positive peak appears at the frequency of $\omega_m$, and the amplitude is the approximate value of the power of signal corresponding to this peak.

- **Case III**

When the amplitude of the DUT generated signal is approximately equal to the amplitude of the reflected stimulus, that is $B_k \approx B_m$, then the phase difference between these two signals, which are not reference-locked, may cause random effects on the total detected signal. This will manifest in a time-varying measured reflection coefficient $\Gamma_i^{On}$ from the VNA. Two situations may then occur in this case. In the constructive situation, the phase sum or difference between the two signals is within $(-\pi/2, \pi/2)$, that is $(2n-1/2)\pi < \theta_k \pm \varphi < (2n+1/2)\pi$, where $n$ is an integer. This leads an increase in the amplitude of total signal; in other words, the RHS of Equation 3.4.7 becomes positive. Therefore, a peak will be observed at the frequency of $\omega_m$ once the DUT outputs the signal. On the other hand, if the phase difference between the two signals is within $(\pi/2, 3\pi/2)$, that is $(2n+1/2)\pi < \theta \pm \varphi < (2n+3/2)\pi$, the total signal will increase if $B_m > 2B_k$ and decrease if $B_m < 2B_k$. Thus a positive peak is observed when $B_m > 2B_k$, a negative peak or a dip is observed when $B_m > 2B_k$, and no change is observed when $B_m = 2B_k$ and $\theta_k \pm \varphi = (2n+1)\pi$.

To summarise the preceding theoretical discussion, the principle of using the VNA to identify an oscillation signal generated by an oscillating active DUT is expressed by Equation 3.4.7. The best situation is Case II in which the signal frequency can be identified and the power of the signal can be calculated. In Case III, the signal can possibly be identified due to its time-varying fluctuation of reflection coefficient as a result of the constructive, destructive, or unchanged effect. Unfortunately, it is impossible to detect any output signals from the DUT in Case I. This analysis can thus provide a theoretical guideline when using the VNA to detect an oscillation from an oscillating DUT. There is no direct relationship between the power of stimulus that is sent out from the test port of the VNA and the power of the signal that is generated by the DUT. This indicates that it is possible for a weak signal provided that its power is higher than the reflected stimulus. The following experiment has been conducted to demonstrate the theory discussed above.

*3.4.2.3 One-port Oscillator DUTs: Experiments*

It has been theoretically discussed in the last section that the VNA can be used to identify an oscillation signal in the frequency domain by simply comparing the measured reflection coefficient of a DUT when it is switched on and off. An experiment to verify the feasibility of this application of the VNA has first been performed using a commercial signal generator.

The commercial signal generator used was an Agilent E8257D that has well controlled output power level (-20 dBm—+15 dBm) and fine frequency resolution [168]. The output port of the signal generator was connected to a 3 dB attenuator which has impedance of 50 Ω over its frequency range of operation (DC-50 GHz) to improve the port matching of the signal generator. Importantly, the attenuator ensures little power of the VNA stimulus is reflected and thus fulfilling the condition discussed in Case II in Section 3.4.2.2. The Agilent E5071B VNA was used for this experiment with the output power between -15 dBm and +10 dBm [167].

Firstly, the output power of the stimulus from the VNA ( $P_1$ in Equation 3.4.2) was fixed at 0 dBm and the VNA was calibrated between 1 GHz and 2 GHz with 801 points by using the SOL method and the calibration standards from an Agilent 85052D 3.5 mm Economy Calibration Kit. The calibration was checked by measuring known artefacts, such as open, short, and broadband 50 Ω load to ensure that the calibrated frequency response was free of resonances/glitches across the complete frequency range prior to the actual device measurements.

The VNA measurement result on the signal generator and the attenuator when it is not activated is plotted in Figure 3-25a. From the measured magnitude of the reflection coefficient, one can calculate the power level of the reflected stimulus using Equation 3.4.2, for example -28 dBm at 1.5 GHz. As discussed in the theoretical analysis from Section 3.4.2.2 Case II, the VNA will be able to detect any signals that have power level much greater than -28 dBm at 1.5 GHz. In order to verify the theory, the output signal power level ( $P_3$ in Equation 3.4.4b) from the signal generator was set from -12 dBm to +12 dBm in steps of 6 dB. One can clearly see from Figure 3-25b-f that a peak in $|S_{11}|$ appears at 1.5

GHz once the signal generator outputted a signal at 1.5 GHz compared with no peaks in Figure 3-25a where the signal generator output was not activated. In addition, the amplitude of the peaks in $|S_{11}|$ increases with the output signal power from the signal generator. The amplitude of the peaks corresponding to the power difference between the signal outputted from the signal generator and the reflected stimulus from the VNA is equal to that calculated using Equation 3.4.8.

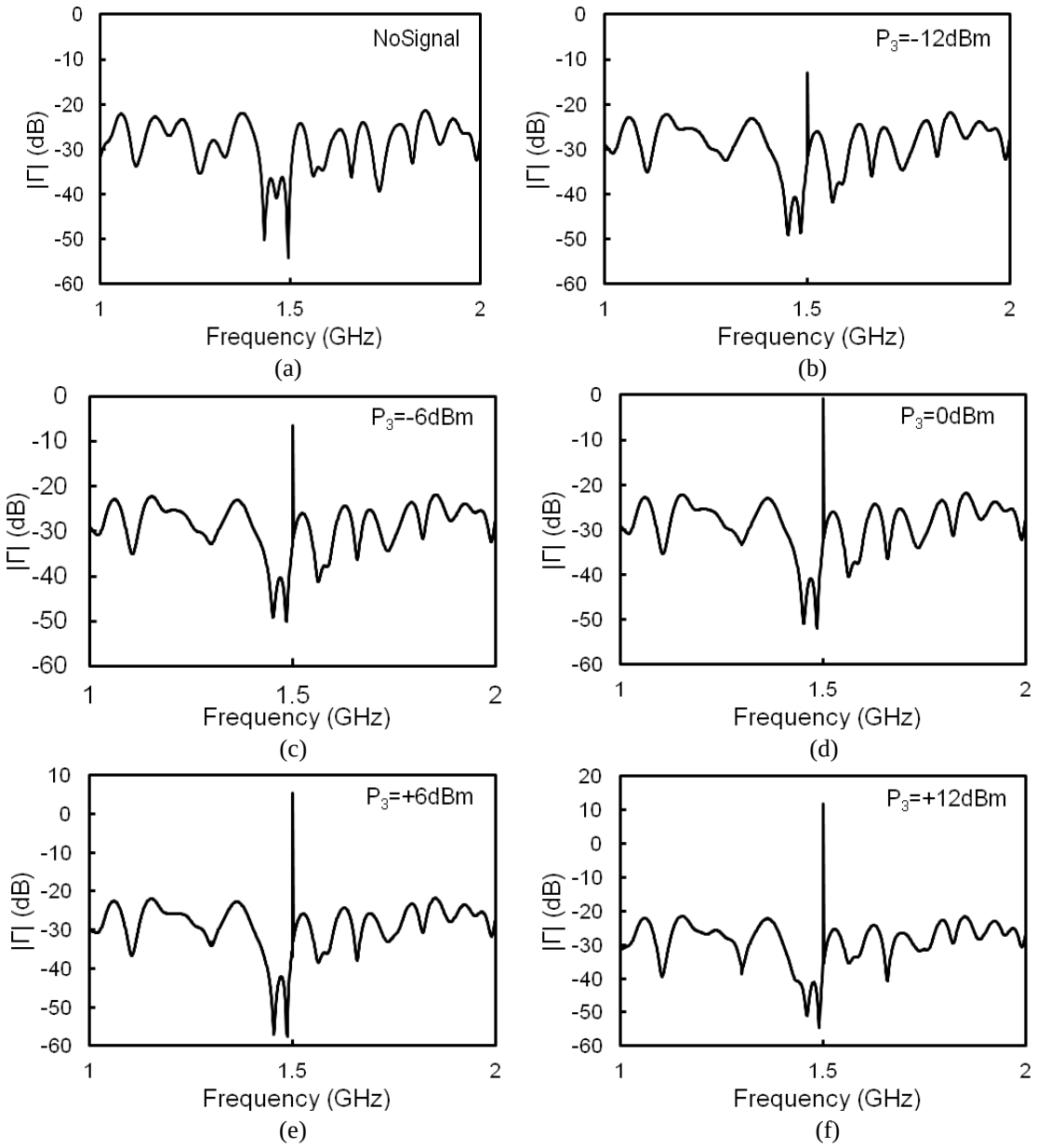


**Figure 3-25** The measured reflection coefficients of a signal source (a) When it was not activated, and (b)-(h) When it generated a signal at 1.5 GHz with output power, $P_3$, from -12 dBm to +12 dBm. A 3-dB attenuator was inserted between the VNA test port and the signal generator output.

This experiment not only verifies the theory which was discussed in the previous section but also conveys a very important message that, unlike [169, 170] in which an oscillation signal is indicated by reflection coefficients $|S_{11}|$ peaks greater than 0 dB, peaks with

amplitude smaller than 0 dB can also accurately indicate the presence of an oscillation signal.

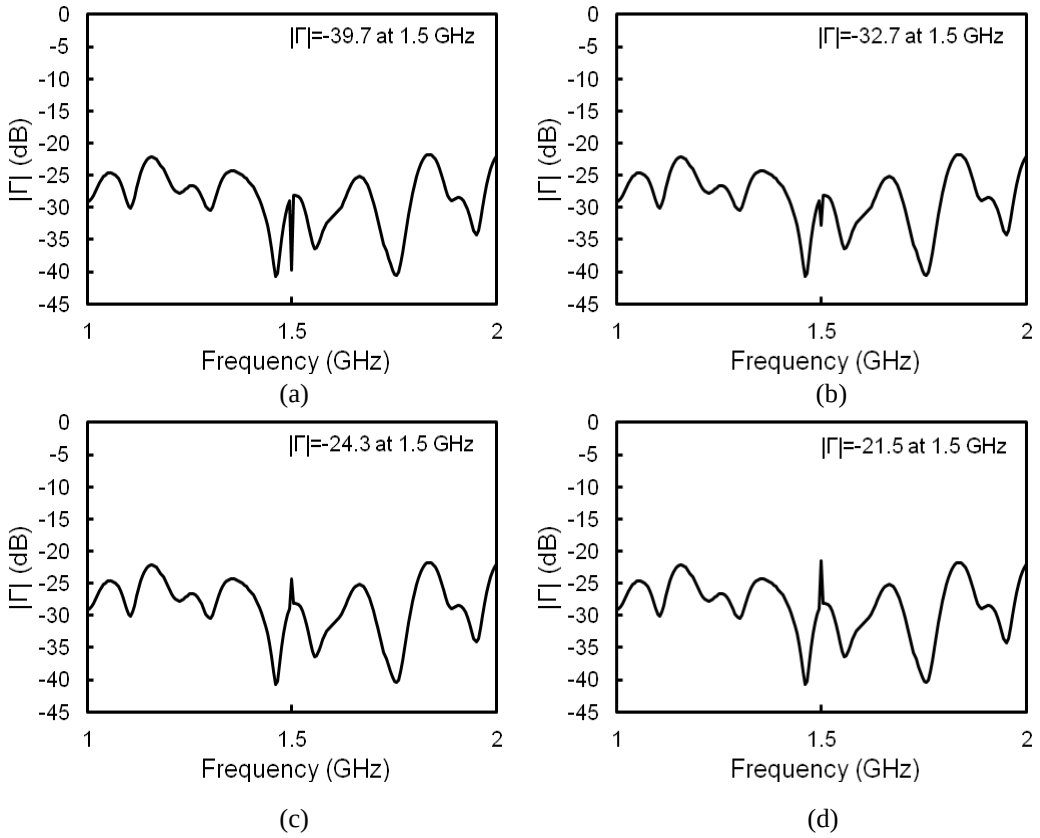


**Figure 3-26** The measured reflection coefficients of the signal source with output power of -18 dBm. The VNA was calibrated with output power of +9 dBm.

Secondly, the output power level from the signal generator $P_3$ was fixed at a certain value (e.g. -18 dBm, -12 dBm -6 dBm, and 0 dBm) and then the VNA was calibrated with different stimulus power level of $P_1$ (e.g. -15 dBm, -9 dBm, -3 dBm, +3 dBm, and +9 dBm). Since the change of VNA stimulus power do not change the reflection coefficients of the DUT but the power level of reflected stimulus. The higher the stimulus power level, the higher the reflected stimulus power level. Therefore, similar results have been found as long as the signal generator power level $P_3$ is much greater than the reflected stimulus power level $P_2$. However, if they are close, for example $P_1 = 9$ dBm and $P_3 = -18$ dBm (Since the reflection coefficient is -28 dB, then the reflected stimulus power level $P_2 = P_1 + 20\log\left|\Gamma_k^{On}\right|$ =9 dBm-28 dB=-19 dBm that is very close to $P_3$-3 dB=-21 dBm), the measured reflection coefficients fluctuate as shown in Figure 3-26. In this case, as discussed in Section 3.4.2.2 Case III, the random phase difference between the reflected signal and the DUT generated signal leads to a time-varying magnitude of reflection

coefficient. The results shown in Figure 3-26a and b indicate that the random phase difference may be within $(-\pi/2, \pi/2)$ when the measurements were taken; however Figure 3-26c and d indicate the random phase difference may be within $(\pi/2, 3\pi/2)$ at that time.

Finally, the VNA was calibrated with output stimulus power level of +15 dBm that leads to the reflected stimulus power level as -13 dBm (+15 dBm-28 dB). When the signal generator power level was below -15 dBm that is -18 dBm at the VNA test port after passing through the 3 dB attenuator, the measured reflection coefficients do not show any change irrespective of the signal generator was being activated or not. This experiment verifies the theoretical discussion in Section 3.4.2.2 Case I where the DUT generated signal has no influence on the power level of the reflected stimulus.

### 3.4.3 Discussion

It has been theoretically discussed and experimentally demonstrated in the previous section that a VNA can be used to identify oscillation frequencies of one-port oscillating DUTs by observing the changes in magnitudes of reflection coefficient before and after the device is switched on. Nevertheless, there are some special attentions that must be considered in order to use this technique effectively and correctly.

#### *3.4.3.1Measuring a DUT with Bias Dependant Impedance or Reflection Coefficients*

The theoretical and experimental analysis presented in the previous section is based on the assumption that the DUT has constant impedance at frequencies other than the DUT oscillating frequencies whether or not the DUT outputs a signal. In fact, many free-running oscillators do not meet this assumption, an RTD oscillator [171], for example, has a voltage-dependent impedance at different frequencies. In this case, the measured reflection coefficients are different in a wide frequency range including the oscillation frequency when the RTD is on and off or at different bias voltages. Figure 3-27a shows the measured reflection coefficients of an RTD oscillator when it was unbiased and biased at 1 V. Figure 3-27b shows the corresponding spectrum of the device measured using a spectrum analyser.

It can be seen in Figure 3-27a that, in addition to the four oscillation tones at 0.69 GHz, 1.38 GHz, 2.07 GHz, and 2.76 GHz which have obvious change of reflection coefficients before and after the device was activated, the reflection coefficients of the device below 1.7 GHz also changes.

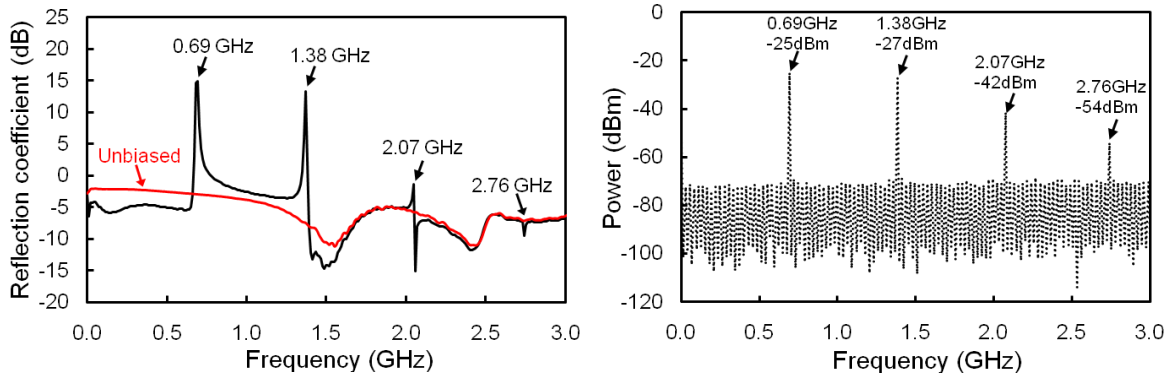


(a) (b)

**Figure 3-27** A free-running RTD oscillator was tested by using (a) a VNA and (b) a spectrum analyser biased at 1V. Both measurement techniques show that the oscillator generated oscillation frequencies at 0.69 GHz, 1.38 GHz, 2.07 GHz and 2.76 GHz.

In this case, two methods may be considered to help identify the oscillation frequencies from the measured reflection coefficients data. One method is to cascade a broadband attenuator between the VNA and the RTD oscillator under test (as demonstrated in Section 3.4.2.3) so that the impedance change of the RTD is masked by the attenuator. Alternatively, by observing an abrupt change (a peak or a dip) of reflection coefficients in the entire frequency span, one may locate the oscillation tones. The second method is based on the fact that most devices have smooth frequency response in their reflection coefficients. In Figure 3-27a, the reflection coefficients have fairly smooth responses at 1 V bias except the four oscillation tones at the four frequencies as indicated.

Similar experiments have also been carried out on a planar Gunn diode [42, 101]. The detailed discussion on this device will be given in the next chapter. Unlike conventional Gunn oscillators which are limited by the cut-off frequency of rectangular waveguides [172], the planar Gunn diode incorporated coplanar test pads so there is no lower cut-off frequency for the CPW structures. This allows one to easily measure the frequency response of such devices over a wide frequency range without changing measurement setups in order to identify the fundamental mode of oscillation. The planar Gunn diode was first tested by using spectrum analyser method from 3 Hz to 110 GHz with three different

setups. This involved using a stand-alone spectrum analyser covering from 3 Hz to 50 GHz, with (i) a 1.85mm coaxial probe (DC-65 GHz), (ii) a *V*-band (50 GHz-75 GHz) waveguide mixer and *V*-band probe, and (iii) a *W*-band probe with *W*-band waveguide mixer. The same device was subsequently tested using the described VNA (10 MHz-110 GHz) and both results are shown in Figure 3-28 for comparison.

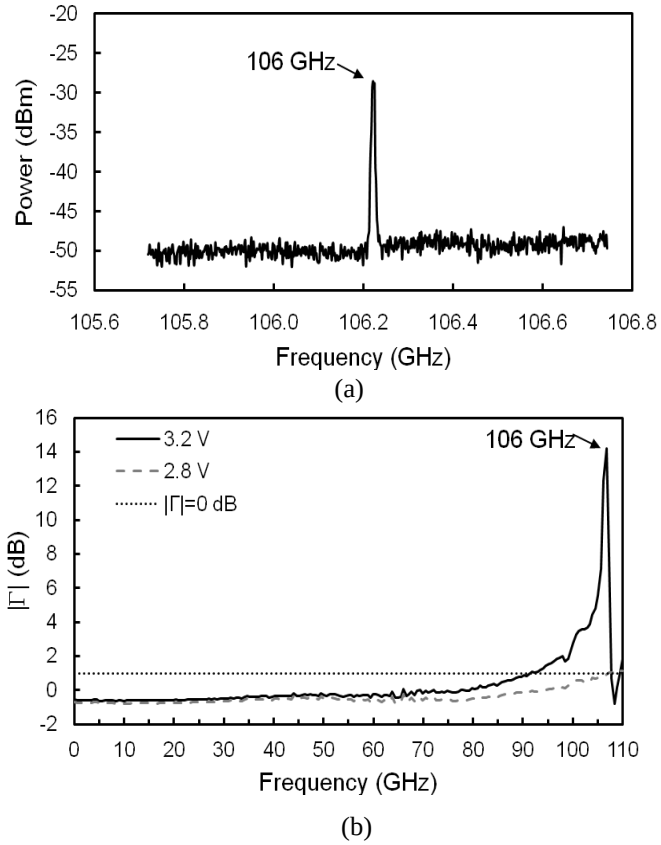


**Figure 3-28** A planar Gunn diode was tested by using spectrum analyser method and VNA method. (a) The spectrum analyser method used a spectrum analyser, a diplexer, a *W*-band mixer and a *W*-band probe. (b) The VNA has 401 sampling points between 10 MHz and 110 GHz. For comparison, the measured reflection coefficients at 3.2 V (oscillating condition) and at 2.8 V (non-oscillating condition) are shown.

One can see that the results from both measurement methods indicate the same oscillation at 106 GHz in Figure 3-28. The VNA measurement results in particular show that the device has a smooth frequency response in the entire frequency band except for the obvious peak at 106 GHz. This confirms the feasibility of the second method of solving the frequency-dependent impedance issue. In addition, this experiment also indicates one of the important advantages of using the VNA technique to detect an oscillation signal of an oscillator; namely that the 106 GHz signal is the fundamental oscillation frequency of this DUT because the single sweep shows only one peak at 106 GHz and no peaks or dips are seen at any other frequency range. This was validated using the three different setups based on the spectrum analyser and its built-in signal identification feature [6]. The same results

are obtained: no oscillation tones below 106 GHz were seen. In essence, the VNA method is a single-sweep setup that can perform the same measurement compared to three setups of the spectrum analyser method. However, some important considerations described below must be taken into account in order to use the VNA technique effectively for oscillation detection.

#### *3.4.3.2 Bias Voltage versus the VNA Stimulus Power*

When using a VNA to measure a VCO, the stimulus signal sent from the VNA will be added on the bias voltage that is applied to the device for inducing an oscillation. In this case, the VNA output level should be kept as low as possible so that this additional voltage will not make a significant effect on the actual bias voltage nor the oscillation conditions.

#### *3.4.3.3 Sampling Points and Phase Noise of the Signal*

The characteristics of the signal generated by DUTs determine the number of sample points needed in the sweep for VNA measurement. If the signal has a high phase noise, it shows a wide bandwidth in frequency domain. This means that a lower number of sampling points is needed within the measurement frequency band. On the other hand, if a signal has a relatively "clean" spectrum, a large number of sample points are required in order not to omit any frequency components. However, the setup of IF bandwidth may compensate this as will be discussed in Section 3.4.3.5.

#### *3.4.3.4 Limitations on the Power Level of DUT Generated Signals*

It was discussed in Section 3.4.2.2 Case II that when the power of the reflected signal is much greater than that of the stimulus (i.e. $B_m >> A_k$ ), the DUT generated signal dominates the VNA test port. In this case, the power level of the DUT signal should not be excessively high. For example, input power on the VNA test port should not exceed typically +10 dBm between 300 kHz and 3 GHz at its test ports [167]. Otherwise, phase lock will be lost or, in the worst case, the VNA test ports can be damaged.

*3.4.3.5 IF bandwidth setup of the VNAs*

The IF filter bandwidth of the VNA determines the accuracy of the measurement results and the speed of measurement. A wider IF bandwidth allows the VNA to sweep faster at the expense of poorer measurement accuracy. It is often desirable to set the IF bandwidth to a small value, e.g. 50 Hz, in VNA's regular application, such as *S*-parameter measurement on passive components, because the narrow IF bandwidth leads to accurate measurement. However, in application of identifying oscillation frequencies the IF bandwidth of VNA is recommended to be larger e.g. 50 kHz. Firstly, this is because a large IF bandwidth makes the measurement faster. Secondly, a large IF bandwidth ensures the signal from the DUT is within either the two neighbouring sample points. This reduces the possibility of omitting the DUT generated signal. Finally, large IF bandwidth leads to more accurate power level measurement.

### 3.4.4 Summary

It has been theoretically discussed and experimentally demonstrated that a VNA can be used to detect the fundamental and harmonic oscillation frequencies of an oscillator. By comparing the VNA measured reflection coefficients of DUT during its on and off state, the oscillation frequencies can be identified by abrupt changes (a positive or a negative peak) in the calibrated $|S_{11}|$ response. Special considerations were highlighted for non-ideal cases and possible solutions have also been suggested.

## 3.5 Conclusion

In this chapter, the key experimental methodologies that are used for accurately characterising planar Gunn devices and passive devices developed in this work has been described in detail. In particular, the commonly used semiconductor material and contact characterisation methods have been included. The basic principles, calibration methods, and applications to passive and oscillation detections using VNAs have also been discussed in detailed. The common spectrum and power measurement setups and system calibrations have been demonstrated too. This chapter will lead to convenient discussion on the characteristics of planar Gunn devices and millimetre-wave components and circuits in the following chapters.

# CHAPTER 4

# DESIGN, MODELLING, AND CHARACTERISATION OF PLANAR GUNN DIODES

The experimental methodologies for characterising planar Gunn devices have been thoroughly discussed in the last chapter. These include the fundamental principles and procedures of widely used semiconductor material and contact characterisation methods as well as spectrum and power measurement setups and related system calibrations for characterising on-wafer oscillator devices in the millimetre-wave frequency range. In addition, vector network analysers that are commonly used for characterising passive and non-oscillating active devices have been discussed for the use of characterising oscillator devices. With these experimental techniques, it becomes convenient to derive device parameters and assess the device performance of planar Gunn devices.

In this chapter the design, modelling, fabrication, and characterisation of planar Gunn diodes (PGDs) are discussed in detail. The device layer design is assisted by using a two-dimensional (2D) drift-diffusion modelling tool (Medici) [102, 173, 174] that can extract a wide range of important physical parameters of planar Gunn diodes that can not be directly measured by the experimental methodologies in the previous chapter. Although its accuracy for modelling devices in the sub-micro range is not as good as that of the Monte-Carlo simulation approach [175, 176], Medici provides reasonably good results for the type of devices (>1 μm) that we are investigating. This is confirmed by appropriate experimental results. Importantly, it is computationally fast. The organisation of this chapter is as follows: Firstly, a short technical review on the first planar Gunn diodes is given in Section 4.1. It also includes a general introduction to wafer growth (conducted by Dr. Martin C. Holland), device fabrication techniques (developed by Dr. Ata Khalid), and contact design [177, 178] in order to make this thesis complete. Followed in Section 4.2 are the detailed descriptions of the modified and new design of planar Gunn diodes for improving the RF

power of the first planar Gunn diodes. It is found in experiments that an increase of carrier concentration in the device channel can increase Gunn domain formation and therefore RF power enhancement. This is achieved by introducing additional δ-doping layers in both sides of the channel. In addition, adding parallel channels in the vertical direction within the devices can also improve the RF performance of the planar Gunn diodes. Finally, the discussion is focused on the development of planar Gunn diodes using $In_{0.23}Ga_{0.77}As$ as Gunn effect medium [102, 174].

## 4.1 Introduction

### 4.1.1 The First GaAs-based Planar Gunn Diodes

Figure 4-1 illustrates a schematic view of the epitaxial layers and an image of planar Gunn diodes that were first demonstrated by Khalid et al [42, 119]. A 50 nm thick un-doped GaAs channel is sandwiched by two $Al_{0.23}Ga_{0.77}As$ barrier layers. The $Al_{0.23}Ga_{0.77}As$ layers are silicon δ–doped with a doping level of $8\times10^{11}$ $cm^{-2}$. The natural conduction band discontinuity between GaAs and $Al_{0.23}Ga_{0.77}As$ forms a quantum well that confines electrons migrating from the supply layers. This device layer design results in a high electron concentration, $N$, ($>10^{17}$ $cm^{-3}$) in the GaAs channel which is not achievable from conventional Gunn diodes ($N\sim10^{16}$ $cm^{-3}$). The high concentration of electrons in the channel is desirable for high frequency Gunn oscillations according to the basic criteria for the transit-time mode of Gunn oscillations. That is, the product of electron concentration and device length must be greater than $10^{12}$ $cm^{-2}$ as introduced in Section 2.3.2.

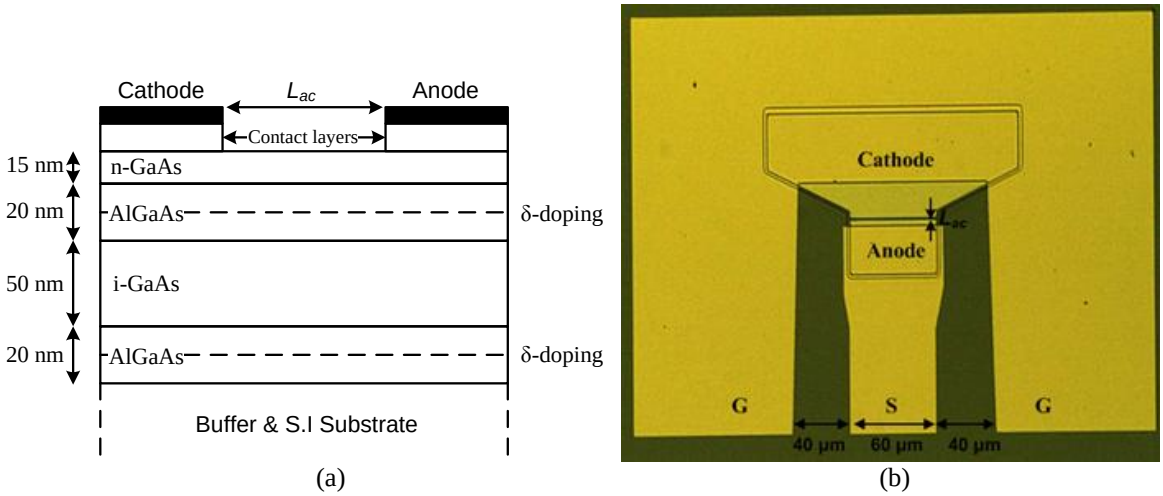


**Figure 4-1**Planar Gunn devices demonstrated by Khalid et al. (a) Schematic view of epitaxial layers, and (b) A micrograph of the actual device constructed in a coplanar test structure.

Experimental results showed an oscillation frequency of 108 GHz was generated by a 1.3 μm planar Gunn diode operating at its fundamental mode [42]. It was further confirmed by Monte-Carlo simulation [175] that Gunn domains are formed in the GaAs channel and the periodic nucleation, transportation, and disappearance of Gunn domains between cathode and anode leads to the current oscillation. The oscillation frequency $f$ is approximated as $v_{domain}/L_{ac}$ where $v_{domain}$ is the domain velocity and $L_{ac}$ is the anode and cathode distance. Figure 4-2 illustrates the internal dynamics of a 2 μm planar Gunn diode simulated using a Monte-Carlo approach [175]. The device has a non-annealed Ohmic cathode (top left) and an annealed Ohmic anode (top right). A detailed discussion on Ohmic contacts is given in the next section. Figure 4-2 shows four key moments of the change of electron concentration in the planar Gunn diode: a high electric field domain (Gunn domain) is disappearing at the anode at a time of $t_0$ (Figure 4-2a), another domain is forming at a time of $t_1$ (Figure 4-2b), the domain is fully developed and travelling towards the anode at a time of $t_2$ (Figure 4-2c), and the domain starts disappearing again at a time of $t_3$ (Figure 4-2d). One can clearly see the change of electron concentration (the more dense the dots the higher the electron concentration) in the $\Gamma$, $L$, $X$ bands at different times indicating a change of Gunn domain. When the electron concentration in the $\Gamma$ band is almost zero but distributed in the $L$ and $X$ bands as shown in Figure 4-2c, a Gunn domain is fully developed. This is because the high electric field of the Gunn domain causes the electrons residing in the $\Gamma$ band to transfer into $L$ or even $X$ bands.

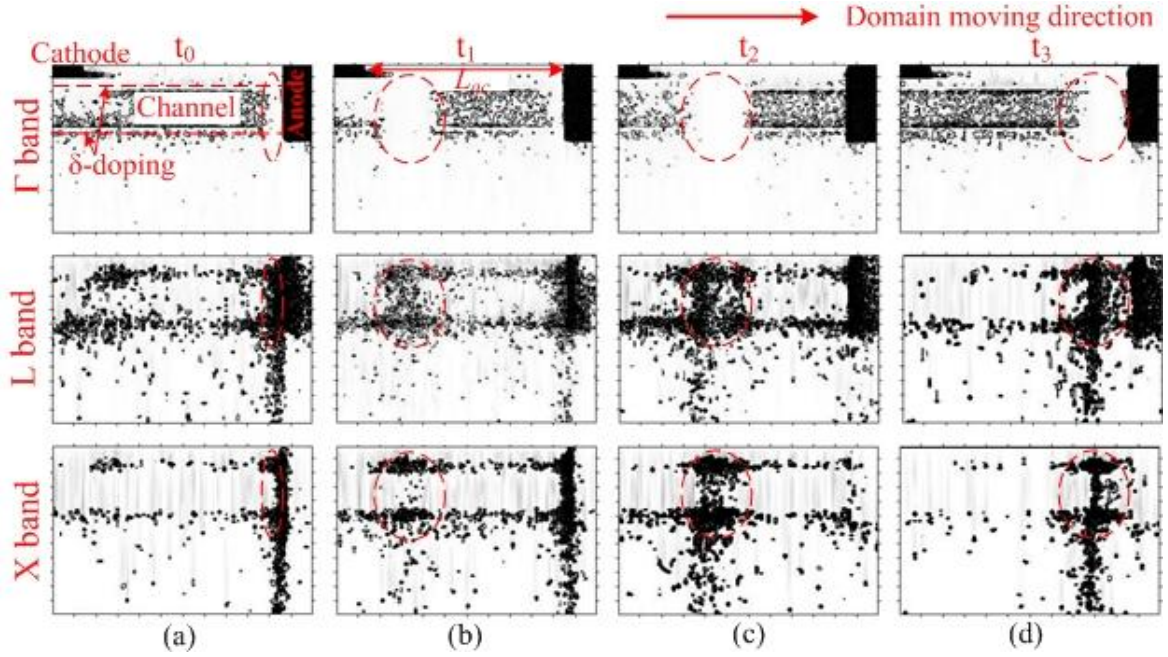


**Figure 4-2** Monte-Carlo simulated electron distribution in $\Gamma$, $L$ and $X$ bands under high electric fields for a 2 μm planar Gunn diode [175]. The device is biased at 4 V. The dashed circles indicate the position of domains in the device. (a) A domain is disappearing at the anode at a time of $t_0$, (b) Another domain starts nucleating near the cathode at $t_1$, (c) A fully developed domain is travelling towards the anode at $t_2$, and (d) The domain starts disappearing at the anode at $t_3$.

The Monte-Carlo simulation results have fairly good agreement with experimental results [175]. These results establish the existence of Gunn oscillations in the heterostructure planar Gunn diodes. The contact design and device fabrication are given in the following sections.

### 4.1.2 Contact Design

The importance of contact design for planar Gunn diodes comes from two aspects. One aspect is the general requirements of Ohmic contacts, such as low contact resistance, good thermal stability, and ease of fabrication. All these factors ensure the planar Gunn devices operate effectively, efficiently and stably. The other aspect, as will be discussed in Section 4.1.2.2, is associated with the design of composite contacts. The composite contacts help planar Gunn devices avoid premature breakdown and improve device lifetime.

#### *4.1.2.1 Ohmic Contacts for Planar Gunn Devices*

It is well-known that Ohmic contacts having low contact resistance are highly desirable in oscillator devices because the Ohmic contacts of a device are resistive. They consume both DC and RF power and reduce the device's efficiency. It was previously mentioned in Section 3.1.2.2 that there are two common methods when designing Ohmic contacts which are (i) reducing the metal-semiconductor barrier ($\phi_{Bn}$), and (ii) increasing the doping level ($N_D$) of the semiconductor.

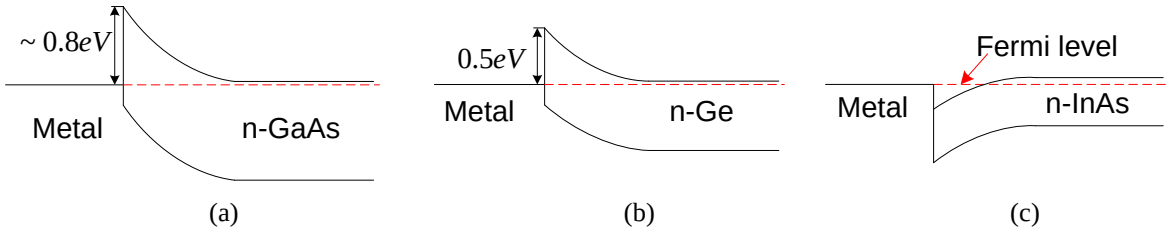


**Figure 4-3** Illustration of metal-semiconductor barriers of (a) n-type GaAs, (b) n-type Ge, and (c) n-type InAs.

It is believed that the metal-semiconductor barrier height is independent of the metal work function [179, 180]. Therefore, it is unlikely to reduce the metal-semiconductor barrier height of n-type GaAs (approximately 0.8 eV) by using different metals. However, it is possible to grow a highly doped epitaxial layer that has lower barrier height e.g. 0.5 eV for

germanium [181-183] or even highly doped InAs that has zero or negative barrier height [136, 184] on the top of GaAs. The metal-semiconductor interfaces for n-GaAs, n-Ge, and n-InAs are shown in Figure 4-3 [185]. Since GaAs (5.653 Å) and Ge (5.658 Å) are approximately lattice-matched, n-Ge can be easily grown on n-GaAs; however, InAs has a lattice constant of 6.05 Å that is higher than that of GaAs, therefore graded band gap layers of $In_xGa_{1-x}As$ are required between n-InAs and n-GaAs. $In_xGa_{1-x}As$ also has an In-dependant barrier height [186] that smoothes out the conduction band at the $In_xGa_{1-x}As$ /GaAs heterointerface and contributes to a low resistance Ohmic contact design [187, 188]. The method of realising Ohmic contacts using intermediate layers is a non-alloyed process that preserves good morphology for planar devices and does not need a high temperature annealing process to achieve low contact resistance. However, this type of Ohmic contact is believed to be further improved by an appropriate annealing process [184].

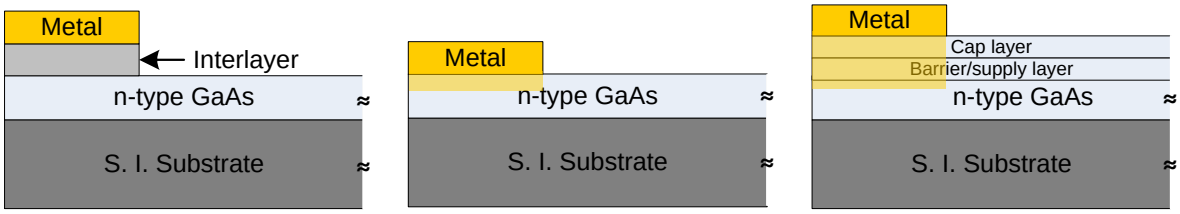


**Figure 4-4** Illustration of different Ohmic contacts for n-GaAs. (a) Interlayer between metal and n-GaAs, (b) Annealed Ohmic contact for n-GaAs, (c) Annealed Ohmic contact for heterojunction GaAs/AlGaAs devices.

However, it is desirable that the Ohmic contact can penetrate through surface barrier layers into the deep channel for heterojunction devices, such as HEMTs or others [189]. In this case annealed Ohmic contacts are required. Figure 4-4 shows different types of Ohmic contacts to n-GaAs for different applications including the Ohmic contact with interlayers as discussed above (Figure 4-4a).

The second method of realising a good Ohmic contact is to increase the doping level on the semiconductor side. By annealing metal into an n-type semiconductor the electron concentration in the semiconductor is enhanced because the metal diffuses into the semiconductor during the annealing process as shown in Figure 4-4b. Therefore, the width of depletion region that is created on the semiconductor side when a metal is in contact with it is narrowed. Once the depletion region is narrow enough the electrons can tunnel through the junction and the tunnelling current overtakes the thermionic field emission generated current and dominates. Thus the contact resistance reduces.

Historically, researchers used Sn to realise Ohmic contacts for n-GaAs based semiconductor technology [190, 191]. However, it was then replaced by Au/Ge (88%:12% by weight). By introducing a nickel overlayer, the Ohmic contact stability and morphology is improved [192]. This technology provides a relatively low contact resistance (e.g. $10^{-6}$ $\Omega\cdot cm^2$). However, it still suffers thermal instability, spiking, poor controllability and reproducibility [193-195]. Although these issues can be improved by using Pd [183], and therefore no high temperature annealing process is required, it is almost impossible to generate deep penetration for heterojunction devices.

Taking into account all the pros and cons of the aforementioned two Ohmic contact design methods, we have designed a double-purpose Ohmic contact for planar Gunn diodes. As shown in Figure 4-1, a planar Gunn diode finishes with a carefully designed 15 nm n-GaAs layer ($3.5\times10^{18}$ $cm^{-3}$) on the top [175]. This n-GaAs allows either a graded gap interlayer to be grown on its top for non-alloyed Ohmic contacts, that can be removed using chemical etching [42] or direct deposition of metal alloys for alloyed Ohmic contacts. The graded band gap $In_xGa_{1-x}As$ layers have a schematic view as shown in Figure 4-5a. It was initially reported that the indium mole composition should start from $x=0$ on the GaAs and finish at $x=1$ at the top surface for metal contact in order to achieve low contact resistance [136]. It was later found that $x=0.65$ may give the lowest contact resistance [196] or $x\leq0.7$ [197]; however, the equation given by [186]

$$\phi_{Bn} = 0.9x^2 - 1.9x + 0.95 \tag{4.1.1}$$

implies the indium molar content should be at least $0.77$ to achieve a zero metal-semiconductor barrier height. In addition, since the $In_xGa_{1-x}As$ material system allows much higher doping level than that of GaAs, e.g. $\geq1\times10^{19}$ $cm^{-3}$, it is sufficient to have $x=0.5$ for the top $In_xGa_{1-x}As$ layer be doped at a level of $N_D=2\times10^{19}$ $cm^{-3}$ to pin the barrier to zero [198] . To ensure the barrier is less than zero, $x=0.53$ and $N_D=5\times10^{19}$ $cm^{-3}$ are finally selected for the design of graded band gap $In_xGa_{1-x}As$ layers for planar Gunn diodes.

Due to the unsatisfactory performance of Au/Ge/Ni-based Ohmic contacts as discussed above, the metal stack of Pd/Ge/Au/Pd/Au [199] is selected for Ohmic contacts of planar Gunn diodes. The difference between the selected metals and normal Au/Ge Ohmic contacts is that the insertion of a Pd layer between Au/Ge and n-GaAs makes the Ga and As oxides on the surface of n-GaAs decomposed under an annealing condition therefore

Ge can penetrate into n-GaAs and increase its doping level [183, 200, 201]. The second Pd layer serves as a diffusion barrier layer [199]. Except on n-GaAs, these Ohmic layers can also be grown on n-$In_xGa_{1-x}As$ [199]. Figure 4-5b shows the composition of each metal for this design. The detailed fabrication procedure is given in the next section. Table 4-I summarises and compares the performance of various Ohmic contacts from other works and this work.

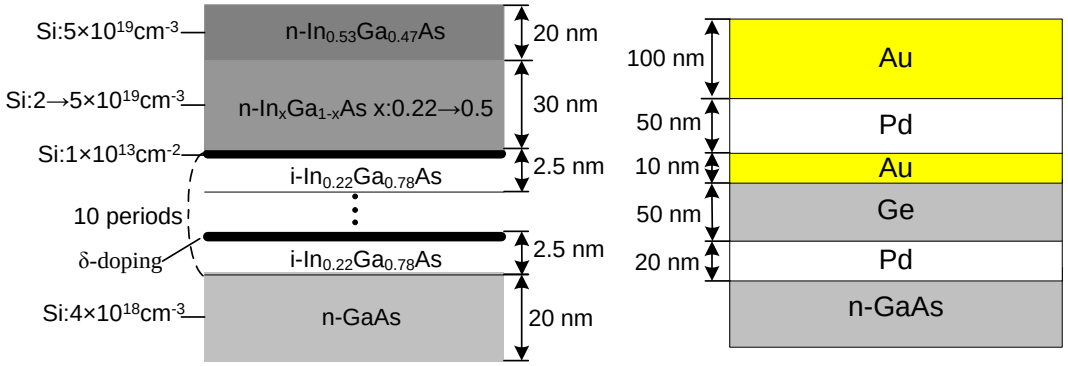


**Figure 4-5** Illustration of (a) the graded band gap $In_xGa_{1-x}As$ layers and (b) metal alloys for Ohmic contacts of planar Gunn devices.

**Table 4-I** Incomplete summary of Ohmic contact data.

| Metallisation | Anneal or interlayer | Doping of n-GaAs ($cm^{-3}$) | $\rho_c$ ($\Omega$•$cm^2$) | $R_c$ ($\Omega$•mm) | Ref |
|---|---|---|---|---|---|
| Ge/Ni | Anneal (450-650 ℃) | $1.1\times10^{17}$ | $3\times10^{-5}$-$5\times10^{-4}$ | N/A | [181] |
| Ge/Au/Ni | Anneal (400 ℃) | $2.0\times10^{18}$ | N/A | 0.2 | [202] |
| Ge/Pd | Anneal (325 ℃) | $1.0\times10^{18}$ | $1\times10^{-6}$-$1\times10^{-5}$ | N/A | [183] |
| Au(or Ag)/Ge/Pd | Anneal (150-175 ℃) | $1.0\times10^{18}$ | $1\times10^{-6}$ | N/A | [203] |
| Pd/Ge/Au/Pd/Au | Anneal (400 ℃) | $6\times10^{17}$ | $2\times10^{-6}$ | N/A | [199] |
| Au/Ni/Au/Ge/Pd n-InGaAs | Interlayer Anneal (400 ℃) | $3.0\times10^{19}$ | $3.7\times10^{-6}$ | N/A | [188] |
| Ni/Ge/Au/Ti/Au InGaAs | Interlayer Anneal (475 ℃) Non-anneal | $1.0\times10^{18}$ | $2.56\times10^{-7}$ $5.32\times10^{-7}$ | 0.019 0.025 | [184] |
| Au/$In_xGa_{1-x}As$ (x=0.25 or 0.35) | Interlayer | $2.4\times10^{19}$ | $5\text{-}8\times10^{-7}$ | N/A | [204] |
| Ni/AuGe/Ni/Au n-InGaAs | Interlayer | $4\times10^{18}$ | $1\times10^{-7}$ | N/A | [198] |
| Pd/Ge/Au/Pd/Au n-InGaAs | Interlayer/ Anneal (400 ℃) | $3.5\times10^{18}$ | $4\times10^{-6}$ | 0.15 | This work |

### *4.1.2.2 Composite Contacts*

In the previous section, the discussion was exclusively focused on the design of Ohmic contacts for low contact resistance, high reliability and thermal stability. These Ohmic

contacts certainly show better performance than Ohmic contacts using Sn/Ag or In/Au [191, 205] for early vertical Gunn devices. However, for planar Gunn diodes there is another contact-related problem (e.g. thermal breakdown) [205, 206]. This device failure was believed to be due to the excess heat generated near the device anode. This is because when a Gunn domain reaches the anode, the high electric field leads to hole injection. The generation of electron-hole pairs increases the current and therefore the heat. This was experimentally confirmed by observing recombination radiation [207]. Several solutions to this problem have been proposed, such as effective cooling at the anode [205, 206], using concentric anode and cathode [207], and enlarged anode mesa area [208]. However, they are either ineffective (only last for a few hours) [206] or inefficient due to the excess non-active area [207, 208].

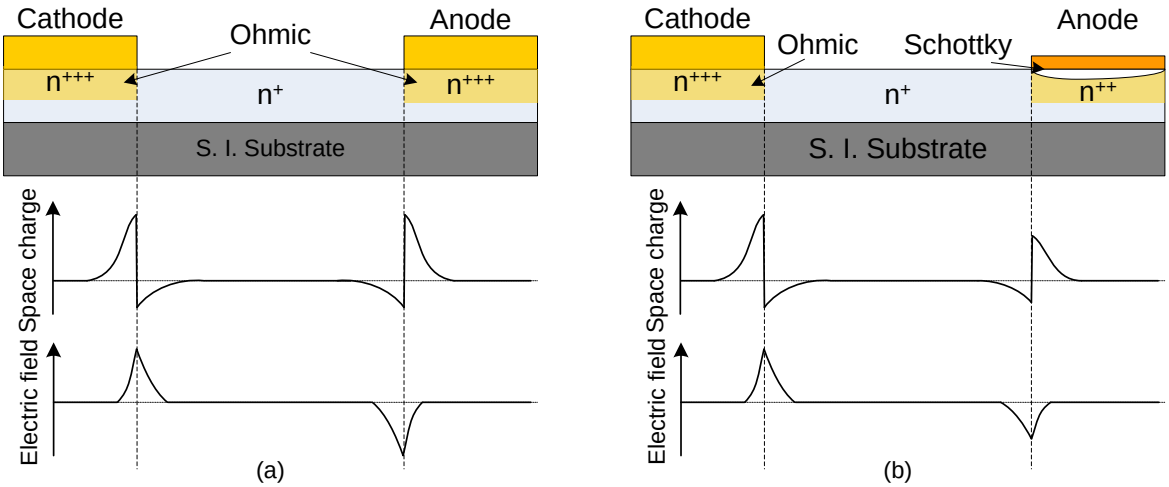


**Figure 4-6** Illustration of space charge and electric field for planar devices. (a) Both anode and cathode are Ohmic, (b) Cathode is Ohmic and anode is Schottky.

Another possible solution is to replace the Ohmic contact of the anode by a Schottky contact as shown in Figure 4-6. Figure 4-6a illustrates a planar Gunn diode that has a normal Ohmic anode contact. The Ohmic contact region has a much higher electron concentration (designated as $n^{+++}$ in the diagram) than the active region ($n^{+}$). Therefore, an electric field spike appears near the anode. When a Schottky contact replaces the Ohmic anode, a depletion region is formed underneath it as shown in Figure 4-6b. The depletion region lowers the electron concentration ($n^{++}$) therefore the space charge and the electric field [209]. The problem with this approach is the Schottky contact has a high built-in potential that reduces device efficiency. An alternative solution is to use a composite contact that has a combined Schottky and Ohmic anode [178, 209]. Figure 4-7 shows a schematic current distribution of a planar Gunn diode with a conventional Ohmic anode contact and a composite anode contact.

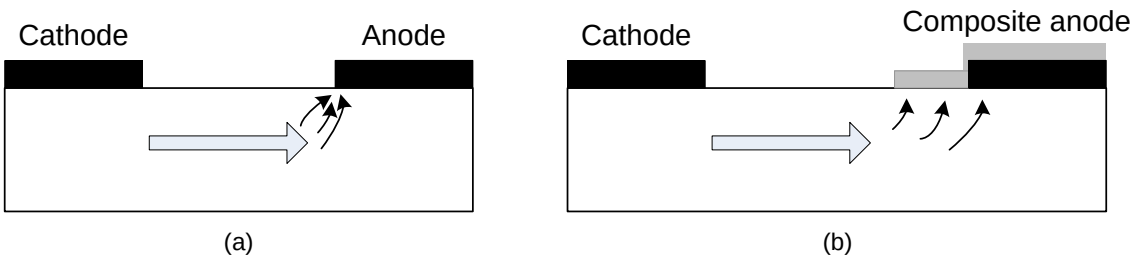


**Figure 4-7** Schematic diagram of planar Gunn diodes showing current crowding at the anode edge (a) With a conventional Ohmic contact, and (b) Current spreading in a composite Ohmic contact due to non-zero depletion in the Schottky extended part of contact.

The composite anode is realised by simple addition of a Schottky extension (using Ti/Au: 20 nm/200 nm) to a conventional Ohmic contact in a planar Gunn diode. The Schottky extension from the edge of the Ohmic region can be varied from 0.1 μm to 0.5 μm. The length of the extension is determined by an optimisation process based on the material doping level used and device type. It was found that the optimum extension was 0.3 μm in order to keep the contact resistance low but breakdown voltage high. Figure 4-7b shows schematically the composite contacts and indicates the mechanism by which the composite Schottky-Ohmic contact structures spread the current to reduce the tendency towards breakdown. It is hypothesised that the Schottky element acts as both a dissipation mechanism and sink for the domain. On approaching the cathode-side edge of the Schottky region, high energy carriers within the domain are able to exit the device over the Schottky barrier. This contributes towards the device current but also reduces the domain strength by dispersing the energy in the dipole field. In this manner the impact of the high energy dipole as it reaches the anode is spread over a larger distance, thus reducing the local electric field.

Simulations of the conventional and composite anode designs were performed using a 2D ensemble Monte Carlo approach that was used to model planar Gunn devices with thermal data extracted through consideration of the net phonon emission [175, 210]. The composite anode was introduced through application of a separate Schottky contact adjacent to the conventional Ohmic contact, with identical biasing but a non-zero negative potential offset to represent the non-Ohmic nature of the additional contact region. This follows standard practice in modelling a Schottky contact and is applied in the simulation through alternate boundary conditions for the solution of the Poisson equation. Results at a bias of 4 V at an ambient temperature of 300 K are shown in Figure 4-8. In both cases the device cathode to

anode separation ($L_{ac}$) is 1.3 µm. Figure 4-8a illustrates the electric field distribution and strength for a planar Gunn diode with conventional Ohmic contacts (both anode and cathode are Ohmic) and Figure 4-8b shows the electric field distribution and strength for a planar Gunn diode with a composite anode (0.5 µm Schottky overlayer) and a normal Ohmic cathode. The legend illustrates the electric field intensity. The reddish colour indicates positive electric fields and the bluish colour indicates negative electric fields. The intensity of the colours indicates the strength of the electric field. It can be seen that the anode edge of conventional contact is subjected to a very high electric field as the domain reaches the edge.

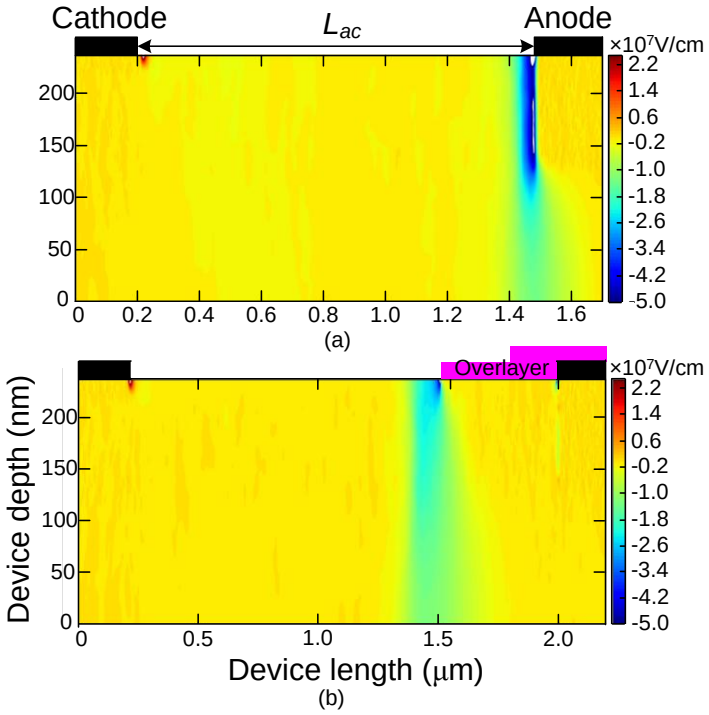


**Figure 4-8** Simulations of the conventional and composite anode designs of the planar Gunn devices showing the electric field and charge distribution in a planar Gunn device (a) with conventional Ohmic contacts and (b) with composite Ohmic contacts.

The Monte Carlo simulation gives a behavioural view of the planar Gunn devic in the active (oscillating) mode of operation. It can be concluded that the Schottky extension of the anode contact plays an effective role in the distribution of the electric potential at the edge of the contact. This spatial re-distribution reduces the electric field spike at the edge of the composite contact. This reduction in the electric field in turn improves device lifetime and the power dissipation, shown in Figure 4-9a, decreases significantly at the edge of composite contact. The measured DC data is plotted for a number of devices with $L_{ac}$ = 1.3 µm in Figure 4-9b. It is found during these measurements that biasing a device at

least one volt lower than the onset of breakdown would ensure that the devices operated without permanent damage. In practice it has been found that the difference in the operating voltage and the breakdown voltage is increased from approximately 1 V to 2 V when using a composite contact. This increase clearly provides a greater safe operating margin. Analysis of the simulation results suggests that the Schottky element acts as a dissipation mechanism and sink for the domain. On approaching the cathode-side edge of the Schottky contact, high energy carriers within the domain are able to exit over the Schottky barrier. This effect contributes towards part of the device current but also reduces the domain strength, with the dipole field and mean carrier energy reducing as the domain traverses further towards the highly-doped region (due to Ohmic contact annealing) under the Ohmic component of the anode. Experimentally measured data confirms the hypothesis and the breakdown voltage is improved in devices with composite anode contacts. In the subsequent sections the detailed composite contact fabrication process is given.

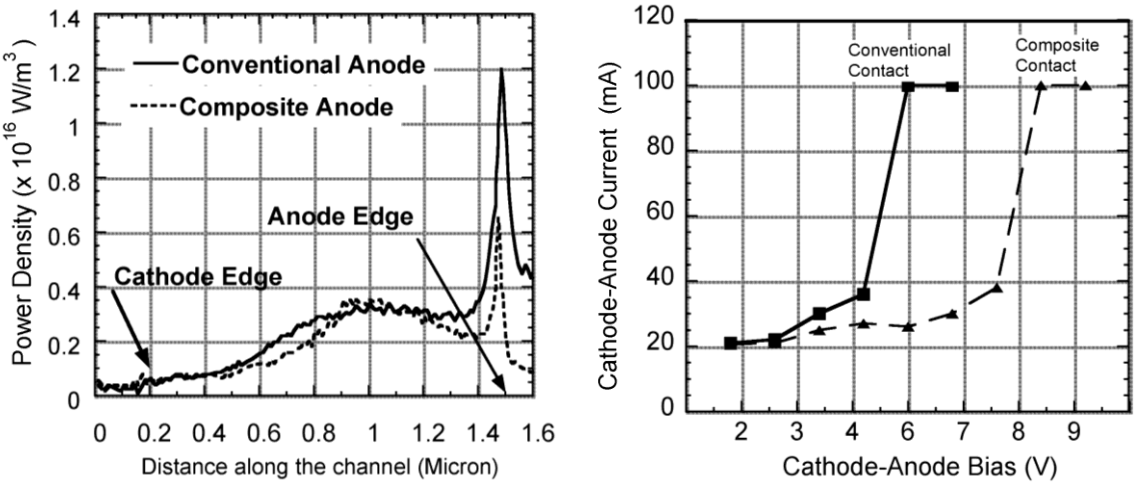


**Figure 4-9** (a) Comparison of simulated power density in planar Gunn devices with and without composite contacts; (b) Measured breakdown voltage in conventional and composite contact planar Gunn devices.

### 4.1.3 Material Growth and Device Fabrication

#### *4.1.3.1 Material Growth*

The methods for epitaxial semiconductor growth are broadly divided into two categories: physical vapour deposition (PVD), e.g. molecular beam epitaxy (MBE) and sputter deposition and chemical vapour depositions (CVD), e.g. metal-organic CVD (MOCVD) and plasma enhanced CVD (PECVD). The former allows elemental material be evaporated within effusion cells and deposited onto a substrate; the latter utilises chemical precursors,

e.g. volatile gases, which react with one another near to or on the substrate surface [211]. The active layers of some early slab-like planar Gunn diodes were grown by using CVD and liquid phase epitaxy (LPE) methods [63, 105]. The CVD process requires high temperature e.g. 850 ℃ to drive the pure arsenic and gallium elements while using the LPE it is difficult to grow thin layers. All materials in this work have been grown using the MBE method that allows growth of very precise compositions of materials of monolayer (ML) thickness [76].

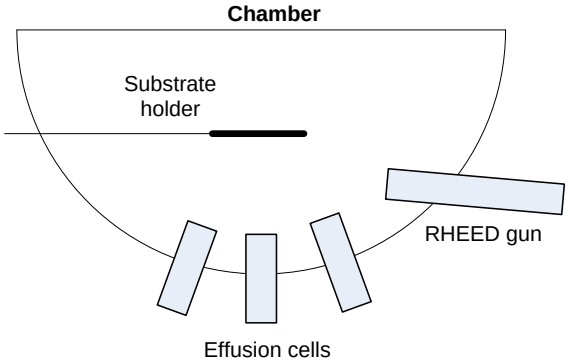


**Figure 4-10** A simplified block diagram of a MBE chamber.

Figure 4-10 illustrates a simplified block diagram of an MBE chamber. It consists mainly of several effusion cells, a substrate holder, a reflection high energy electron diffraction (RHEED) gun, and several spectrometers (not shown in the diagram). Each individual effusion cell contains a pure condensed or gaseous elementary or molecular source material e.g. Ga or $Si_2H_6$. The substrate holder is rotatable and has heating capability to enable the substrate to be heated up to a required temperature, e.g. 600 ℃. The RHEED gun is used to monitor the material growth rate and quality. Before growth the chamber is set to a very low pressure (e.g. $10^{-8}$ Pa) to meet the ultra high vacuum (UHV) growing requirement of MBE. The source materials in the effusion cells are heated to a gaseous state and then emitted to the heated substrate within their mean free paths. In terms of growing GaAs, solid gallium and arsenic molecules are used as the source materials. The undoped GaAs layers are typically p-type (the dopant is carbon that is from CO; the CO is believed to be a common background spices in UHV) and have an approximate doping concentration between $10^{13}$ $cm^{-3}$ and $10^{15}$ $cm^{-3}$ [76]. The typical dopants of n-type and p-type GaAs are silicon and beryllium, respectively.

Figure 4-11 illustrates the MBE grown single channel GaAs-based material system (the wafer is named as C114). All epitaxial layers are grown on a 620 μm thick semi-insulating

GaAs substrate that has a resistivity in the range of 0.5-1×$10^4$ Ω•cm. A 0.5 μm thick layer of un-doped GaAs, that acts as a buffer layer, is first grown on the substrate. This process takes approximately 30 minutes. It is then followed by 20 periods of 9-monolayer (ML) GaAs and 9-ML AlGaAs and finishes with another 9 MLs of GaAs. The GaAs/AlGaAs superlattice layers serve to getter impurities from the substrate [212]. It takes a further 60 minutes to grow the 1 μm thick intrinsic $Al_{0.23}Ga_{0.77}As$ barrier layer, on top of which another 10 nm $Al_{0.23}Ga_{0.77}As$ is grown to form the bottom of the electron supply layer. The thick $Al_{0.23}Ga_{0.77}As$ prevents electron penetration into the substrate. Silicon is used for δ-doping and its level is 8×$10^{11}$ $cm^{-2}$. The δ-doping layer is deposited between the 10 nm $Al_{0.23}Ga_{0.77}As$ barrier and a 4.34 nm $Al_{0.23}Ga_{0.77}As$ barrier. The intrinsic 50 nm GaAs channel layer is grown on top of multiple periods of GaAs/AlAs that has a composition of 4ML/1ML. The GaAs/AlAs superlattice buffer layer provides better electron confinement in the channel due to the presence of minigaps in the superlattice that result in a barrier of 0.6 eV [213]. The top $Al_{0.23}Ga_{0.77}As$ supply/barrier layer is equally separated by another silicon δ-doping (8×$10^{11}$ $cm^{-2}$). 15 nm of highly doped GaAs (3.5×$10^{18}$ $cm^{-3}$) is grown on top of the upper $Al_{0.23}Ga_{0.77}As$ barrier layer. This GaAs layer serves as a cap layer and enables good metal contacts. It is followed by a 5 nm $Al_{0.8}Ga_{0.2}As$ etch stop layer doped at 4×$10^{18}$ $cm^{-3}$.

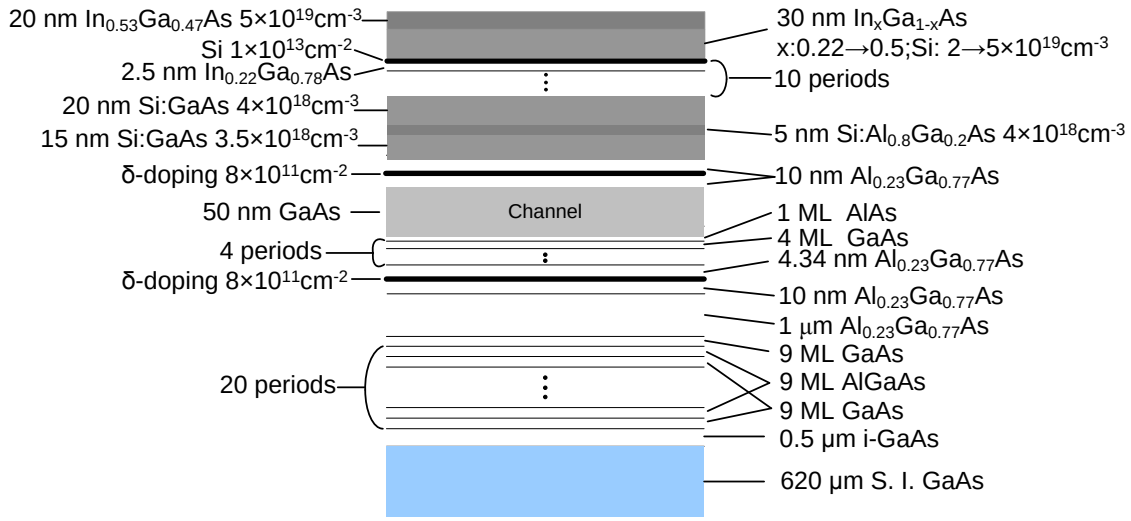


**Figure 4-11** Schematic view of the epitaxial layers as grown by MBE method for planar Gunn devices.

So far, all grown epitaxial layers are device body layers to achieve the designed layers as shown in Figure 4-1. Anything grown after serves for the formation of graded band gap Ohmic contacts. It starts from 20 nm highly doped GaAs (4×$10^{18}$ $cm^{-3}$) and then 10 periods of a 2.5 nm thick of $In_{0.22}Ga_{0.78}As$ and a silicon δ-doping layer (1×$10^{13}$ $cm^{-2}$). Followed is

the 30 nm graded band gap layer of $In_xGa_{1-x}As$. The indium mole composition begins with 0.22 and finishes with 0.5. The doping level for this layer also increases as the indium mole fraction increases. It starts from $2\times10^{19}$ $cm^{-3}$ when $x=0.22$ and terminates with $5\times10^{19}$ $cm^{-3}$ at $x=0.5$. The top of the wafer is finished with a 20 nm thick layer of $In_{0.53}Ga_{0.47}As$ uniformly doped with $5\times10^{19}$ $cm^{-3}$.

*4.1.3.2 Device Fabrication*

Electron beam lithography (EBL) and photolithography are two commonly used methods for developing micro and nano-sized structures and circuits. EBL technology uses an electron beam to bombard polymer resists e.g. Polymethyl-methacrylate (PMMA) to create high resolution patterns. However, photolithography utilises the light sensitivity property of some materials called photoresists. Structures defined in a mask plate are transferred into the photoresist by exposing with light and developing either the exposed (for positive tone resist) or unexposed (negative tone) regions. Photolithography technology has the disadvantages of poor flexibility and low resolution compared to EBL however photolithography has higher throughput and is much cheaper. Nevertheless, since EBL has been used throughout this work, a general description of an EBL fabrication process is introduced here.

Figure 4-12a illustrates the fundamental fabrication process of a single layer using EBL (Leica VB6 UHR EWF). Firstly, the sample needs to be cleaned. The dust, grease or oil on the surface of a sample can be removed by dipping the sample in opticlear and acetone and rinsing in de-ionised (DI) water. Sometimes ultrasonic bathing is used to speed up the process or remove any stubborn dirt. The sample is then dried using a nitrogen gun before being baked to ensure there is no moisture on the substrate surface. Once the sample is completely dry, a chosen EBL resist can be spin-coated on the sample. The recipe (e.g. speed and time) of the spinner is selected according to the type of resist used and the desired resist thickness. After the resist is spun, it should be post-baked to drive all the remaining solvent from the resist film before being sent to the EBL machine for pattern writing. Occasionally, multiple resist layers, which may be of the same or different resist, depending on the required application, are needed. The pattern file can now be transferred to the EBL machine for electron beam writing. The dose and energy of the electron beam

are the two main parameters to be determined by users according to their application. After being written, the pattern is developed using the corresponding resist developer. The pattern geometry after development depends on whether or not the resist is positive or negative. Positive resist is dissolved in the solvent after being exposed to the electron beam; however, negative resist exposed by the electron beam remains on the sample after development.

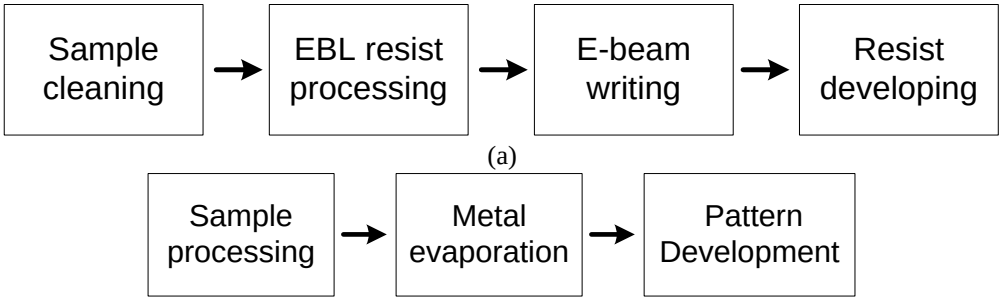


**Figure 4-12** Block diagrams of (a) EBL process of a single layer and (b) metallisation development process.

Most applications require metallisation after the pattern on the sample has been developed. Two methods are widely used in a cleanroom: electron beam physical vapour deposition and sputter coating. The former permits precise control of thin metals layers e.g. several tens or hundreds of nanometres and the latter can deposit several micrometres of metals. Since all metallisation in this work were performed using evaporation technology, the sputtering coating technique will not be included here. As illustrated in Figure 4-12b, a sample after undergoing the EBL patterning process needs to be pre-processed before being loaded to the electron beam evaporation machine (Plassys series). A short oxygen cleaning process is done to ensure complete removal of the developed resist from the desired metal contact area. The recipes for the metallisation are set according to individual requirements. Once the metal or metal alloys are evaporated and deposited onto the sample, the unwanted metal is removed by a lift-off process. This is done by immersing the sample in hot acetone (55 ℃) for a few hours.

It is common to remove selected parts of material from a sample in a process called etching. There are two types of etching methods: wet and dry. Wet etching is a chemical process where the chemical etchant reacts with and dissolves the unwanted material; whereas dry etching is a physical and chemical process that uses a plasma of reactive gases e.g. oxygen or mixtures of other gases to bombard the substrate and remove unwanted material. Wet

etching is typically much faster than dry etching; however, it is also typically less controllable.

After introducing some fundamental cleanroom practices, the specific fabrication processes and procedures undertaken for the development of planar Gunn devices using EBL technology is detailed in the following section. This process consists of many fabrication phases (or layers to be made) as schematically illustrated in Figure 4-13. Each phase has several steps and each step is comprised of sample cleaning, resist coating, and EBL pattern writing or metal deposition as described above. In order not to lose the focus of this thesis, the detailed description of each step in each phase is not included here but the overall process is stressed for completeness.

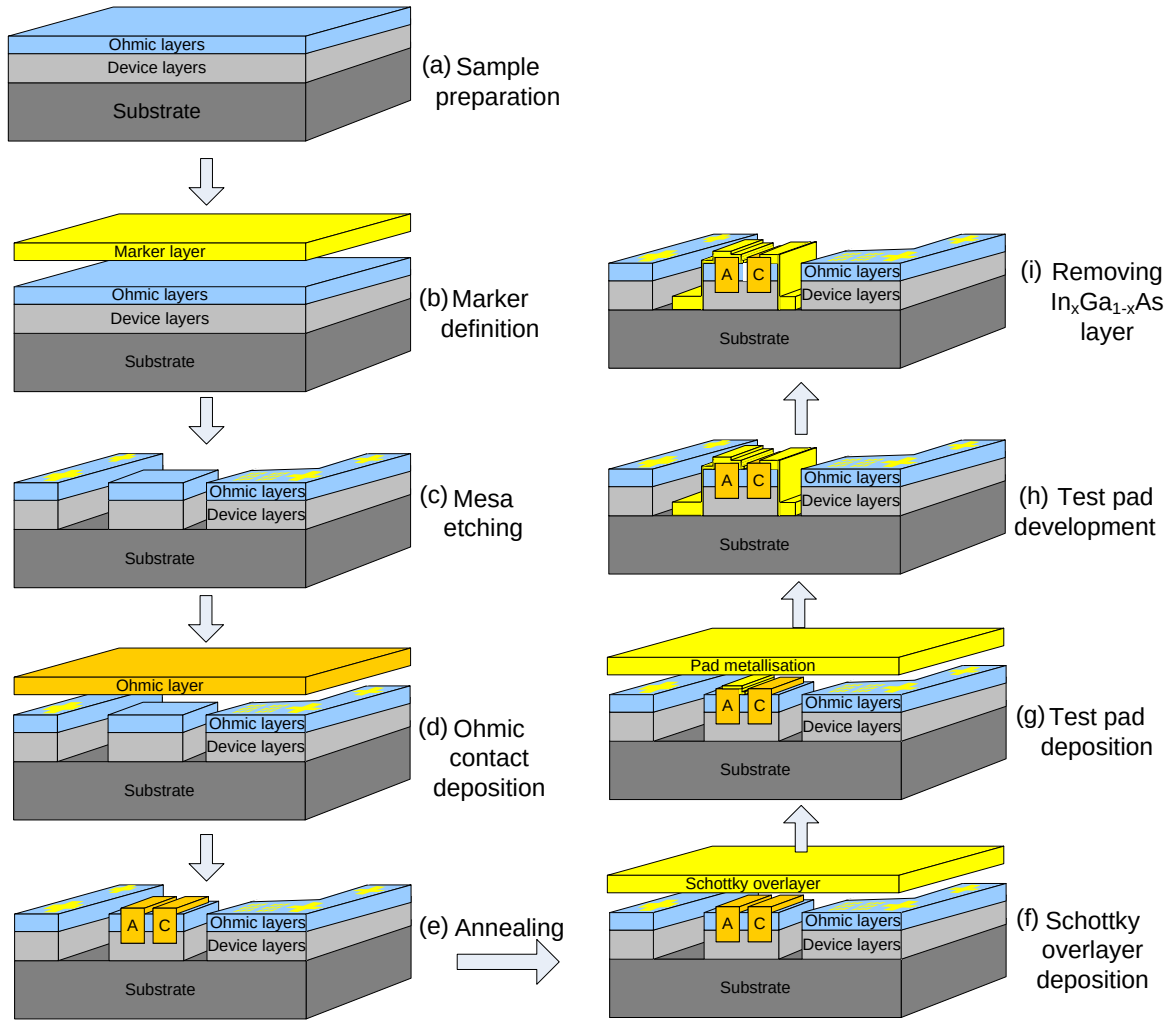


**Figure 4-13** Illustration of the fabrication processes developed for making planar Gunn diodes with annealed Ohmic contacts. (a) Sample preparation, (b) Marker definition, (c) Mesa etching, (d) Depositing Pd/Ge/Au/Pd/Au Ohmic metal stack, (e) Annealing the Ohmic contacts, (f) Evaporating gold for Schottky overlayer to make a composite contact, (g) Depositing gold for coplanar test pads, (h) Developing coplanar test pads, (i) Wet-etching graded band gap Ohmic layers.

Once a wafer (3 inch in diameter), which has all active layers and the interlayer Ohmic contacts, is grown by using MBE technology, it is then scribed and cleaved into many smaller chips (e.g. 12 mm × 12 mm) for device development. Figure 4-13a schematically shows a small chip that contains a semi-insulating substrate and MBE grown active and Ohmic layers.

The fabrication process starts with depositing a 10/100 nm thick layer of Ti/Au to create EBL alignment markers for the fabrication of subsequent layers (Figure 4-4b). There are two types of makers: big crosses (sometimes bars are used) and small squares. The big crosses are coarse alignment markers that act as a reference point for the EBL operator. The small squares, of size 50 μm by 50 μm, are fine alignment markers that are used by the EBL machine to locate the origin of the pattern coordinates and ensure accurate alignment between the previous layer and the new layer to be written.

The next step is mesa development as shown in Figure 4-13c. The height of the mesa (active layers for Gunn diodes and interlayer Ohmic layers) varies depending on the device layer design. It ranges between 200 nm to 1000 nm. A wet etching approach is used for its non-damaging effect to the active layers. The etchant is citric acid/hydrogen peroxide and the etching rate at 20 ℃ is 1000 Å/min [214]. The total etching time is determined by the mesa thickness.

Figures 4-13d and e shows the process of deposition and development of metal (Pd/Ge/Au/Pd/Au) Ohmic contacts. The metal stack is deposited using e-beam evaporation technology and the annealing is done in a rapid thermal annealler (RTA) at a temperature of 400 ℃ for 60 seconds. This gives the lowest contact resistance which is 0.15 Ω•mm. This process also defines the device length $L_{ac}$ of planar Gunn diodes. It may be divided into two steps when making short channel devices e.g. $L_{ac}$<1.3 μm due to the potential of unparallel definition of contact edges. Each step only contributes to realising one of the contacts.

After formation of annealed Ohmic contacts, a layer of 10/200 nm Ti/Au is evaporated at the anode with a small portion of extension, e.g. 0.1 μm-0.5 μm, towards the cathode to

make a Schottky contact as shown in Figure 4-13f. A further layer of 10/200 or 10/400 nm Ti/Au is deposited to form the complete composite contacts for anodes and coplanar test pads for the entire devices (4-13g and h). Again the final metal deposition can be divided into two steps to separate the anode and cathode contacts if short channel devices are involved.

The final step of the fabrication process is to remove the graded band gap $In_xGa_{1-x}As$ layer. This is completed by using wet-etching technology and the etchant is 3: 1 citric acid:$H_2O_2$ solution. The etching depth for 20 seconds is 100 nm. It stops at a $Al_{0.8}Ga_{0.2}As$ etch stop layer that is inserted during wafer growth [215]. The citric acid:$H_2O_2$ solution system has a good selectivity between $Al_xGa_{1-x}As$ and GaAs for $x>0.7$ because the etch rate decreases rapidly with increasing aluminium composition [215].

The above demonstration is only one of several possible fabrication processes for making planar Gunn diodes with annealed Ohmic contacts. Another process may start with the definition of Ohmic contacts, the Schottky overlayers, then etch the mesas, deposit test pads and remove the graded band gap layers.

However, for devices with non-annealed Ohmic contacts with or without graded band gap layers, and annealed Ohmic contacts without graded band gap layers, the fabrication processes are slightly different. Step (i) in the demonstrated fabrication process should be first initiated if the graded band gap layers are not required. Step (e) is not needed if non-annealed devices are preferred. Otherwise compatible processes may be achieved by selectively protecting and developing certain areas of the sample using EBL. For example, devices without graded band gap layers can be made using the above demonstrated fabrication process by exposing the desired device area under the e-beam and adding the step of wet-etching the graded gap layers (or Step (i) in the diagram) before Step (c) so that only the exposed area is removed by the etchant. The subsequent Ohmic contact deposition and annealing processed on the top developed area will finally lead to annealed Ohmic contacts without having the graded band gap materials.

## 4.2 Improved GaAs-based Planar Gunn Diodes

In the previous section the first planar Gunn diodes having AlGaAs/GaAs heterojunctions were introduced. Although the devices made demonstrated a frequency record (i.e. 108 GHz) for GaAs-based Gunn diodes for the fundamental oscillation [42, 175], they did not produce significant RF power (i.e. -43 dBm [42]). In order to improve the RF power of this type of planar Gunn device, several approaches have been explored in this work.

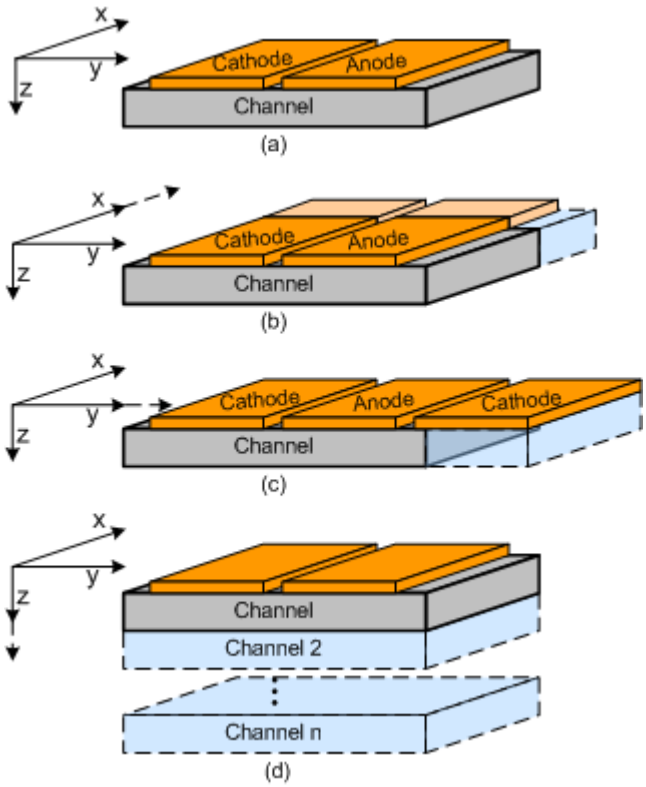


**Figure 4-14** Illustration of methods that have been investigated to improve power performance of planar Gunn devices in this project. (a) The original planar Gunn diode, (b) Extending the device width (along *x*-axis), (c) Combining two devices back-to-back (along *y*-axis), (d) Increasing number of channels or δ-doping layers along *z*-axis.

All these power increasing techniques can be described in three dimensions (3D) as illustrated in Figure 4-14. Figure 4-14a shows a simplified layout of the first planar Gunn diodes. The simplest approach to improve the output power, as shown in Figure 4-14b, is to extend the width of the planar Gunn diode in the *x*-axis direction, for example from the originally demonstrated 60 μm to 120 μm or even wider. Secondly, two planar Gunn diodes are combined in a back-to-back form in the *y*-axis direction. This combining technique does not need an external power combiner but fully utilises the natural layout of the coplanar waveguide-like (ground-signal-ground) test pads. The first two methods can be considered as "horizontal" or "planar" methods because they make a change of the

original design on the surface plane (*x*-axis and *y*-axis directions). However, these methods only change the device dimensionally but not intrinsically. The third method of improving RF power of a planar Gunn diode is to keep the test structure and the contact design of the original design unchanged but make modifications in the vertical direction or *z*-axis direction as shown in Figure 4-14d. In this section, a detailed discussion on the design, modelling, and experimental results on the realisation of the third approach is given.

A 2D device modelling tool, Medici, is used to simulate planar Gunn diodes. Firstly, a brief introduction to the tool is given in this section. Following this, the model description and its verification using the first planar Gunn diode is given. Once the model is validated, modified or new device designs are then devised from simulation results. Experimental results, where appropriate, are compared with the simulation data.

### 4.2.1 Medici Model for Planar Gunn Diodes

#### *4.2.1.1 Introduction to Medici*

Medici solves three basic partial differential equations (PDEs), namely Poisson's equation, Continuity equation, and Boltzmann transport theory self-consistently for distributions of electrostatic potential and for carrier concentrations in a device. The three PDEs are given as [216],

$$\varepsilon_r \varepsilon_0 \cdot \nabla^2 \psi = -q\left(p - n + N_D^+ - N_A^-\right) - \rho_s \tag{4.2.1}$$

$$\frac{\partial n}{\partial t} = \frac{1}{q}\vec{\nabla} \cdot \vec{J}_n - \left(U_n - G_n\right) = F_n\left(\psi, n, p\right) \tag{4.2.2 a}$$

$$\frac{\partial p}{\partial t} = \frac{1}{q}\vec{\nabla} \cdot \vec{J}_p - \left(U_p - G_p\right) = F_p\left(\psi, n, p\right) \tag{4.2.2 b}$$

$$\vec{J}_n = -q\mu_n n\vec{\nabla}\phi_n \tag{4.2.3 a}$$

$$\vec{J}_p = -q\mu_p p\vec{\nabla}\phi_p \tag{4.2.3 b}$$

Alternatively, Equations 4.2.3 can be written as [216]

$$\vec{J}_n = -q\mu_n n\vec{E}_n + qD_n\vec{\nabla}n \tag{4.2.4 a}$$

$$\vec{J}_p = q\mu_p p\vec{E}_p - qD_p\vec{\nabla}p \tag{4.2.4 b}$$

**Table 4-II** Parameter and symbol definitions for Equations 4.2.1-4.2.4 [216].

| Parameter | Definition | Parameter | Definition |
|---|---|---|---|
| $n$ | Electron concentration | $p$ | Hole concentration |
| $N_D^+$ | Ionised electron concentration | $N_A^-$ | Ionised hole concentration |
| $\vec{J}_n$ | Electron current density | $\vec{J}_p$ | Hole current density |
| $U_n$ | Net electron recombination rate | $U_p$ | Net hole recombination rate |
| $G_n$ | Net electron generation rate | $G_p$ | Net hole generation rate |
| $\mu_n$ | Electron mobility | $\mu_p$ | Hole mobility |
| $\phi_n$ | Quasi-Fermi potential for electrons | $\phi_p$ | Quasi-Fermi potential for holes |
| $D_n$ | Electron diffusion coefficient | $D_p$ | Hole diffusion coefficient |
| $\varepsilon$ | Material permittivity | $\psi$ | Intrinsic Fermi potential |
| $\rho_S$ | Surface charge density | $q$ | Single electron charge |

All parameters in the Equations 4.2.1-4.2.4 are defined in Table 4-II. Users can select default or self-defined values for these parameters. One also needs to choose appropriate models to calculate these parameters. For example, there are three models for recombination rate calculation which are Shockley-Read-Hall (SRH), Auger, and direct recombination. Users should also consider the following factors when solving a device problem:

**Mobility models:** There are several mobility models one can choose according to individual applications. These mobility models include low field mobility models and high field mobility models, temperature, stress and concentration dependant mobility models, and so on. These models can be applied for both electrons and holes.

**Boundary conditions:** Boundary conditions include metal-semiconductor interfaces (Ohmic contacts and Schottky contacts), semiconductor-semiconductor interfaces, semiconductor-insulator interfaces, surface charges and traps. Most time Medici can calculate interfaces using default settings, such as Neumann boundaries for suspended (noncontacted) edges of devices that only allows current flow through contacts rather than into the air. However exceptions occur for interfaces involving δ-doping, surface depletion, contact resistance etc. that have to be defined by users.

**Numerical methods:** Appropriate numerical methods are required to solve the nonlinear and coupled PDEs on each mesh point of a device. Initial guesses along with multiple iterations ensure to meet the converge criteria for the method selected. The most stable method is Newton's method that may be expensive in terms of time and memory for two-carrier devices such HBTs.

Except those, other models (e.g. heat effect model, transient effect model, and small-signal analysis) and advanced application modules (AAMs) e.g. Trapped charge AAM, Heterojunction AAMs, and Circuit Analysis AAMs are useful in solving various requests.

*4.2.1.2 Using the Medici Model to simulate the First Planar Gunn Diodes*

The planar Gunn diode having a single channel and two δ-doping layers (made from wafer C114) is modelled using Medici as follows: Figure 4-15a shows the left half of the device. In the model, the annealed Ohmic contact is assumed to reach between the channel and the lower δ-doping layer. It is modelled by using a block metal (blue rectangle in the diagram) that has a default barrier height (i.e. 0.8 eV) and a thin layer of highly doped materials (dark grey around the metal region). The contact resistance is externally defined according to the measured value, which is 0.15 Ω•mm in this case. The thin highly doped layer (e.g. $3\times10^{19}$ $cm^{-3}$) inserted between the metal and the semiconductor is to achieve a good Ohmic contact. The cap layer is modelled using a thin layer of GaAs ($3\times10^{18}$ $cm^{-3}$) which is adjustable depending on whether it is partially or fully depleted by the surface charge [175]. All un-doped materials, such as $Al_{0.23}Ga_{0.77}As$ barriers and GaAs channels and buffers are doped with n-type dopant at a level of $10^2$ $cm^{-3}$. The semi-insulating GaAs substrate is p-type doped and has a doping level of $5\times10^{15}$ $cm^{-3}$ to achieve the manufacturer specified resistivity of the substrate.

**Table 4-III** Material properties used in the simulation of the first planar Gunn diode.

| Parameter | GaAs | $Al_{0.23}Ga_{0.77}As$ |
|---|---|---|
| Permittivity | 12.9 | 12.2 |
| Bandgap (eV) | 1.424 | 1.71 |
| Affinity (eV) | 4.07 | 3.82 |
| Effective conduction band density of states ($cm^{-3}$) | $4.7\times10^{17}$ | $5.9\times10^{17}$ |
| Low field mobility ($cm^2•V^{-1}s^{-1}$) | 8500 | 4000 |
| Electron saturation velocity ($cm•s^{-1}$) | $1.0\times10^7$ | $0.8\times10^7$ |

The material properties used in the simulation are listed in Table 4-III [122, 217]. All the materials used have GaAs-like mobility that shows negative differential mobility (Equation 2.3.13) when the electric field exceeds a threshold value, e.g. 3.2 kV/cm for GaAs. The Newton method is selected to solve Poisson's equation and the continuity equation for electrons only. The anode and cathode distance $L_{ac}$ in the simulation is set to be 1.3 μm. No composite contacts are included in this model.

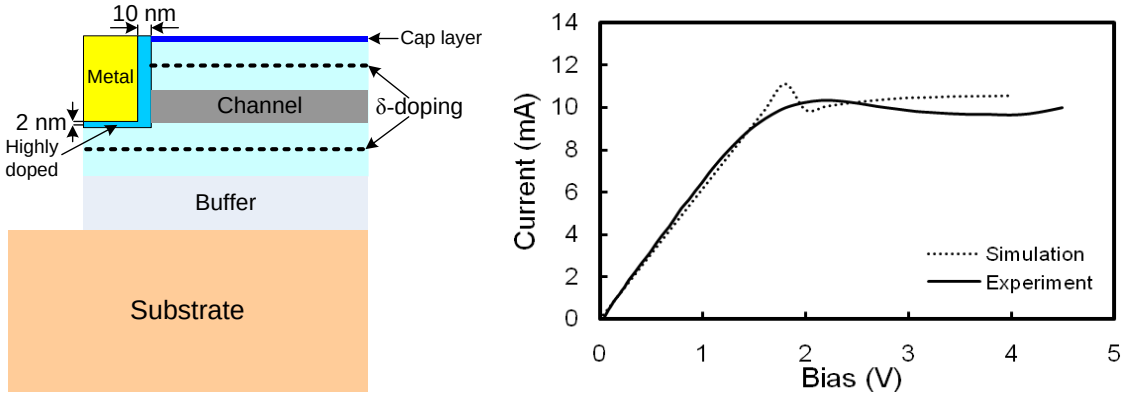


**Figure 4-15** (a) Illustration of the left half of a planar Gunn diode in the Medici model. (b) Comparison of the measured and simulated I-V characteristics of a 1.3 μm planar Gunn diode using wafer C114.

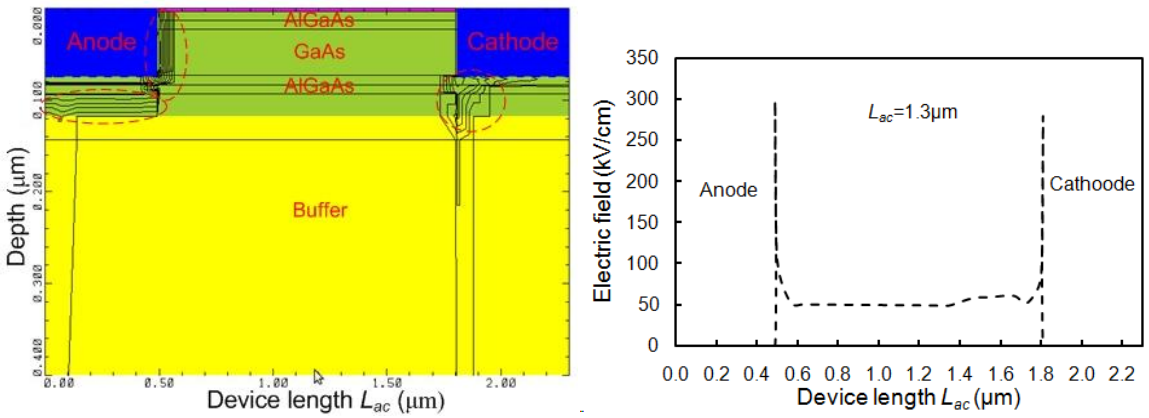


**Figure 4-16** (a) Simulated impact ionisation (within the red dashed circles) and (b) electric field distribution in the channel of a 1.3 μm single channel device with two δ-doping layers.

The simulated I-V characteristics are shown in Figure 4-15b. For comparison, the measured I-V characteristics are also plotted in the diagram. It can be seen that they have fairly good agreement. The small discrepancies exist for the peak current ($I_{pk}$) and current levels above the threshold voltages (e.g. ≥2 V). This can be attributed to the fact that Medici simulations are performed at room temperature, which is 300 K whereas an actual device has a higher temperature than 300 K when operating and therefore lower current

[176]. From the simulated I-V characteristics one can also see that the current starts rising as the bias voltage increases above 2 V. This is mainly due to impact ionisation occurring near the anode as shown in Figure 4-16a. Figure 4-16b shows the simulated electric field distribution horizontally across the centre of the GaAs channel. The high electric field near the electrodes is responsible for the impact ionisation. The contact effect has been discussed in Section 4.1 and the solution to suppress this high electric field near the anode Ohmic contact edges is to implement a composite anode contact.

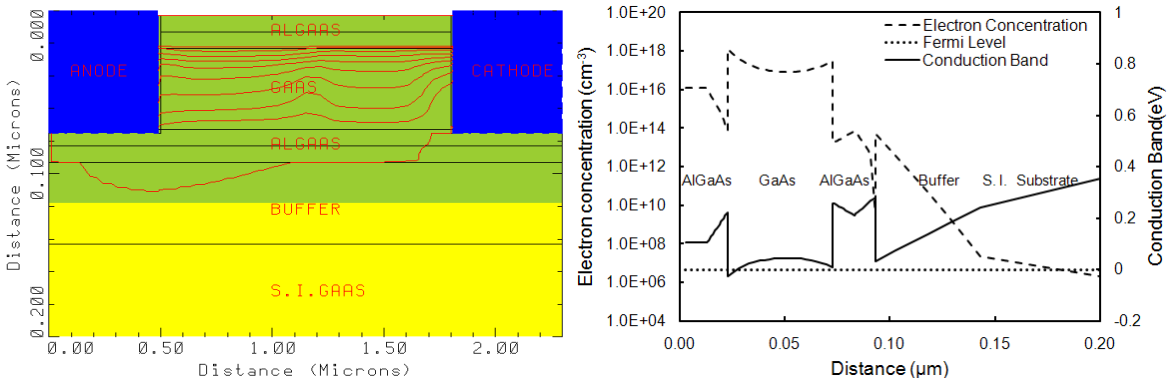


(a) (b)

**Figure 4-17** Simulated (a) current contours in the 1.3 μm device at 3 V and its (b) electron concentration distribution and conduction band energies at 0 V.

Figure 4-17a shows the current contours at a bias voltage of 3 V which is greater than the threshold voltage (i.e. 2 V) of the device. One can see that majority of the current follows within the GaAs channel but a small portion penetrates into the buffer layer and flows parallel to the channel. This result has a good agreement with the Monte-Carlo simulation results [175]. Figure 4-17b further illustrates the electron concentration distribution and conduction band energies of the layers in the device along the central line vertically at no external bias. The electron concentration in the channel is on the order of $10^{17}$ $cm^{-3}$ which gives an *NL* product of the 1.3 μm device greater than $1.3\times10^{13}$ $cm^{-2}$ meeting the basic requirement for the transit-time mode of the Gunn effect.

Several points can be made according to the simulation results: Firstly, with this layer design the majority of the electrons are well confined in the channel even if the bias voltage is higher than the threshold voltage (e.g. 3 V). Secondly, although this model does not include composite contacts to suppress the impact ionisation occurring at the anode edge, it can derive relatively accurate results for the threshold bias voltage, current level, and potential existence of NDR. These parameters are good indicators for Gunn

oscillations. Thirdly, this layer design gives an electron concentration in the channel of approximately $10^{17}$ $cm^{-3}$, in order to achieve higher frequency and higher power Gunn oscillations the electron concentration in the channel must be greater than $10^{17}$ $cm^{-3}$.

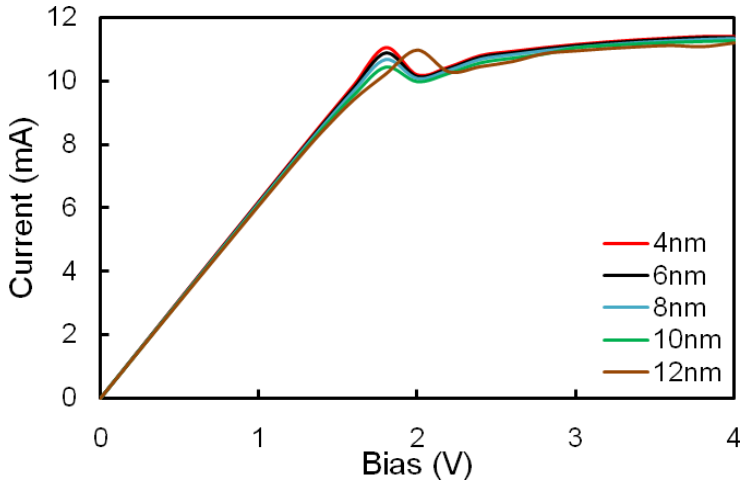


**Figure 4-18** Simulated I-V characteristics of a 1.3 μm device when its lower δ-doping layer is separated from the channel by 4 nm, 6 nm, 8 nm, 10 nm, and 12 nm, respectively on the condition of not changing other parameters.

In order to improve the electron density in the channel, one simple solution is just to bring the δ-doping layers closer to the channel so that the electrons can more easily to get into the channel [218]. In the original design δ-doping layers are 10 nm away from the channel on its either side, Figure 4-18 illustrates the simulated I-V characteristics when the lower δ-doping layer is separated from the channel by 4 nm to 12 nm but with other parameters unchanged. One can see that the average current increases as the separation between the δ-doping layer and the channel decreases.

### 4.2.2 Planar Gunn Diodes with Single Channel and Four δ-doping Layers

#### *4.2.2.1 Introduction*

With the success of modelling the first planar Gunn diode using the Medici model, it is possible to design new or modify existing devices. As like other power devices, such as HEMTs [219], increasing the current density in the channel is one of the effective solutions to increase the planar Gunn devices' power performance. To achieve this several techniques have been applied. Among them a four δ-doping technique that was initially developed for pHEMT devices [219] is first investigated.

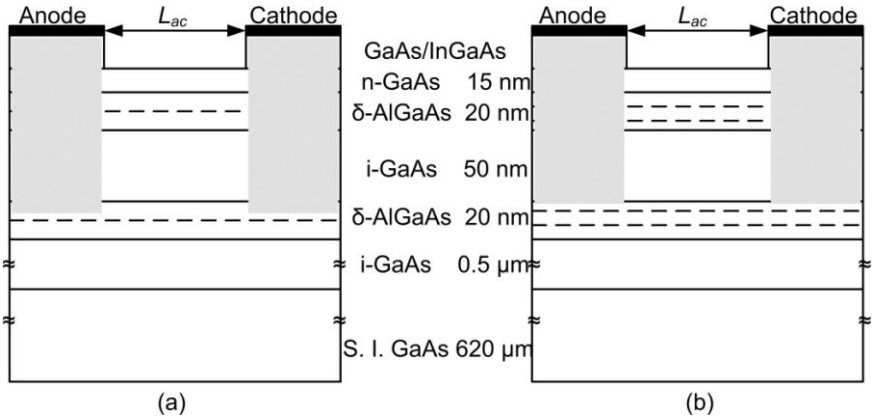


**Figure 4-19** Illustration of the devices with different δ-doping layers. (a) Single δ-doping layer on either side of the channel, (b) Two δ-doping layers on either side of the channel. The shaded areas indicate the annealed Ohmic contact regions. The dashed lines represent δ-doping layers.

The device has an epitaxial layer structure as schematically shown in Figure 4-19b. Compared with the previously demonstrated device that has two δ-doping layers (Figure 4-19a), the modified design still has two AlGaAs layers whose heights are still 10 nm but with the addition of an extra δ-doping layer with the same doping level ($8\times10^{11}$ $cm^{-2}$) in each AlGaAs layer. The δ-doping layers are approximately evenly distributed in each AlGaAs layer. This design leads to the original two δ-doping layers (one from the top and one from the bottom) much closer to the channel (e.g. 4 nm instead 10 nm as before). According to the simulation results (Figure 4-18), closer δ-doping layers can raise the electron concentration in the channel and therefore achieve a higher current level. In addition, the added δ-doping layers may also contribute to the electron concentration level in the channel.

*4.2.2.2 Device Simulation and Realisation*

The device is simulated using the previously developed model with a slight modification on the δ-doping layers and AlGaAs barrier layers. The material parameters are the same as shown in Table 4-III. The Newton method is used to solve the Poisson equation and the continuity equation for electrons only. The simulated I-V characteristics, electron concentration distribution, and the conduction band energies are plotted in Figure 4-20. For comparison, parameters from the device with two δ-doping layers are also included in the diagram. It can be clearly seen that the device with double δ-doping layers on either side of the channel shows higher electron concentration in the GaAs channel. This is due to the formation of the second two-dimensional electron gas (2DEG) between the channel and the second $Al_{0.23}Ga_{0.77}As$ layer when extra δ-doping is introduced. The second 2DEG corresponds to the conduction band dip in the well below the electron quasi-Fermi level as

seen in Figure 4-20a. The average electron concentration in the channel is approximately $2.7\times10^{17}$ $cm^{-3}$ and $4\times10^{17}$ $cm^{-3}$ for Gunn diodes with two and four δ-doping layers, respectively. The average current (as shown in Figure 4-20b) after the onset of threshold for a device with four δ-doping layers is 120% greater than that from a device with two δ-doping layers. The increased current results from better electron confinement in the channel and electrons contributing from the added δ-doping layers. In addition, one can see that the measured current level is slightly higher than that of the simulated. This may result from the incompletely depleted cap layer as discussed in [175]. The originally designed 15 nm cap layer can be fully depleted by its surface potential if all the topmost layers are completely removed. However, the final etching process (to remove the grade band gap layers) may have not removed all the Ohmic layers but leave a thin layer of highly doped GaAs that may lead to the surface charge being unable to completely deplete the cap layer so that the remaining part of the cap layer participates in current conduction and therefore the total current increases [175].

The wafer growth process for the four δ-doped device is similar as that for wafer C114 except the insertions of additional δ-doping layers and re-position of the two existing δ-doping layers in the two AlGaAs layers. The wafer based on this design is named as wafer C340 whose detailed description of growth process is not included here. Similarly, the device fabrication process is the same as the previous one and is not covered here.

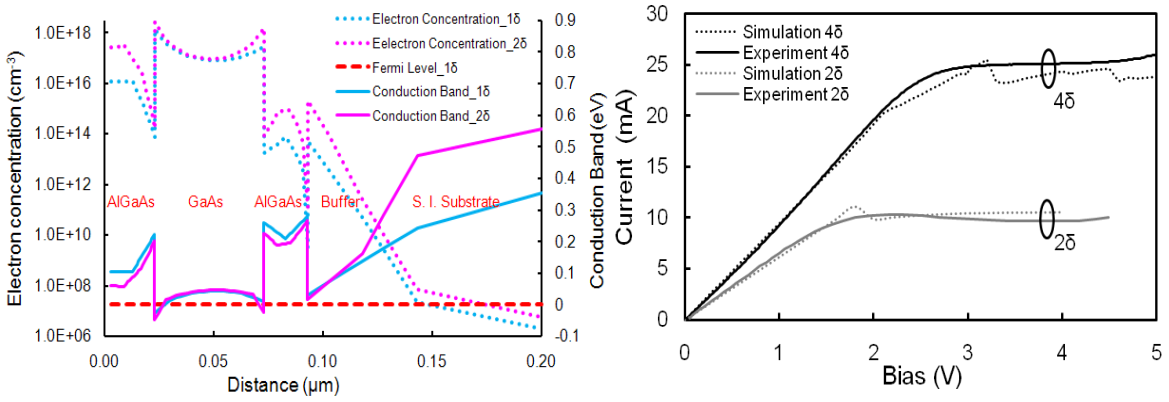


(a) (b)

**Figure 4-20** Comparisons of (a) simulated electron concentration distribution and conduction band energies and (b) simulated and measured I-V characteristics of a 1.3 μm device with two and four δ-doping layers.

For device characterisation, apart from the measured IV characteristics of the 1.3 μm device that are plotted in Figure 4-20b, the spectrum is measured using a *W*-band GSG probe with 100 μm pitch separation (ACP110-100 from CascadeMicrotech), *W*-band mixer (WHMP-10 from Farran Technology), and a spectrum analyser (E4448A from Agilent

Technologies). The device starts to oscillate when the bias voltage is between 1.2 and 1.5 times the threshold voltage (e.g. 3.1 V; in contrast it is 2.8 V for a device with two δ-doping layers). The output spectra are plotted in Figure 4-21 in comparison with those of the device made from wafer C114. It can be seen that the device with two δ-doping layers show a noisy peak with a peak output power of -43.5 dBm at 108.12 GHz. In contrast, the device with four δ-doping layers shows twice the power and a slightly increased oscillation frequency. Although the output power is still relatively low, the improved spectral response for the device with four δ-doping is evident. It is understood that the lower noise in the device with four δ doping layers improved domain formation as a consequence of the higher free electron concentration.

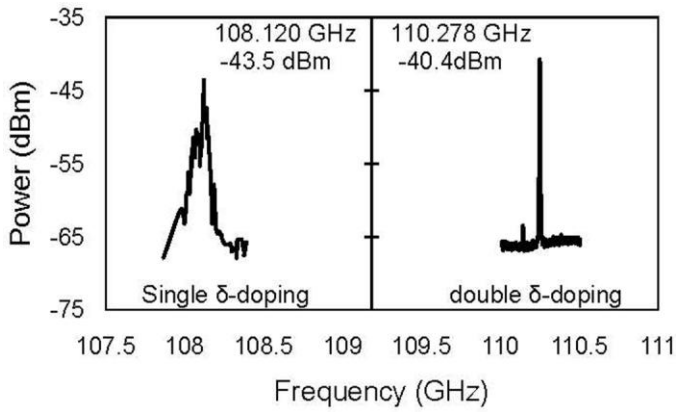


**Figure 4-21** Spectra of 1.3 μm planar Gunn diodes with two δ-doping layers (Left) and four δ-doping layers (Right).

Small-signal measurement using two sets of VNAs covering the frequency range from DC to 110 GHz and 140 to 220 GHz are used to measure impedances of the 1.3 μm devices. Both sets of VNAs use GSG 100 μm-pitch probes that are from GGB industries. The calibration substrates (Cascade Microtech) are 109-102B for DC-110 GHz and CS-15 for 140-220 GHz, respectively. Figure 4-22 shows the measured results of a 1.3 μm planar Gunn diode after being de-embedded from CPW measuring pads over the frequency range of 140-160 GHz. It can be seen from Figure 4-22a that the magnitude of reflection coefficient ($|S_{11}|$) of the planar Gunn diode is over 0 dB up to 158 GHz when the bias is 2.8 V; this shows negative resistance for the diode, as seen in Figure 4-22b, according to the following equation

$$Z_{11} = \frac{1 - S_{11}}{1 + S_{11}} \cdot Z_0 \tag{4.2.5}$$

where $Z_0 = 50\Omega$. In addition, the maximum frequency for a 0 dB reflection coefficient decreases as bias increases. For frequencies between 10 MHz to 110 GHz, the refection coefficients are always less than 0 dB no matter how high the bias is increased.

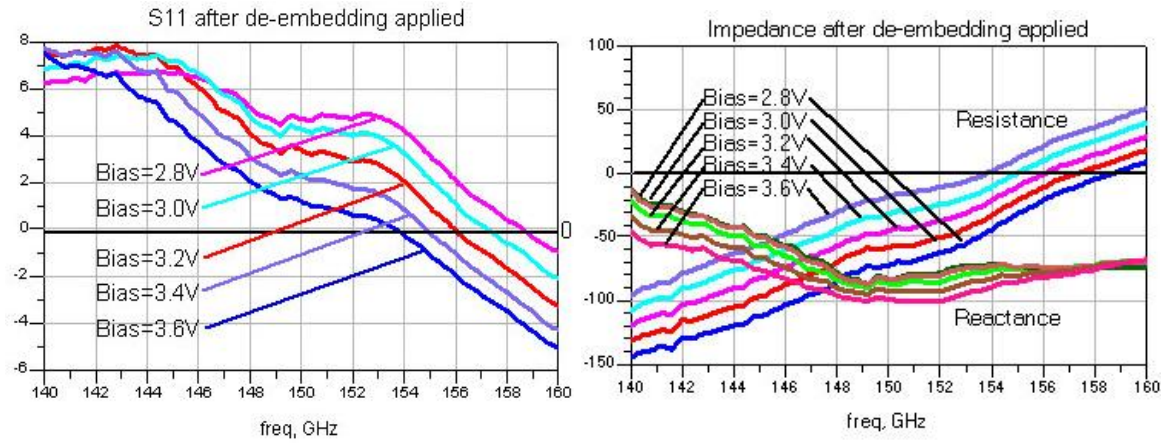


**Figure 4-22** Measured (a) one-port reflection coefficient $|S_{11}|$ and (b) impedances (resistance and reactance) of a 1.3 μm planar Gunn diodes with four δ-doping layers.

*4.2.2.3 Summary*

To conclude, a modified design of planar Gunn diodes having four δ-doping layers has been numerically studied and experimentally demonstrated. Simulation results show an obvious improvement in the electron concentration in the channel when extra δ-doping layers are introduced. The simulated and measured current-voltage characteristics of a device with $L_{ac}$=1.3 μm show good agreement and confirm that the four δ-doped device shows an average 120 % increase of output current. RF measurements on the same devices indicate that both the power and oscillation frequency are enhanced for four δ-doped devices. Importantly some devices exhibit negative resistance up to 158 GHz and this is the highest record of negative resistance for the fundamental mode of operation for GaAs based Gunn diodes.

### 4.2.3 Multiple-channel Planar Gunn Diodes

*4.2.3.1 Two Channel Planar Gunn diodes*

Instead of using four δ-doping layers the second method to increase the current density of a device is to introduce a duplicate "channel" underneath the original channel. It is expected that the second channel can also generate Gunn oscillations which can be self-synchronised to the Gunn oscillation from the top channel therefore total RF power is enhanced. The device epitaxial layers are illustrated in Figure 4-23. The device layers are the same as that from wafer C114 except for the addition of a duplicate channel and its barrier layers and δ-doping layers.

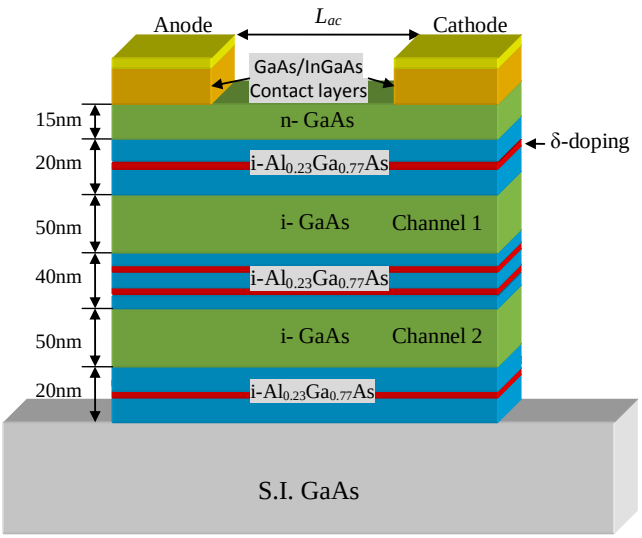


**Figure 4-23** Illustration of epitaxial layers structure of a planar Gunn diode with two parallel channels.

The Medici model used for modelling single channel planar Gunn diodes with two and four δ-doping layers is now used to simulate the two-channel devices. It is assumed that the annealed Ohmic contacts reach just 2 nm below the second channel. Other parameters remain unchanged as those previously used for modelling other devices. Figure 4-24 illustrates the simulated conduction band energies and electron concentration distribution of a 1.3 μm device with two channels and four δ-doping layers. It can be seen that both channels have high electron concentrations and all four 2DEGs pin the conduction band below the Fermi level.

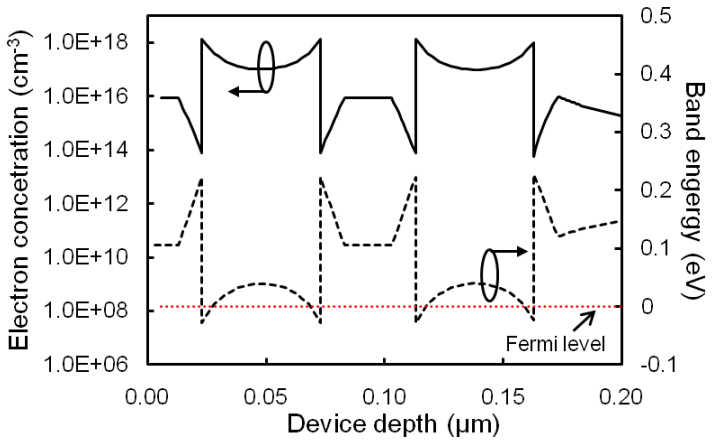


**Figure 4-24** The simulated conduction band energy and electron concentration of a 1.3 μm device with two channels and four δ-doping layers.

The simulated I-V characteristics of the device is show in Figure 4-25a. For comparison, the I-V characteristics of a 1.3 μm device with a single channel and four δ-doping layers is also plotted in the same diagram. It is clearly seen that the two-channel device has approximately twice the current of the single-channel device. The significant improvement

of current level indicates that higher efficiency can be achieved using two separate channels rather than a single channel when the same number of δ-doping layers is used.

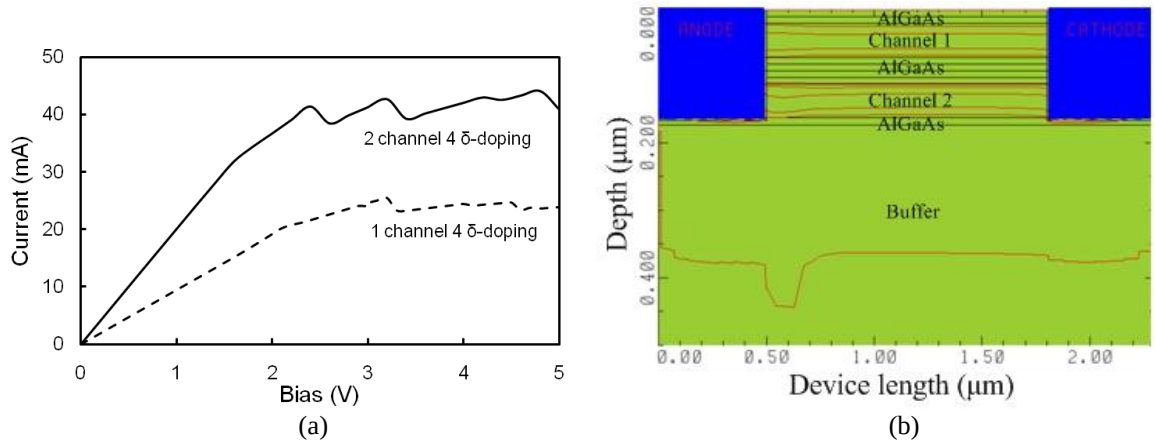


**Figure 4-25** (a) Comparison of simulated I-V characteristics of a 1.3 μm device with four δ-doping layers but different number of channels. (b) Simulated current flow in the device with two channels and four δ-doping layers at a bias of 3 V.

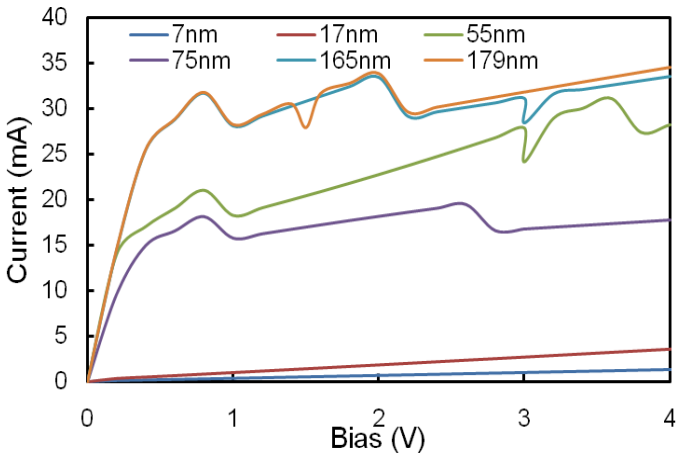


**Figure 4-26** Simulated I-V characteristics of a 1.3 μm device with two channels for various annealed Ohmic contact depths. Note that the unexpected dips at 1.4 V (179 nm), and 3 V (55nm and 165 nm) are a result of coarse meshing in Medici and not expected to occur in a real device.

The wafer (named as C230) underwent an almost identical growth process as the single channel two-δ doped wafer (wafer C114) with the exception of adding an additional period of AlGaAs/GaAs/AlGaAs layer to obtain the second channel. Although the fabrication process for devices on other wafers can be used for making devices on wafer C230, it is slightly different when considering the annealed contacts. This is because when the second channel and its barrier layers are added, an extra 90 nm of AlGaAs/GaAs/AlGaAs layers is added. In this case, the annealed Ohmic may not reach as deep as the assumed depth in simulation. If this is true, the device may behave differently. In order to investigate how the annealed depth affect the device behaviors, simulations are performed on a 1.3 μm device having different depths of the annealed Ohmic contacts. The depths are 7 nm, 17 nm, 55 nm, 75 nm, 165 nm, and 179 nm with reference to the surface of the top AlGaAs

layer. These depths correspond to a position just above the upper δ-doping layer for channel 1 (7 nm), a position between the upper δ-doping layer and channel 1 (17 nm), a position in the channel 1 (55 nm), a position between channel 1 and its lower δ-doping layer (75 nm), a position between the upper δ-doping layer of channel 2 and the channel 2 (165 nm), and a position between the channel 2 and its lower δ-doping layer, respectively. The simulated I-V characteristics of the device having various depths are plotted in Figure 4-26. Some of the corresponding current flows are illustrated in Figure 4-27.

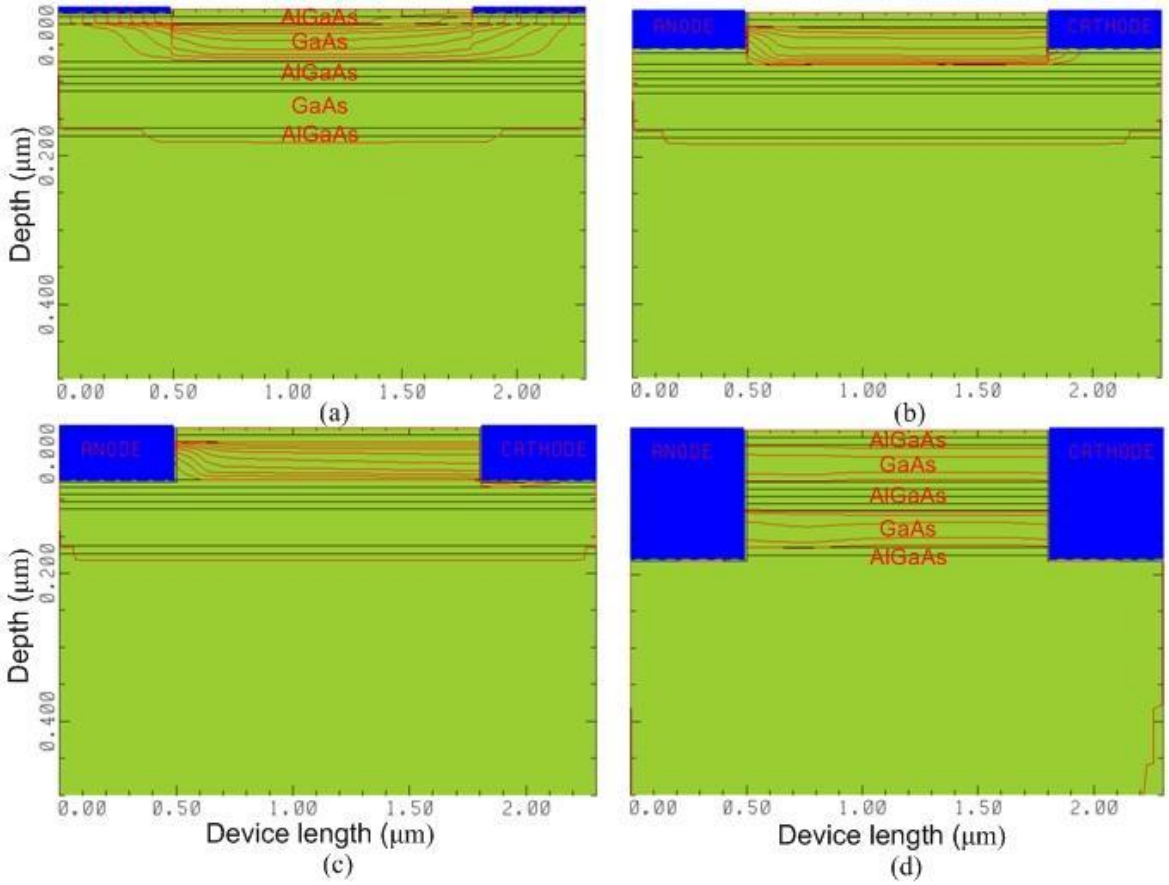


**Figure 4-27** Illustration of current flow in a 1.3 μm device with two channels for different depths of annealed Ohmic contacts. (a) The annealed Ohmic contacts just reach the 7 nm depth into the AlGaAs layer, (b) The annealed Ohmic contacts reach mid of top channel (55 nm down from the surface), (c) The annealed Ohmic contacts reach just below the top channel, and (d) The annealed Ohmic contacts are below the second channel.

It can be seen that if the annealed Ohmic contacts cannot reach as deep as a channel, it is unlikely that the corresponding channel can fully participate in conducting current. In addition, even if the annealed Ohmic contacts are deeper than the second channel (e.g. 165 nm and 179 nm); there is no obvious difference in terms of the total current level. This is an indication that annealed Ohmic contacts with deep penetration into the device may be desirable for planar Gunn diodes. Alternatively, asymmetric Ohmic contacts (annealed anode and non-annealed cathode) may also provide similar performance [175].

The results from the simulation study of a two channel structure were very encouraging. We therefore decided to extend the investigation by carrying out a simulation study for a 7-channel structure. The structure that we investigated was similar to one that had already been described in [117]. The motivation for this was to try and find more improvement in the device performance.

### *4.2.3.2 Seven Channel Planar Gunn Diodes*

The device layer of the 7-channel wafer (C605) is schematically shown in 4-28a. The simulated I-V characteristics of a 1.1 µm planar Gunn diode (no measured contact resistance is applied) is shown in Figure 4-28b. According to the simulation results, a 7-channel device should produce up-to 130 mA peak current ($I_{pk}$); however, the measured direct current and pulsed current characteristics of the devices show completely different results (Figure 4-28c).

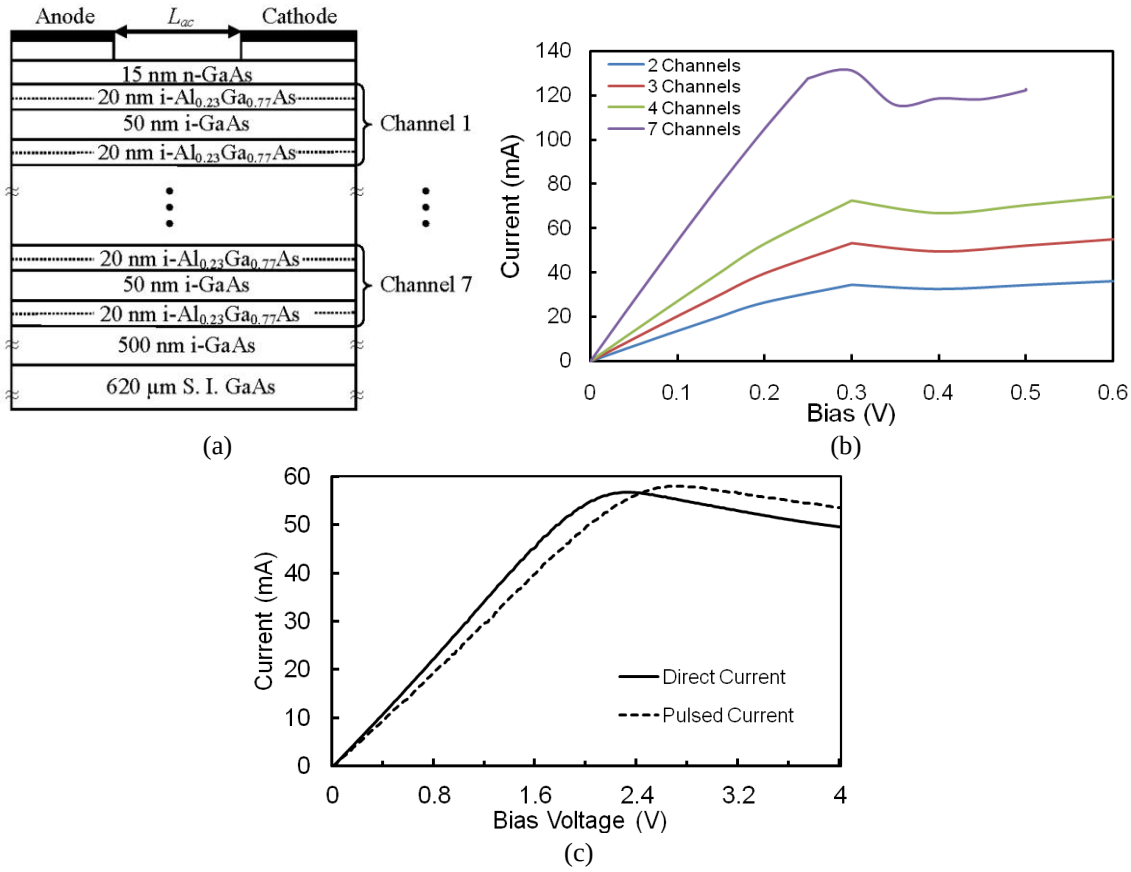


**Figure 4-28** (a) Illustration of the epitaxial layer structure of the 7 channel planar Gunn diodes. (b) Simulated I-V characteristics of a 1.1 µm 7-channel device with two, three, four, and seven participating channels. (c) Measured direct current and pulsed current of the 1.1 µm device.

The DC and pulsed I-V measurement is carried out using a semiconductor device analyser (Agilent Technologies B1500A) on a semi-automated probe station (Cascade Microtech

Summit 12K). For pulsed I-V measurement, the pulse width and period is set to 0.5 ms and 50 ms, respectively. It can be seen in Figure 4-28c that for the device with $L_{ac}$=1.1 µm the pulsed I-V has higher negative differential region (NDR) peak voltage, $V_{pk}$, of 2.5 V and higher peak current of 58 mA. Due to the bias associated heating effect, the DC I-V curve has $V_{pk}$ = 2.3 V and $I_{pk}$ = 56.8 mA.

The discrepancy between the simulated and the measured current level is likely due to the annealed Ohmic contacts. According to the simulated I-V characteristics of the two-channel device (Section 4.2.3.1), the depth of Ohmic contact determines the total number of channels that contribute to the total current. Simulation on the variation of the number of channels for the 7-channel device is carried out. The simulated I-V characteristics for two, three, and four active channels are plotted against that from seven channels in Figure 4-28b. From these results one can tell that it is possible that only four channels are participating in current conduction in the fabricated device. This indicates that better annealed Ohmic contacts that can penetrate deep inside the device are required to obtain current flow from all the channels.

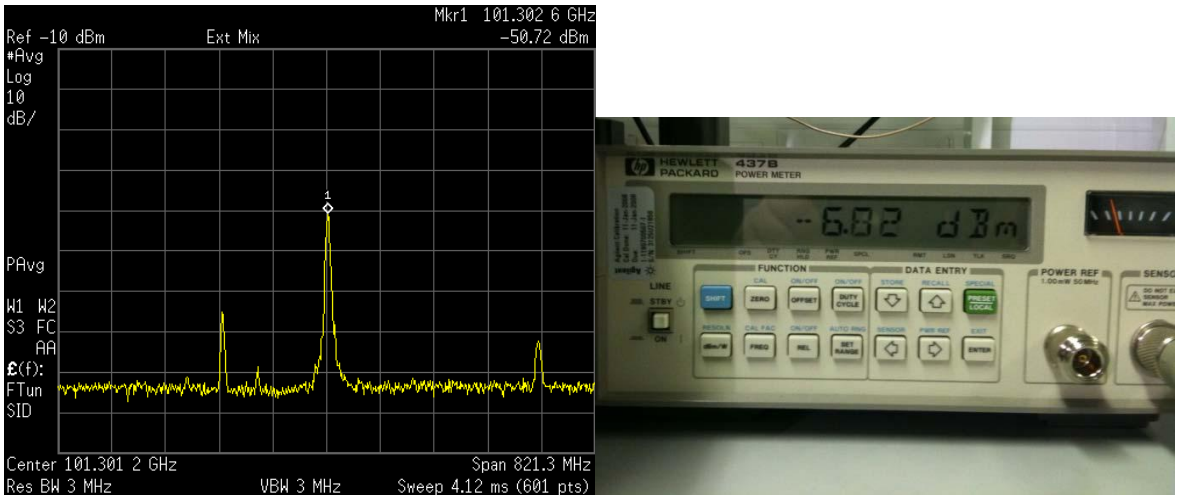


(a) (b)

**Figure 4-29** Measured spectrum of a 1.1 µm planar Gunn diode with 7 channels. (a) Frequency (i.e.101.3026 GHz ) of the device measured by using a *W*-band spectrum analyser setup (the shown power is uncalibrated), (b) Power (i.e. -6.72 dBm) measured using a *W*-band power meter measurement setup.

The RF performance of the device is measured using a spectrum analyser (Agilent Technologies E4448A) and two different external subharmonic mixers (Farran Technology WHMP-10 and WHM-05) to cover both the fundamental and second-harmonic frequency bands up to 220 GHz. The device is biased at 3.2 V that is 1.3 times higher than the bias threshold voltage $V_{pk}$ at which the onset of NDR occurs to ensure stable oscillation. The

measured frequency (i.e. 101.3 GHz) is shown in Figure 4-29a. The output power is measured using a power meter (HP 8563) with a calibrated *W*-band sensor as shown in Figure 4-29b. It is -6.7 dBm or -4.5 dBm after deducting the transmission loss of the *W*-band probe. The spectrum for the second-harmonic oscillation measurement is estimated to be -26.6 dBm after taking into account all system losses.

Other devices with longer anode and cathode distance have also been measured. A 4 μm device produces its highest power -0.6 dBm at 16.9 GHz. The bias is 5.33 V and current is 52.5 mA. It is noticeable that these seven-channel devices have much lower oscillation frequencies than the single channel devices. For example, a 4.0 μm and a 1.3 μm single channel two δ-doped device produce oscillations at 24.5 GHz and 108 GHz; on the contrary, the 4.0 μm and 1.1 μm seven channel devices generate 16.7 GHz and 101.3 GHz oscillations. A possible explanation for the decreasing frequency performance is the excess heat created by the high current. The increase of heat increases electron scattering and therefore decreases average electron mobility. This is further experimentally discussed in the next chapter.

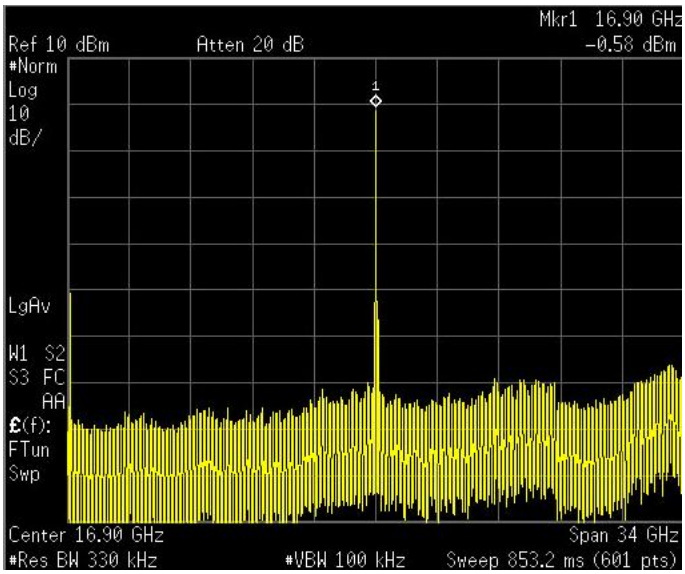


**Figure 4-30** Measured spectrum of a 4 μm 7-channel planar Gunn diode. The device oscillated at 16.7 GHz with output power of -0.6 dBm.

To conclude, multiple channel planar Gunn diodes have been designed for high power performance. The simulated results have shown higher electron concentrations in the channels than that of single channel devices. Although experimentally measured current levels are only half of the predicted due to some of the lower non-active channels, the measured RF results have shown significant power enhancement, for example from -34

dBm to -0.6 dBm for 4 μm devices and -43 dBm to -4.5 dBm for devices operating at over 100 GHz. However the seven-channel devices suffer from low oscillation frequency. It seems a compromise has to be met in order to achieve higher frequency or high power for GaAs-based planar Gunn diodes. This may be achieved using other material systems, such as indium compounds.

## 4.3 $In_{0.23}Ga_{0.77}As$-based Planar Gunn Diodes

### 4.3.1 Introduction

$In_xGa_{1-x}As$ is a promising material with superior electrical properties to GaAs that exhibits the Gunn effect [40, 63, 108, 220, 221]; it can be grown on an InP substrate for lattice-matched structures with $x=0.53$ or on a GaAs substrate to make lattice-strained layers for any other mole combination of indium and gallium. In the past, there have been a number of experimental investigations into lattice-matched $In_xGa_{1-x}As$ for Gunn oscillations [63, 108, 220]. However, oscillation frequencies of only a few gigahertzes were achieved. Although slightly higher oscillation frequencies (approximately 20 GHz) were observed in three-terminal pseudomorphic high electron mobility transistor (pHEMT) structures using lattice-strained $In_{0.15}Ga_{0.85}As$, it was believed that the oscillations resulted from a real-space transfer effect rather than a *k*-space transfer effect (i.e. the Gunn or transferred electron effect) [169].

Early theoretical investigations showed that the high energy relaxation time of $In_{0.53}Ga_{0.47}As$ might limit Gunn oscillation to no more than 50 GHz [222]. More recently, however, theoretical studies on two-terminal, carefully shaped, planar $In_{0.53}Ga_{0.47}As$-based self-switching diodes showed that operation towards the millimetre-wave frequency range was feasible [40]. In addition, Monte-Carlo simulation showed that ultrafast quasi-ballistic electrons in the Γ-valley would, under the influence of a high electric field caused by an etched recess, achieve a velocity of up to $10^8$ cm/s. Consequently, lattice-strained devices ($In_{0.7}Ga_{0.3}As$) with submicron dimensions would generate Gunn-like oscillations in the terahertz frequency range [41, 221].

On the contrary, there has been little work on lattice-strained $In_xGa_{1-x}As$ for Gunn oscillations [92]. The first report appeared in [92] where Monte-Carlo simulations

confirmed that the "kink" effect in HEMT devices resulted from Gunn domains. In this section lattice-strained $In_{0.23}Ga_{0.77}As$ for planar Gunn diodes is investigated.

### 4.3.2 Device Design and Modelling

#### *4.3.2.1 Prototype Design*

As with GaAs and InP, several intrinsic properties of the ternary compound $In_xGa_{1-x}As$ make it a suitable candidate for Gunn oscillators. It has a direct bandgap for all values of $x$ and negative differential mobility when a high electric field is applied. $In_xGa_{1-x}As$ is lattice-matched to InP for only $x=0.53$ [223]. Early work on $In_{0.53}Ga_{0.47}As$ planar Gunn diodes could only investigate simple bar or "H" shaped planar devices, without heterostructures, fabricated on InP substrates [63, 108]. Lattice-matched heterojunctions can be made with $In_{0.52}Al_{0.48}As$ and the quaternary compound semiconductor InGaAsP and InAlGaAs for appropriate alloy mixes [223]. However, as technology has progressed, it has become possible to grow pseudomorphic $In_xGa_{1-x}As$ on to GaAs and AlGaAs. Using this method strained AlGaAs/InGaAs/GaAs or AlGaAs/InGaAs/AlGaAs heterostructures could be realised [224, 225]. PHEMTs based on these structures have already demonstrated better performance than conventional GaAs-based HEMTS, such as low noise and high peak electron drift velocity because these heterojunctions result in a larger conduction band discontinuity that ensures greater electron confinement and density. Furthermore, the lattice strain and large conduction band discontinuity enhance the efficiency of any modulation doping. The reduction in ionised donor scattering in the channel leads to improved electron mobility. Therefore, it is expected Gunn diodes made using $In_{0.23}Ga_{0.77}As$/AlGaAs heterojunctions may exhibit better performance than those made using GaAs/AlGaAs heterojunctions.

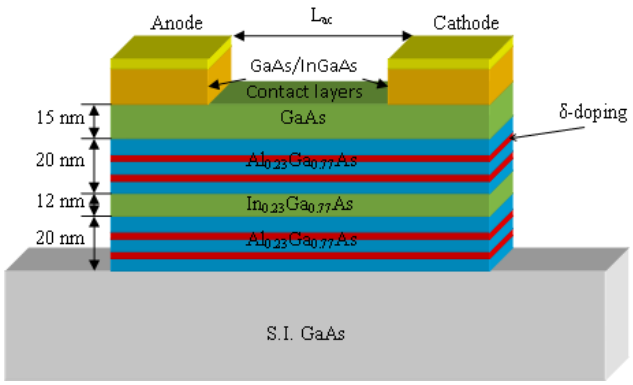


**Figure 4-31** Schematic view of the epitaxial layers of $In_{0.23}Ga_{0.77}As$ based planar Gunn diodes and the arrangement of the contacts and channel recess. The δ-doping layer has a doping density of $8\times10^{11}$ $cm^{-2}$.

Figure 4-31 shows the layer structure and device architecture that has been investigated. The 12 nm undoped $In_{0.23}Ga_{0.77}As$ channel is sandwiched between two double δ-doped $Al_{0.23}Ga_{0.77}As$ layers. The channel thickness was chosen so as not to exceed the critical value $d_{cr}$(nm)≈-3.6+3.66$x$ in order to obtain a defect-free channel [218]. The mole fraction of aluminum in the AlGaAs layers was chosen so as to avoid possible DX centres, and to maximise the conduction band discontinuity [226]. Each δ-doping layer has a sheet density of $8\times10^{11}$ $cm^{-2}$. Double δ-doping has been demonstrated to increase the carrier concentration in a 2DEG [219].

*4.3.2.2 Device Simulation*

Detailed simulations for the device are performed using the Medici model. The highly doped 15 nm GaAs cap layer is assumed to be partially depleted by its surface potential. Therefore, the simulated cap layer height is 5 nm to give a good agreement with experimental results. The annealed anode and cathode Ohmic contact regions were assumed to reach just below the $In_{0.23}Ga_{0.77}As$ channel. This is reasonably true for the device 38 nm thinner than the first Gunn diodes when an annealed process is applied onto metal alloy contacts. The specific contact resistance used in the model is based on the measured value of $4\times10^{-6}$ $\Omega\cdot cm^2$. Other important material parameters are listed in Table 4-IV.

**Table 4-IV** Semiconductor material parameters used in the simulation

| Parameter (at 300K) | $In_{0.23}Ga_{0.77}As$ | GaAs | $Al_{0.23}Ga_{0.77}As$ |
|---|---|---|---|
| Permittivity | 13.9 | 12.9 | 12.2 |
| Bandgap (eV) | 1.1 | 1.424 | 1.71 |
| Affinity (eV) | 4.26 | 4.07 | 3.82 |
| Effective conduction band density of states ($cm^{-3}$) | $2.9\times10^{17}$ | $4.7\times10^{17}$ | $5.9\times10^{17}$ |
| Low field mobility ($cm^2/(V\cdot s)$) | 8000 | 8500 | 4000 |
| Electron saturation velocity (cm/s) | $2\times10^7$ | $1\times10^7$ | $0.8\times10^7$ |

Figure 4-32 shows the anticipated conduction band edge discontinuity (approximately 0.43 eV) between the $In_{0.23}Ga_{0.77}As$ well and $Al_{0.23}Ga_{0.77}As$ barriers. The Fermi energy inside the $In_{0.23}Ga_{0.77}As$ well is above the conduction band edge at zero bias indicating a high concentration of free electrons that is far more obvious than GaAs-channel planar Gunn

diodes. The calculated electron concentration is also plotted in Figure 4-32 and the high electron concentration (approximately $10^{18}$ $cm^{-3}$) in the $In_{0.23}Ga_{0.77}As$ well is observable. Since the channel is electron rich and no parasitic parallel conduction paths are evident, it is expected that the majority of the current will flow in the $In_{0.23}Ga_{0.77}As$ well. The simulated current contours for a 1.45 μm device with an anode-cathode bias voltage ($V_{ac}$) of 2.5 V are shown in Figure 4-33. The current-voltage characteristics from simulations for several $L_{ac}$ (1.45 μm, 3 μm and 4 μm) are plotted against the experimental results in Figure 4-34. One can see from Figure 4-34 that (a) there is no prominent NDR as the bias voltage exceeds the threshold values but saturate for long devices (3 μm and 4 μm) and increase for the short device (1.45 μm); (b) the current level of shorter devices is higher than that of longer devices. Such I-V characteristics may result from either the impact ionisation as discussed for GaAs-based planar Gunn devices or injecting electrons from the cathode, especially for short devices [227, 228].

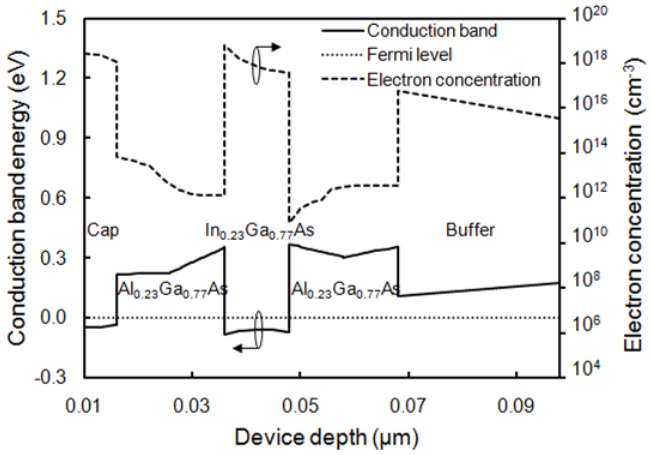


**Figure 4-32** Simulated conduction band structure of the $In_{0.23}Ga_{0.77}As$ device with $L_{ac}$=1.45 μm and electron concentration in each layer at zero bias. The buffer is partially shown and the semi-insulating substrate is not shown due to the large size compared to the active layers.

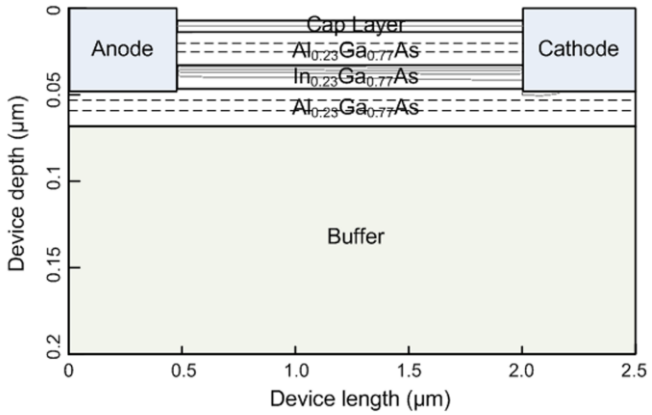


**Figure 4-33** Simulated current flow in the 1.45 μm $In_{0.23}Ga_{0.77}As$ device. The contours show that the majority of the current is in the $In_{0.23}Ga_{0.77}As$ channel. The entire device was modelled, but only a small region is shown for clarity.

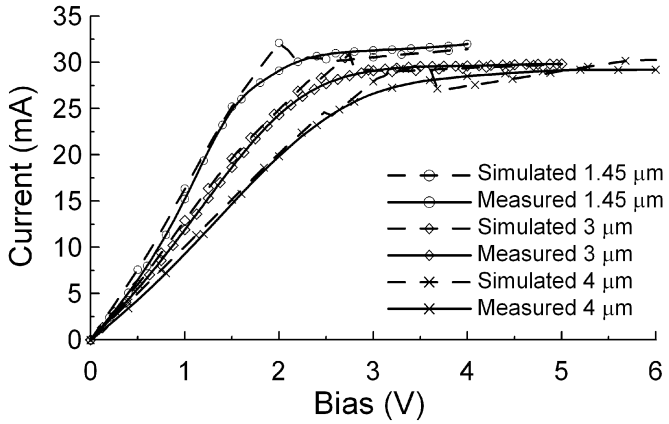


**Figure 4-34** Simulated and measured current-voltage characteristics of $In_{0.23}Ga_{0.77}As$ devices with $L_{ac}$ = 1.45 μm, $L_{ac}$ = 3 μm and $L_{ac}$ = 4 μm.

### 4.3.3 Material Growth and Device Fabrication

The epitaxial layers were grown by MBE as schematically shown in Figure 4-35a. A 0.5 μm GaAs buffer layer was first grown on a 620 μm semi-insulating GaAs substrate followed by 20 periods of GaAs/AlGaAs superlattices. The active channel was made of un-doped $In_{0.23}Ga_{0.77}As$ that was sandwiched by two double δ-doped $Al_{0.23}Ga_{0.77}As$ layers. The δ-doping layer has a sheet density of $8\times10^{11}$ $cm^{-2}$. 15 nm of highly doped GaAs was grown on top of the upper $Al_{0.23}Ga_{0.77}As$ barrier layer to serve as a cap layer. This was followed by a 5 nm $Al_{0.8}Ga_{0.2}As$ etch stop layer doped at $4\times10^{18}$ $cm^{-3}$. The top of the wafer was then finished with multiple graded layers of GaAs/InGaAs to facilitate good Ohmic contact formation.

The device fabrication process is the same as previously shown for single-channel GaAs based devices. Devices with $L_{ac}$ ranging from 1.0 μm up to 4.0 μm are fabricated on the same chip. Figure 4-35b shows an SEM of a device with a channel width of 60 μm. The $L_{ac}$ is 1.45 μm. It is also clear to identify a short extension layer over the mesa at the anode side of the device in the SEM image.

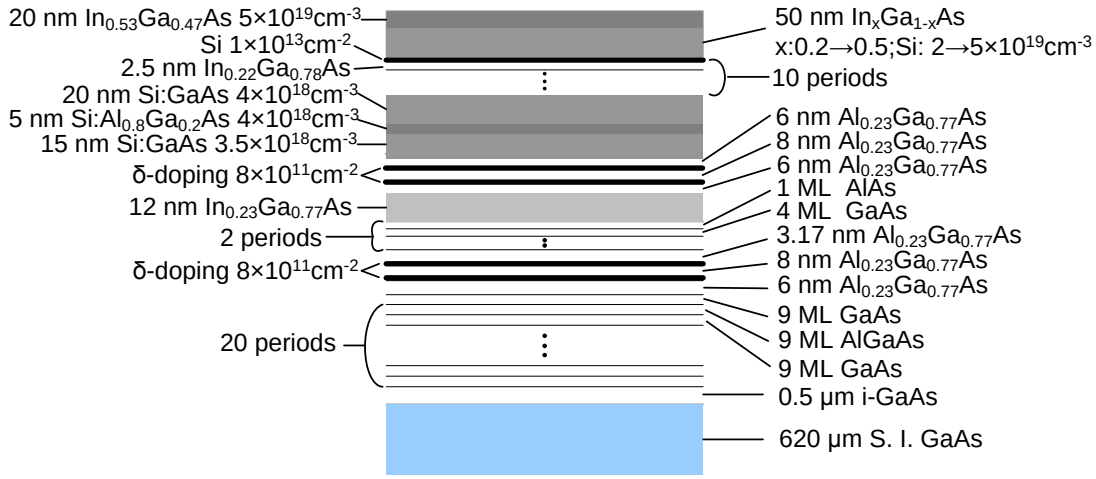


(a)

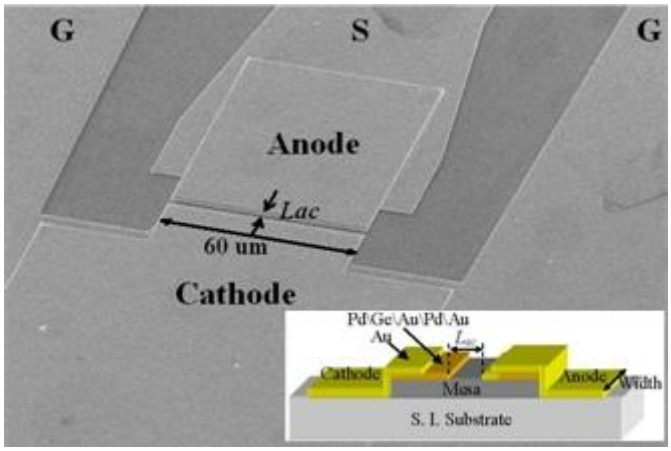


(b)

**Figure 4-35** (a) Schematic view of the epitaxial wafer layers as grown for $In_{0.23}Ga_{0.77}As$-based planar Gunn diodes. (b) Scanning electron micrograph of a 1.45 μm device. Coplanar waveguide signal (S) and ground (G) tracks are labelled. Inset of (b) shows a schematic view of a fabricated device.

### 4.3.4 Experimental Results and Discussion

The current-voltage characteristics of the devices are measured using an Agilent B1500A semiconductor device analyser and a pair of Kevin probes on a Cascade auto-prober station. Unfortunately, short devices with $L_{ac}<1.4$ μm breakdown easily due to overheating. Nevertheless, experimentally measured current-voltage characteristics for devices with $L_{ac}$ ranging from 1.45 μm to 4.0 μm are plotted in Figure 4-34.

The RF output spectra of these devices are studied using a spectrum analyser (Agilent 4448A), the operating range of which is extended using external mixers. Appropriate GSG probes with either an external or an integrated bias-T was used to apply a DC anode-cathode voltage to the devices and probe the resulting AC oscillation at different frequencies. For devices oscillating below 75 GHz, the spectrum analyser by itself, or in

conjunction with a *V*-band (50-75 GHz) mixer (Farran Technology WHMP-15) is used to measure the spectrum. In order to make measurements in the *W*-band (75-110 GHz) the spectrum analyser is fitted with a *W*-band mixer (Farran Technology WHMP-10).

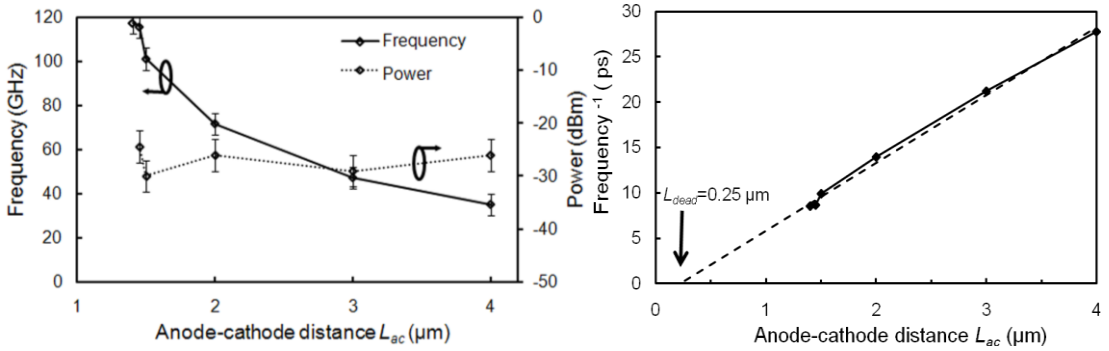


**Figure 4-36** (a) Variation of output power and frequency versus anode-cathode distance for the $In_{0.23}Ga_{0.77}As$ planar Gunn diodes; (b) linearly extrapolating the inverse frequency curve to determine the "dead" zone of the devices.

The fabricated devices, with $L_{ac}$ in the range 1.4 μm to 4.0 μm, exhibit oscillation frequencies between 36 GHz and 118 GHz (Figure 4-36a). Typical bias voltages for $In_{0.23}Ga_{0.77}As$ based planar Gunn diodes are on the order of 3 V for the shortest devices, extending up to 5.5-6 V for the devices with largest $L_{ac}$. As expected, the devices with smaller $L_{ac}$ oscillate at higher frequency. The measured power is, on average, approximately -25 dBm and relatively invariant as a function of $L_{ac}$. These results still indicate that $In_{0.23}Ga_{0.77}As$-based planar Gunn diodes have slightly better performance than GaAs-based planar Gunn diodes of similar design.

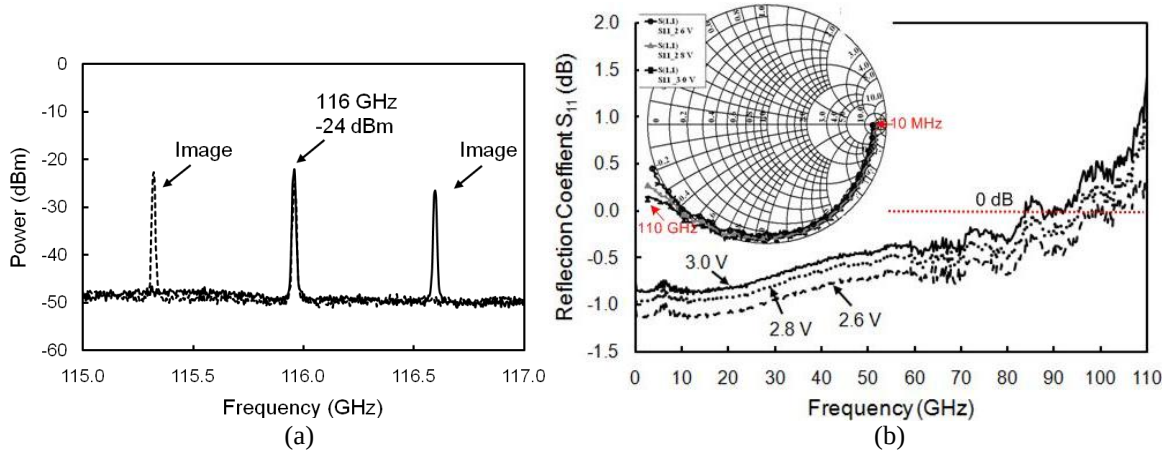


**Figure 4-37** Measured spectrum and reflection coefficients of the 1.45 $In_{0.23}Ga_{0.77}As$ device. (a) Spectrum analyser measured spectrum that shows an oscillation tone at 116 GHz when the device is biased at 2.96 V and the power is measured by using a *W*-band power meter setup, (b) VNA measured reflection coefficients in a Smith chart (inset) and s rectangular chart at 2.6 V, 2.8 V, and 3.0 V. The measured reflection coefficients also confirm there is no oscillation below 80 GHz for this device.

A device with $L_{ac}$ = 1.45 μm that is biased at 2.96 V and a current of 30.14 mA shows a peak power of -24 dBm at a frequency of 116 GHz . It is further confirmed by using a VNA measurement technique that the 116 GHz oscillation is the fundamental oscillation rather than a harmonic of some lower mode [172]. The measured phase noise of this device is -71 dBc/Hz at 10 MHz offset. The effect of varying bias voltage on the frequency and power of this device has also been investigated as shown in Figure 4-38. The power output rises slightly as the bias is increased towards 2.96 V, before decreasing again at higher voltages. On the other hand, the frequency decreases slightly (150 MHz/V) as the voltage increases. The latter phenomenon has also been observed in conventional GaAs-based vertical Gunn diodes [229] as well as MMIC-vertical Gunn diodes [230].

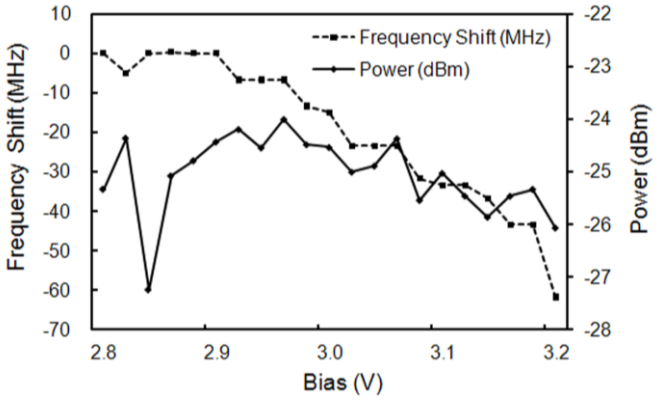


**Figure 4-38** Frequency shift and power variation as bias voltage is altered for a 1.45 μm $In_{0.23}Ga_{0.77}As$ planar Gunn diode.

One of the explanations for frequency changing with $V_{ac}$ is based on the Gunn effect itself. The effect relies on electrons accelerated in an electric field decelerating as the electric field in the channel increases, scattering the fast electrons from the $\Gamma$-valley into the high effective mass $L$-valley. As a consequence, the slow electrons are caught up by the fast electrons emerging from the cathode, leading to the formation of a Gunn domain and therefore a reduction in current. Once a Gunn domain reaches the anode and is removed from the channel, the current returns to its original level; meanwhile, another Gunn domain starts forming near the cathode. This generates a complete cycle of oscillation and the oscillation frequency is inverse to the transit time of the domain between the cathode and the anode. In order for the oscillation frequency to decline it is necessary for the rate of domain formation and transport to be reduced. The first explanation, therefore, for the behaviour we observe is that in our devices, an increase in bias voltage increases the electric field in the channel so that electrons scatter and decelerate more rapidly, or earlier.

This has the effect of reducing the average velocity of electrons, hence domains, in the channel, leading to a lower frequency of oscillation.

An alternative explanation is that the change in bias leads to a modification of the device impedance. This explanation is consistent with our high frequency observations (below resonance) as seen in inset of Figure 4-37. However the data offers no detailed physical explanation of the origin of the effect.

Finally, we suggest that there may be a small amount of channel-length modulation occurring in the device as a function of $V_{ac}$. For devices with large $L_{ac}$ the oscillation frequency, $f$, is approximately determined by $L_{ac}^{-1}$. However, as can be clearly seen from Figure 4-36a. for small $L_{ac}$, this relationship fails. This is because there is a small "dead" zone in the channel, so that we find

$$f = \frac{v}{L_{ac} - L_{dead}} \tag{4.3.1}$$

This is entirely consistent with the aforementioned explanation for frequency variation based on the alteration of the average electron drift velocity, $v$. By linearly extrapolating the graph of $f^{-1}$ vs $L_{ac}$ to $f^{-1} = 0$ (Figure 4-36b), we estimate a typical $L_{dead}$ for the devices of 0.25 μm that is in good agreement with earlier work for vertical Gunn diodes. If channel length modulation is the origin of the variation in frequency with $V_{ac}$, the results would be consistent with a change in $L_{dead}$ with bias. This behaviour is consistent with a movement in the domain nucleation point towards the cathode with increasing bias voltage. This may occur if electrons in the channel heat more rapidly, leading to earlier onset of domain formation. In effect, the dead zone length is decreased, giving rise to a lower frequency of oscillation. The channel length modulation and early scattering model are thus in fact the same.

### 4.3.5 Summary

$In_{0.23}Ga_{0.77}As$-based planar Gunn diodes constructed in pseudomorphic structures that can generate Gunn oscillations in the millimetre wave frequency range have been demonstrated. Although only slight better performance in terms of oscillation frequency and output power

has been found in these devices when compared to GaAs-based diodes, this work establishes $In_{0.23}Ga_{0.77}As$ as an alternative semiconductor material for planar Gunn devices.

## 4.4 Conclusion

In this chapter, the design, modelling and characterisation of planar Gunn diodes with modified or new designs for RF power enhancement were discussed. The single channel GaAs based design with four δ-doping layers were proved to enhance power and frequency performance. Further modification of the device design by introducing additional channels, particularly 7 channels have shown significant RF power improvement by almost 4 orders although still not all channels are actively participating. One drawback of seven-channel devices is lower frequencies than signal channel devices. However, this may be compensated by using alternative materials, such as $In_xGa_{1-x}As$. As an initial exploration into this material system, $In_{0.23}Ga_{0.77}As$ has been investigated. Slight improvements in power and frequency than similar structures used for GaAs may further trigger experiments on similar materials with higher indium composition due to its high mobility.

In addition, the Ohmic contact and the composite contact design have been introduced. With a short Schottky overlayer from the composite contact, the high electric field near the anode contact edge is effectively suppressed. Premature breakdown of planar Gunn diodes is therefore avoided. This prolongs the lifetime of planar Gunn diodes.

# CHAPTER 5

# EXPLORATION OF DEVICE FUNCTION AND BEHAVIOR

Planar Gunn diodes have been systematically described in the previous chapter. The general electrical properties and spectrum characteristics of planar Gunn devices have been discussed in detail. As emerging Gunn devices, planar Gunn diodes have also exhibited many special features, such as multiple-domain oscillations [231] and self-oscillating mixing effect [232]. These features may lead to future potential applications. In addition, it has also been found that planar Gunn devices are sensitive to light. Oscillation frequency and power vary subject to the change of light intensity. Heat may limit devices' power and frequency performance. However, by simply thinning and metallising the semi-insulating substrate, heat dissipation can be partially improved.

In this chapter, the multiple-domain oscillations will be first discussed in Section 5.1. It is followed by an investigation on the self-oscillating mixing effect of planar Gunn devices in Section 5.2. In Section 5.3, the heat effect on power and frequency performance of planar Gunn devices is examined and two examples are given to prove that processing the substrate, for example, thinning and metallising the substrate, could be one of the solutions to solve the overheating problem. Finally, the effect of illumination and the stability of planar Gunn diodes are studied in Sections 5.4 and 5.5, respectively.

## 5.1 Multiple-domain Oscillations

### 5.1.1 Introduction

Multiple oscillations in a single planar Gunn diode have been observed. As an example, a device fabricated in the AlGaAs/GaAs quantum well structure (Wafer C114) showing multiple oscillations at 29 GHz, 33 GHz and 35 GHz is demonstrated here. The device has a single channel and one δ-doping layer on each side of the channel. The anode-cathode distance ($L_{ac}$) is 4 μm and device width is 60 μm. A schematic view of device layer structure was shown in Chapter 4 and simplified here as Figure 5-1 for convenience.

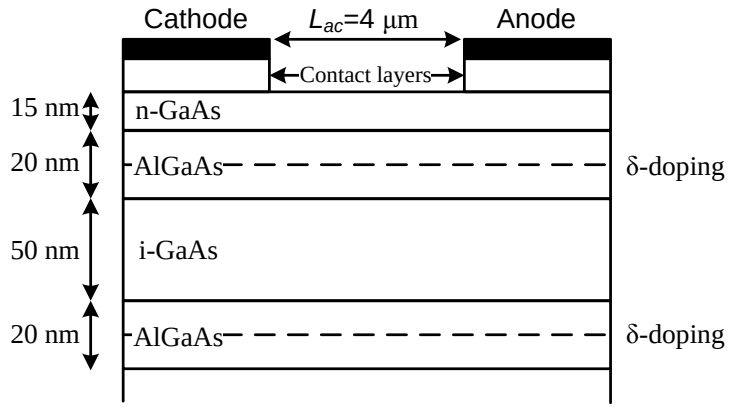


**Figure 5-1** Illustration of the epitaxial layer structure of the planar Gunn diode used for investigating multiple oscillations.

### 5.1.2 Experimental Results

The material growth and device fabrication were described in Chapter 4 and are not repeated here. Prior to making RF measurements, the device was probed at DC bias to evaluate its current-voltage characteristics using a semiconductor parameter analyser (Agilent 4145B). The results are plotted in Figure 5-2. The RF measurements were carried out using a *V*-band on-wafer probe attached to a 40 GHz spectrum analyser (Agilent 8564EC). As the applied voltage $V_{ac}$ reached 7.4 V, an oscillation of 29 GHz was first observed. An increase in $V_{ac}$ to 8.3 V reduced the frequency of oscillation to 27.8 GHz. At the same time a second oscillation started appearing at 33 GHz when $V_{ac}$ was 7.7 V. A third oscillation at 35 GHz showed up when $V_{ac}$ was 8 V. Figure 5-2 shows the measured oscillation frequencies as a function of the applied bias $V_{ac}$.

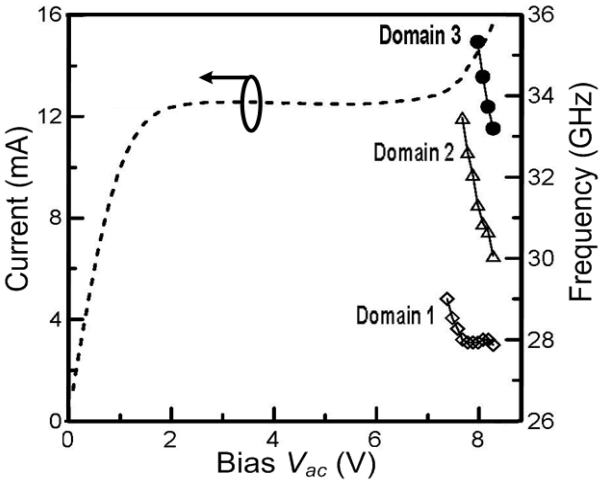


**Figure 5-2** Measured DC IV characteristics and oscillation frequencies versus bias voltage for a 4 μm GaAs-based single channel planar Gunn diode.

The current voltage curve of the device, as illustrated in Figure 5-2 has an "N" shape. It shows an apparent increase of current at high $V_{ac}$ (>7 V) that corresponds to the bias voltages required for all oscillations. The breakdown-like characteristic that is fully recoverable is not believed to be associated with the conventional breakdown mechanisms such as impact ionisation that are known to perturb Gunn domains [233]. However, the increase in current at high applied bias could be explained by considering an increase in channel carrier density due to carrier injection giving barrier injection transit-time diode-like characteristics [234].

### 5.1.3 Discussion

The first oscillation at $f = 29\,\text{GHz}$ can be easily explained using the classic transit-time mode oscillation of a Gunn diode. The domain velocity, $v_{domain}$, is assumed to be $10^7$ cm/s. Using this velocity it is estimated that for a Gunn diode with an active transit length in the range 3.0—3.5 μm that a corresponding range of oscillation frequencies of 29—27.8 GHz would result. The length of the available transit region varies as a function of the bias voltage, as discussed in the previous chapter (Section 4.4.5), giving rise to the observed tuning effect. It is estimated that the dead zone, in which no domain transit occurs, is of the order of 0.5—0.7 μm for this device. This is a well-known Gunn device phenomenon, i.e. the dead zone shrinks as the $V_{ac}$ is increased, thereby lowering the frequency of oscillation. However, the observation of the second and third peaks is more puzzling since they behave as if they are associated with Gunn domains, but with shorter transit lengths than expected for a device of this length.

Two possible explanations have been considered for the observed phenomenon. It could be speculated that there is more than one domain nucleation site in the device between the anode and the cathode. As a consequence, the domains originating from the different nucleation sites would have different transit distances resulting in different oscillation frequencies. Thus, the second observed oscillation that starts appearing at 33 GHz corresponds to a total domain transit length of 3 μm using the same domain velocity ($v_{domain} = 10^7$ cm/s). The third oscillation starting from 35 GHz indicates the domain transit distance is 2.8 μm assuming the third domain still travels at the same speed as the other two domains. The three domain transit lengths are illustrated against bias in Figure 5-3.

However, it is believed that the existence of such well defined nucleation sites giving rise to well resolved frequencies is unlikely. A random scatter of nucleation sites would be more likely to give rise to a spread in transit times that would manifest themselves as phase noise around a single tone in the spectrum. Furthermore, the multiple oscillations phenomenon is consistently observed from device to device suggesting a more systematic origin.

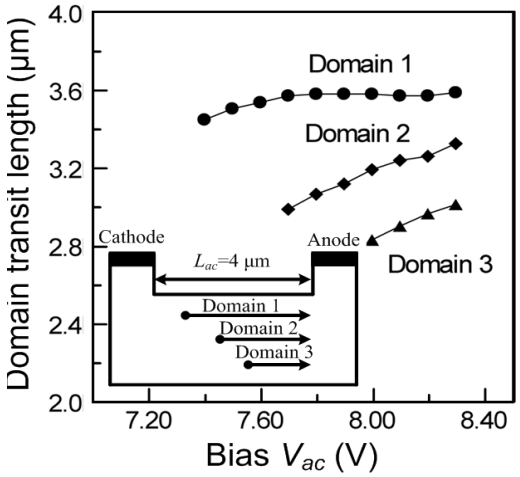


**Figure 5-3** Estimated transit lengths versus applied bias $V_{ac}$ for three Gunn domains in a 4 μm planar Gunn diode.

The second explanation is that electron injection into layers beneath the intended active layer takes place due to the higher applied bias voltage required for the device with unalloyed contacts. This is shown schematically in the inset of Figure 5-3 where multiple domains form in parallel in the quantum well structures, and the transit length of each domain varies according to the depth. Domain 1 nucleates at the top "channel" that is close to the device surface under relatively lower bias voltage. The domain 1 travels longer distance to reach the anode than domains 2 and 3 do, therefore a lower frequency (e.g. 29

GHz) is observed. Domain 2 nucleates at a slightly deeper level when the bias voltage is increased and travels shorter distance to reach the anode where it disappears than domain 1 does. Thus a slightly higher frequency (e.g. 33 GHz) is observed. Similarly, domain 3 starts forming at even lower depth of the channel and travels the shortest distance among all the three domains. This shortest distance that domain 3 has travelled certainly gives the highest frequency (e.g. 35 GHz) as observed. The phenomenon may also account for the observed current-voltage characteristics.

### 5.1.4 Multiple Oscillations in $In_{0.23}Ga_{0.77}As$-based Planar Gunn Diodes

Similar multi-oscillation behaviour has also been observed in $In_{0.23}Ga_{0.77}As$ based planar Gunn diodes. A 3 μm device with 60 μm width was tested using a VNA that was calibrated between 10 MHz and 67 GHz with 401 points. The measured port 1 reflection coefficients ($|S_{11}|$) at 4.3 V, 4.4 V and 4.5 V are shown in Figure 5-4. Two oscillations at 43.72 GHz and 56.95 GHz were detected by the VNA within the operating frequency range when the bias was 4.3 V. When the bias was increased to 4.4 V, the first and the second oscillations decreased by 1.34 GHz and 0.67 GHz, respectively, meanwhile another oscillation appeared at 67 GHz. Once the bias voltage reached 4.5 V, all three oscillations shifted further downwards by 1.0 GHz, 0.5 GHz, and 0.5 GHz, respectively.

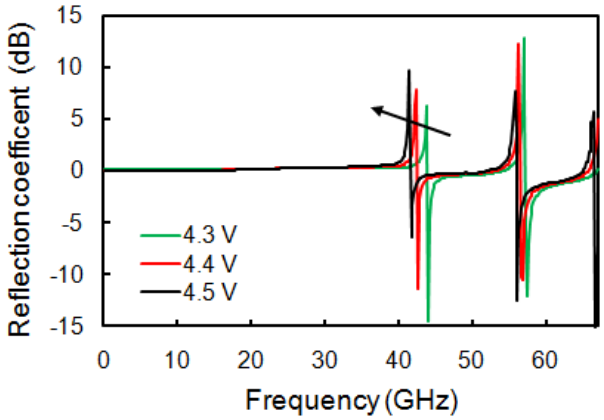


**Figure 5-4** Measured magnitude of reflection coefficient $|S_{11}|$ (dB) of a 3 μm $In_{0.23}Ga_{0.77}As$-based planar Gunn diode using a VNA calibrated between 10 MHz and 67 GHz. Three oscillation peaks that are not in harmonics show down-shifting frequencies as the bias voltage is increased.

Although oscillation frequencies, biasing conditions, and so on are different for planar Gunn diodes using GaAs as a channel and $In_{0.23}Ga_{0.77}As$ as a channel, similar multiple oscillation phenomena have been observed. The multiple oscillations start being observed once the bias voltage reaches a certain value and the oscillation frequencies shift downwards as the bias voltage increases.

### 5.1.5 Summary

Experimental observations of multiple oscillations were found in early Gunn devices [235, 236]. Some theoretical studies for multiple Gunn domains operation have also been studied [237]. However, multiple oscillation frequencies in GaAs and $In_{0.23}Ga_{0.77}As$-based planar Gunn diodes having quantum-well structure have been observed for the first time. Our current understanding is that this phenomenon arises as a consequence of electron injection into deeper device layers than intended. It is possible that such devices, if fully developed, could have a potential application as multiple frequency generators.

## 5.2 Self-oscillating Mixing Effect

Gunn devices exhibit intrinsic nonlinearities of conductance and capacitance characteristics that make it theoretically possible to design frequency mixers [238, 239]. Conversion gain may also be achieved due to the negative differential resistance [240]. This multi-functionality permits the concept of compact self-oscillating mixers.

### 5.2.1 Experimental Setup

In order to explore the possibility of the self-oscillating mixing effect in planar Gunn devices, a planar Gunn diode test structure was configured in a series circuit topology by trimming the ground metal along the cathode mesa edges as shown in Figure 5-5. This topology essentially allows the device to be used in a two port configuration, where an RF input can be applied and the down-converted IF signal extracted from different ports.

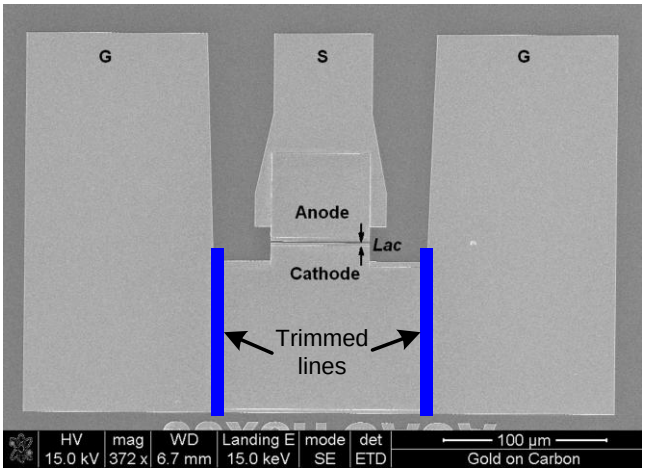


**Figure 5-5** SEM image of the device test structure. Two lines along the mesa edges at the cathode side of the device are trimmed using a high power laser. Coplanar waveguide signal (S) and ground (G) tracks are labelled.

The planar Gunn diode having a nominal $L_{ac}$ of 3 μm, width of 60 μm and oscillating at around 30 GHz was chosen for the experiment in order to demonstrate the self-mixing effect within a single swept measurement setup (the stand-alone spectrum analyser Agilent E4448A measures 3 Hz to 50 GHz with a single frequency sweep).

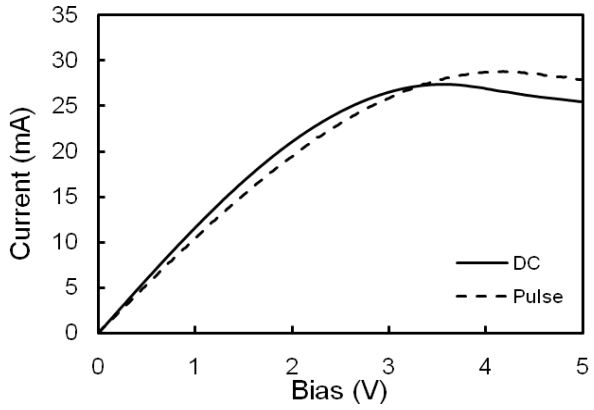


**Figure 5-6** Measured DC and pulsed IV characteristics of the device before it was trimmed.

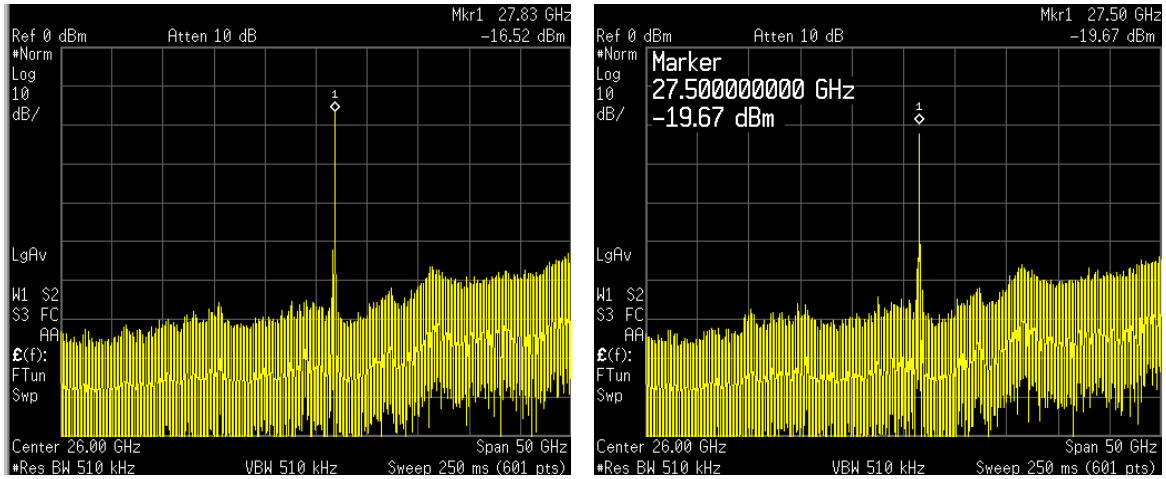


(a) (b)

**Figure 5-7** Measured spectrum of the planar Gunn device for demonstration of self-oscillating mixing effect (a) before it was trimmed and (b) after it was trimmed.

Figure 5-6 illustrates the DC and pulsed IV (pulse width is 0.5 ms and period is 100 ms) characteristics of the diode before it was trimmed. Obvious NDR is easily identified on both IV characteristics. A slight increase of current level from the pulsed measurement due to the reduction of heat is seen. Figure 5-7 shows a comparison of the RF performance for the same diode before and after being trimmed. The measured frequency and RF power decreased slightly by 0.33 GHz and 2 dB, respectively while the bias voltage for the same current level increased by 0.7 V. The increased bias voltage for the same level current and

the reduction in RF power result from the added measurement setup components at the cathode side of the diode, e.g. the probe, cable and bias-tee, which consume some DC bias.

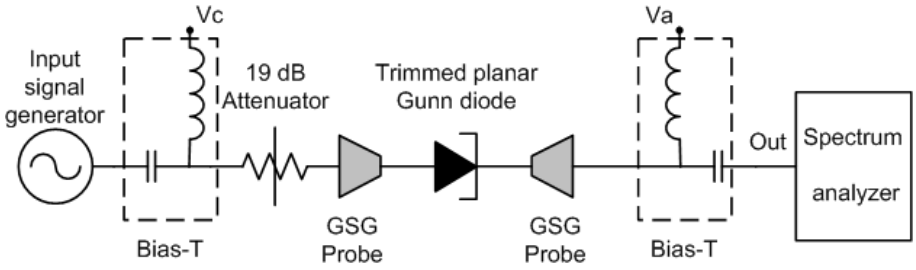


**Figure 5-8** Experimental setup of the self-oscillating mixer using a planar Gunn diode.

Figure 5-8 shows the experimental setup used to demonstrate the self-mixing effect with a planar Gunn diode. The diode was biased through two bias-tees (Anritsu 250V) using two DC power supply units. The power supply connecting to the left bias-tee acted as a ground i.e. $V_c$ = 0 V and the power supply connecting to the right bias-tee was where the diode bias ($V_a$) was applied from. The two power supplies had a common ground. The input millimetre-wave signal (RF) was applied from an external signal generator (Wiltron 68369B) to the cathode side of the Gunn diode through a GSG probe. The output (IF) was directly extracted from the anode side with another GSG probe and measured on the spectrum analyser. In fact, all three frequency components (RF, LO, and IF) could be displayed on the spectrum analyser at the same time. Three wide band attenuators (DC-50 GHz) contributing 19 dB attenuation in total were applied between the probe and the bias-tee at the cathode-side to protect the signal generator from being damaged by any reflected signals. The attenuators also provide good matching between the bias-tee and the probe. The diode was biased at 4.2 V and 24.5 mA yielding an oscillation with an output power of -19.7 dBm at 27.5 GHz as shown in Figure 5-7b.

### 5.2.2 Results and Discussion

The signal generator was first set to output a signal ( $f_{RF}$ ) with a power of 0 dBm at 30 GHz that is 2.5 GHz higher than the oscillation frequency ( $f_{LO}$ ) of the planar Gunn diode. Figure 5-9 shows the measured output spectrum which clearly indicates the input signal, local oscillator signal from the Gunn diode, and the down-converted mixing product IF ( $f_{IF} = f_{RF} - f_{LO} = 2.5\,\text{GHz}$). Due to limitations of the spectrum analyser the up-converted mixing product ( $f_{up} = f_{RF} + f_{LO} = 57.5$ GHz) was not able to be observed. For this proof-

of-concept, no attempt was made to match the port embedding impedances to achieve minimum conversion loss performance. Taking into account losses through the input network, the measured conversion loss from this self-oscillating mixer demonstrator is around 20±2.5 dB.

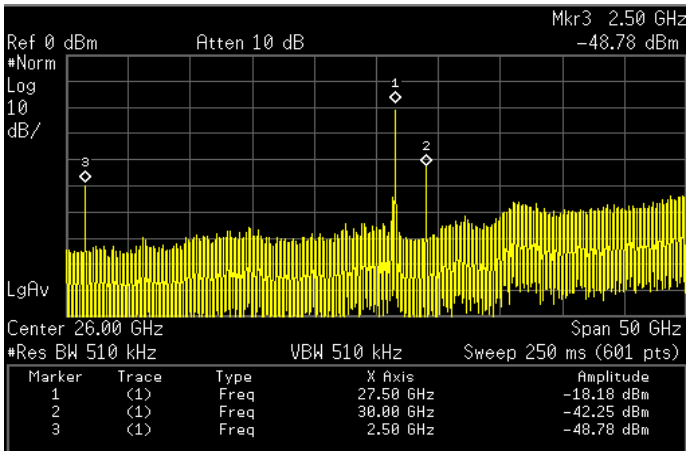


**Figure 5-9** Measured output spectrum from the self-oscillating mixer using a planar Gunn diode. Markers 1, 2 and 3 indicate the oscillation frequency of the diode, the external input signal, and the down-converted IF signal, respectively. (Marker 1: 27.5 GHz, -18.2 dBm; Mark 2: 30 GHz, -42.3 dBm; Marker 3: 2.5 GHz, -48.8 dBm).

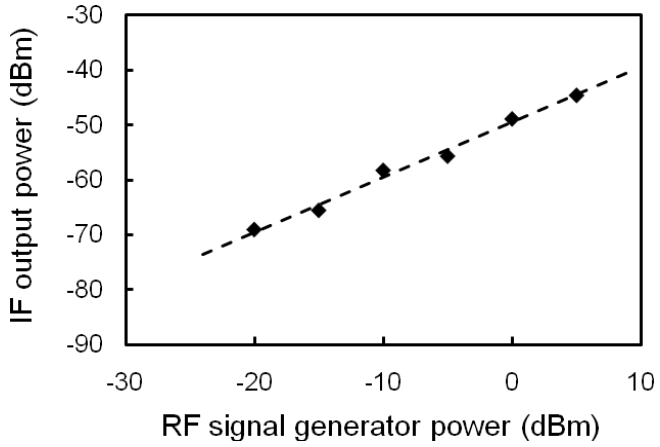


**Figure 5-10** Linearity test of the self-oscillating planar Gunn diode mixer versus input RF power at 30 GHz. The system insertion loss was not excluded.

Secondly, the power level from the external signal generator was swept from -20 dBm to +5 dBm by steps of 5 dB at a fixed frequency of 30 GHz in order to test the mixer linearity. The system insertion loss was not excluded. The variation of the output IF power level at 2.5 GHz is shown in Figure 5-10. It can be clearly seen that the mixer shows excellent linearity as the power of the incident signal varies in the 25 dB ranges.

Thirdly, the input RF power to the diode or the output power of the signal generator was fixed at 0 dBm but the frequency was varied from 15.5 GHz to 40.2 GHz in random steps.

The measured IF power ( $P_{IF}$ ) of the self-oscillating planar Gunn diode mixer versus input frequency is shown in Figure 5-11. The system insertion loss ( $P_{SL}$ ) has also been measured in the corresponding frequency range. Therefore the conversion loss ( $P_{CL} = |P_{IF} + P_{SL}|$ ) of the planar Gunn diode mixer is also plotted in Figure 5-11.

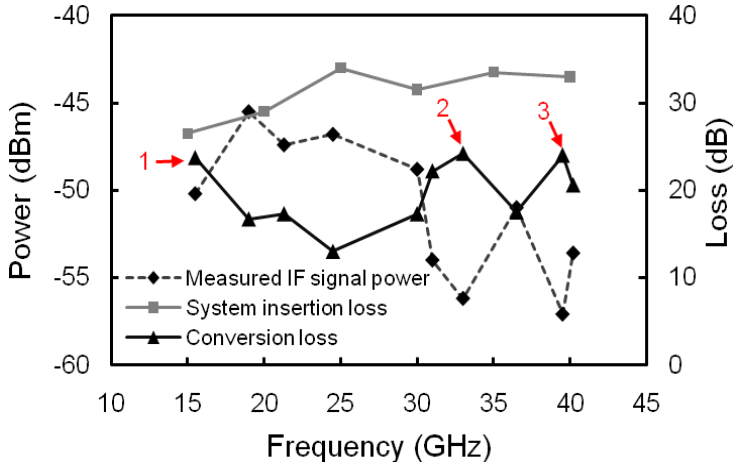


**Figure 5-11** Measured IF power, system insertion loss and conversion loss of the self-oscillating planar Gunn diode mixer versus input RF frequency. Markers 1, 2, 3 indicating three conversion loss maxima correspond to 23.7 dB at 15.5 GHz, 24.2 dB at 33 GHz and 24 dB at 39.5 GHz, respectively.

It can be clearly seen that the conversion loss reaches a minimum of 13 dB at 24.5 GHz which is near the LO (27.5 GHz) and increases as the RF frequency spreads in both higher and lower frequencies of the LO. It reaches peaks (>20 dB) at points 1, 2 and 3. The fluctuating phenomenon of conversion loss can be explained by observing the change of measured spectrum at those RF points. It has been shown in Figure 5-9 that there are three peaks corresponding to $f_{RF}$ , $f_{LO}$ , and $f_{IF}$ ($=|f_{RF} - f_{LO}|$) in the frequency range between 3 Hz and 50 GHz displayed on the spectrum analyser screen when $f_{RF}$ was close to $f_{LO}$ . However, as $f_{RF}$ is swept away from $f_{LO}$ in the direction of higher frequencies or lower frequencies, or in another word as $f_{IF}$ increased, the spectrum changed dramatically and more peaks were seen on the spectrum analyser.

Figure 5-12 shows the measured spectra of the mixing effect of the planar Gunn diode for a number of incident RF frequencies, e.g. 15.5 GHz (Figure 5-12a), 19 GHz (Figure 5-12b), 21.3 GHz (Figure 5-12c), 24.5 GHz (Figure 5-12d), 30 GHz (Figure 5-12e), 31GHz (Figure 5-12f), 33 GHz (Figure 5-12g), 36.5 GHz (Figure 5-12h), 39.5 GHz (Figure 5-12i), and 40.17 GHz (Figure 5-12j), respectively. One can see that when $f_{RF} = 30$ GHz (Figure 5-12e), there are only three peaks corresponding to $f_{LO}$ (27.5 GHz), $f_{RF}$ , and $f_{IF}$ (2.5 GHz)

on the display of the spectrum analyser. However, as $f_{RF}$ decreases or increases bidirectionally with reference to the $f_{LO}$, an additional mixing product $f_{IF}^{''}$ (the frequency difference between the second harmonic oscillation of the diode, $2f_{LO}$ and the $f_{RF}$) appears initially. This phenomenon can be observed when $f_{RF}$ is 19.0 GHz, 21.3 GHz, 24.5 GHz, 30.0 GHz, 31.0 GHz, 33.0 GHz, or 36.5 GHz. The conversion loss increases as the $f_{RF}$ departs from the $f_{LO}$ as shown in Figure 5-11 and it reaches maxima when $f_{RF} = 15.5\,\text{GHz}$ and 40.17 GHz where other mixing products, such as $f_{LO} - f_{IF}^{'}$, $f_{LO} + f_{IF}^{'}$, $f_{IF}^{''} - f_{IF}$, and $f_{IF} + f_{IF}^{'''}$ start appearing. The aforementioned discussion may have established that the mixing effect in Gunn devices has the best performance when the $f_{RF}$ is close to $f_{LO}$.

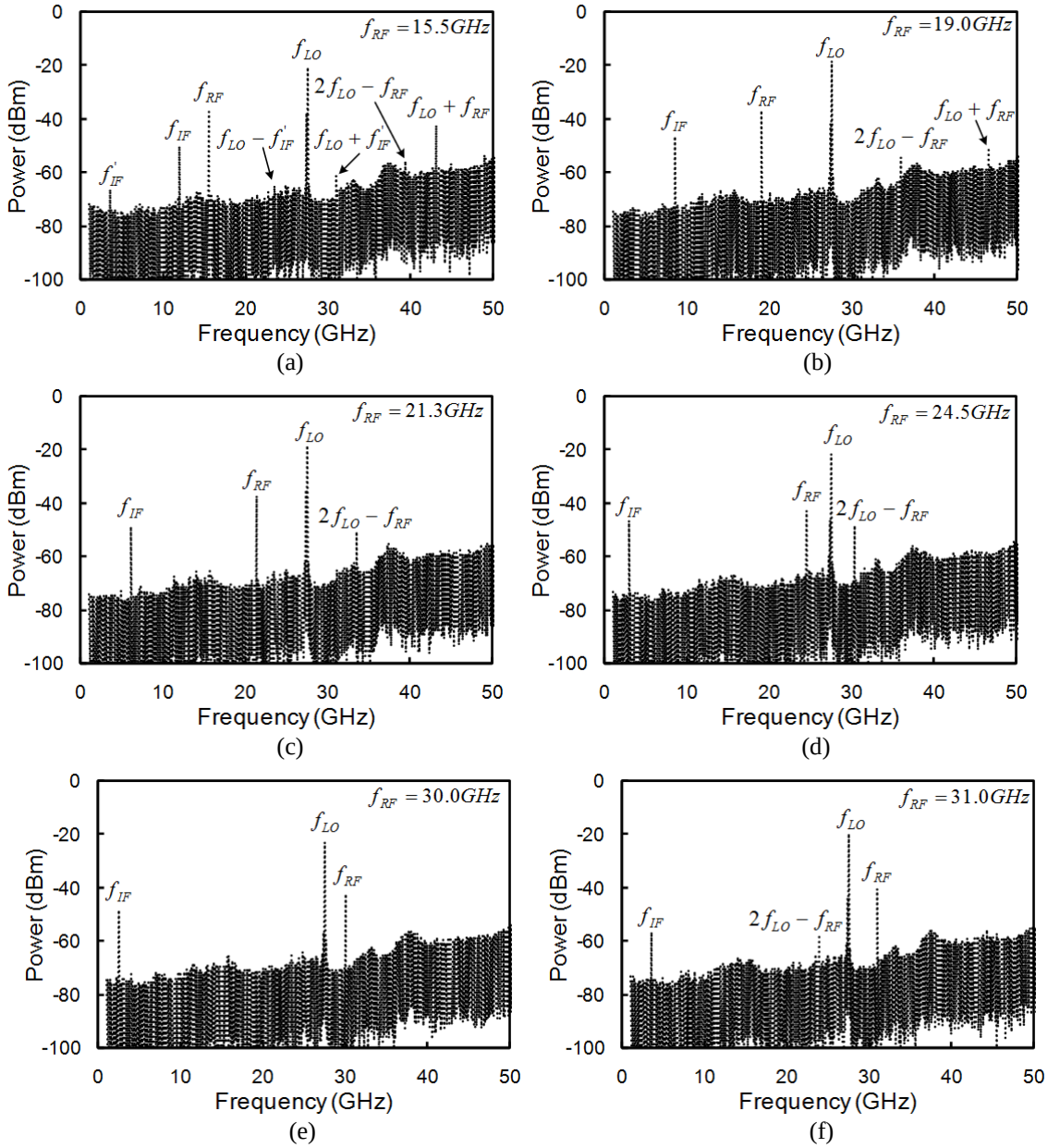

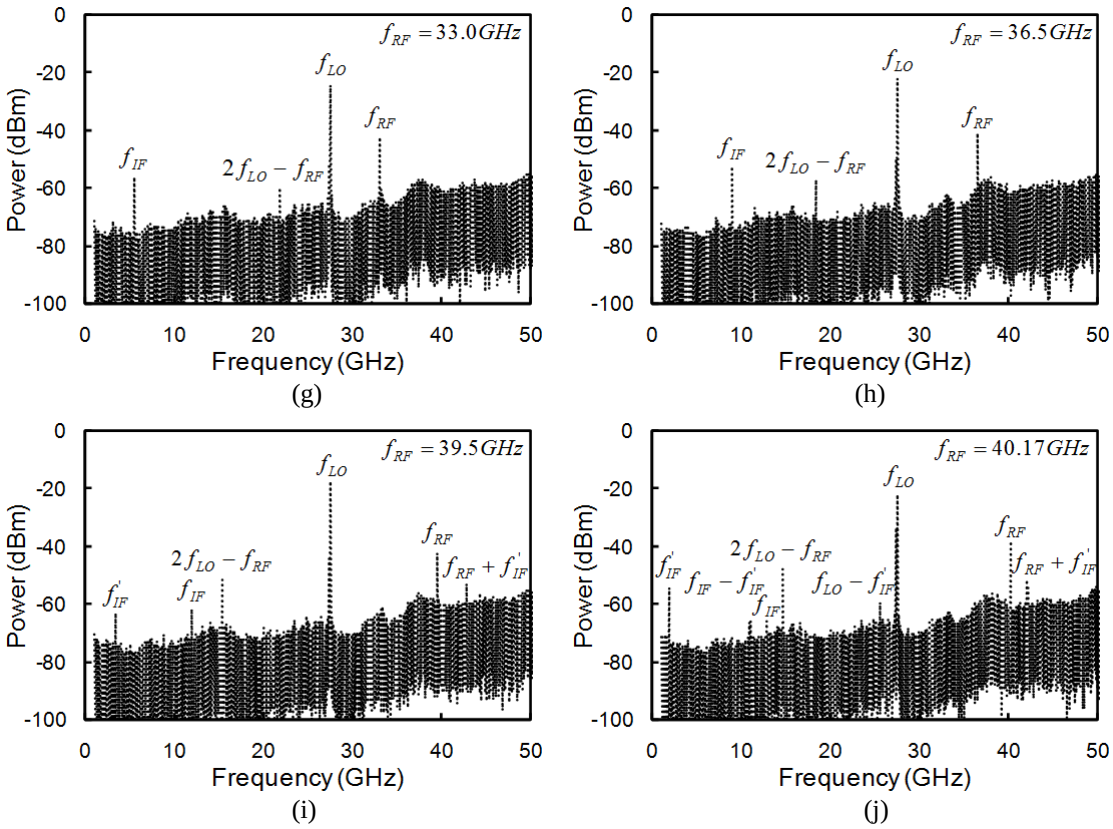


**Figure 5-12** Spectra of Gunn diode mixing effect regard to different RF frequencies at a fixed power level.

### 5.2.3 Summary

It has been demonstrated that planar Gunn diodes can function as self-oscillating mixers. The measured conversion loss from this self-oscillating mixer demonstrator is better than 20 dB. Improved conversion loss performance can be achieved by implementing matching circuits at input and output ports of the diode. The device also shows good linearity while the power level from the external signal generator was swept from -20 dBm to +5 dBm at a fixed frequency of 30 GHz. In addition, due to the existence of harmonic oscillations, the RF signals are mixed with both the fundamental and harmonic oscillations. Therefore, multiple mixing products were observed. Nevertheless, this proof-of-concept opens up the possibility for realising compact self-heterodyne front-ends for microwave applications.

## 5.3 Heating Effects in Planar Gunn Devices

### 5.3.1 Introduction

It is well-known that heat is one of the factors limiting Gunn devices' performance [47, 75]. Especially for vertical Gunn devices a lot of heat is generated when several hundreds of

mAs of current passes through the devices. Since GaAs has a low thermal conductivity (i.e. 55 W/(m·K)) [76], its poor heat dissipation capability can not overcome the excessive heat. Vertical Gunn devices are commonly fabricated in a cylindrical geometry and have the contacts on the top and bottom. In such a configuration the devices' mesa is surrounded by air. Due to the low heat conductivity (0.025 W/(m·K)) of air, the heat generated within the devices may eventually melt the contacts and cause device failure. One common solution to this problem is to add a heat sink at the bottom of the Gunn diode as previously shown in Figure 2-2 so that the heat can be conducted away via the heat sink. The most widely used materials for the heat sink are copper and diamond that have thermal conductivities of 401 and 900-2320 W/(m·K), respectively. Alternatively, a pulsed bias can be used for thick or high power devices to avoid the overheating-induced device failure.

For planar Gunn devices, the heat limitation on the device performance may not be as obvious as that of vertical devices. The reasons are twofold. Firstly, from the structure point of view, the planar Gunn devices have one side (top side) exposed to the air and the other side (bottom side) contacting the semi-insulating GaAs substrate (Strictly speaking, the current conducting channel is sandwiched by two AlGaAs layers). Therefore the substrate (or AlGaAs layers) is considered as a heat conductor and although they do not have high thermal conductivity it is still better than air. Thus, unlike vertical Gunn diodes that have only air surrounding the channel, for planar Gunn diodes at least one side of the channel aids to conduct the heat. In addition, because the bottom side of the device contacts the substrate, a specific heat sink if needed can be applied next to the substrate so that the heat can be conducted away from the bottom. Secondly, the main limitation of heat effect on vertical Gunn diodes is that a high volume of current that may reach to several amperes in order to achieve desirable performance (harmonic extractions for W-band or above applications) concentrates within the cylindrical device. However, the current in a planar Gunn diode is constrained to flow in a quasi-2D sheet that is distributed along the width of the anode-cathode region. The spread-over of the current in planar Gunn devices allows more surface of current path (thin) exposed to cooler regions and therefore reduces the possibility of overheating.

Nevertheless, it is still necessary to investigate any effects on the spectrum and power performance of planar Gunn devices as temperature changes. In this section, an

experiment using a temperature-controlled probe station to evaluate the effect of temperature on Gunn diode behaviour is devised. It is then followed by an example showing how heat dissipation of planar Gunn devices is possible by simply thinning and metallising the substrate.

### 5.3.2 Investigating Heat Effect on Power and Frequency Performance of a Planar Gunn Diode

The probe station used for this experiment has a temperature control unit (Series 800 Temperature controller, Alpha Omega Instruments) that was connected to a temperature sensitive chuck. The temperature on the surface of the chuck had a controllable range from -10 ℃ to 60 ℃. In addition, an external thermometer was also used to confirm the actual temperature readings on the chuck surface.

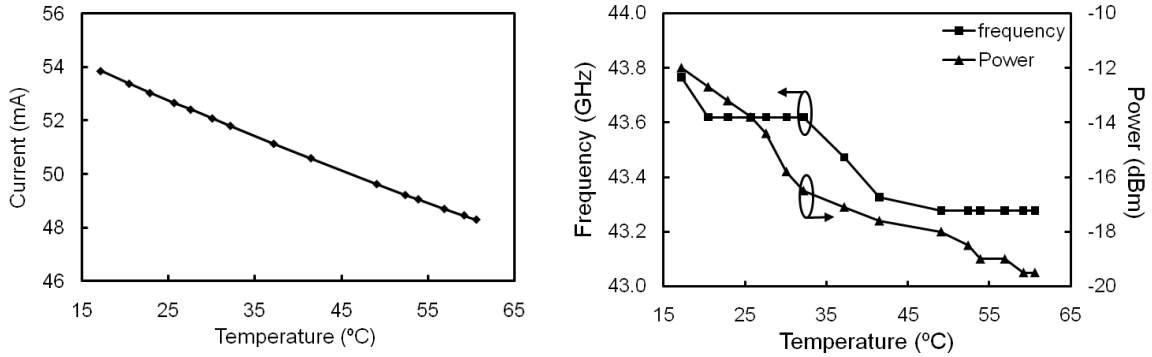


(a) (b)

**Figure 5-13** Variations of (a) Current and (b) Frequency and power as chuck surface temperature changes from 17.2 ℃ to 60.6 ℃.

The sample used was from Wafer C605 which has 7 GaAs channels. The anode-cathode distance $L_{ac}$ and width of the device were 2 μm and 60 μm. A standalone spectrum analyser measurement setup was used for this experiment. The V-band probe permits an application for the intended temperature range according to the manufacturer specification sheet. Since the experiment was carried out in an open area, the moisture in air and ambient temperature were not strictly controlled. To reduce any moisture induced on the surface of the chuck at low temperature, the actual temperature for this experiment was set between 17.2 ℃ and 60.6 ℃. The experimental results are plotted in Figure 5-13. One can see that current, frequency, and power decrease as the temperature increases. This is consistent with Monte-Carlo simulation [176] and the work of others [241]. The current varies linearly at a rate of 128 μA/ ℃ as the temperature varies. The power decreases

monotonically from -12 dBm to -19.5 dBm as the temperature rises from 17.2 ℃ to 60.6 ℃. By contrast the frequency shifts downwards by less than 0.5 GHz.

Since the relationship between electron drift velocity and absolute temperature, $T$ , (300 $K$-600 $K$) is written in the modified version of Equation 2.3.13 as [241]

$$v_{drift}(E,T)=\frac{2.25\times10^{9}E}{T}\left\{\left[1+\frac{0.265(E/E_0)^3}{(1-5.3\times10^{-4}T)}\right]\Big/\left[1+\left(\frac{E}{E_0}\right)^4\right]\right\} \tag{5.3.1}$$

The increase of temperature leads to increase of electron scattering rate, and the increase of electron scattering rate has a decreasing effect on the electron mobility or electron drift velocity as seen in Equation 5.3.1. The current therefore decreases as the temperature increases. The decrease of electron mobility and drift velocity, on the other hand, leads to the time that the Gunn domains take to travel between cathode and anodes being longer. Thus the oscillation frequency decreases as temperature rises. An alternative equivalent circuit method reported in [242] can be used to analyse the temperature dependent frequency drift phenomenon. The power or the DC-RF conversion efficiency decrease is due to the reduction of peak to valley current ratio as temperature increases [243].

### 5.3.3 Thinning and Metallising the Semi-insulating Substrate

As was demonstrated in the last section, the rise of temperature from the bottom of the substrate deteriorated the power performance of planar Gunn devices. Therefore, it is necessary to improve heat dissipation and reduce the temperature to achieve desirable performance. Two experiments have been carried out to test the possibility of improving the heat dissipation by thinning and metallising the substrate. Gold was selected for the back-conducting material because it has a relatively good thermal conductivity (i.e. 318 W/(m·K)) and easiness of deposition.

The first device under investigation was from Wafer 340 that has a single GaAs-channel and two δ-doping layers on either side of the channel. The substrate was first lapped down from the original thickness of 620 μm to 200 μm and then a thickness of 800 nm gold was evaporated at the back of the sample using e-beam evaporation. The anode-cathode distance $L_{ac}$ and width of the device were 3 μm and 60 μm, respectively. The device was

placed on a quartz holder for characterisation. The one-port reflection coefficient of the device at different bias voltages was measured using a VNA before and after the substrate was thinned and back-metallised. The results are plotted in Figure 5-14. It is clearly seen that the device did not show negative resistance before the substrate was processed. However, after the substrate was thinned and metallised, the device has shown voltage-dependent negative resistance.

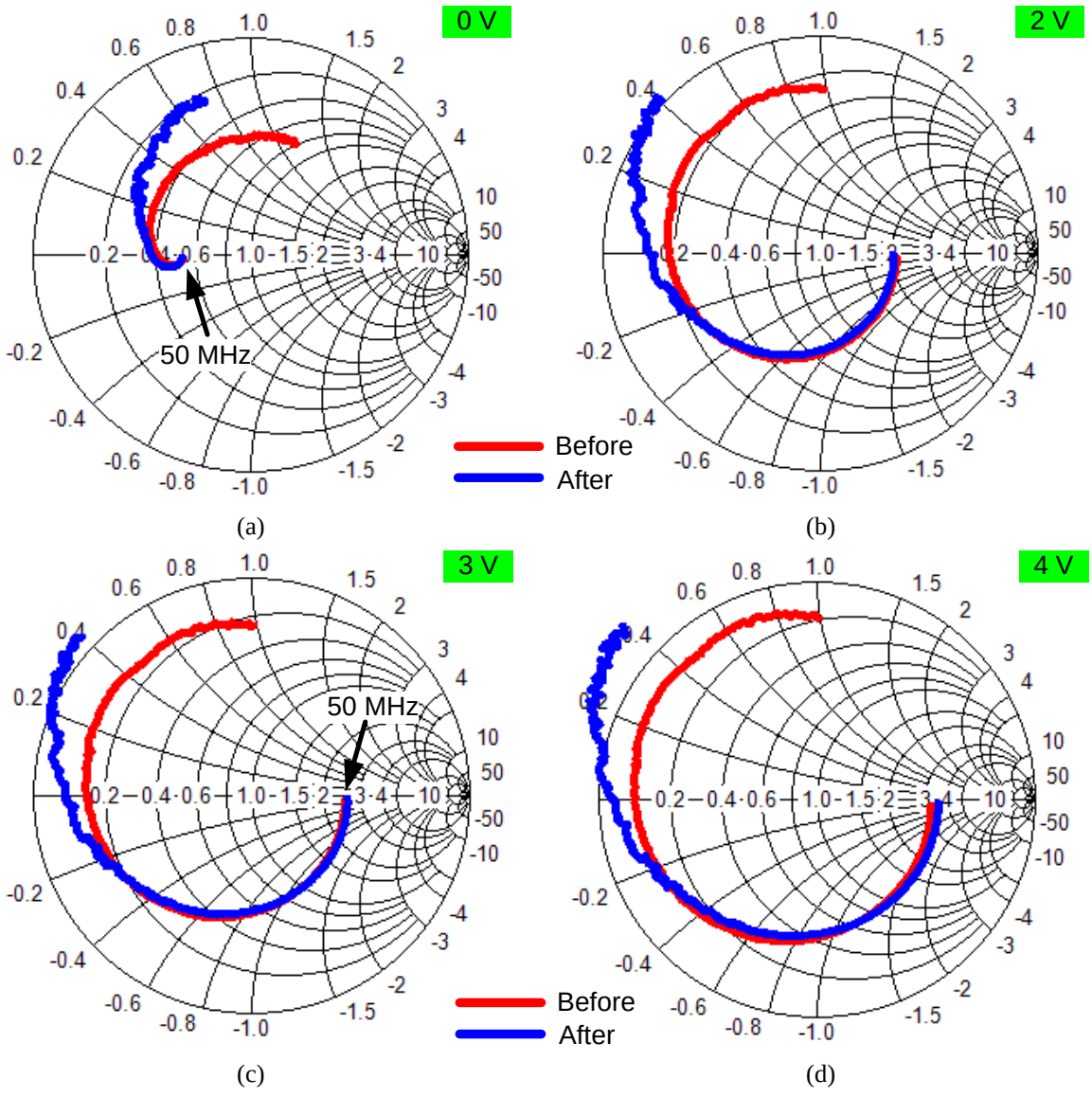


**Figure 5-14** Comparison of the measured S-parameters of a device at bias voltages of (a) 0 V, (b) 2 V, (c) 3 V, and (d) 4 V in the frequency range of 50 MHz-110 GHz before and after the substrate was thinned and metallised.

The second tested device was fabricated on wafer C341 that has a single $In_{0.23}Ga_{0.77}As$-channel with two δ-doping layers on either side of the channel. The device has an anode-cathode distance of 1.5 µm and width of 60 µm. Table 5-I shows the parameters when the substrate was 620 µm, 200 µm, and 200 µm and metallised.

**Table 5-I** Measured current, frequency, and power of a planar Gunn diode before and after the substrate was processed.

| Substrate | Bias (V) | Current (mA) | Frequency (GHz) | Power (dBm) |
|---|---|---|---|---|
| 620 μm | 2.7 | N/A | 101.3707 | -35.51 |
| 200 μm | 2.7 | 23.42 | 101.4324 | -28.25 |
| 200 μm+metal | 2.7 | 23.52 | 101.4620 | -25.67 |

It can be seen from Table 5-I that for the same device when biased at the same voltage (e.g. 2.7 V), the current, oscillation frequency, and power are different before and after the substrate was processed (unfortunately, the current was not recorded before the substrate was thinned). The current increases from 23.42 mA to 23.52 mA once the thinned substrate was metallised. Meanwhile the oscillation frequency and power increases after the substrate was thinned, and they further increases once the thinned substrate was metallised. This is because the thinner substrate has better heat dissipation capability and the additionally deposited gold at the back of the substrate further assists heat dissipation. As discussed in Section 5.4.2, reducing the temperature from the bottom of a normal substrate increased the devices' current, oscillation frequency, and RF power; similarly by thinning and metallising the substrate device performance improvement can also be achieved.

## 5.4 Effect of Illumination on Planar Gunn Devices

### 5.4.1 Introduction

Light has an effect on frequency and power performance of Gunn devices. For devices with relatively long channels (e.g. $L_{ac}$>10 μm), the effect of illumination on oscillation frequency depends on where the light is exposed onto, such as near the anode, near the cathode, or in the middle of the devices [244]. The reason for this is because electron-hole pairs are generated when a Gunn device is exposed to light. The creation of electron-hole pairs leads to increase in electron concentration and decrease of local electric field, therefore a change of Gunn domains.

For the planar Gunn devices we have designed, the anode-cathode distance $L_{ac}$ is smaller than or equal to 4 μm. It is difficult to perform aforementioned experiments to investigate

the influence of device performance due to partial illumination on the channel. In fact, we carried out an experiment in which the entire device was exposed to a light.

### 5.4.2 Experimental Results

The light used for this experiment was generated from a group of white LED lights. It has six intensity levels designated in the range of "0" to "5". "0" indicates light-off. "1" is the lowest intensity and "5" gives the highest intensity. Although the intensity was not calibrated, its change corresponding to the change of level number was easily distinguished by the naked eyes.

The device used for this experiment was fabricated on Wafer C340 that has a single GaAs channel and two δ-doping layers on each side of the channel. The anode-cathode distance $L_{ac}$ and the width of the device are 1.5 μm and 60 μm, respectively. The device was biased at 3.9 V. Table 5-II shows the current, power, and frequency variations as the light intensity changes from "1" to "5". One can clearly see that current and power increase as the light intensity increases; however, the frequency decreases as the light intensity increases. In addition, both frequency and power tends to saturate as power intensity increase to a certain level.

**Table 5-II** Changes of current, frequency, and RF power of a planar Gunn diode as the intensity of the imposing light changes.

| Light intensity (a.u.) | Current (mA) | Frequency (GHz) | RF Power (dBm) |
|---|---|---|---|
| 1 | 46.97 | 105.4781 | -31.5 |
| 3 | 48.26 | 103.9739 | -20.55 |
| 5 | 49.31 | 103.9591 | -20.52 |

### 5.4.3 Discussion

The observation of change of frequency and power corresponding to the change of light intensity results is exactly the same as described in [245]. It is believed that since the material is comparatively free of deep levels, the generation of electron-hole pairs across the bandgap occurs during the illumination and the generated electrons may smooth any

existing electron density gradients in the channel. This certainly leads to a more uniform channel and therefore the better formation of Gunn domains.

However, it has also been found that if the light was suddenly switched on while a device was working, the device would be killed. An obvious burn-out mark would be observed between electrodes. The burn-out is associated with sudden increase of current and this is believed to result from the sudden increase of electrons from the generation of electron-hole pairs. To avoid this, it is recommended switch the light before applying the bias to the device.

## 5.5 Investigation of Drift of Current, Frequency, and Power of Planar Gunn Devices

The drift of current, frequency, and RF power as time passes by has been investigated. The device was from Wafer C341 that has an $In_{0.23}Ga_{0.77}As$-channel and two δ-doping layers on each side of the channel. The anode-cathode distance of the device $L_{ac}$ and width are 4 μm of 60 μm, respectively. The device was biased at 7.5 V and the initial current, frequency, and power are 30.01 mA, 40.1218 GHz, and -28 dBm, respectively.

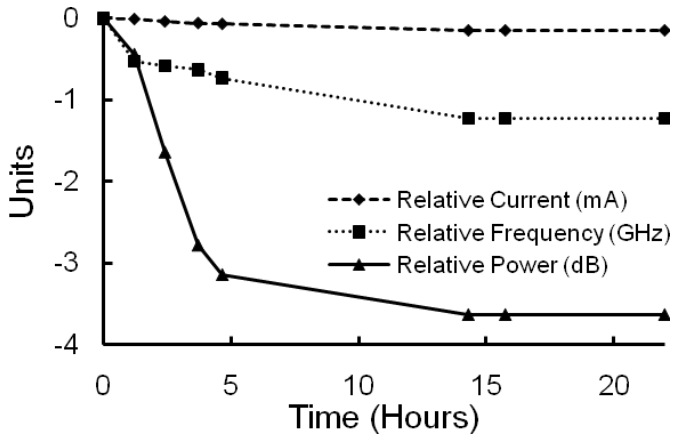


**Figure 5-15** Life time measurement on a 4 μm planar Gun device from Wafer C341.

The device was powered on and readings of current, frequency, and power were taken at random times with irregular time intervals e.g. 1.2, 2.4, 3.7, 4.7, 14.3, 15.8, and 22 hours. The results are plotted in Figure 5-15. It can be seen that current decreases slowly as time passes by. However, both frequency and power decrease significantly (frequency decreases

up to 0.8 GHz and power reduces up to 3 dB, respectively,) in the first 5 hours but stabilises afterwards.

The cause of the frequency and power decreases as time passes by may be due to the heat effect as discussed in the Section 5.3. Within the first hours, the continuous input of DC bias leads to accumulation of heat that rises up temperature inside of the device, therefore both frequency and power decrease. However, as time continues passing by, the thermal equilibrium may be achieved when the ambient temperature and the temperature inside the device are balanced. The device therefore performs stably.

## 5.6 Conclusion

In this chapter, many miscellaneous aspects of planar Gunn devices have been reported. Multiple oscillations have been observed in both GaAs and $In_{0.23}Ga_{0.77}As$-based devices while being biased at sufficiently high voltages. The cause of this phenomenon was believed to result from the penetration of electrons into deeper channels at high electric fields thus several domains may form simultaneously. The self-oscillating mixing effect has also been found in planar Gunn devices. The nonlinear characteristics of device impedance lead to the mixing effect. This property of planar Gunn devices may simplify transceiver systems for future applications. Heating and cooling a working Gunn device from the bottom of its substrate by using a temperature adjustable probe station was demonstrated. The influence of the heat triggered investigation of thinning the substrate and depositing a heat conductor to assist heat dissipation and therefore improving the power and frequency performance of the devices. Other investigations, such as illumination and life-time measurements, have also been shown in this chapter. The results help understand planar Gunn devices not only from a device performance point of view but also from practical application aspect.

# CHAPTER 6

# PASSIVE COMPONENTS AND CIRCUITS FOR INTEGRAED PLANAR GUNN OSCILLATORS

Chapter 4 has shown the intrinsic power and frequency performance of the planar Gunn diodes. To meet requirement of practical applications, the power performance must be increased and this can be achieved using circuit design techniques to bias the diode, filter unwanted harmonics, and power combining. Hence this chapter focuses on the passive components and circuits.

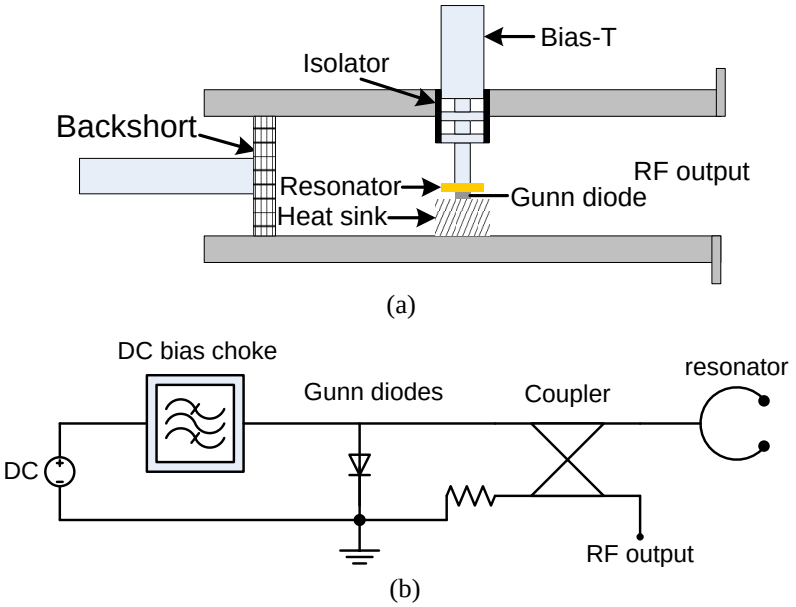


**Figure 6-1** Illustrations of (a) a Gunn oscillator constructed in a conventional waveguide structure and (b) a simplified circuit layout of an integrated planar Gunn oscillator.

It is well-known that a Gunn diode is intrinsically an oscillator that can generate a self-sustaining oscillation as was first demonstrated by Gunn [1]. However, the RF performance of this type of Gunn diode, in terms of the output power, frequency tuneability and stability, and temperature stability and noise, does not meet the requirements of practical applications. Therefore a Gunn diode is usually embedded in

waveguide circuits in order to improve its RF performance [47]. The circuits include many major passive elements in microwave and millimetre-wave engineering, such as transmission lines, resonators, filters, and couplers as was shown in Figure 2-2 in Chapter 2 now re-plotted as Figure 6-1a for convenience. Power combiners can also be used for improving the RF power level further.

For a conventionally constructed Gunn oscillator, e.g. Figure 6-1a, the transmission line is either a rectangular waveguide [246] or a coaxial waveguide [67]. The resonator is a metallic disc with high quality factor, *Q* (in the order of thousands), that ensures the Gunn oscillator has good frequency stability and low phase noise [47]. The filter in a Gunn oscillator circuit is mainly a low pass filter (LPF) that serves as a DC bias choke. This allows a DC bias to be applied to the Gunn diode meanwhile the RF signals are blocked. The commonly deployed LPFs are radial line resonators that have a cylindrical geometry. The RF signal is extracted by using an appropriate coupler. A standard *W*-band rectangular waveguide assembly for a vertical Gunn oscillator is shown in Figure 6-1a.

Similar passive components and circuits are needed to implement a *planar* Gunn oscillator with improved RF performance. Figure 6-1b illustrates a simplified circuit layout of an integrated planar Gunn oscillator. Since a planar Gunn diode has a uniplanar geometry, implementing these passive elements in uniplanar form is most suitable. Planar Gunn diodes are also compatible with other planar techniques, such as (substrate integrated waveguides, microstrip lines, etc), but appropriate coplanar waveguide transitions, with their additional losses, are necessary.

In this chapter, the design, modelling, fabrication and characterisation of coplanar passive components and circuits for implementing millimetre-wave planar Gunn oscillators are described. The passive components and circuits include uniplanar transmission lines, thin-film resistors and airbridges in Section 6.1, resonators in Section 6.2, LPFs for bias tees in Section 6.3, couplers in Section 6.4 and power dividers/combiners in Section 6.5. The deployment of passive components in the build-up of proposed planar Gunn oscillators is given where appropriate.

## 6.1 Planar Passive Components

Truly planar Gunn oscillators require passive components which have uniplanar structures, where all circuit elements are fabricated on one side of the substrate, in order to be compatible with planar Gunn diodes. These uniplanar devices can be realised in many forms, such as coplanar waveguide (CPW) [247, 248], coplanar striplines (CPS) [248, 249], and slotlines [250, 251]. However, other non-uniplanar on-chip structures such as striplines [252, 253], microstrip lines [251, 254], and double-sided parallel-strip line (DSPSL) [255, 256] can be used with the appropriate waveguide transitions. Figure 6-2 shows several typical on-chip transmission lines and the electric field and magnetic field distribution of their dominant mode of propagation. Each transmission medium has its own pros and cons in terms of power handing capability, cut-off frequency, cost, ease of fabrication.

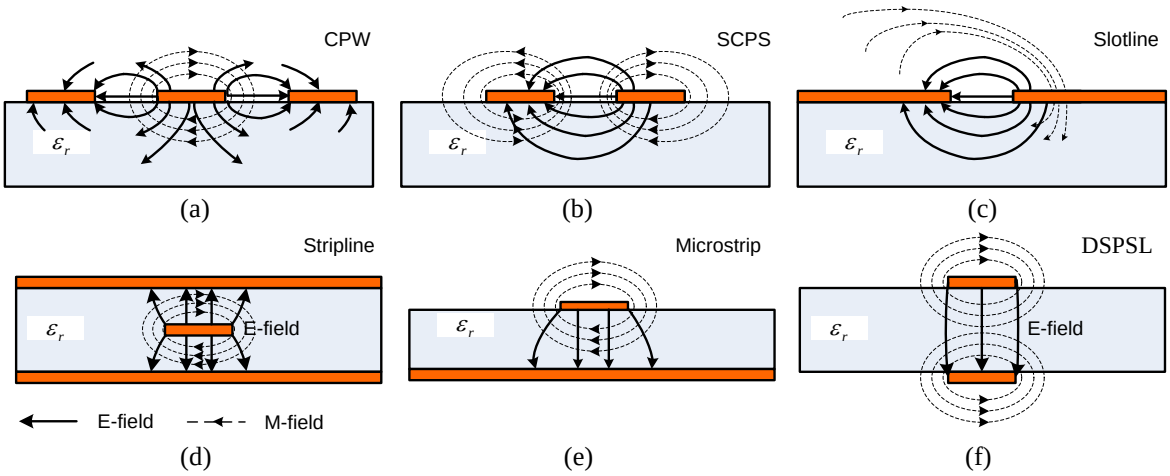


**Figure 6-2** Typical planar transmission lines. (a) Coplanar waveguide, (b) Symmetrical coplanar striplines, (c) Slotlines, (d) Striplines, (e) Microstrips, and (f) Double-sided parallel-strip line.

In this project, CPW has been chosen as the primary transmission line media for all passive components and circuits in order to reduce the fabrication complexity, although in some cases better performance can be obtained with other forms of transmission lines. In addition, CPW has a good compatibility with on-wafer probes for the purpose of device characterisation and measurement. In our millimetre-wave laboratory, there is the availability of probes with GSG or CPW pattern and pitch separations ranging from 50 μm to 150 μm depending on the frequency range of application. Besides symmetrical CPS (SCPS) was used in power combiner/divider circuits in which appropriate transition between CPW and SCPS was applied.

In this section, some basic transmission line theories of CPW and SCPS will be first given in Section 6.1.1. Lumped elements including resistors and airbridges are discussed in Sections 6.1.2 and 6.1.3, respectively. The CPW-based resonators, filters, couplers and combiners/dividers are introduced in Sections 6.2 to 6.5, accordingly.

### 6.1.1 Coplanar Waveguides and Coplanar Striplines

#### *6.1.1.1 Coplanar Waveguides*

Coplanar waveguide was first demonstrated by Wen in 1969 [247]. The conventional CPW has a central signal conductor sandwiched laterally by two ground conductors with equal distance on the top side of the substrate. The characteristic impedance of CPW ($Z_{CPW}$) depends on the width of signal conductor ($w_{CPW}$), the gap between the signal and grounds ($s_{CPW}$), and the effective dielectric constant ($\varepsilon_{eff}^{CPW}$) that is related to dielectric constant of the substrate ($\varepsilon_r$). The originally proposed CPW had semi-infinitely wide ground planes and infinite thick substrate that are unrealistic in practice. More practical CPWs having finite ground conductors and thickness of substrate have been developed into various forms, such as CPW with a cover shield, conductor-backed CPW, conductor-backed CPW with a cover shield, multilayered CPW [251], and elevated CPW [257]. Figure 6-3a shows a CPW having finite ground plane and finite substrate.

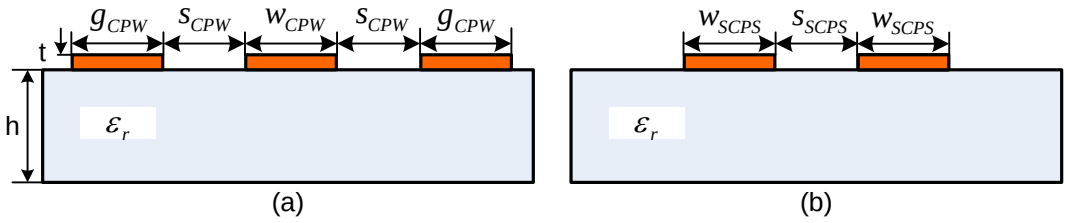


**Figure 6-3** Cross-sectional views of (a) an FG-CPW and (b) an SCPS.

The closed-form equations for effective dielectric constant and characteristic impedance of a CPW with finite ground (FG-CPW) on a finite substrate are given by [258]

$$\varepsilon_{eff}^{CPW} = 1 + \frac{\varepsilon_r - 1}{2} \frac{K(k_1')}{K(k_1)} \frac{K(k_2)}{K(k_2')} \tag{6.1.1}$$

$$Z_{CPW} = \frac{30\pi}{\sqrt{\varepsilon_{eff}^{CPW}}} \frac{K(k_1')}{K(k_1)} \tag{6.1.2}$$

where

$$k_1 = \frac{w_{CPW}}{w_{CPW} + 2s_{CPW}} \sqrt{\frac{g_{CPW}(w_{CPW} + 2s_{CPW} + g_{CPW})}{(s_{CPW} + g_{CPW})(w_{CPW} + s_{CPW} + g_{CPW})}} \tag{6.1.3}$$

$$k_2 = \frac{\sinh(\pi w_{CPW}/4h)}{\sinh[\pi(w_{CPW} + 2s_{CPW})/4h]} \cdot A \tag{6.1.4a}$$

$$A = \sqrt{\frac{1 - \sinh^2[\pi(w_{CPW} + 2s_{CPW})/4h] / \sinh^2[\pi(w_{CPW} + 2s_{CPW} + 2g_{CPW})/4h]}{1 - \sinh^2(\pi w_{CPW}/4h) / \sinh^2[\pi(w_{CPW} + 2s_{CPW} + 2g_{CPW})/4h]}} \tag{6.1.4b}$$

$k_1' = \sqrt{1 - k_1^2}$ and $K(\bullet)$ is the complete elliptic integral of the first kind. $h$ and $\varepsilon_r$ are the thickness and dielectric constant of the substrate, respectively. The calculated effective dielectric constant and characteristic impedance of FG-CPW for variation of slot width against central conductor width using the above equations are plotted in Figure 6-4.

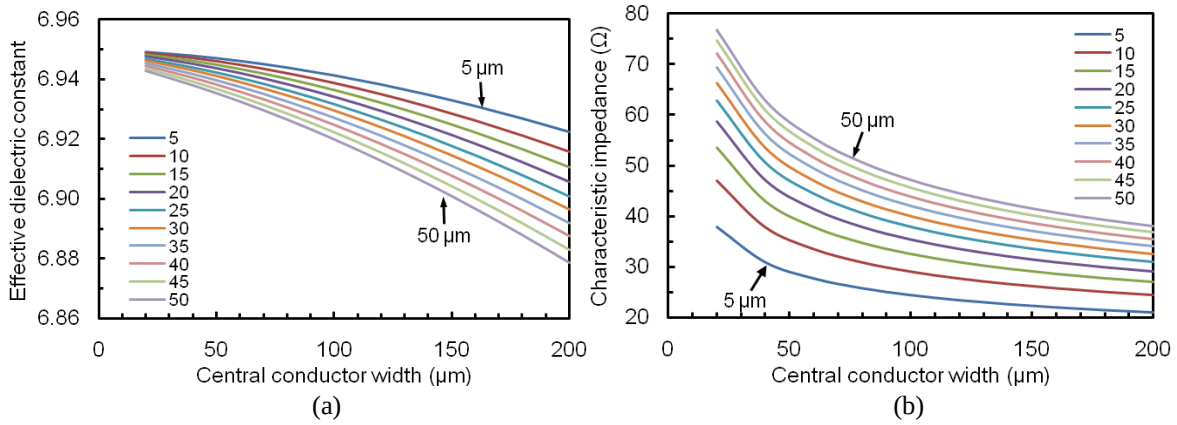


**Figure 6-4** Calculated (a) effective dielectric constant and (b) characteristic impedance of an FG-CPW for variation of slot width versus central conductor width. The width of ground planes $g_{cpw}$ was fixed at 200 µm.

### *6.1.1.2 Symmetrical Coplanar Striplines*

Symmetrical coplanar stripline (SCPS) [249] has two parallel conductors with equal width ($w_{SCPS}$) separated by a narrow gap ($s_{SCPS}$) as shown in Figure 6-3b. Unlike CPW, the SCPS is a balanced transmission line that is widely used in balanced mixers, dipole antennas and optical integrated circuits [251]. Other forms of SCPS include asymmetric CPS (ACPS) and CPS with isolating ground planes (CPSSIG) [248]. The former allows

wider range of propagation constant and characteristic impedance by adjusting one of the conductor widths. The latter reduces good isolation from neighbouring lines and suppresses parasitic propagation mode.

The closed-form design equations of effective dielectric constant $\varepsilon_{eff}^{SCPS}$ and characteristic impedance $Z_{SCPS}$ for an SCPS are given by [259]

$$\varepsilon_{eff}^{SCPS} = 1 + \frac{\varepsilon_r - 1}{2} \frac{K'(k_3)}{K(k_3)} \frac{K(k_4)}{K'(k_4)} \tag{6.1.5}$$

and

$$Z_{SCPS} = \frac{120\pi}{\sqrt{\varepsilon_{eff}^{SCPS}}} \frac{K(k_3)}{K'(k_4)} \tag{6.1.6}$$

where

$$k_3 = \frac{s_{SCPS}}{s_{SCPS} + 2w_{SCPS}} \tag{6.1.7}$$

$$k_4 = \frac{\sinh(\pi s_{SCPS}/4h)}{\sinh[\pi(2w_{SCPS} + s_{SCPS})/4h]} \tag{6.1.8}$$

Figure 6-5 shows the calculated characteristic impedance and effective dielectric constant for various conductor width and gap width using the above equations.

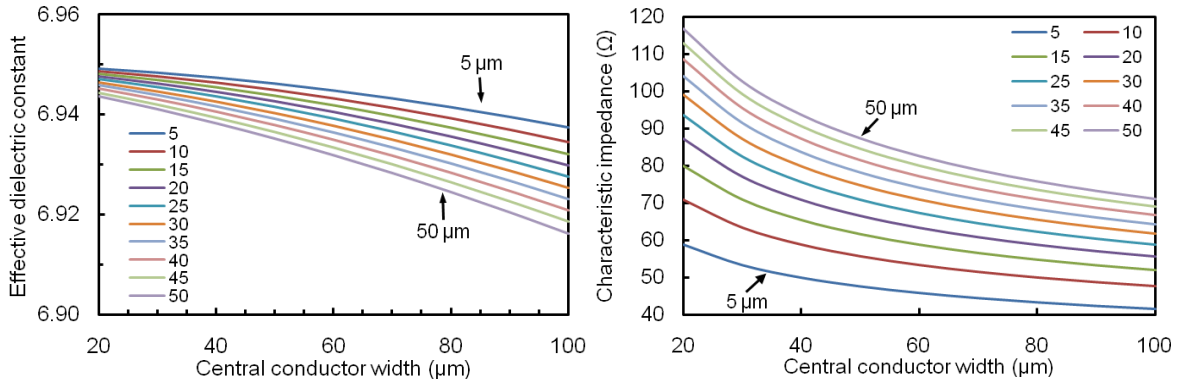


(a) (b)

**Figure 6-5** Calculated effective dielectric constant (a) and characteristic impedance (b) of SCPS for variation of slot width versus central conductor width using Equations 6.1.5-6.1.8.

Apart from the synthesis equations given above, an odd-even mode method can be applied to analyse the characteristic impedances of the SCPS because SCPS can also be considered

as a pair of parallel-coupled transmission lines. The odd and even mode impedances of the ideal coupled-lines, $Z_{0o}^{SCPS}$ and $Z_{0e}^{SCPS}$, respectively are given by:

$$Z_{0o}^{SCPS} = Z_0^{SCPS}\sqrt{\frac{1-k}{1+k}} \tag{6.1.9}$$

$$Z_{0e}^{SCPS} = Z_0^{SCPS}\sqrt{\frac{1+k}{1-k}} \tag{6.1.10}$$

where $Z_0^{SCPS}$ is the characteristic impedance of the SCPS, and $k$ is the coupling coefficient, which is defined by

$$k = \frac{Z_{0e}^{SCPS} - Z_{0o}^{SCPS}}{Z_{0e}^{SCPS} + Z_{0o}^{SCPS}} \tag{6.1.11}$$

The HFSS simulated odd-mode and even-mode characteristic impedances and coupling factor are plotted against the conductor width and gap width in Figure 6-6.

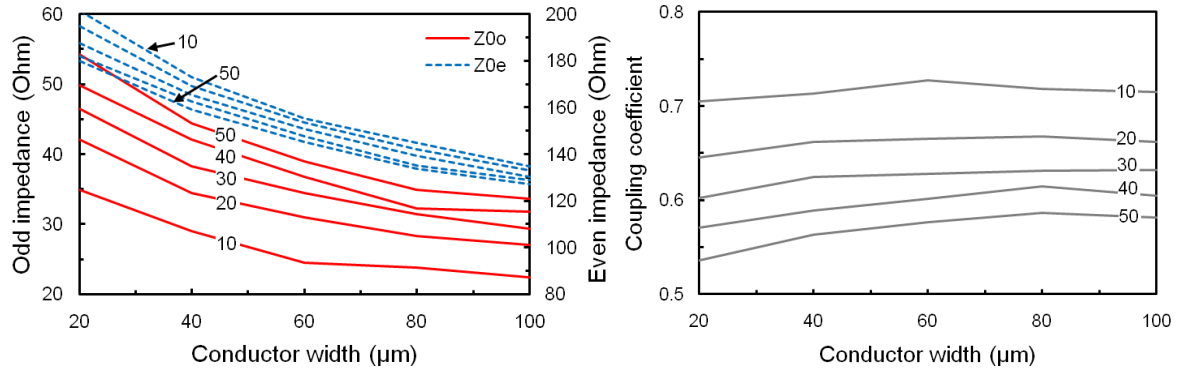


(a) (b)

**Figure 6-6** Simulated (a) even and odd-mode characteristic impedance, and (b) coupling coefficient versus the SCPS conductor width ( $w_{SCPS}$ ) for different values of conductor spacing ( $s_{SCPS}$ ).

### *6.1.1.3 CPW-SCPS Baluns*

A CPW is an unbalanced transmission line where currents of equal magnitude flow in central conductor and two ground planes in opposite directions, whereas an SCPS is a balanced transmission line where currents of equal magnitude flow in two conductors travel in opposite directions. To connect between them, a balun is needed. The word "balun" is an abbreviation for balanced-unbalanced. Several CPW-SCPS baluns have been proposed [260-264]. Figure 6-7a shows a CPW-SCPS balun using a slotline radial line stub to terminate one of the slots of the CPW. The radial line open stub has a broadband

operation so that the balun has a bandwidth greater than two octaves. The angle of the radial line stub can be adjusted for better impedance matching [260]. Figure 6-7b shows that a balun realised by superimposing a CPW "Y" with up-left arm open-circuited and up-right arm short-circuited onto an inverted SCPS "Y" that has its bottom-left arm short-circuited and bottom-right are open-circuited. This type of balun gives approximate four-decade bandwidth [263]. Figure 6-7c illustrates a modified version [264] of Mouw's hybrid junction [265]. It has a "T" shape and has been shown a wide operation bandwidth.

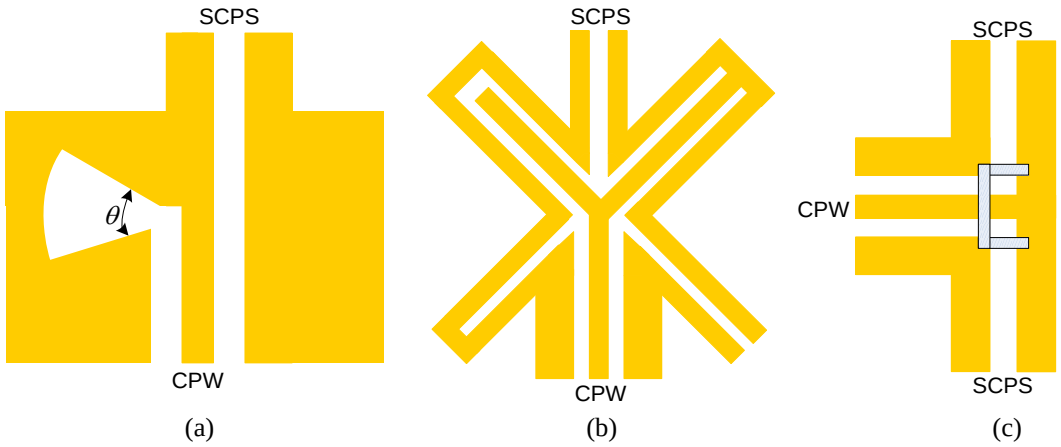


**Figure 6-7** Three types of CPW-SCPS baluns using (a) a slotline radial line stub [260], (b) double "Y" junction [263], and (c) "T" junction [264], respectively.

### 6.1.2 Thin-film Resistors

The applications of thin-film resistors in planar circuits include current-limitation, isolation, termination, matching and feedback networks. The common materials for thin-film resistors are nickel-chrome alloy or nichrome (NiCr) that has a resistivity of approximate 100 μΩ·cm [266] and tantalum nitride (TaN) that has resistivity values of 200 μΩ·cm to 1000 μΩ·cm [267] or even 80 μΩ·cm reported in [268]. Other materials that are used are nickel vanadium NiV [269], silicon chrome (SiCr) [270], and germanium [271]. A summary of the resistivity of common resistive materials for thin-film resistors are given in Table 6-I.

**Table 6-I** Resistivity of commonly used materials for thin-film resistors.

| Materials | NiCr | TaN | NiV | SiCr | Ge |
|---|---|---|---|---|---|
| Resistivity (μΩ·cm) | ~100 | 80-1250 | 60 | $\sim 2\times10^{4}$ | $4.6\times10^{7}$ |
| References | [266] | [267], [268], [272] | [269] | [270] | [271] |

In this project, thin-film resistors have been used in passive test structures e.g. matching loads as well as in power dividers to improve their output isolation. The material used was NiCr due to their availability in the cleanroom. It was demonstrated 15 years ago that 35 nm thickness of NiCr gave approximately a resistance of 50 Ω per square [273]. To verify the present performance of NiCr material for resistors, two fabrication processes have been tested: (1). Deposit the surrounding gold conductors first and then evaporate NiCr alloy between the conductors with slight extension on both sides to ensure complete contact between the gold and NiCr as shown in Figure 6-8a. (2). Evaporate the thin-film resistors first and then deposit the surrounding gold on the top as shown in Figure 6-8c. The former method has an advantage of saving one step of fabrication process because the gold conductors can be deposited while marker layer is formed. Therefore, only two steps are required to make gold patterns, markers and NiCr resistor layers. On the contrary, the latter requires three steps to complete this: the marker layer is formed first, followed by the resistor layer and then another layer of gold is needed to form the conductor patterns.

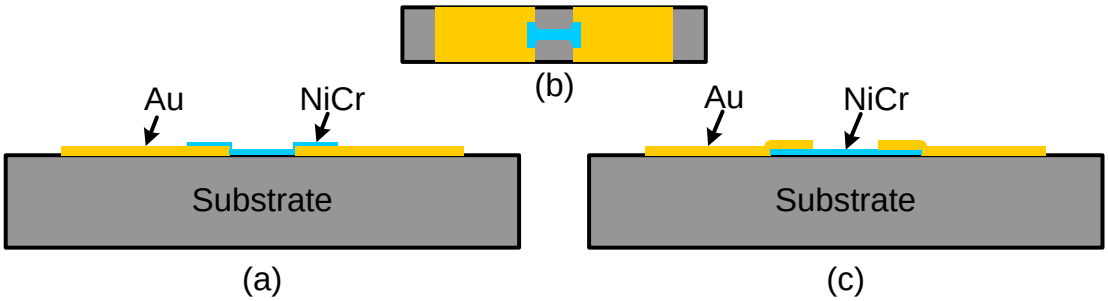


**Figure 6-8** Illustration of NiCr resistor fabricated using different processes. (a) Deposit the NiCr alloy after forming the gold conductors; (b) Taper added near the edges between NiCr resistors and gold conductors; (c) Deposit NiCr resistors before forming gold conductors.

However, it has been found that the first process does not provide good reproducibility and reliability because open circuits are frequently found. The open circuits come from physical discontinuity at the edge between a gold conductor and a thin-film resistor. The gold conductor has a nominal thickness between 400 nm and 800 nm however the thin-film resistor has a thickness of less than one tenth of gold conductor thickness. Although, an overlayer is added as shown in Figure 6-8a, the large edge discontinuity still creates a lot of failures. One of the solutions to this problem is to introduce a small taper at the NiCr sides as shown in Figure 6-8b. The gradual increase of this NiCr transition area provides larger contacting area at the edges. Experimental results demonstrate that reproducibility and reliability are improved although lower resistance suffers. The second fabrication process, on the other hand, provides very high yield and accuracy without suffering any

open-circuited edge problems. Detailed analysis about the DC and RF performance of the resistors that were fabricated using the second fabrication process is discussed as follows.

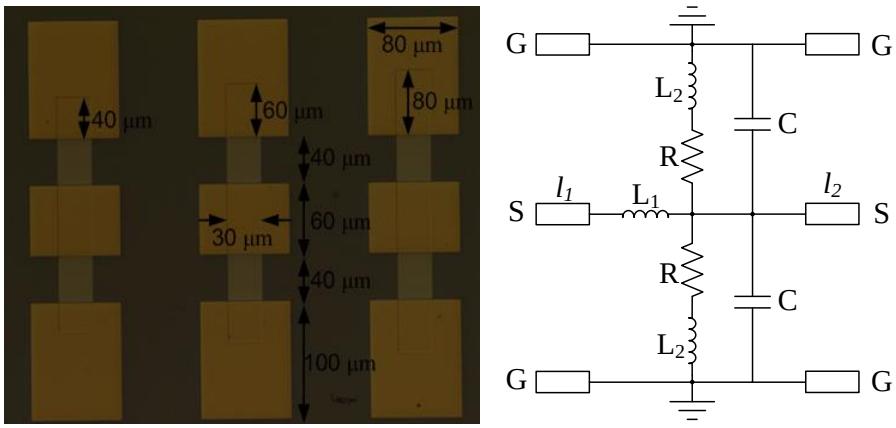


(a) (b)

**Figure 6-9** (a) Micrograph of fabricated NiCr resistors in CPW test structures. (b) The equivalent circuit.

Four groups of resistors for different resistive values (50 Ω, 40 Ω, 33.3 Ω, 25 Ω) have been fabricated in standard 60 μm/40 μm CPW test structure on a 620 μm semi-insulating GaAs substrate. The corresponding geometries for the resistors are listed in Table 6-II. Several test fabrications for various thicknesses of NiCr have been tested, and it was found that 33 nm gives the resistivity close to 50 Ω/Square. A set of fabricated resistors with actual resistive area of 40 μm×30 μm (length × width) is shown in Figure 6-9a. The equivalent circuit (EC) of the thin-film resistors constructed in CPW structure is illustrated in Figure 6-9b [274, 275]. The EC consists of two short lengths of test CPWs designated as $l_1$ and $l_2$, a contact inductor $L_1$, two parallel resistors R, inductors $L_2$, and two shunt capacitors.

**Table 6-II** Summary of performance and values of the lumped elements of the equivalent circuits for 20 Ω, 25 Ω, 33.3 Ω, and 50 Ω NiCr resistors fabricated in 60 μm/40 μm CPW test structures.

| Expected resistance (Ω) | | 20 | 25 | 33.3 | 50 |
|---|---|---|---|---|---|
| Geometry of each resistor Lengh (μm)×Width (μm) | | 40×50 | 40×40 | 40×30 | 40×20 |
| Measured DC resistance (Ω) | | 20.7 | 25.7 | 34.1 | 50.7 |
| ECs: | $l_1$(μm),<br>$l_2$(μm),<br>R(Ω),<br>L1(pH),<br>L2(pH),<br>C(pF) | 5,<br>5,<br>41.4,<br>12,<br>6,<br>10 | 5,<br>10,<br>51.4,<br>10,<br>6,<br>8.5 | 5,<br>15,<br>68.2,<br>10,<br>6,<br>7.5 | 10,<br>20,<br>102.7,<br>12,<br>11.5,<br>5 |

Both DC and RF (10 MHz-110 GHz) measurements were carried out using an on-wafer probe (GGB). Table 6-II summarizes the DC performance of the four group resistors. It can be seen that DC resistance has 0.7 Ω higher than the expected for all four groups. This extra resistance partially comes from the build-in resistance of the probe and the resistor fabrication tolerance. Figure 6-10a shows the measured RF resistance of the four resistors in the frequency range of 10 MHz and 110 GHz. It can be observed that for low value resistors, e.g. 20 Ω, 25 Ω and 33.3 Ω the resistance remains constant from DC up to 110 GHz. However, for high value resistors e.g. 50 Ω, the resistance decreases as frequency increases. The measured and simulated one-port reflection coefficients have good agreement as shown in Figure 6-10b.

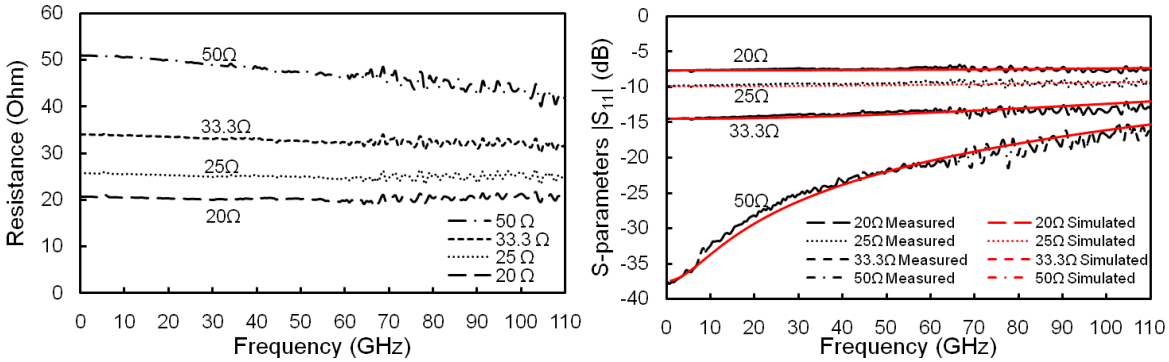


**Figure 6-10** (a) Measured resistance and (b) Simulated and measured reflection coefficient of four groups of NiCr resistors fabricated in 60 µm/40 µm CPW test structures in the frequency range of 10 MHz-110 GHz.

### 6.1.3 Airbridges

#### *6.1.3.1 Introduction*

Airbridges are not only used to suppress parasitic modes of propagation, for example the CPS mode on CPW [276, 277] due to exist of discontinuities but also as electrodes [278] and RF switches [279] . Additionally, they are also important parts for connecting between parts for many important components, such as Lange couplers [280] to replace conventional bond wires or via holes for highly compact microwave and millimetre-wave circuits. The commonly used airbridge development technology is based on photolithography because it has the advantages of low cost and simplicity [281]. However it has also limitation on flexibility. Once any part of the design is changed, a new mask for the airbridge layer has to be made. On the other hand, EBL offers greatest degree of flexibility to meet the demand of modern fast device development process. An EBL-based

airbridge technology makes the entire process compatible and flexible [282-285]. The majority of EBL airbridge fabrication schemes are based on one of two types. One method is to use precise control of the exposure dose and multiple steps using sacrificial metal removal to produce the required 3D topography for an airbridge [282], or to use a single write stage and vary the dose and beam voltage to expose the resist and create the required shape to form the posts and span of an airbridge [283]. A simpler airbridge fabrication technology that uses relatively fewer, but more easily controlled fabrication process steps has been developed in this research project.

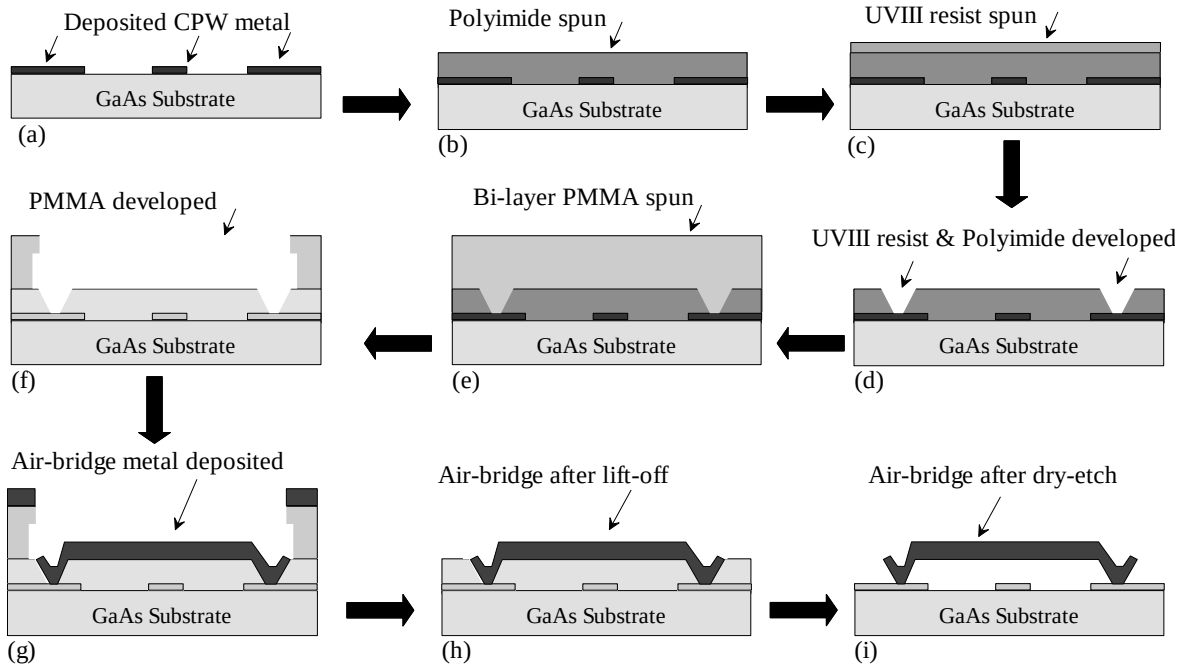


**Figure 6-11** A new airbridge fabrication process flow using electron beam lithography.

### *6.1.3.2 Fabrication Process*

The design and fabrication process flow for an airbridge is described in Figure 6-11. The airbridge process begins with a stage that creates a mask for the posts of the airbridge (Figure 6-11a-d). Polyimide is spin-cast to the desired height of the airbridge; in this case it is 4 μm. Dupont PI2545 polyimide is used due to its wet developing characteristics and stability in the pre-cure baked state. Next, UVIII resist is spin-cast on top of the polyimide and baked at 138 ℃ for 90 seconds. To complete the first fabrication stage the e-beam pattern is written for the airbridge post foundations. The sample is then baked at 138 ℃ for 90 seconds before developing in CD-26 for 15 seconds as shown in Figure 6-11d. The second stage of this airbridge process, as shown in Figure 6-11e-h is to use a bi-layer of

PMMA for the airbridge span, evaporate metal and then lift-off in acetone. The final step, shown in Figure 6-11i, is a completely dry process, which means there is no need for a critical point dryer to avoid the collapse of the airbridges-a necessary requirement of any wet processing of an airbridge. In this step, the sample is exposed to an $O_2$ plasma to etch the sacrificial polyimide layer everywhere. The results presented here, as shown in Figure 6-12, were achieved using a barrel plasma asher.

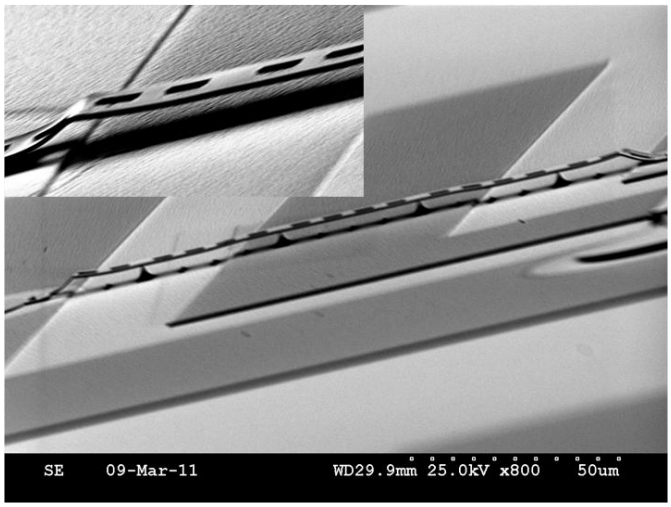


**Figure 6-12** The SEM image shows an airbridge where not all the polyimide has been removed. Small polyimide pillars are visible under the bridge. In the top left corner a close up of a fully cleaned up holey airbridge is shown.

*6.1.3.3 Measurements*

The reliability and electrical performance of airbridges have been tested on a pair of 1 mm long uniform CPWs (Figure 6-13 a and b) and a pair of 1 mm long right-angled CPWs (Figure 6-14 a and b) using a VNA. The VNA was calibrated between 10 MHz and 110 GHz with 201 points using LRRM method. Figure 6-13c shows the measured *S*-parameters for the uniform CPW line with three airbriges. Figure 6-13d shows that the three airbridges contribute to less than 0.2 dB transmission loss and less than 70 degree phase shift up-to 110 GHz.

The pair of right-angled CPWs with and without airbridges (Figure 6-14 a and b) have also been tested. The results are shown in Figure 6-14c, in which one can see that the right-angled CPW having no airbridges has a transmission notch at near 39 GHz and higher transmission loss at above 70 GHz. This is due to the onset of parasitic mode at the right

angle bend of the transmission line. On the contrary, there is no transmission notch when airbridges were applied because the parasitic mode has been suppressed. In addition the transmission loss is also reduced above 70 GHz.

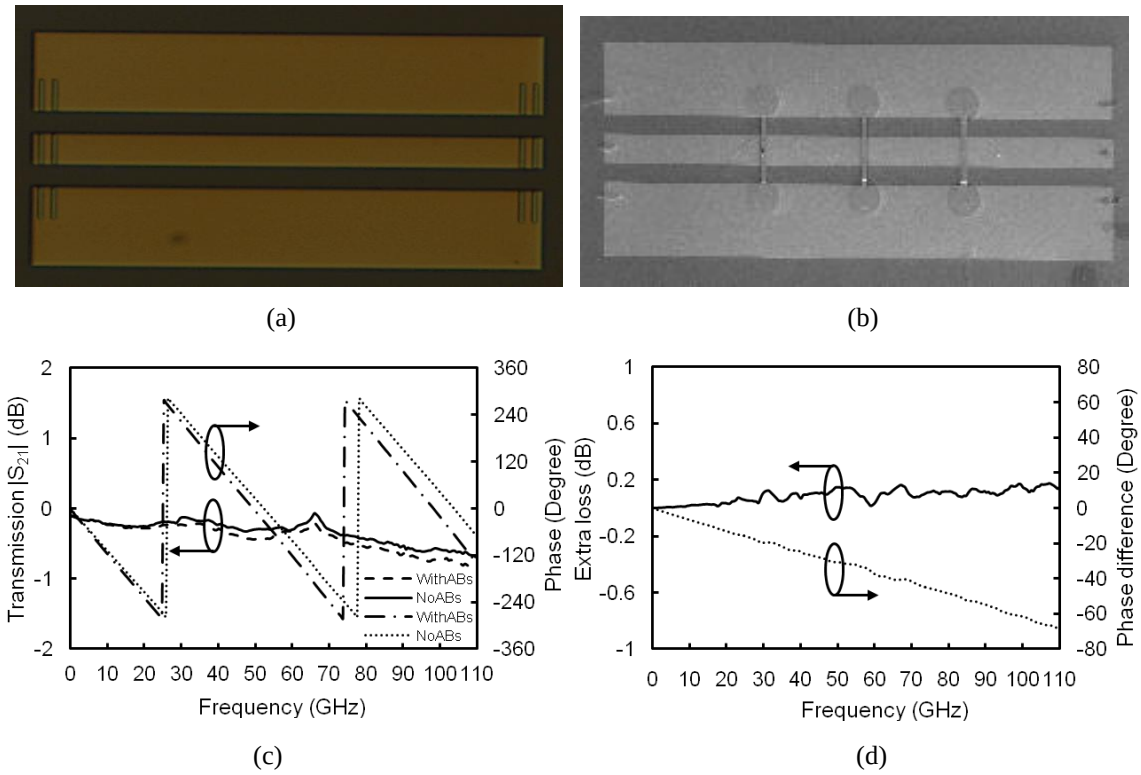


**Figure 6-13** Measured performance of a 1 mm CPW without airbridges and with three airbridges. (a) The fabricated 1 mm uniform CPW line without airbridges, (b) The 1 mm CPW line with airbridges, (c) transmission $|S_{21}|$ and phase, and (d) extra loss and phase shift compared to the CPW with same length but without airbridges.

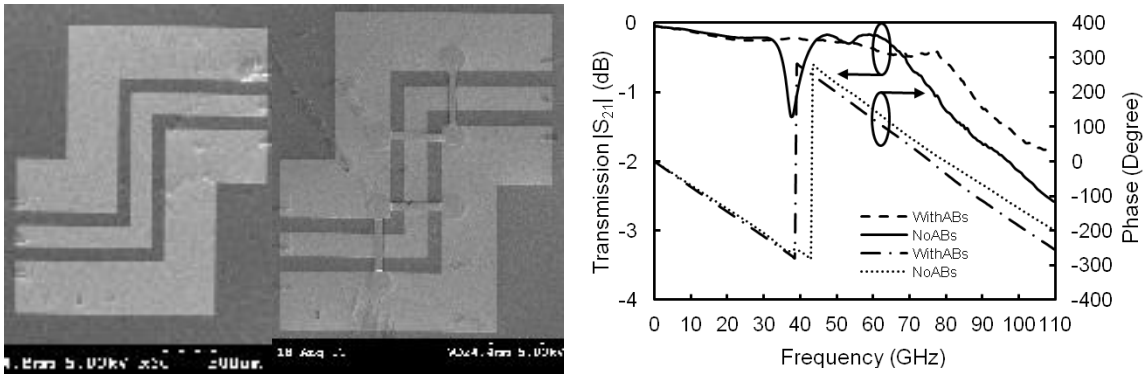


**Figure 6-14** Comparison of a pair of CPWs with and without airbridges. A transmission notch and excess loss indicates existence of parasitic modes generated at the right angles. The 1 mm right-angled CPW line (a) without airbridges, (b) with air bridges, and (c) the measured transmission loss and phases.

## 6.2 Resonators

### 6.2.1 Introduction

Microwave and millimetre-wave resonators provide various applications in both passive and active circuits. For passive circuits such as filters and antennas, the resonators are used to select operating frequency and to facilitate power coupling. For active devices such as oscillators, the resonators offer frequency selectivity and ensure frequency stability. The basic theory of a microwave and millimetre-wave resonator can be described using lumped elements [286]. Figure 6-15 shows two types of resonator circuits constructed using a resistor, an inductor and a capacitor (*RLC*) in series and parallel.

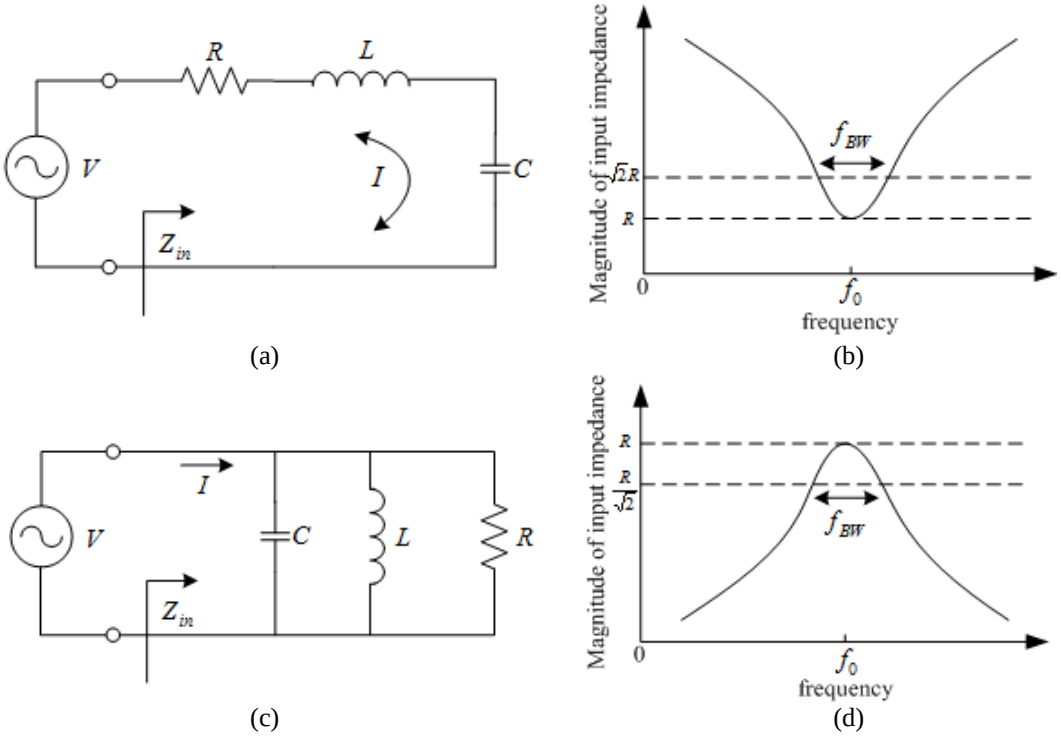


**Figure 6-15** *RLC* constructed resonators and their responses. (a) A series RLC resonator and (b) its magnitude of input impedance response to the frequency; (c) A parallel *RLC* resonator and (d) its magnitude of input impedance response to the frequency.

The input impedance of the series resonator is [286]

$$Z_{in}^{Series} = R + j\omega L - j/\omega C \tag{6.2.1}$$

and it can be written as

$$Z_{in}^{Series} = R + j4L\pi\Delta f \tag{6.2.2}$$

at near the resonant frequency of $f_0$, which is defined as

$$f_0 = \frac{1}{2\pi\sqrt{LC}} \tag{6.2.3}$$

The input impedance of the parallel resonator is [286]

$$Z_{in}^{Parallel} = \left(1/R + 1/j\omega L + j\omega C\right)^{-1} \tag{6.2.4}$$

and it can be written as

$$Z_{in}^{Parallel} = \frac{R}{1 + j4\pi\Delta fRC} \tag{6.2.5}$$

at near the resonant frequency of $f_0$. Since the input impedances of distributed elements such as open and short-circuited $\lambda_g/2$ or $\lambda_g/4$ transmission lines have similar forms as those of lumped *RLC* resonator circuits as summarised in Table 6-III, they can be treated as a series or parallel lumped resonant circuit. $\alpha$ is the attenuation constant; $l$ is the length of the transmission line and $Z_0$ is the characteristic impedance of the transmission line.

**Table 6-III** Summary of the input impedances and equivalent *RLC* of transmission line stubs [286].

| | Input impedance | Equivalent *R* | Equivalent *L* | Equivalent *C* |
|---|---|---|---|---|
| Open-circuited $\lambda_g/2$ stub | $Z_0 \Big/ \left(\alpha l + j\frac{\Delta f\pi}{f_0}\right)$ | $Z_0/\alpha l$ | $Z_0/\pi^2 f_0$ | $\left(4f_0Z_0\right)^{-1}$ |
| Open-circuited $\lambda_g/4$ stub | $Z_0\left(\alpha l + j\frac{\Delta f\pi}{2f_0}\right)$ | $Z_0\alpha l$ | $Z_0/8f_0$ | $2\left(\pi^2 f_0Z_0\right)^{-1}$ |
| short-circuited $\lambda_g/2$ stub | $Z_0\left(\alpha l + j\frac{\Delta f\pi}{f_0}\right)$ | $Z_0\alpha l$ | $Z_0/4f_0$ | $\left(\pi^2 f_0Z_0\right)^{-1}$ |
| Short-circuited $\lambda_g/4$ stub | $Z_0 \Big/ \left(\alpha l + j\frac{\Delta f\pi}{2f_0}\right)$ | $Z_0/\alpha l$ | $2Z_0/\pi^2 f_0$ | $\left(8f_0Z_0\right)^{-1}$ |

Quality factor, $Q$, that is a measure of the loss of a resonant circuit is defined by [286]

$$Q = 2\pi\frac{P_S}{P_L} \tag{6.2.6}$$

where $P_S$ and $P_L$ are the average energy stored and lost in the resonator, respectively. The $Q$ for the series resonant circuit is derived as [286]

$$Q = \frac{2L\pi f_0}{R} = \frac{1}{2RC\pi f_0} \tag{6.2.7}$$

and for the parallel resonant circuit is derived as [286]

$$Q = \left(\frac{2L\pi f_0}{R}\right)^{-1} = 2RC\pi f_0 \tag{6.2.8}$$

Thus, the $Q$ for transmission line resonators can be written in relation to the propagation constant $\beta$ and attenuation constant $\alpha$ as [286]

$$Q = \frac{\beta}{2\alpha} \tag{6.2.9}$$

### 6.2.2 Resonators for Gunn Devices

Resonator is a crucial component in a Gunn oscillator because the Q of the resonator affects the oscillator's noise performance. The higher is the Q the lower is the FM noise [47]. For conventional Gunn oscillators, disc-like metallic resonators are used and mounted in the cavity. The typical Q or (unloaded Q) of this type of resonator is several thousands. However, for MIC and MMIC Gunn oscillators, only planar types of resonator, such as dielectric resonators [287] and open-circuited or short-circuited transmission line resonators are possible. Dielectric resonators have high temperature stability and low noise at low microwave frequency range [288] but they become lossy at millimetre-wave frequencies. Planar open-circuited or short-circuited transmission line resonators that are half or quarter-wavelength transmission line [127] are big in size. Modification and improvement include open-ring resonators [289], hair-pin resonators [290] and radial line stub resonators [291] etc. Radial line stub resonators have advantages of shorter physical length and wider bandwidth compared to the conventional open stub resonators [291].

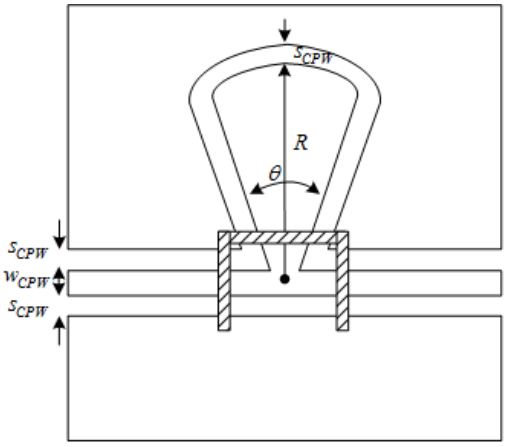


**Figure 6-16** Schematic view of a radial line single-stub constructed in a CPW.

The single coplanar open-ended radial line stub resonator was first reported by Simons [291], and later a double-stub resonator was introduced [292]. The validity of the closed-

form equations given in [291] for the relationship between resonant frequency and stub radius and angle is very limited because they were derived by curve-fitting the measured data; however, they serve as an initial design guide and the final parameters can be obtained by HFSS simulations. Figure 6-16 shows a schematic view of a single-stub radial line resonator. The resonant frequency variation to the radius $R$ and sectorial angle $\theta$ was simulated by using HFSS. The substrate is a 620 μm semi-insulating GaAs having a dielectric constant of 12.9. The metal conductor was made of 0.4 μm thick gold. The simulation results are plotted in Figure 6-17.

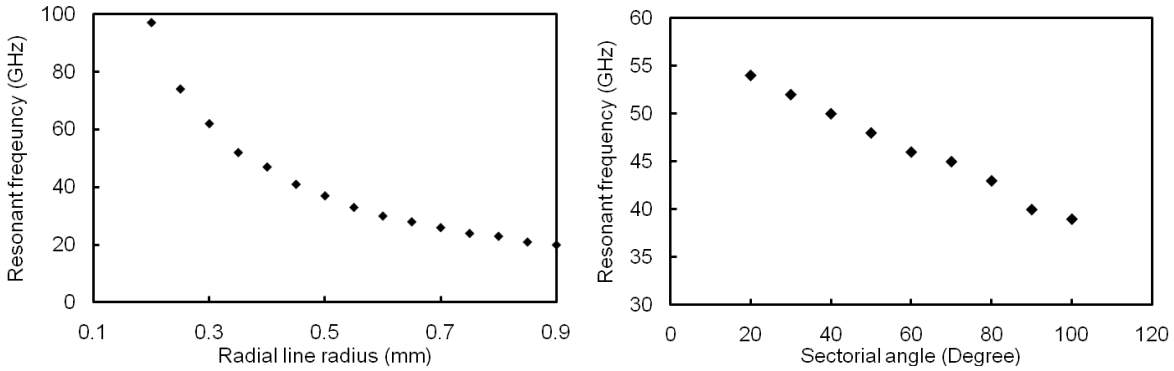


**Figure 6-17** (a) Resonant frequency of a single radial line resonator with variation of radius from 0.1 mm to 0.9 mm for a sectoral angle of 60 degree, (b) resonant frequency of a single radial line resonator with variation of sectorial angles from 20 degree to 100 degree for a radius of 0.4 mm.

By curve-fitting, the equations for the resonant frequency versus radial line radius with a fixed sectorial angle of 60 degree is given by

$$f_0 = 1060.1R^4 - 2768R^3 + 2713.1R^2 - 1231.5R + 253.76 \qquad (6.2.10)$$

Units of the resonant frequency and the radial line radius $R$ are GHz and mm, respectively. Similarly, the relationship between resonant frequency and sectorial angle for a 0.4 mm single radial line resonator is rather linear and govern by

$$f_0 = -0.1883\theta + 57.633 \qquad (6.2.11)$$

where $\theta$ is the sectorial angle.

## 6.3 Low Pass Filters for Bias Tee Application

### 6.3.1 Introduction

A low pass filter (LPF) allows signals with frequencies lower than its cut-off frequency $f_c$ to pass through but attenuates any signal with frequencies higher than the cut-off frequency. An application of a LPF, for example in an oscillator circuit, is to use it as a bias tee so that DC bias can be applied onto the active devices while any RF signals generated by the oscillator will be blocked from the bias source [74].

An insertion loss method [127] can be used to synthesis a LPF. The insertion loss $P_{IL}$ is defined by the ratio of power available from the source $P_S$ to power delivered to the load $P_L$ and can be written in the form of [286]

$$P_{IL} = 10\log\frac{P_S}{P_L} \tag{6.3.1}$$

or

$$P_{IL} = -20\log|S_{21}| \tag{6.3.2}$$

when both source and load are matched. For a maximally flat LPF as shown in Figure 6-18a, Equation 6.3.1 can be written as [286]

$$P_{IL} = 10\log\left[1+\left(f/f_c\right)^{2N}\right] \tag{6.3.3}$$

$f_c$ is the frequency point where $P_{IL}$ increases by 3 dB. $N$ is the number of orders. For $f > f_c$, $P_{IL}$ increases rapidly.

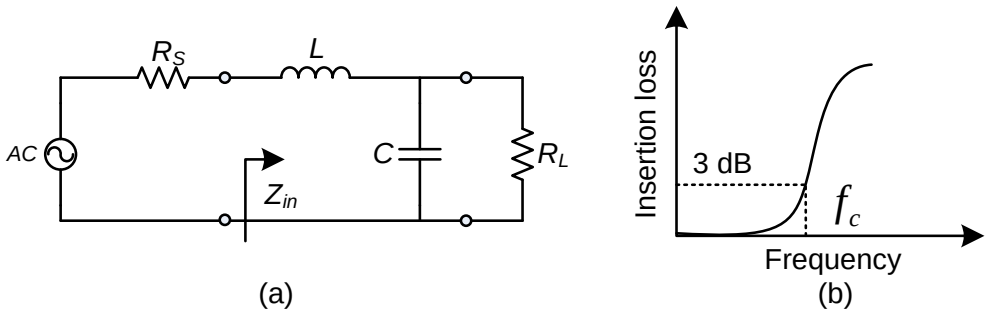


**Figure 6-18** (a) An ideal flat-top LPF with two reactive elements: an inductor and a capacitor and (b) its schematic transmission spectrum [286].

For an equal-ripple LPF, Equation 6.3.1 can be written as [286]

$$P_{IL} = 10\log\left[1+k^2T_N^2(f)\right] \tag{6.3.4}$$

Several factors must be considered in designing a LPF. For example, if insertion loss is a high priority, transmission loss in passband has to be minimised; if a fast roll-off or sharp cut-off is desirable, a higher order equal-ripple LPF can be used. By choosing appropriate types of LPFs and number of orders, a sharp cut-off and a moderate transmission loss is obtainable.

### 6.3.2 LPFs for Bias Tees

Since LPFs are used for bias tees purpose in this project, the most important factors for design consideration are not insertion loss and phase linearity in the passband but the cutoff frequency and stopband reflection (or attenuation) rate . The cutoff frequency of a LPF has to be smaller than the oscillation frequency of the Gunn oscillator so that only DC bias can go through the LPF and RF signal will be blocked. Ideally the oscillator frequency should coincide with the frequency where the stopband reflection coefficient is maximised (or maximum attenuation). In this case, minimum amount of the signal power will leak through the filter and most of it will be reflected back and coupled out via a coupler. In addition, it is also desirable to have a wide stopband so that the second harmonic oscillation of the Gunn oscillator is also blocked. For instance, if a Gunn oscillator generates an oscillation at 50 GHz, the LPF must allow DC bias to pass through and have a maximum reflection coefficient at 50 GHz and reasonably big reflection coefficient at 100 GHz and even at 150 GHz.

An ideal LPF has infinite attenuation and 0 dB reflection in the stopband as demonstrated in Section 6.3.1; however, this is impractical. The attenuation of an LPF is achieved by deploying resonators because the resonances form transmission zeros. In order to achieve wideband attenuation, several resonators with different resonant frequencies and appropriate distances are needed. Considering the flexible tuneability of resonant frequencies, radial stub resonators are used for implementing wide stopband LPFs. By cascading radial line stubs of different radiuses, several LPFs having different cutoff frequencies and stopband bandwidths have been designed, fabricated and tested.

### *6.3.2.1 A LPF Using Two Double Radial Line Stub Resonators with Equal Radiuses for W-band Application*

It has been discussed in Section 6.2.3 that single radial line open stub can be used as a resonator. Thus, it can work as a transmission zero for a bandstop filter [291]. Double radial line stubs have been demonstrated to have sharper cutoff frequency and wider stopband bandwidth [292]. In this project, an LPF using two double radial line stubs has been designed for even sharper cutoff and higher attenuation in the stopband.

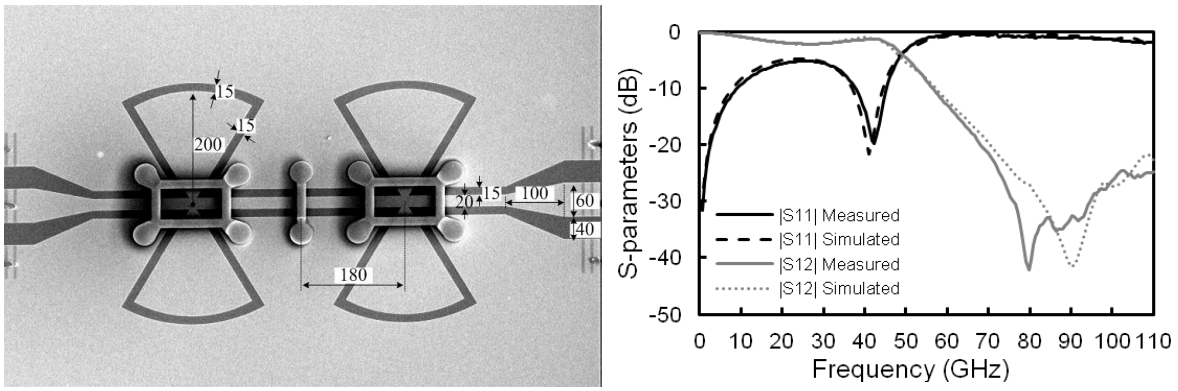


(a) (b)

**Figure 6-19** (a) SEM image of a second order double radial line LPF and its (b) *S*-parameters. The radius of the radial line is 200 μm and its sectorial angle is 60 ° and the distance between the two double radial line resonators is 360 μm.

Figure 6-19a shows the SEM image of the fabricated component and Figure 6-19b shows the measured and HFSS-simulated *S*-parameters for the components. Each radial line stub has a radius of 200 μm and sectorial angle of 60 ° that provides a resonant frequency of 78 GHz according to Figure 6-17. To minimise the coupling between two radial line stubs, the minimum distance, *L*, between them was set to be 360 μm. One can see from Figure 6-19b that the LPF has a cut-off frequency at near 50 GHz. The port reflection coefficient is better than 1 dB and transmission coefficient is better than 15 dB from 60 GHz to 110 GHz. This device can work as a bias "T" for a *W*-band Gunn oscillator.

Since the distance between the two double radial line resonators also affect the bandwidth of this LPF, simulation on the LPF regarding to the increase of *L* has been carried out using HFSS. The results are plotted in Figure 6-20. It can be seen that the increment of *L* decreases the cut-off frequency as well as downshifts the transmission zeros. These results indicate that the stopband region of the LPF can be shifted in a certain range by changing the distance between the double radial line resonators.

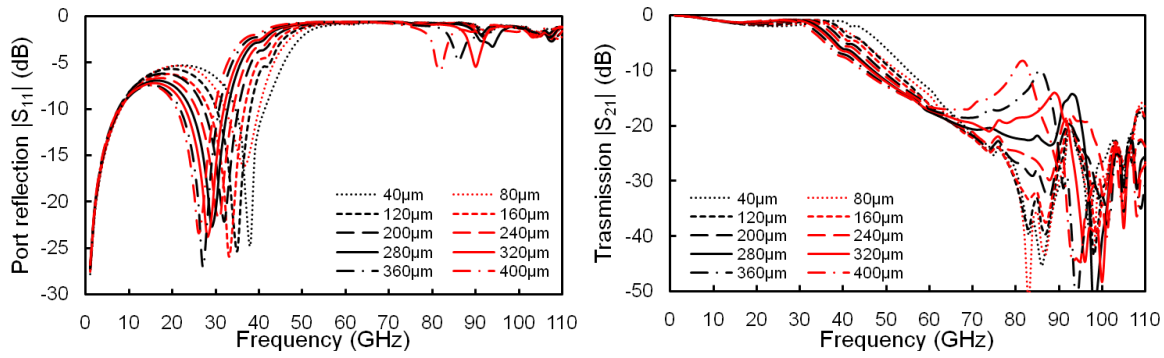


(a) (b)

**Figure 6-20** The simulated *S*-parameters of the LPF as the distance between the two double radial line resonators increases from 360 μm to by a step of 40 μm.

### *6.3.2.2 A LPF Using Two Double Radial Line Resonators with Unequal Radiuses for V and W-band Applications*

Two double radial line stub resonators with different radiuses (400 μm and 200 μm) were used to make an LPF with lower cutoff frequency and wider stopband bandwidth.

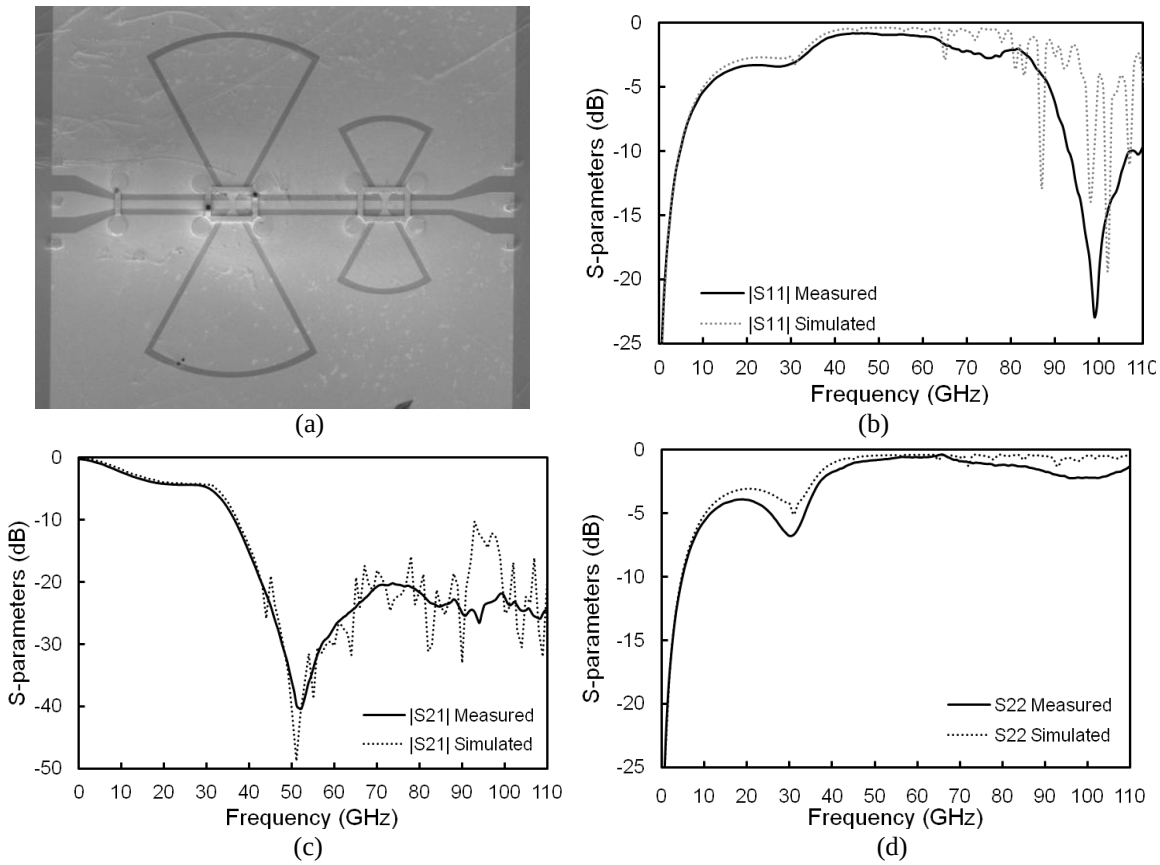


(a) (b) (c) (d)

**Figure 6-21** A second-order LPF bias choke for higher order harmonic suppression up to 110 GHz. The radiuses of two different double-radial line stubs are 400 μm, and 200 μm. (a) SEM image of the LPF, and its the simulated and measured (b) reflection coefficients of port 1 (left port), (c) transmission, and (d) reflection coefficient of port 2 (right port).

According to Figure 6-17 in Section 6.2, 400 μm and 200 μm radial line stubs resonate at 45 GHz and 78 GHz, respectively. Thus, the LPF using these stubs should give reasonable attenuation in the *V*-band and *W*-band. The distance between the two asymmetric double radial line resonators is 390 μm in order to minimise the cross couplings between radial line stubs. Figure 6-21 shows the micrograph of the LPF filter and its simulated and measured *S*-parameters. It can be seen that port 2 reflection coefficient $|S_{22}|$ is better than 2 dB and transmission is better than 15 dB from 45 GHz to 110 GHz. This leads to its application for a 50 GHz Gunn oscillator to block its both fundamental and second harmonic oscillation or a 100 GHz Gunn oscillator to prevent its fundamental oscillation from leaking through the filter.

### *6.3.2.3 Ultra Wide Stopband LPF Using Three Double Radial Line Open Stub Resonators*

If a number of double radial stubs with different radiuses are cascaded, the stopband bandwidth is inevitably increased. Figure 6-22 shows a LPF with three sets of double radial line resonators. The radiuses are 400 μm, 200 μm, and 100 μm.

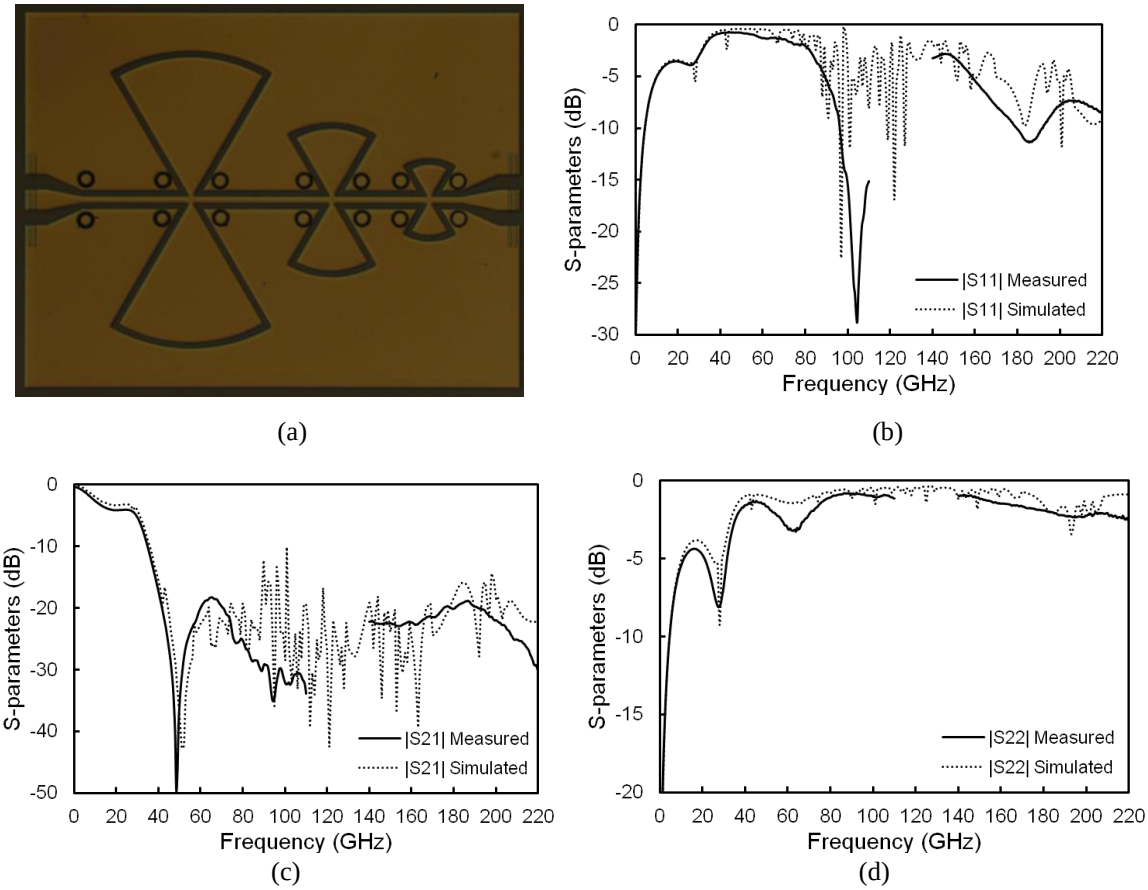


**Figure 6-22** A third-order LPF bias choke for higher order harmonic suppression up to 220 GHz. The radiuses for three different double-radial line stubs are 400 μm, 200 μm, and 100 μm. (a) Micrograph of the LPF, and its the simulated and measured (b) reflection coefficients of port 1 (left port), (c) transmission, and (d) reflection coefficient of port 2 (right port).

The distances between the 400 μm and 200 μm double radial line resonators and between the 200 μm and 100 μm double radial line resonators are 390 μm and 280 μm, respectively in order to minimise the cross couplings between radial line stubs. Figure 6-26a shows the micrograph of the LPF before airbridges were fabricated. The simulated and measured results of the complete LPF shown in Figure 6-22b-d indicates a stopband ($|S_{21}|$<-20 dB) from approximately 40 GHz to above 220 GHz, and port 2 reflection ($|S_{22}|$>-2 dB) from 80 GHz to 220 GHz. This LPF is suitable for biasing a *W*-band Gunn oscillation up to its second harmonic, or even third harmonic oscillation blocked from passing through the filter.

## 6.4 Couplers for RF By-passing and DC-blocking

### 6.4.1 Introduction

Couplers are used to transfer signals from one component or device to another. Microwave and millimetre-wave couplers can have three-ports or four-ports. A four-port directional coupler can be made into a three-port coupler by terminating the isolated port with a matched load. The commonly used directional couplers are the 90º and 180º hybrids, coupled-line coupler, Lange coupler and so on. The former two hybrid couplers are both DC and AC coupled, while the latter two are AC coupled only. This is ideal for implementing a planar Gunn oscillator, because the RF power of high frequency Gunn oscillators needs to be tested by using an on-wafer probe which has a limited DC current rating. If the DC current exceeds this limit, which is typically 100 mA at high frequencies e.g. 100 GHz, the probe can be damaged. Therefore the coupler works as a RF by-passing and DC-blocking component. The simplest coupler of this type is interdigital capacitor coupler.

### 6.4.2 Interdigital Capacitor

A coplanar interdigital capacitor has a layout as shown in Figure 6-23a. Its equivalent circuit can be simplified as Figure 6-23b when the length of fingers is short ($L_f$ < 100 μm) [293] and Figure 6-23c when the width of fingers $w_g$ becomes narrower and $L_f$ is longer [294]. The number of fingers may be limited by the central conductor width $w_{CPW}$ and the

gap between fingers $s_g$ and $w_g$. However, it is a good option to achieve higher equivalent capacitance by increasing the number of finger $N$ [293].

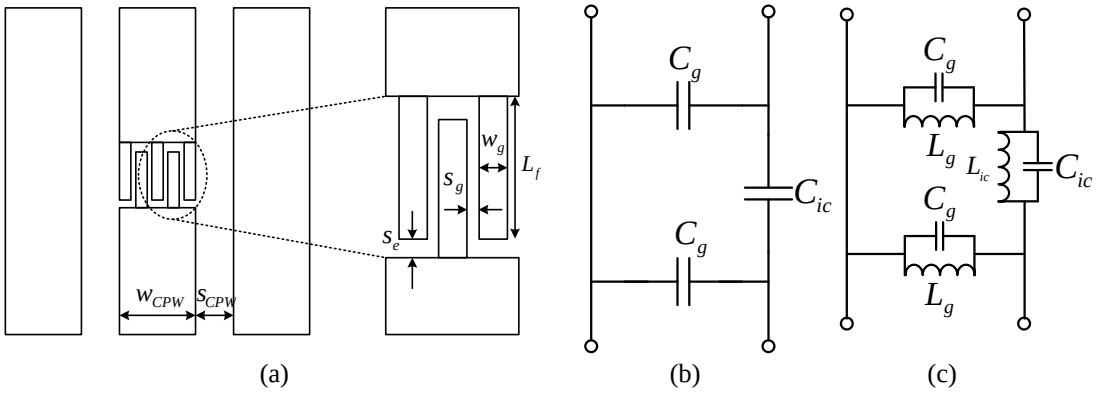


**Figure 6-23** (a) Coplanar interdigital capacitor and its equivalent circuits, (b) equivalent circuit from [293] (c) equivalent circuit from [294] .

### 6.4.3 Interdigital Couplers

A seven finger ( $N$ =7) interdigital capacitor has been designed in this project. The device was initially designed by using the data from [293, 294] and further optimised using HFSS simulation. The simulated *S*-parameters (as the transmission and port matching are crucial for a coupler) for variations of $s_g$, $w_g$, and $L_f$ are shown in Figure 6-24. It can be seen in Figure 6-24a that the transmission zero or resonance frequency shifts downwards for the increase of $s_g$ when all other parameters ( $w_g$ =22 μm, $s_e$ =14 μm, $L_f$ =200 μm) were fixed. This is because an increase of gap width between fingers leads to increase of total width of the capacitor. Thus the total capacitance as shown in Figure 6-23c increases and therefore the resonance frequency decreases. Similarly, Figure 6-24b shows the change of port reflection and transmission versus the change of conductor width. With all else being equal, the increase of conductor width will lead to an increase of total capacitance and therefore a decrease in the resonant frequency. Figure 6-24c and d also indicates increase of finger length decreases the resonant frequency. The parasitic capacitance, $C_g$, remains unchanged during the those simulations due to the unchanged distance between the fingers and the ground conductors [294].

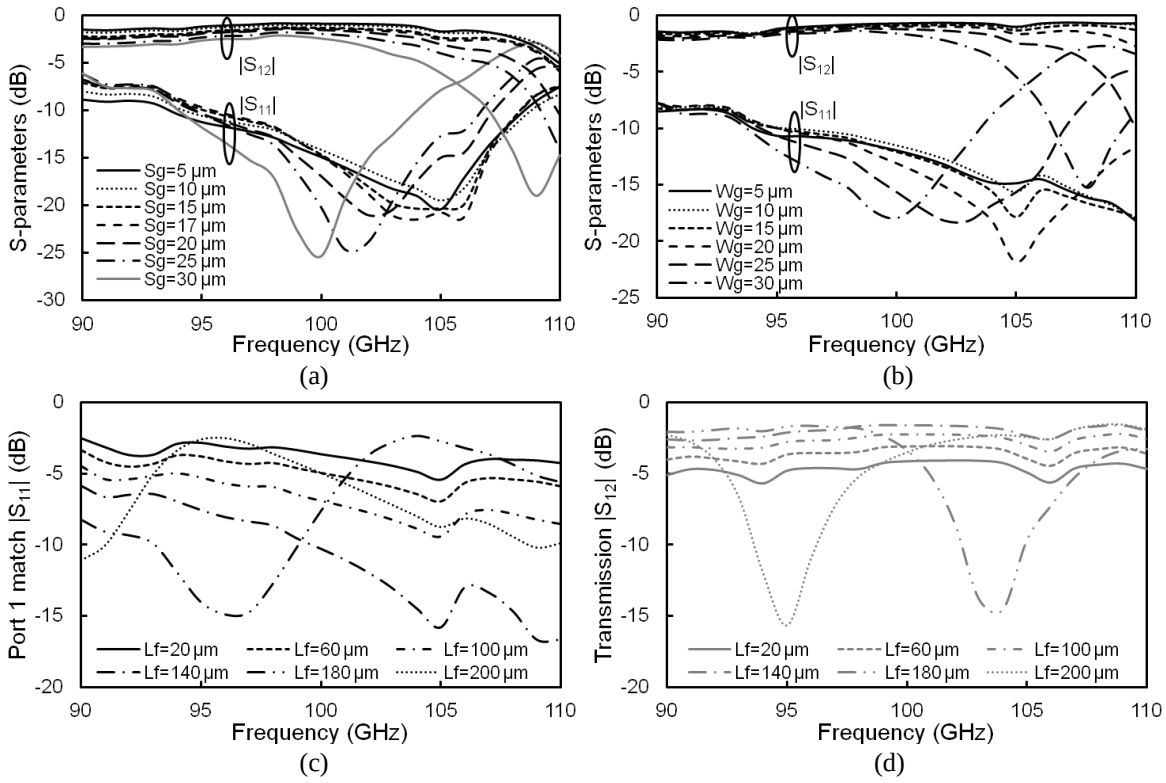


**Figure 6-24** Simulated *S*-parameters of interdigital capacitor in the frequency range of 90 GHz to 110 GHz. (a), with all other parameters were fixed the gap between fingers $s_g$ was varied from 5 µm to 30 µm, (b) with all other parameters were fixed the finger width $w_g$ was varied from 5 µm to 30 µm, (c) and (d) indicate the port 1 reflection and the transmission, respectively, as the finger length $L_f$ varied from 20 µm to 200 µm.

The finalised parameters for the coupler that has the highest transmission and lowest reflection at 90 GHz are shown in Table 6-IV. Figure 6-25 shows the measured S-parameters of the fabricated interdigital coupler. The coupler has an insertion loss of 1.8 dB and ports 1 and 2 reflections of -31 and -23 dB, respectively.

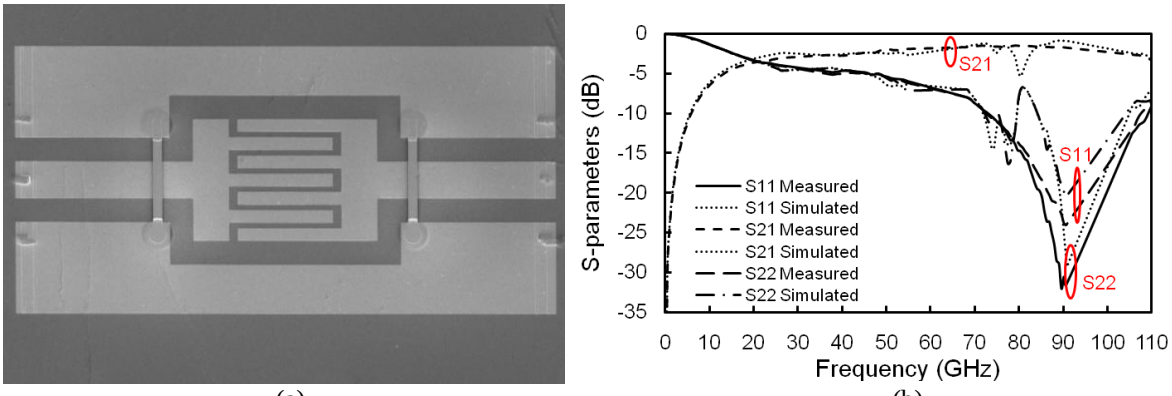


**Figure 6-25** (a) SEM image of the interdigital coupler (b) The measured and HFSS simulated coupler using a 7-finger interdigital capacitor for 90 GHz operation.

**Table 6-IV** The parameters for an interdigital coupler optimized for operating at 90 GHz.

| | $L_f$ ( μm) | $w_g$ ( μm) | $s_g$ ( μm) | $s_e$ ( μm) | $\|S_{11}\|$ (dB) | $\|S_{21}\|$ (dB) | $\|S_{22}\|$ (dB) |
|---|---|---|---|---|---|---|---|
| Value | 175 | 20 | 10 | 15 | -31 | -1.8 | -23 |

### 6.4.4 Proposed Integrated Planar Gunn Oscillators

Figure 6-26 illustrates one of the proposed integrated planar Gunn oscillators operating over 100 GHz. The integrated planar Gunn oscillator consists of four parts, namely a LBF, a pair of planar Gunn diodes, a double stub resonator, and an interdigital coupler. The LBF, as demonstrated in Section 6.3.2.3, has three double radial line stub resonators. It shows a stopband from approximately 40 GHz to above 220 GHz, and port reflection $|S_{22}|$>-2 dB from 80 GHz to 220 GHz. The two planar Gunn diodes are identical with anode-cathode distance ($L_{ac}$) of 1.1 μm. They are constructed in a back-to-back layout. The single device performance has been given in Chapter 4, Section 4.2.3.2. It produces a maximum power of -4.5 dBm (-6.7 dBm before deducing the test system loss) at 101.3 GHz. The double stub radial line resonator has a resonance frequency of 100 GHz and an approximate Q factor of 150. The interdigital coupler has the same parameters as the demonstrated 90 GHz coupler (Figure 6-25) except the gap width, $s_g$, between fingers which is 20 μm for this design. According to the simulation results shown in Figure 6-24, the coupler has port matching better than -15 dB and transmission better than -2.0 dB at near 100 GHz.

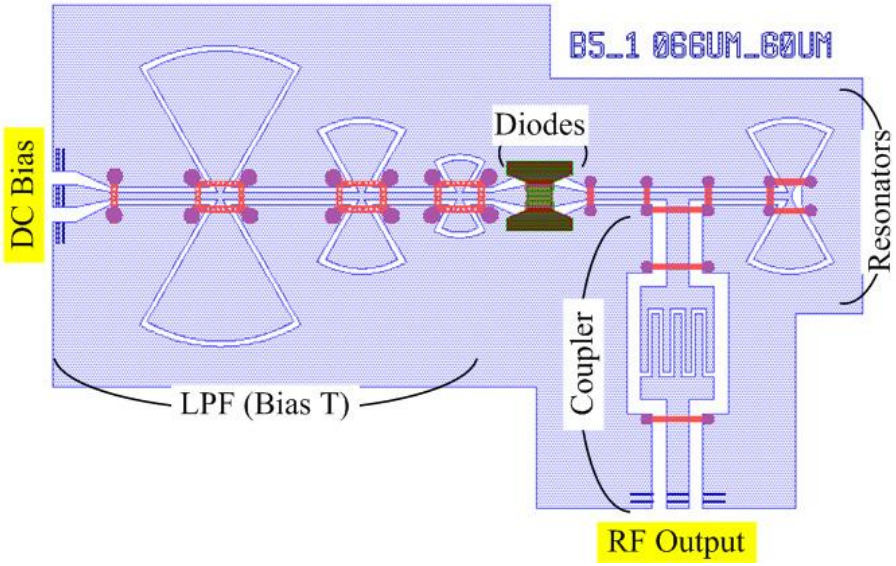


**Figure 6-26** A proposed integrated planar Gunn oscillator.

A GSG probe having high current performance can be placed on the LHS of the proposed planar Gunn oscillator for biasing the planar Gunn diodes as shown in Figure 6-26. The expected high frequency current oscillation (~100 GHz) is coupled out from the interdigital coupler. Ideally, no fundamental and second harmonic signals can leak through the LPF.

## 6.5 Power Combiners/Dividers

Power combiners have been investigated for the purpose of combining multiple planar Gunn diode oscillators to improve the overall output power. The most commonly used power combiners is Wilkinson combiners/dividers [295] that can combine two and (or) more in-phase signals. Several modified Wilkinson combiners/dividers have been reported to achieve wider bandwidth, better port matching, less transmission loss and high port isolation [296-304].

### 6.5.1 Analysis of Conventional Wilkinson Dividers

Figure 6-27 shows a schematic circuit of an ideal 3-dB Wilkinson power divider and its simulated *S*-parameters. The divider has port 1 as an input and port 2 and port 3 as outputs when working as a power divider. Due to reciprocity, port 1 becomes the output when port 2 and port 3 are used inputs in the case of a power combiner. Two guided quarter-wave length transmission lines connect the input port and output port. A resistor is inserted between two output ports to provide port isolations. For equal power splitting and good matching at all ports at design centre frequency $f_0$, the two quarter-wave transmission lines should have characteristic impedance of $\sqrt{2}Z_0$ and the isolation resistor has resistance of $2Z_0$. For arbitrary power splitting with power of $P_2$ and $P_3$ at ports 2 and 3, respectively, the characteristic impedances of the two quarter-wave transmission lines $Z_0^{12}$ (between ports 1 and 2) and $Z_0^{13}$ (between ports 1 and 3) and the isolation resistor $R_{ISO}$ (between ports 2 and 3) are governed by the following equations [286],

$$Z_0^{13} = Z_0\sqrt{\frac{1+k^2}{k^3}} \tag{6.5.1}$$

$$Z_0^{12} = k^2 Z_0^{13} = Z_0\sqrt{k(1+k^2)} \tag{6.5.2}$$

$$R_{ISO} = Z_0(k + \frac{1}{k}) \tag{6.5.3}$$

where $k = \sqrt{P_3/P_2}$ .

Simulated S-parameters of the device with ideal components using Advance Design System (ADS) are plotted against normalised frequency in Figure 6-27b. It can be seen that ports are well-matched and isolation between output ports is good in a narrow bandwidth around the centre frequency.

To analyse the circuit and determine the isolation resistors and characteristic impedance of the quarter-wave transmission lines for equal power division, the even-odd mode analysis method is used. Since the device is symmetric to the central reference line, Figure 6-27a is redrawn and plotted in Figure 6-28a when two excitations with equal amplitude are applied to output ports 2 and 3. Assuming all ports are matched to $Z_0$, then port 1 can be considered as being terminated by two parallel resistors with resistance of $2Z_0$. The isolation resistor can also be split into two halves that are mirrored along the reference line.

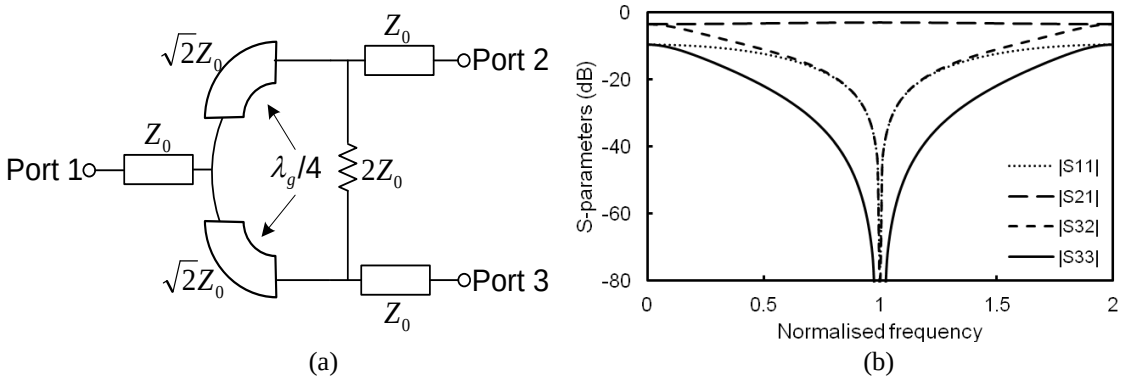


(a) (b)

**Figure 6-27** (a) Schematic circuit of a 3-dB Wilkinson divider and (b) its simulated ideal *S*-parameters. The frequency is normalised to the design centre frequency.

For even mode operation, the excitations at ports 2 and 3 are equal in both amplitude and polarization. The voltage potentials at point 2 and point 3 (Figure 6-28a) are equal, and there is no current flow between these two points. Hence, it looks like an open circuit in-between the two halved resistors. Similarly, potentials at point 1 are equal at both arms and it can be seen open-circuited between two arms at point 1. Finally, the entire device can be equally split into two parts along the reference line, for simplicity only top part is shown in Figure 6-28b. Therefore, the characteristic impedance of the quarter-wave length

transmission is derived by $\sqrt{2}Z_0$ for good port matching at port 2 or 3.

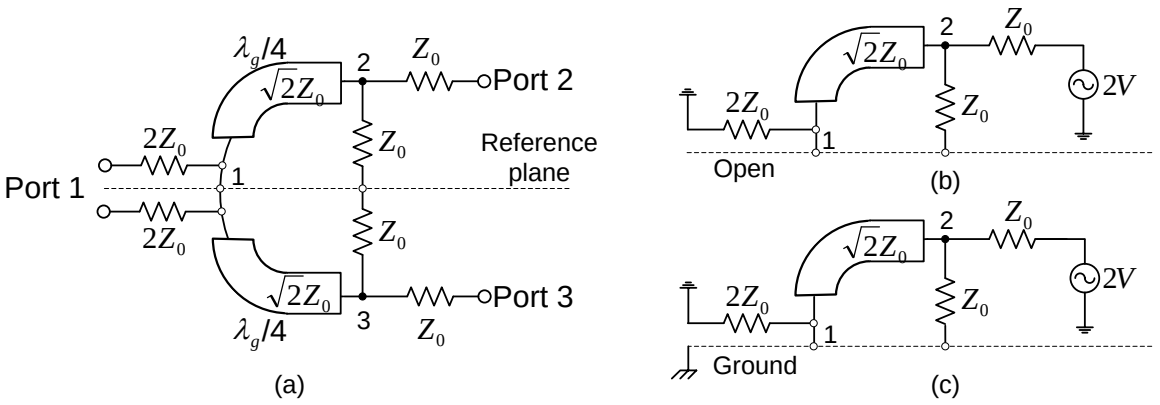


**Figure 6-28** Using even-odd mode method to analyse Wilkinson combiner/divider. (a) a re-drawn circuit of Figure 6-27a, (b) half of the even mode equivalent circuit when excitation was applied on output port, (c) half of the odd mode equivalent circuit when excitation was applied on output port.

For odd mode operation, excitations at ports 2 and 3 are equal in amplitude and opposite in polarisation. The opposite potentials at point 2 and point 3 (Figure 6-28a) lead to a virtual ground between two resistors. Similarly, there is a virtual ground between two transmission lines at point 1. Thus, the top half of the divider can be drawn as Figure 6-28c. The port matching condition is satisfied when there is no reflection at point 2 in Figure 6-28c, therefore, half of the isolation must equal to the port characteristic impedance $Z_0$.

### 6.5.2 Ring Wilkinson Combiner/Divider with Ultra-wideband Isolation

One disadvantage of the conventional Wilkinson divider is its narrowband port isolation performance. A modified form of the Wilkinson divider to achieve a broadband isolation response was proposed by Xue *et al*. [298]. They replaced the single isolation resistor with a lumped-distributed network that comprised two quarter-wavelength transmission lines, a phase inverter, and two resistors. The topology was demonstrated using parallel striplines (PS) and made use of two through substrate vias to form the phase inverter. The tapered baluns also required in the design occupied a large proportion of the overall circuit area. Two uniplanar implementations were later realised using slotline and asymmetric coplanar stripline [305]. The disadvantage of these is the greater occupied area due to the quarter-wavelength radial stubs used in the design.

A new compact ring divider topology using a combination of SCPS and CPW was

investigated in this project [303, 304]. A prototype has been developed at *K*-band as a proof-of-concept, and subsequently, a design at *W*-band has been performed to realise a power combined planar Gunn diode oscillator. The coplanar design enables the phase inverter to be realised using an airbridge cross-over [306] that twists the signal and ground paths of a CPS. Compared to other implementations, this results in minimal parasitics and no significant penalty of increased circuit area. The proposed coplanar design can therefore be fabricated with a smaller size. More reliable performance is expected.

### *6.5.2.1 Design*

- **Synthesis**

A simplified layout of the proposed ring power divider is shown in Figure 6-29. It comprises four quarter wavelength coupled lines that are connected in a ring configuration. The transition to coplanar waveguide ports are accomplished by compact dual baluns [264] that are formed by two CPW to SCPS tee-junctions [307]. The phase inverter is implemented using a single airbridge cross-over. Three other airbridges are used to equalise the ground potentials in the CPW-to-SCPS balun transition.

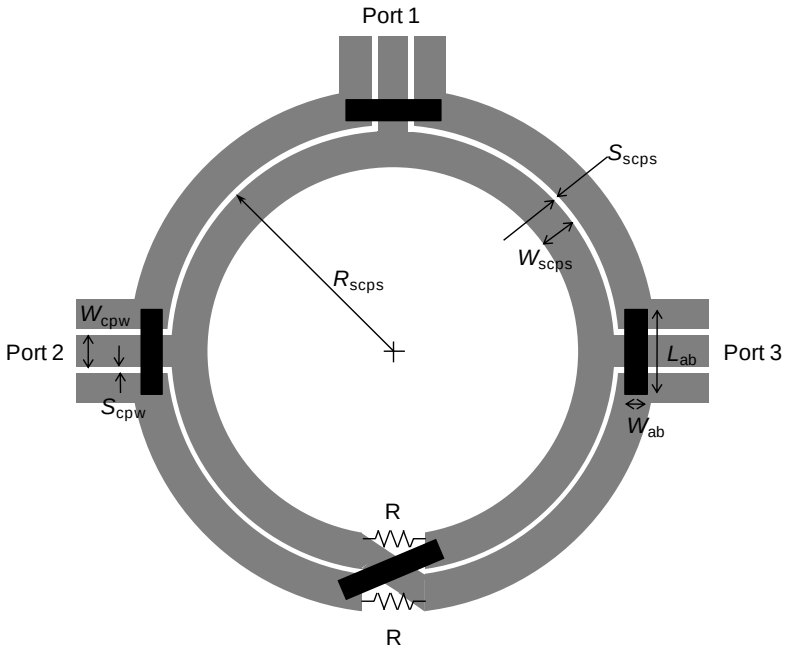


**Figure 6-29** Simplified layout view of the SCPS ring divider.

For a 50 Ω design, the required characteristic impedance of the SCPS lines is 70.7 Ω and odd-mode impedance is approximately 35.3 Ω [264]. Two dividers have been designed for

operating frequency range in the *K*-band and *W*-band. The CPW trace widths were chosen to be 60 μm for the *K*-band design and 20 μm for the *W*-band design (transitions from 20 μm to 60 μm have been used for *W*-band operation for a compatibility with on-wafer measurement probes). Using these same values for the SCPS width, the required spacings of the SCPS transmission lines were synthesised to be 24 μm and 8 μm according to Figure 6-6. The simulations of the ring divider were performed using the HFSS. Physical dimensions for *K*-band and *W*-band ring power combiner/divider of the final optimised design are given in Table 6-V.

**Table 6-V** Dimensions for the optimised *K*-band and *W*-band ring power combiner/divider.

| **Parameters** | **Description** | **Value (*K*-band)** | **Value (*W*-band)** |
|---|---|---|---|
| $W_{SCPS}$ | Conductor width of SCPS | 60 μm | 20 μm |
| $S_{SCPS}$ | Gap between SCPS conductors | 24 μm | 8 μm |
| $R_{SCPS}$ | Radius of the ring | 672 μm | 206 μm |
| $W_{CPW}$ | Center conductor width of CPW | 60 μm | 20 μm |
| $S_{CPW}$ | Gap between centre and ground conductors of CPW | 40 μm | 15 μm |
| $G_{CPW}$ | Ground conductor width of CPW | 60 μm | 20 μm |
| $W_{AB}$ | Width of the airbridges | 50 μm | 10 μm |
| $L_{AB}$ | Length of airbridges | 200 μm | 70 μm |
| $H_{AB}$ | Height of airbridges | 4 μm | 4 μm |

- **Cross-over phase inverter**

The phase inverter design is based on an SCPS airbridge cross-over. The dimensions of the airbridge cross-overs are 50 μm × 200 μm for *K*-band, and 12 μm × 50 μm for *W*-band that were optimised for low loss and good matching using the HFSS simulation tool. The dimensions of the isolation resistors are 40 μm × 20 μm for *K*-band and 16 μm × 8 μm for *W*-band to achieve a resistance of 100 Ω. The simulation results shown in Figure 6-30 indicate that the SCPS cross-over has less than 0.05 dB extra loss and 180 ºphase shift with approximately 5.5 ºphase difference up to 50 GHz for *K*-band application, and less than 0.1 dB extra loss and 4 º phase difference up to 110 GHz for *W*-band application when compared with uniform SCPS of the same physical length. These performances are better suited for millimetre-wave frequency operation in comparison to the via-based phase inverter implementation which has been previously reported in [298] because the elevated airbridge cross-overs have lower parasitic inductance.

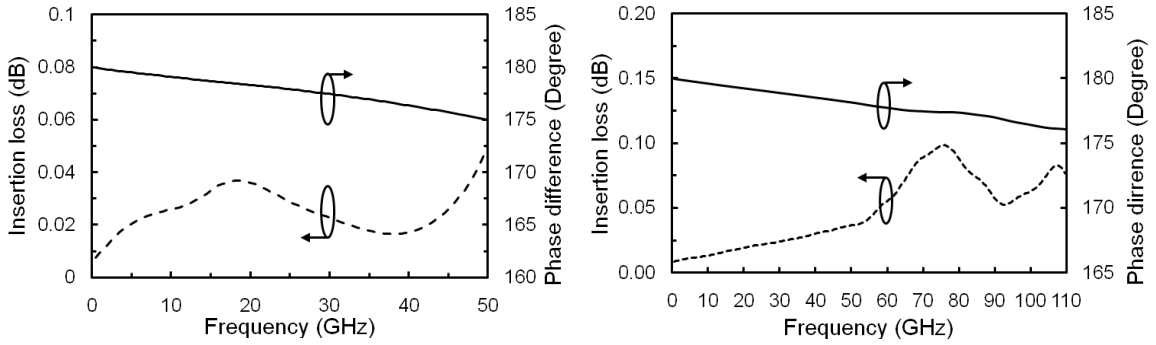


**Figure 6-30** Simulated extra losses and phase differences for SCPS airbridge cross-overs compared with uniform SCPS of the same physical length for (a) *K*-band, and (b) *W*-band applications.

### *6.5.2.1 Effect of Resistor Tolerance*

The output isolation responses and output port matching of the ring divider are sensitive to the tolerance of the on-chip resistors. To investigate this, a parametric analysis was performed using HFSS to vary the resistivity value of the isolation resistors. The simulated variation in the output isolation responses and output reflection coefficients for both *K*-band and *W*-band applications are shown in Figure 6-31.

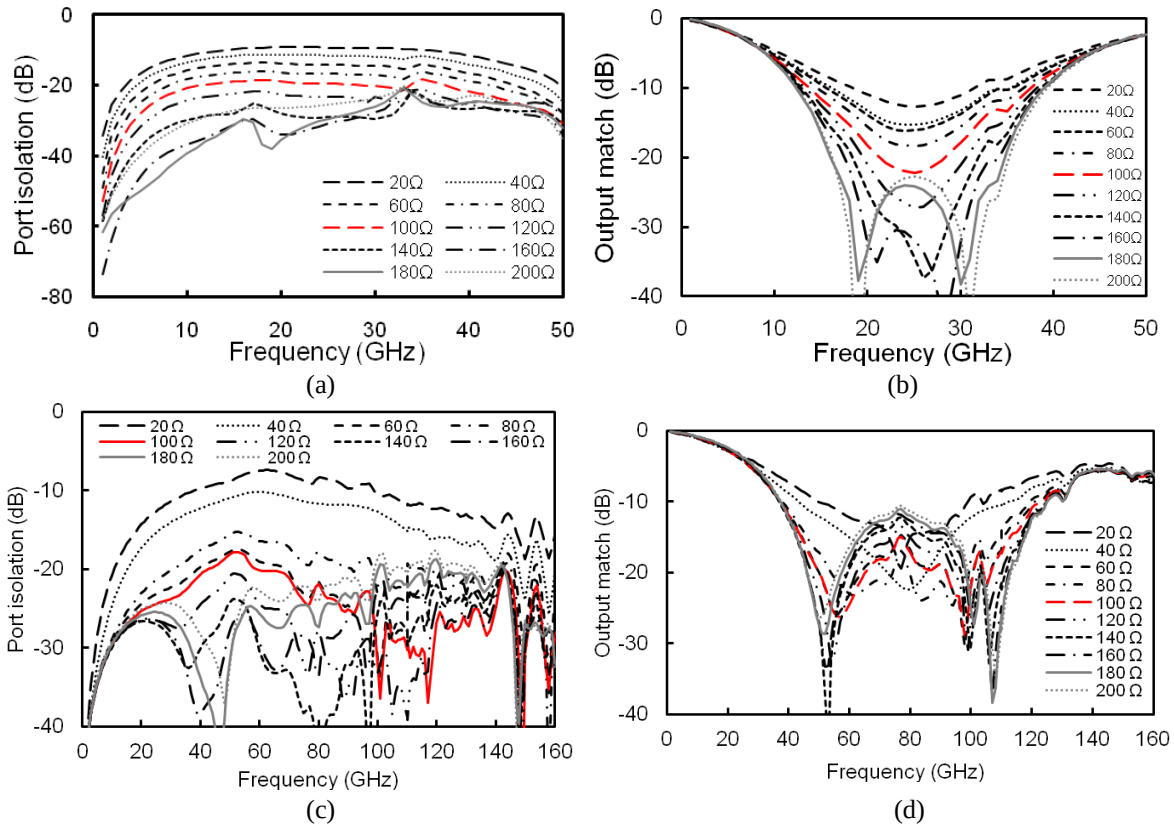


**Figure 6-31** Simulated (a) and (c) variation of output port isolations, and (b) and (d) output port matches for different resistor values (in 20 Ω steps).

The responses for $|S_{22}|$ and $|S_{33}|$ are similar to each other. It can be clearly seen from Figure 6-31a and c that the port isolations improve as the resistor values increase but begin to degrade at higher frequencies as the resistor values increase above 120 Ω. This indicates that a typical tolerance of ±20 Ω from the theoretical optimum resistor value, calculated using Equation 6.5.3, can provide a good isolation performance across a wide bandwidth. However, Figure 6-31b and d indicate that higher resistor values improve output port matching.

### 6.5.3 Experiments

#### *6.5.3.1 Component Fabrication*

To validate the proposed concept, the two ring divider designs were fabricated on a semi-insulating GaAs substrate of 620 $\mu$m thickness.

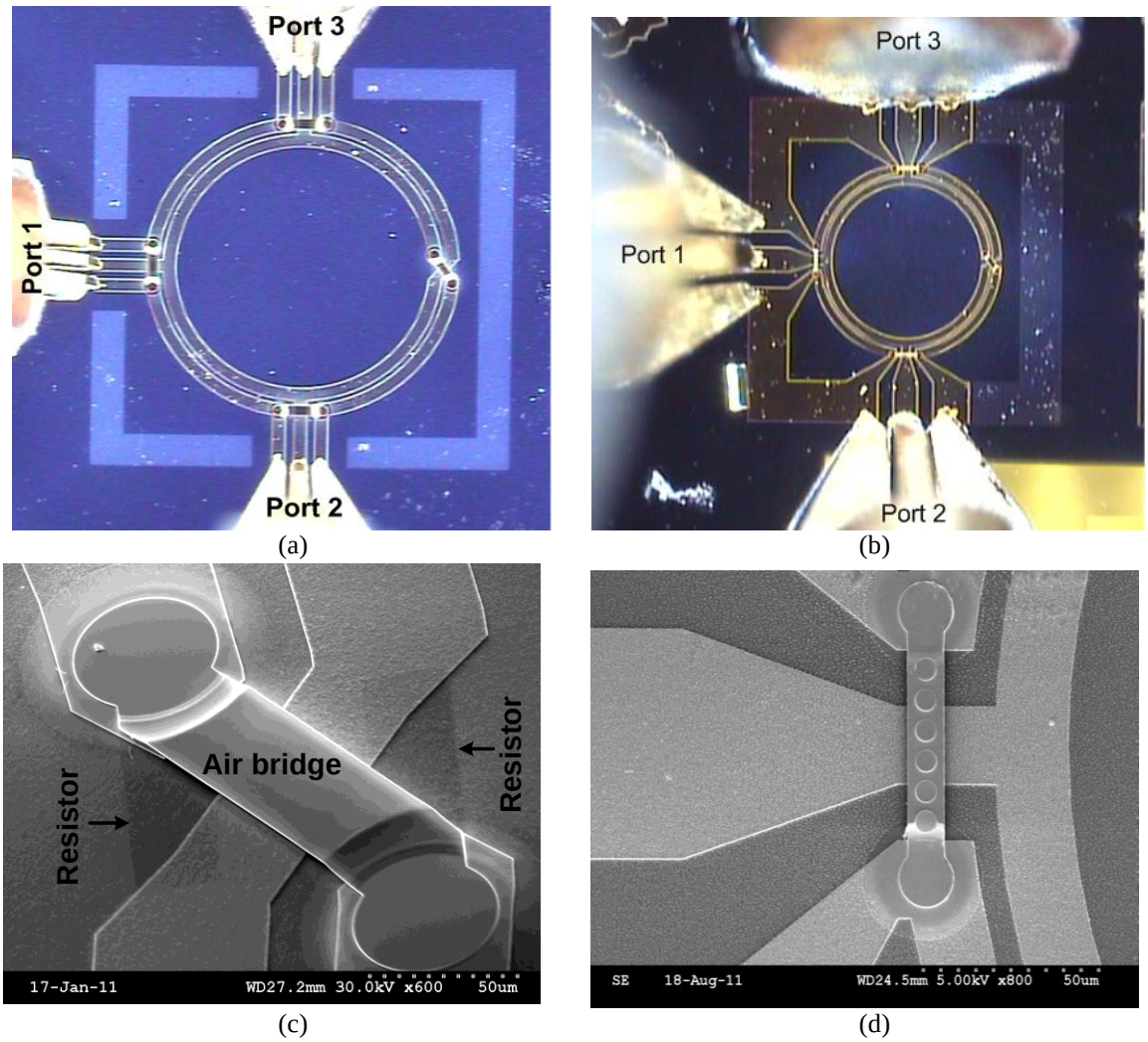


**Figure 6-32** (a) and (b) Microphotographs of the fabricated ring divider under tests, and (c) and (d) SEM images of the airbridge cross-over section of the *K*-band divider and the port 1 airbridge of the *W*-band divider, respectively.

The metal conductor patterns in gold were defined using EBL techniques with an evaporated gold thickness of 0.5 μm. The isolation resistors were formed using NiCr. The airbridges connecting the CPW ground conductors and forming the SCPS cross-over were also defined by EBL and fabricated using a dry etch process. The electrical performance of the resistors and airbridges were discussed in Section 6.1.2 and 6.1.3, respectively. Microphotographs of the two divider under tests and SEM images of the airbridge cross-over sections are shown in Figure 6-32. The chip sizes, including the probe pad feeds, are 1.9 mm × 1.9 mm for the *K*-band divider and 0.8 mm × 0.8 mm for the *W*-band divider.

*6.5.3.2 Component Characterisation*

The method of choice for characterising passive multi-port components, such as combiners, circulators and couplers, is to measure the insertion (transmission) and reflection parameters using VNA. However, at millimetre-wave frequencies, VNAs most commonly have only two test ports making it difficult to accurately test multi-port components. The conventional solution to this problem is to do a two-port measurement with the other ports terminated with a 50 Ω standard. For coaxial and rectangular waveguide-based multiport components, this solution works very well using a moveable twisted waveguide termination for example, but clearly this cannot be accomplished when using on-wafer waveguides. To overcome this problem, a series of duplicate components are fabricated in two-port configuration for on-wafer test, and the other ports terminated with 50 Ω thin-film resistor [280]. However, on-wafer probe systems impose a mechanical constraint that the two probes must always be in line with one another. Components must therefore deviate from their ideal design in order to accommodate the test system by introducing a 90˚ bend in a planar waveguide for compatibility with the measurement probe. As a consequence, components made for test are not strictly the same as the components made for final use in which no additional 90˚ waveguide bend would be added. Because of this modification for test components it becomes difficult to make entirely reliable measurements, and results can be controversial particularly at millimetre-wave frequencies [308].

As a result, a simple but accurate on-wafer measurement technique has been investigated for multi-port passive components. The measurement technique still uses a two-port VNA but additional probes with matched standard loads are used to terminate the unused ports. This allows the same component, rather than duplicate components, to be tested without

any modification of the test port. This technique has been used to test the three-port power dividers. The measurement setup is shown in Figure 6-33a. Calibration of the probes as shown in Figure 6-33b for the probe setup was performed using the SOLR thru method of calibration [155] which, until now, has not been validated above 50 GHz. A commercial alumina ISS CS-15 containing right-angled standards was used. Since the ports of the power divider are orthogonal to each other, three separate calibrations as shown in Figure 6-37c-e were carried out on a standard probe station with two probes while a third probe was used as the broadband load. The *S*-parameters of the ring divider were reconstructed based on the three sets of two-port scattering parameter measurements. By choosing the SOLR calibration technique, the need to fabricate replica components with the added constraint of only having in-line port layouts is avoided. This not only saves on costly chip area, but the resultant *S*-parameters are measured from a single device to give a true indication of its frequency response.

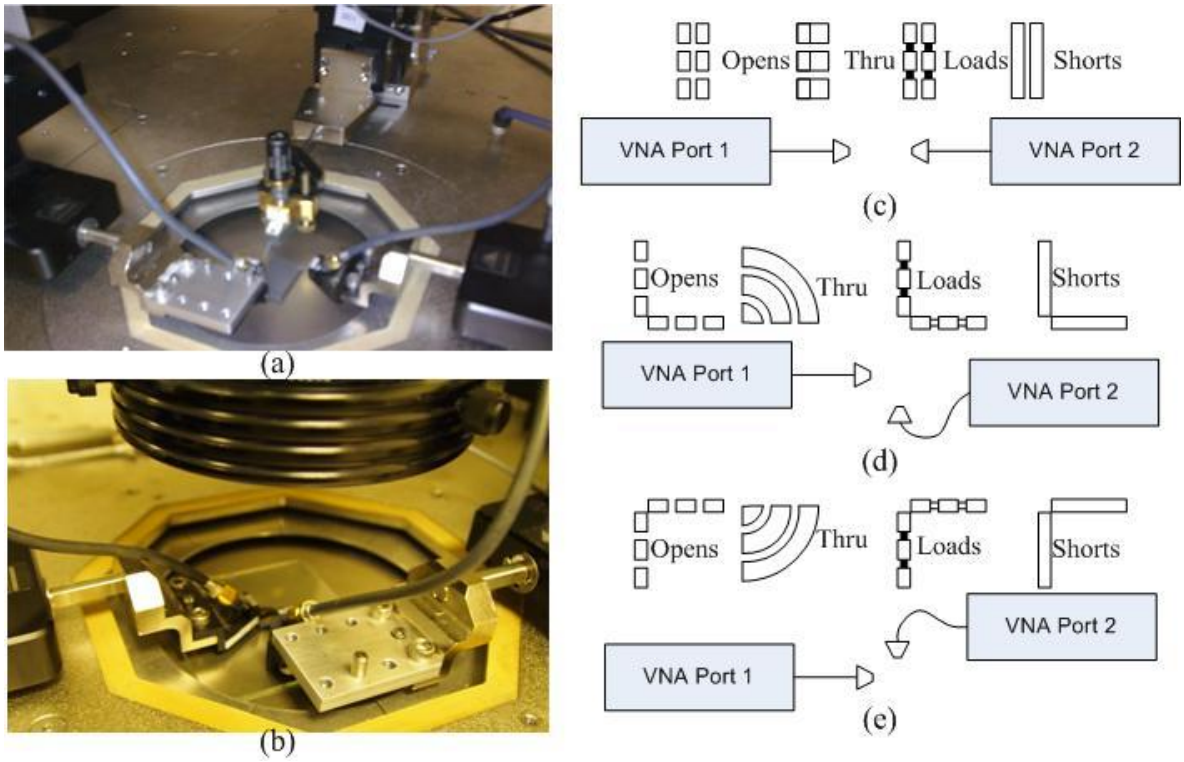


**Figure 6-33** On-wafer VNA measurement setup for components with orthogonal ports and illustration of SOLR calibration procedure. (a) The actual three-port measurement setup with the unused port terminated by a third probe and a broadband matched load, (b) SOLR calibration setup for orthogonal ports, (c)-(e) illustration of three separate calibrations for three different probe positions.

### *6.5.3.3 Measurement Results: K-band Power Divider*

Figure 6-34a-d shows the measured results that are in good agreement with the simulations. It can be seen that port isolation better than 20 dB is achieved across the bandwidth from

10 MHz to 50 GHz as predicted. The in-band insertion loss and port return losses are 0.6 dB and 15 dB over the frequency range from 15 GHz to 32 GHz, respectively. Slight discrepancies in the input port and output port matching are seen in Figure 6-34a and b, respectively. This difference may come from either the fabrication tolerance of the isolation resistors, as discussed in Section 6.5.2.1, or a slight error in positioning the probes during measurement. The measured amplitude and phase balance of the ring divider is shown in Figure 6-34e. These indicate that the output amplitude and phase balance are within ±0.5 dB and ±2 °, respectively, in the bandwidth from 10 MHz to 43 GHz.

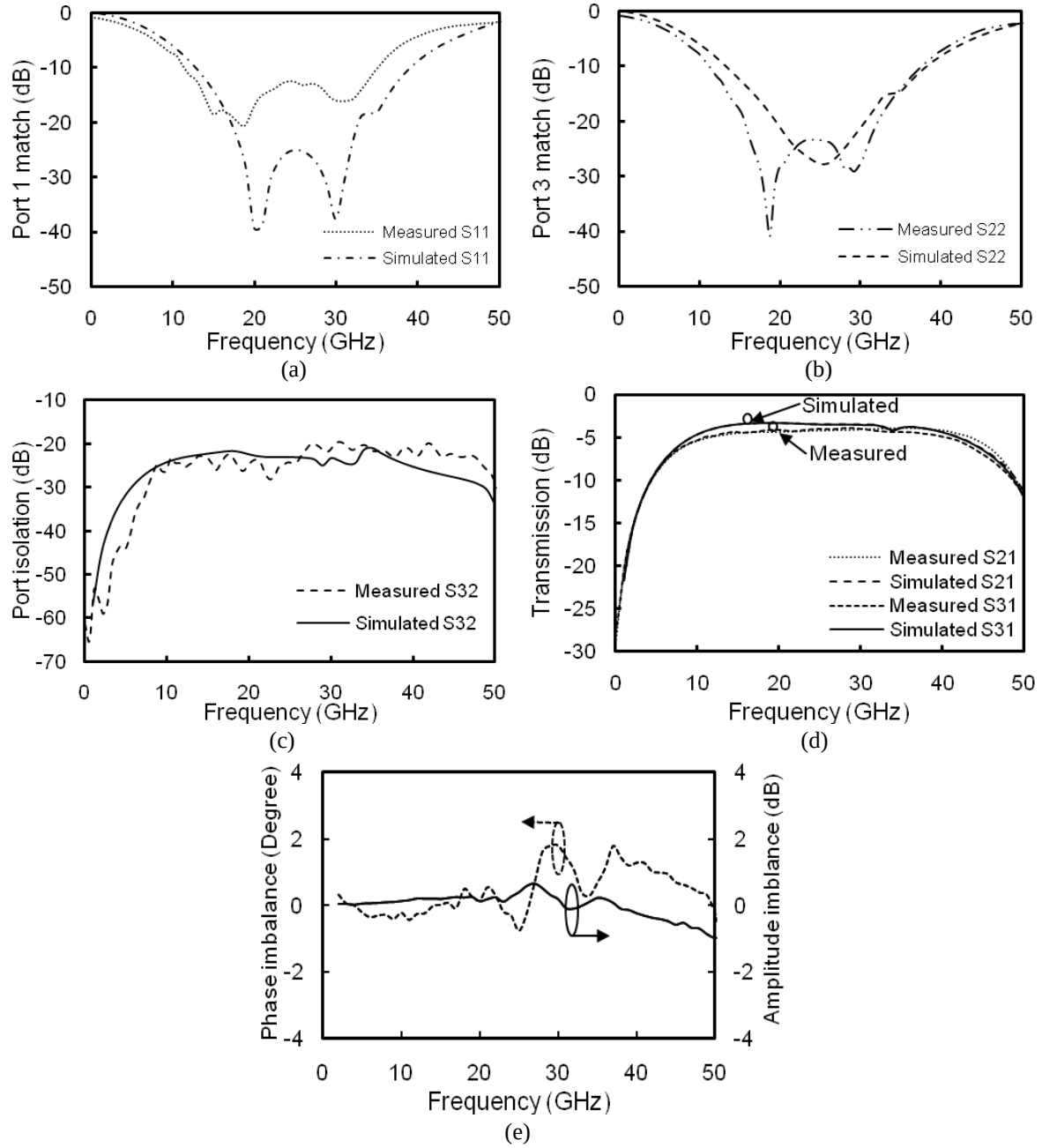


**Figure 6-34** Measured and simulated *S*-parameters of the *K*-band ring power combiner/divider. (a) Port 1 reflection $|S_{11}|$, (b) Port 3 reflection $|S_{33}|$, (c) Output port isolation $|S_{32}|$, (d) Port 1 to Port 2 transmission $|S_{21}|$, and (e) Measured phase $(S_{31}/S_{21})$and amplitude $|S_{31}/S_{21}|$balance response.

*6.5.3.4 Measurement Results: W-band Power Divider*

Figure 6-35a-d shows the measured results that are in excellent agreement with the simulations. It can be seen that port isolation better than 20 dB is achieved across the bandwidth from 10 MHz to 110 GHz as predicted. The in-band insertion loss and port return losses are 1.3 dB and 15 dB over the frequency range from 35 GHz to 110 GHz, respectively. The measured amplitude and phase balance of the ring divider is shown in Figure 6-35e. These indicate that the output amplitude and phase balance are within -0.15—0.05 dB and -1 °—-10 º, respectively, in the bandwidth from 10 MHz to 110 GHz.

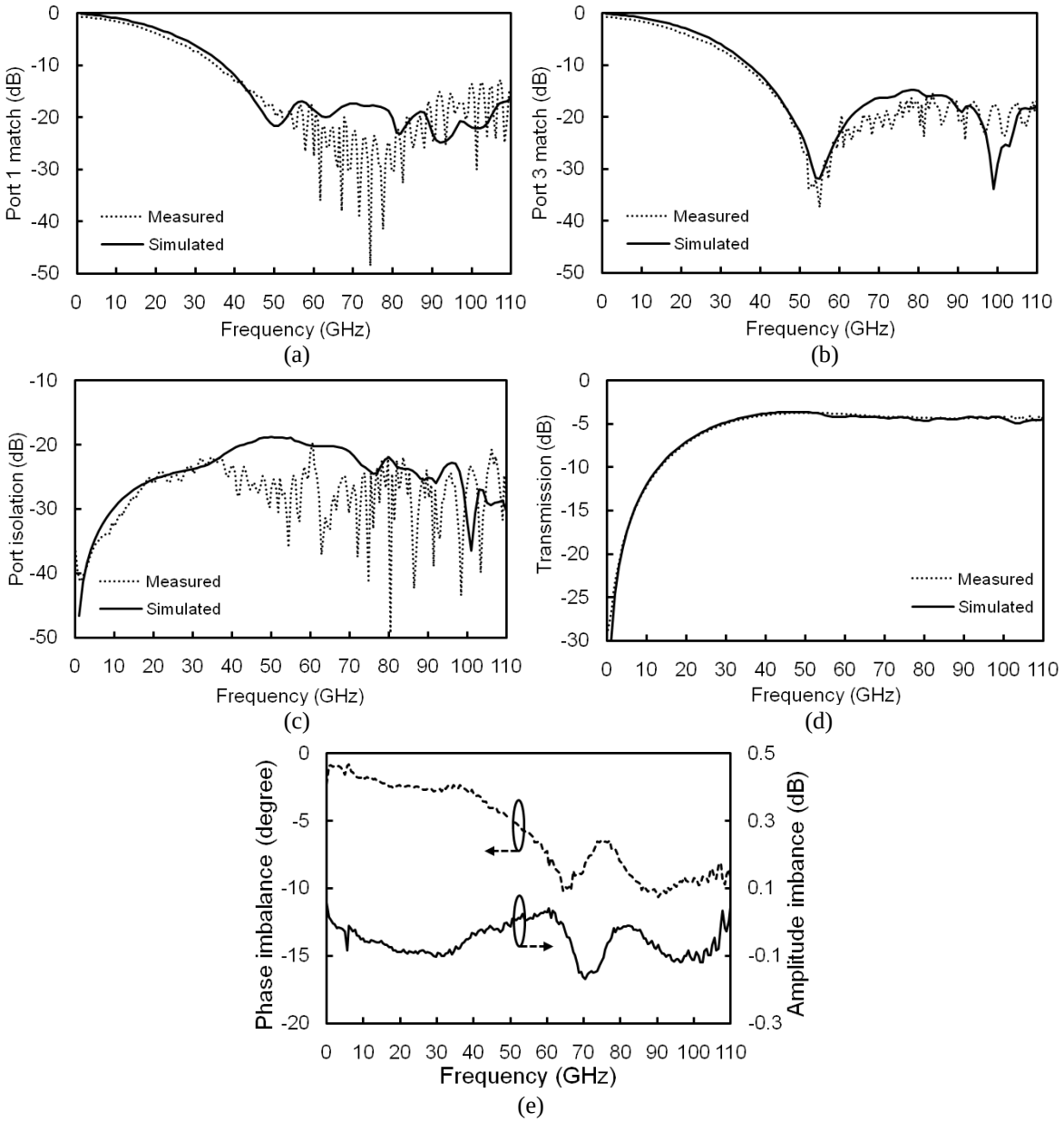


**Figure 6-35** Measured and simulated *S*-parameters of the *W*-band ring power combiner/divider. (a) Port 1 reflection $|S_{11}|$, (b) Port 3 reflection $|S_{33}|$, (c) Output port isolation $|S_{32}|$, and (d) Port 1 to Port 2 transmission $|S_{21}|$, and (e) Measured phase $(S_{31}/S_{21})$and amplitude $|S_{31}/S_{21}|$balance response.

*6.5.3.4 Comparison with Other Works*

Table 6-VI summarises the performance of the proposed power divider compared to recently published work by other authors. It can be seen that the proposed power divider demonstrate the combined advantages of a compact size, wideband high isolation, and uniplanar fabrication characteristics. Devices with comparatively smaller size demonstrate lower isolation bandwidth and require more complicated multilayer fabrication processes [296, 301].

**Table 6-VI** Comparison of performance characteristics of power dividers with broadband isolation implemented using different technologies and techniques.

| Reference | Centre Frequency ($f_0$) | Bandwidth ($\Delta f/f_o$) | | | Size | Technology | Fabrication |
|---|---|---|---|---|---|---|---|
| | | Reflection >15 dB | Transmission <4 dB | Isolation >20 dB | | | |
| [299] | 2 GHz | 75% | 120% | 234% | $0.52\lambda_g \times 0.73\lambda_g$ | Parallel-Strip lines | Double-sided |
| [305] | 0.75 GHz | 69%/ 79% | 105%/ 123% | 168%/ 240% | $0.46\lambda_g \times 0.64\lambda_g$ | ACPS Slotlines | Uniplanar |
| [301] | 30 GHz | <100% | † | 107% | $0.13\lambda_g \times 0.29\lambda_g$ | Microstrip & CPW | Multilayer |
| [297] | 15 GHz | 12% | <10% | ‡ | $>3\lambda_g \times 1.3\lambda_g$ | SIW | Vias required |
| [296] | ~10 GHz | ~110% | 140% | 150% | $\sim 0.42\lambda_g \times 0.14\lambda_g$ | Multiple wafer-level packaging | Multilayer |
| This work | 25 GHz/ 78 GHz* | 68%/ >35% | 76%/ >40% | >200 %/ >100% | $0.45\lambda_g \times 0.45\lambda_g$/ $0.54\lambda_g \times 0.54\lambda_g$ | CPW & SCPS | Uniplanar |

†Transmission loss is greater than 5 dB;

‡Isolation is less than 15 dB

*Full-band measurement is limited by the instrument. Only 10 MHz to 110 GHz were tested.

### 6.5.4 Combining Integrated Planar Gunn Oscillators

Figure 6-36 illustrates a proposed power combining circuit for combining two integrated planar Gunn oscillators operating over 100 GHz. The integrated planar Gunn oscillators have been described in Section 6.4.4. The DC inputs for the two individual oscillators are jointed at the LHS of the circuit and the RF outputs of the oscillators are combined using a

*W*-band ring power combiner. The proposed circuit can theoretically generate up-to 0 dBm power at 100 GHz.

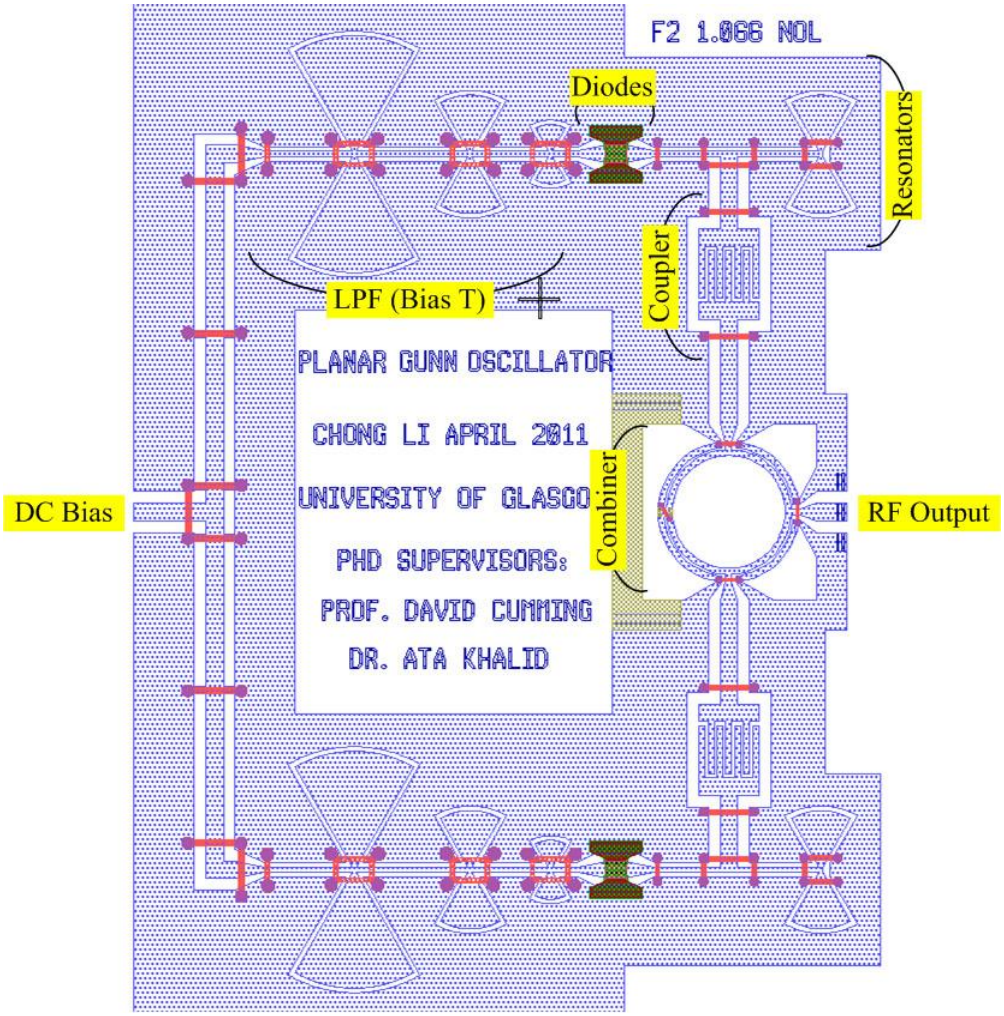


**Figure 6-36** A design circuit for combining two integrated planar Gunn oscillators using a ring combiner.

## 6.6 Conclusion

This chapter has described the design, modelling, fabrication and characterisation of planar passive components and circuits for planar Gunn oscillators. Fundamental passive elements, such as coplanar waveguides, coplanar striplines, thin-film resistors, and airbridges were first demonstrated. The design and (or) characterisation of radial line resonators, low pass filter bias chokes, couplers and power combiners/dividers were given separately in Section 6.1 to Section 6.5. The application of these passive components for integrated planar Gunn oscillators and for combined integrated planar Gunn oscillators were proposed in Section 6.4.4 and Section 6.5.4, respectively.

# CHAPTER 7

# CONCLUSIONS AND FUTURE WORK

In the past several years, the fast growing millimetre-wave and terahertz application market, such as communications, radar, imaging, spectroscopy, and security screening has driven the development of reliable and flexible signal sources. Gunn devices or transferred electron devices are excellent candidates to meet the demand due to their small size, excellent phase noise performance and simple structure. However, the conventional Gunn devices are limited by the fundamental operation frequency, such as 90 GHz for GaAs and 160 GHz for InP. Higher frequency operation is possible by extracting harmonics. However, the device efficiency is low when operating in the harmonic modes.

Heterojunction planar Gunn devices have demonstrated a record output frequency level, i.e. 108 GHz for GaAs based material system and could potentially operate at even higher frequencies. However, the first devices have shown weak RF power (e.g. -43.5 dBm) and low DC-to-RF efficiency. Therefore, it is the aim of this project to improve the power performance of such devices.

As shown in the thesis, several approaches have been investigated to achieve the power enhancement for planar Gunn devices. Optimising the original device design based on a GaAs material system has been proved to be an effective approach. By introducing additional δ-doping layers, the electron concentration in the channel is improved. This directly leads to higher power (doubled) and higher frequency (158 GHz for the fundamental mode oscillation) compared to the previous devices. Alternatively, introducing additional channels underneath the original channel can enhance the current density of the entire device therefore the RF power level although at slightly lower frequencies. The highest power obtained using this method reaches -4.5 dBm at 101 GHz

which is almost four orders higher than that from the previously demonstrated devices. Furthermore, another material system, $In_{0.23}Ga_{0.77}As$ for planar Gunn devices has also been investigated. The added 23% indium composition leads to wider a conduction band discontinuity between the channel and the barriers, better electron confinement, higher electron concentration in the channel, and higher frequency and power level of planar Gunn diodes made with this material than GaAs material.

Further explorations on planar Gunn devices have found multi-domain led multiple oscillations from a single device at high bias voltage conditions. The self-oscillating mixing effect has also been experimentally demonstrated. This feature of planar Gunn devices may lead to a simpler design topology of millimetre-wave front-ends from using a separate oscillator and a mixer to using a single Gunn device. Other experiments have shown planar Gunn devices are sensitive to light illumination, heat limitation for their output frequency and power as well as stability and lifetime.

The second approach to improve power performance for planar Gunn devices is to implement circuit technology. It is possible to combine multiple devices using power combiners. Benefiting from the planar topology of heterojunction Gunn devices, making highly integrated planar Gunn oscillators are possible. Several millimetre-wave planar components and circuits, operating at frequencies over 100 GHz, have been developed during this PhD work. They include basic elements, such as thin-film resistors, airbridges, coplanar waveguide-to-coplanar stripline transitions and coplanar waveguide based circuits, such as low-pass filters for bias tee applications, interdigital capacitor-based couplers, and ultra broadband ring combiner/dividers with high isolation. These components and circuits have been numerically simulated and experimentally validated and shown high performance for the proposed power combining circuits.

Another important aspect of contribution from this project is the development of several device/circuit characterisation methodologies. These include the one-port load-pull measurement technique for investigating the loading effect on the power and frequency performance of any one-port oscillator devices, using a VNA to detect oscillation, validation of the SOLR calibration method for *W*-band applications, and a novel

measurement technique for characterising planar multiport passive components using a two-port VNA system.

There are several potential directions for future development of planar Gunn devices, for example further device optimisation for high power and high frequency operations and circuit integrations.

Regarding to device optimisation, the current work focused on the development of planar Gunn diodes for transit-time mode of operation. This mode of Gunn oscillation is believed to be not as efficient in terms of DC-to-RF conversion efficiency as other modes of operation, such as LSA mode and quenched domain mode. In addition, oscillation frequency and power of other modes of operation are also superior to the transit-time mode. Therefore, it is worthwhile exploring the application of LSA or quenched modes of operation for planar Gunn devices in the future, especially for seven-channel devices due to their clear exhibition of NDR.

Since other operation modes of Gunn devices are circuit dependant, detailed knowledge of devices' circuit behaviours is necessary and essential in order to build high performance planar Gunn diode oscillators. Therefore, constructing accurate small-signal equivalent circuits for planar Gunn diodes are required. Another circuit related factor that may affect the performance of planar Gunn oscillators is the resonators. As discussed in Chapter 6, a high Q resonator ensures good frequency selectivity and stability of a Gunn oscillator. However, it is difficult to achieve Q factors using planar circuit technologies, as large as that obtained using lumped circuit technologies, such as air-filled metallic cavities. Nevertheless, other quasi planar technologies, such as substrate integrated waveguides may achieve this requirement. Therefore, it is possible to integrate planar Gunn diodes with such circuits in order to achieve low phase noise and high power planar Gunn oscillators.

Other future work includes deployment of other materials for planar Gunn diodes, investigation of Ohmic contacts with higher penetration capability, development of high

reliability device fabrication technology for short channel devices, reduction of the thermal effect, and improvement of high efficiency power combining circuits and techniques.

As discussed in Section 4.3, $In_{0.23}Ga_{0.77}As$-based planar Gunn diodes have shown better frequency and power performance than those of GaAs-based planar Gunn diodes due to the addition of indium element that leads to higher electron mobility and wider conduction band discontinuity between the well and the barriers. Further work should be centred on investigating $In_xGa_{1-x}As$ with a higher mole fraction, which can further improve the aforementioned properties, such as $x = 0.53$ on an InP substrate for a lattice matched structure or $x \geq 0.7$ on GaAs substrate for metamorphic structure. The indium mole fraction can be further increased to 1 for a complete InP material for Gunn oscillations. Future work should also study alternative materials with a wide bandgap e.g. GaN for high frequency and high power operation. GaN has been successfully demonstrated in HEMTs, MESFETS, and laser diodes due to its excellent properties, such as its wide bandgap, high breakdown voltage, high mobility, high heat capacity, and thermal conductivity. However, there has been lack of success in fabricating vertical Gunn diodes. This is mainly due to high level of impurities of the material. Nevertheless, as wafer growth technology progresses quickly, it is possible and worthwhile exploring GaN for planar Gunn diodes.

Multiple-channel planar Gunn diodes have shown significant power improvement compared to single channel planar Gunn diodes (-4.5 dBm vs -43.5 dBm) as discussed in Section 4.2.3. However, both numerical and experimental results indicate inefficiency of the number of channels actively involved in producing Gunn oscillations. The reason is believed to be due to the Ohmic contacts that are not as deep as the lowest channel. Therefore, in the near future experimental work may be carried out to investigate different Ohmic contacts with deeper penetration capability as well as less spreading so that more channels can participate in generating Gunn oscillations and therefore improve RF power level.

So far, we have been concentrating on planar Gunn diodes with $L_{ac}$ in the range of 1 μm and 4 μm. In order to make devices generate higher oscillation frequencies e.g. greater than 100 GHz, $L_{ac}$ has to be further reduced to the sub-micron range. Previous work has shown

low yield for devices having $L_{ac}$ in the range of 1 μm. This is mainly due to the non-uniform electric field distribution arising as a consequence of the gap between the anode and cathode being non-uniform in a fabricated device. Breakdown happens at the narrowest gap between the two electrodes where the excessive high electric field is generated. One of the solutions is to separate and divide the anode and cathode Ohmic fabrication process into two steps so that the e-beam can write precisely each step for individual Ohmic contact development. The other reason for the low fabrication yield of short channel devices is the etching process. Wet etching has been used throughout of the project. It has been found there is a lack of precise controllability using a wet etching approach. A critical dry etching process may be applicable in the future for device fabrication with sub-micron $L_{ac}$.

The thermal effect has a significant influence on the power and frequency performance of planar Gunn diodes as demonstrated in Section 5.3. Simply lapping down the thickness of the substrate has been proved to reduce the thermal effect; however, the efficiency of this technique is low. Further work on improving thermal conductivity or introducing other cooling methods, such as a micro-cooler underneath the device, is highly desirable.

The demonstrated ultra wideband coplanar ring power dividers in Section 6.5 have shown superb performance in terms of bandwidth, port match, and output isolation. However, the transmission is not highly desirable when it operates as a power combiner at near 100 GHz or above. The transmission loss is approximately 1.0 dB that leads to poor combining efficiency, e.g. 1.0 dB. Therefore, it is necessary to reduce the transmission loss while keeping other performance unchanged. One of the solutions is to make a complete CPW-based ring power combiner that can suppress conversion losses generated when the signal is being converted from CPW to SCPS or vice versa in the demonstrated circuits. Simulation results conducted after the original submission of the thesis and not shown here indicate as little as 0.5 dB transmission loss at 100 GHz for a CPW-based ring power combiner. Future work should be done on the realisation and characterisation of the proposed CPW-based power combiner.

In summary, this work has lead to a significant improvement of power performance of planar Gunn diodes. Further contributions to the realisation of passive components and the

development of device characterisation methodologies would benefit better understanding of devices and devising devices with better performance. Meanwhile, future work should also focus on exploring other means, such as other modes of operation, alternative materials, improved fabrication process, integrating high performance circuits and good thermal handling techniques to improve devices.

# APPENDICES

## A.1 Medici Codes

### A.1.1 Single-channel GaAs-based Planar Gunn Diodes with Two δ-doping Layers

```
$ 07/05/2010
$ Version GaAs0102 Single channel GaAs based planar Gunn diodes with two delta-doping layers
$ channel thickness=50 nm
$ Lac=1.3 um
$ Create a mesh************************************************************
$ All distances in microns (WIDTH, DEPTH, L, H1, Y.MIN)
MESH SMOOTH=1
$ DEFINE WIDTH
X.MESH WIDTH=0.49 H1=0.07
X.MESH WIDTH=0.01 H1=0.01
X.MESH WIDTH=1.3 H1=0.065
X.MESH WIDTH=0.01 H1=0.01
X.MESH WIDTH=0.49 H1=0.07
$ DEFINE DEPTH
Y.MESH DEPTH=0.003 H1=0.003
Y.MESH DEPTH=0.02 H1=0.002
Y.MESH DEPTH=0.05 H1=0.005
Y.MESH DEPTH=0.02 H1=0.002
Y.MESH DEPTH=0.5 H1=0.25
Y.MESH DEPTH=5 H1=0.5
$ Specify regions**********************************************************
$ All distances in microns (Y.MIN, Y.MAX)
REGION NAME=BLANK NITRIDE PERMITTI=1
REGION NAME=AALGAAS1 ALGAAS X.MIN=0.49 X.MAX=0.5 Y.MIN=0.003 Y.MAX=0.023 X.MOLE=0.23
REGION NAME=CALGAAS1 ALGAAS X.MIN=1.8 X.MAX=1.81 Y.MIN=0.003 Y.MAX=0.023 X.MOLE=0.23
REGION NAME=ALGAAS1 ALGAAS X.MIN=0.5 X.MAX=1.8 Y.MIN=0.003 Y.MAX=0.013 X.MOLE=0.23
REGION NAME=ALGAAS2 ALGAAS X.MIN=0.5 X.MAX=1.8 Y.MIN=0.013 Y.MAX=0.023 X.MOLE=0.23
REGION NAME=AGAAS GAAS X.MIN=0.49 X.MAX=0.5 Y.MIN=0.023 Y.MAX=0.073
REGION NAME=CGAAS GAAS X.MIN=1.8 X.MAX=1.81 Y.MIN=0.023 Y.MAX=0.073
REGION NAME=GAAS GAAS X.MIN=0.5 X.MAX=1.8 Y.MIN=0.023 Y.MAX=0.073
REGION NAME=AALGAAS2 ALGAAS X.MIN=0.49 X.MAX=0.5 Y.MIN=0.073 Y.MAX=0.075 X.MOLE=0.23
REGION NAME=CALGAAS2 ALGAAS X.MIN=1.8 X.MAX=1.81 Y.MIN=0.073 Y.MAX=0.075 X.MOLE=0.23
REGION NAME=ALGAAS3 ALGAAS POLYGON X.POLY=(0,0,0.5,0.5,1.8,1.8,2.3,2.3)
Y.POLY=(0.083,0.075,0.075,0.073,0.073,0.075,0.075,0.083) X.MOLE=0.23
REGION NAME=ALGAAS4 ALGAAS Y.MIN=0.083 Y.MAX=0.093 X.MOLE=0.23
REGION NAME=BGAAS GAAS Y.MIN=0.093 Y.MAX=0.593
REGION NAME=SIGAAS GAAS Y.MIN=0.593 Y.MAX=5.593
$ Electrode definition****************************************************
$ All distances in microns (X.MIN, X.MAX)
ELECTR NAME=Anode X.MIN=0 X.MAX=0.49 Y.MIN=0 Y.MAX=0.075
ELECTR NAME=Cathode X.MIN=1.81 X.MAX=2.3 Y.MIN=0 Y.MAX=0.075
$ Specify the doping throughout the device*********************************
$ Doping quantities in cm-3 (N.PEAK)
$ All distances in microns (X.MIN, WIDTH, Y.MIN, Y.CHAR, Y.JUNC)
PROFILE REGION=ALGAAS1 N-TYPE CONC=1E2 UNIFORM OUT.FILE=GAASDOPING_0102
PROFILE REGION=ALGAAS2 N-TYPE CONC=1E2 UNIFORM
PROFILE REGION=GAAS N-TYPE CONC=1E2 UNIFORM
```

```
PROFILE REGION=ALGAAS3 N-TYPE CONC=1E2 UNIFORM
PROFILE REGION=ALGAAS4 N-TYPE CONC=1E2 UNIFORM
$PROFILE REGION=ALGAAS5 N-TYPE CONC=1E2 UNIFORM
$PROFILE REGION=ALGAAS6 N-TYPE CONC=1E2 UNIFORM
PROFILE REGION=AALGAAS1 N-TYPE CONC=2E20 UNIFORM
PROFILE REGION=CALGAAS1 N-TYPE CONC=2E20 UNIFORM
PROFILE REGION=AALGAAS2 N-TYPE CONC=2E20 UNIFORM
PROFILE REGION=CALGAAS2 N-TYPE CONC=2E20 UNIFORM
PROFILE REGION=AGAAS N-TYPE CONC=2E20 UNIFORM
PROFILE REGION=CGAAS N-TYPE CONC=2E20 UNIFORM
PROFILE REGION=BGAAS N-TYPE CONC=1E2 UNIFORM
PROFILE REGION=SIGAAS P-TYPE CONC=5E15 UNIFORM
INTERFACE REGION=(ALGAAS1,ALGAAS2) QF=8E11
INTERFACE REGION=(ALGAAS3,ALGAAS4) QF=8E11
$ Define materials**********************************************************************
MATERIAL REGION=BLANK PERMITTI=1
$ GaAs
MATERIAL REGION=(GAAS,AGAAS,CGAAS,BGAAS,SIGAAS) PERMITTI=12.9 EG.MODEL=0
+ EG300=1.425 EG.X1=0.0 EG.X2=0.0 AFFINITY=4.07 AF.X1=0.0 AF.X2=0.0 NC300=4.7E17
$ AlGaAs (X=0.23)
MATERIAL REGION=(AALGAAS1,AALGAAS2,ALGAAS1,ALGAAS2,ALGAAS3,ALGAAS4, CALGAAS1,
CALGAAS2)  PERMITTI=12.2 EG.MODEL=0 EG300=1.71 AFFINITY=3.82 +NC300=5.9E17 AF.X1=0 AF.X2=0
EG.X1=0 EG.X2=0
$ GaAs
MOBILITY REGION=(GAAS,AGAAS,CGAAS,BGAAS,SIGAAS) MUN0=8500 FLDMOB=2 VSATN=1.0E7
BETAN=1.0
$ AlGaAs (X=0.23)
MOBILITY REGION=(AALGAAS1,AALGAAS2,ALGAAS1,ALGAAS2,CALGAAS1,CALGAAS2, ALGAAS3,
ALGAAS4) MUN0=4000 FLDMOB=2 VSATN=0.9E7 BETAN=1.0
$ Plot the mesh*************************************************************************
PLOT.2D GRID Y.MIN=0 Y.MAX=0.2
+TITLE="GaAs_01Channel_02DeltaDoping- Grid" FILL PLOT.OUT="Grid_0102_10nm"
$ Select models, numerical methods, and initial guess**********************************************
MODELS  CONSRH AUGER FLDMOB=2
SYMB NEWT CARR=0
SOLVE V(Anode)=0 V(Cathode)=0
$ band structure plot
PLOT.1D COND X.START=1.5 X.END=1.5 Y.START=0 Y.END=0.2 x.size=0.4 y.size=0.4 SYMBOL=2  COLOR=11
NEG BOT=-0.2 TITLE="BAND STRUCTURE UNDER 0 BIAS_01Channel_02DeltaDoping"
OUT.FILE="ConducBand_0102_10nm_0V"
PLOT.1D QFN X.START=1.5 X.END=1.5 x.size=0.4 y.size=0.4 COLOR=5 NEG UNCH
+OUT.FILE="FermiLevel_0102_10nm_0V"
LABEL LABEL=ALGAAS col=2 x=0.005 y=.5 C.SIZE=0.4
LABEL LABEL=INGAAS col=2 x=.023 y=.5 C.SIZE=0.4
LABEL LABEL=ALGAAS col=2 x=0.04 y=.5 C.SIZE=0.4
LABEL LABEL="FERMI LEVEL" col=2 x=0.07 y=-0.04 C.SIZE=0.4
LABEL LABEL="BUFFER & S.I.GAAS" col=2 x=.06 y=.5 C.SIZE=0.4
$ Contact resistance*******************************************************************
CONTACT NAME=Cathode CON.RES=3E-6
CONTACT NAME=Anode CON.RES=3E-6
$ Symbolic factorization, solve, and save the solution at 0.5V*************************************
SYMB NEWTON CARRIERS=1 ELEC
METHOD ITLIMIT=1000 STACK=10
SOLVE V(Cathode)=0 V(Anode)=0.5 OUT.FILE=MDGUNNGaAs_0102_10nm05
$Plot current contour at 0.5 V
Plot.2D y.min=0 y.max=0.2 FILL BOUND x.size=0.4 y.size=0.4 TITLE="CURRENT FLOW_0102_10nm AT 0.5 V"
CONTOUR FLOW COLOR=2
FILL REGION=BLANK COLOR=0
LABEL LABEL=ANODE col=2 x=0.1 y=0.04 C.SIZE=0.4
LABEL LABEL=CATHODE col=2 x=1.9 y=0.04 C.SIZE=0.4
LABEL LABEL=ALGAAS col=2 x=1. y=0.015 C.SIZE=0.4
LABEL LABEL=GAAS col=2 x=1. y=0.05 C.SIZE=0.4
LABEL LABEL=ALGAAS col=2 x=1. y=0.085 C.SIZE=0.4
LABEL LABEL=BUFFER col=2 x=1. y=0.125 C.SIZE=0.4
LABEL LABEL=S.I.GAAS col=2 x=1. y=0.175 C.SIZE=0.4
$Plot Band Structure at 0.5 V
PLOT.1D COND X.START=1.5 X.END=1.5 Y.START=0 Y.END=0.2  x.size=0.4 y.size=0.4 SYMBOL=2  COLOR=11
NEG BOT=-0.2 TITLE="BAND STRUCTURE UNDER 0.5V GaAs0102_10nm"
OUT.FILE="ConducBand_0102_10nm_05V"
```

```
PLOT.1D QFN X.START=1.5 X.END=1.5 x.size=0.4 y.size=0.4 COLOR=5 NEG UNCH
OUT.FILE="FermiLevel_0102_10nm_05V"
LABEL LABEL=ALGAAS col=2 x=0.005 y=.5 C.SIZE=0.4
LABEL LABEL=INGAAS col=2 x=.023 y=.5 C.SIZE=0.4
LABEL LABEL=ALGAAS col=2 x=0.04 y=.5 C.SIZE=0.4
LABEL LABEL="FERMI LEVEL" col=2 x=0.07 y=-0.04 C.SIZE=0.4
LABEL LABEL="BUFFER & S.I.GAAS" col=2 x=.06 y=.5 C.SIZE=0.4
PLOT.1D E.Field y.start=0.028 y.end=0.028 t.size=0.4 x.size=0.4 y.size=0.4 TITLE="|E| at 0.5V"
OUT.FILE="EField_0102_10nm_05V"
$ Symbolic factorization, solve, and save the solution at 3.0V************************************
SYMB NEWTON CARRIERS=1 ELEC
METHOD ITLIMIT=1000 STACK=10
SOLVE V(Cathode)=0 V(Anode)=3.0 OUT.FILE=MDGUNNGaAs_0102_10nm30
$ dopings and electrons profile plots
PLOT.1D DOPING X.START=1.5 X.END=1.5 Y.START=0 Y.END=0.2 x.size=0.4 y.size=0.4 SYMBOL=2
COLOR=11 Y.LOG TITLE="DOPING PROFILE_01Channel_02DeltaDoping"
OUT.FILE="Impurity_Profile_0102_10nm"
PLOT.1D ELECT X.START=1.5 X.END=1.5 x.size=0.4 y.size=0.4 COLOR=11 SYMBOL=4 Y.LOG Y.START=0
Y.END=0.2 TITLE="ELECTRON DISTRIBUTION IN EACH LAYER_01Channel_02DeltaDoping"
OUT.FILE="ElectronV_Profile_0102_10nm"
LABEL LABEL=ALGAAS col=2 x=0.005 y=1e10 C.SIZE=0.4
LABEL LABEL=INGAAS col=2 x=.023 y=1e10 C.SIZE=0.4
LABEL LABEL=ALGAAS col=2 x=0.04 y=1e10 C.SIZE=0.4
LABEL LABEL="BUFFER & S.I.GAAS" col=2 x=.06 y=1e10 C.SIZE=0.4
PLOT.1D N.TOTAL Y.START=0.04 Y.END=0.04 x.size=0.4 y.size=0.4 COLOR=2  SYMBOL=4 Y.LOG
+TITLE="IMPURITY DISTRIBUTION IN CHANNEL LAYER_0102_10nm"
OUT.FILE="ElectronH_Profile_0102_10nm"
 PLOT.1D COND X.START=1.5 X.END=1.5 Y.START=0 Y.END=0.2 x.size=0.4 y.size=0.4 SYMBOL=2 COLOR=11
NEG TITLE="BAND STRUCTURE_0102_10nm AT 3 V" OUT.FILE="ConducBand_0102_10nm_3V"
PLOT.1D QFN X.START=1.5 X.END=1.5 x.size=0.4 y.size=0.4 COLOR=2 NEG UNCH
OUT.FILE="FermiLevel_0102_10nm_3V"
$ Impurity contour plot*************************************************************************
PLOT.2D BOUND Y.MIN=0 Y.MAX=0.2 TITLE="Gunn_0102_10nm-Impurity Contours" FILL X.MAX=2.3
CONTOUR DOPING LOG MIN=10 MAX=20 DEL=.5 COLOR=2
CONTOUR DOPING LOG MIN=-16 MAX=-15 DEL=.5 COLOR=1 LINE=2
$ Plot current flow*****************************************************************************
Plot.2D Y.MIN=0 Y.MAX=0.2 FILL BOUND x.size=0.4 y.size=0.4 TITLE="CURRENT +FLOW_GaAs0102_10nm
AT 3.0 V"
CONTOUR FLOW COLOR=2
FILL REGION=BLANK COLOR=0
LABEL LABEL=ANODE col=2 x=0.1 y=0.04 C.SIZE=0.4
LABEL LABEL=CATHODE col=2 x=1.9 y=0.04 C.SIZE=0.4
LABEL LABEL=ALGAAS col=2 x=1. y=0.015 C.SIZE=0.4
LABEL LABEL=GAAS col=2 x=1. y=0.05 C.SIZE=0.4
LABEL LABEL=ALGAAS col=2 x=1. y=0.085 C.SIZE=0.4
LABEL LABEL=BUFFER col=2 x=1. y=0.125 C.SIZE=0.4
LABEL LABEL=S.I.GAAS col=2 x=1. y=0.175 C.SIZE=0.4
PLOT.3D Y.MIN=0 Y.MAX=0.2 ELECTRON LOG TITLE="ELECTRON DISTRIBUTION" ^FRAME PHI=110
3D.SURF COLOR=4
LOOP STEPS=1
        ASSIGN NAME=VC10nm N.VALUE=(0,-4,-3.5,-3,-2.5 -2, -1.5, -0.5, 0)
$ Use Newtons method for the solution
        SYMB NEWTON CARRIERS=1 ELEC
        METHOD ITLIMIT=1500 STACK=10
        SOLVE V(Cathode)=@VC10nm V(Anode)=0 ELEC=Anode VSTEP=0.2 NSTEP=20
$ Plot Ia vs. Va
        PLOT.1D Y.AXIS=I(Anode) X.AXIS=V(Anode) x.size=0.4 y.size=0.4 TITLE="IV
+CHARACTERISTICS_0102_10nm" OUT.FILE="IV_0102_10nm"@VC10nm UNCH
        LOG CLOSE
L.END
$ Save the mesh
SAVE MESH OUT.FILE=GAAS0102_10nm
```

## A.1.2 Single-channel GaAs-based Planar Gunn Diodes with Four δ-doping Layers

```
$ 01/06/2010
$ Version GaAs0104
$ Single channel with four delta-dopings
$ channel thickness=50 nm
$Create a mesh*****************************************************************************
$ All distances in microns (WIDTH, DEPTH, L, H1, Y.MIN)
MESH SMOOTH=1
$Define width
X.MESH WIDTH=0.49 H1=0.07
X.MESH WIDTH=0.01 H1=0.01
X.MESH WIDTH=1.3 H1=0.065
X.MESH WIDTH=0.01 H1=0.01
X.MESH WIDTH=0.49 H1=0.07
$Define depth
Y.MESH DEPTH=0.003 H1=0.003
Y.MESH DEPTH=0.02 H1=0.002
Y.MESH DEPTH=0.05 H1=0.005
Y.MESH DEPTH=0.02 H1=0.002
Y.MESH DEPTH=0.5 H1=0.25
Y.MESH DEPTH=5 H1=0.5
$ Specify regions**************************************************************************
$ All distances in microns (Y.MIN, Y.MAX)
REGION NAME=BLANK NITRIDE
REGION NAME=AALGAAS1 ALGAAS X.MIN=0.49 X.MAX=0.5 Y.MIN=0.003 Y.MAX=0.023 X.MOLE=0.23
REGION NAME=CALGAAS1 ALGAAS X.MIN=1.8 X.MAX=1.81 Y.MIN=0.003 Y.MAX=0.023 X.MOLE=0.23
REGION NAME=ALGAAS1 ALGAAS X.MIN=0.5 X.MAX=1.8 Y.MIN=0.003 Y.MAX=0.009 X.MOLE=0.23
REGION NAME=ALGAAS2 ALGAAS X.MIN=0.5 X.MAX=1.8 Y.MIN=0.009 Y.MAX=0.017 X.MOLE=0.23
REGION NAME=ALGAAS3 ALGAAS X.MIN=0.5 X.MAX=1.8 Y.MIN=0.017 Y.MAX=0.023 X.MOLE=0.23
REGION NAME=AGAAS GAAS X.MIN=0.49 X.MAX=0.5 Y.MIN=0.023 Y.MAX=0.073
REGION NAME=CGAAS GAAS X.MIN=1.8 X.MAX=1.81 Y.MIN=0.023 Y.MAX=0.073
REGION NAME=GAAS GAAS X.MIN=0.5 X.MAX=1.8 Y.MIN=0.023 Y.MAX=0.073
REGION NAME=AALGAAS2 ALGAAS X.MIN=0.49 X.MAX=0.5 Y.MIN=0.073 Y.MAX=0.075 X.MOLE=0.23
REGION NAME=CALGAAS2 ALGAAS X.MIN=1.8 X.MAX=1.81 Y.MIN=0.073 Y.MAX=0.075 X.MOLE=0.23
Y.POLY=(0.077,0.073,0.073,0.075,0.075,0.077) X.MOLE=0.23
REGION NAME=ALGAAS4 ALGAAS POLYGON X.POLY=(0,0,0.5,0.5,1.8,1.8,2.3,2.3)
Y.POLY=(0.079,0.075,0.075,0.073,0.073,0.075,0.075,0.079) X.MOLE=0.23
REGION NAME=ALGAAS5 ALGAAS Y.MIN=0.079 Y.MAX=0.085 X.MOLE=0.23
REGION NAME=ALGAAS6 ALGAAS Y.MIN=0.085 Y.MAX=0.093 X.MOLE=0.23
REGION NAME=BGAAS GAAS Y.MIN=0.093 Y.MAX=0.593
REGION NAME=SIGAAS GAAS Y.MIN=0.593 Y.MAX=5.593
$ Electrode definition*********************************************************************************************
$ All distances in microns (X.MIN, X.MAX)
ELECTR NAME=Anode X.MIN=0 X.MAX=0.49 Y.MIN=0 Y.MAX=0.075
ELECTR NAME=Cathode X.MIN=1.81 X.MAX=2.3 Y.MIN=0 Y.MAX=0.075
$ Specify the doping throughout the device*************************************************************************
$ Doping quantities in cm-3 (N.PEAK)
$ All distances in microns (X.MIN, WIDTH, Y.MIN, Y.CHAR, Y.JUNC)
PROFILE REGION=ALGAAS1 N-TYPE CONC=1E2 UNIFORM OUT.FILE=GAASDOPING_0104_2
PROFILE REGION=ALGAAS2 N-TYPE CONC=1E2 UNIFORM
PROFILE REGION=GAAS N-TYPE CONC=1E2 UNIFORM
PROFILE REGION=ALGAAS3 N-TYPE CONC=1E2 UNIFORM
PROFILE REGION=ALGAAS4 N-TYPE CONC=1E2 UNIFORM
PROFILE REGION=ALGAAS5 N-TYPE CONC=1E2 UNIFORM
PROFILE REGION=ALGAAS6 N-TYPE CONC=1E2 UNIFORM
PROFILE REGION=AALGAAS1 N-TYPE CONC=1E20 UNIFORM
PROFILE REGION=CALGAAS1 N-TYPE CONC=1E20 UNIFORM
PROFILE REGION=AALGAAS2 N-TYPE CONC=1E20 UNIFORM
PROFILE REGION=CALGAAS2 N-TYPE CONC=1E20 UNIFORM
PROFILE REGION=AGAAS N-TYPE CONC=1E20 UNIFORM
PROFILE REGION=CGAAS N-TYPE CONC=1E20 UNIFORM
PROFILE REGION=BGAAS N-TYPE CONC=1E2 UNIFORM
PROFILE REGION=SIGAAS P-TYPE CONC=5E15 UNIFORM
INTERFACE REGION=(ALGAAS1,ALGAAS2) QF=1.6E12
INTERFACE REGION=(ALGAAS3,ALGAAS2) QF=1.6E12
```

```
INTERFACE REGION=(ALGAAS4,ALGAAS5) QF=1.6E12
INTERFACE REGION=(ALGAAS5,ALGAAS6) QF=1.6E12
$ Define materials**********************************************************************************
MATERIAL REGION=BLANK PERMITTI=1
$ GaAs
MATERIAL REGION=(AGAAS,CGAAS,GAAS,BGAAS,SIGAAS) PERMITTI=12.9 EG.MODEL=0 EG300=1.425
+EG.X1=0.0 EG.X2=0.0 AFFINITY=4.07 AF.X1=0.0 AF.X2=0.0 NC300=4.7E17
$ AlGaAs (X=0.23)
MATERIAL REGION=(AALGAAS1,AALGAAS2,ALGAAS1,ALGAAS2,ALGAAS3,ALGAAS4,ALGAAS5,
ALGAAS6,CALGAAS1,CALGAAS2) PERMITTI=12.2 EG.MODEL=0 EG300=1.71 AFFINITY=3.82 NC300=5.9E17
+ AF.X1=0 AF.X2=0 EG.X1=0 EG.X2=0
$ GaAs
MOBILITY REGION=(AGAAS,CGAAS,GAAS,BGAAS,SIGAAS) MUN0=8500 FLDMOB=2 VSATN=1.0E7
+BETAN=1.0
$ AlGaAs (X=0.23)
MOBILITY REGION=(AALGAAS1,AALGAAS2,ALGAAS1,ALGAAS2,CALGAAS1,CALGAAS2,ALGAAS3,
+ALGAAS4,ALGAAS5,ALGAAS6) MUN0=4000 FLDMOB=2 VSATN=1.0E7 BETAN=1.0
$ Plot the mesh**************************************************************************************
PLOT.2D GRID Y.MIN=0 Y.MAX=0.2 TITLE="GaAs_01Channel_04DeltaDoping- Grid" FILL
+PLOT.OUT="Grid_0104_2"
$ Select models, numerical methods, and initial guess**********************************************
MODELS  CONSRH AUGER FLDMOB=2
SYMB NEWT CARR=0
SOLVE V(Anode)=0 V(Cathode)=0
$ band structure plot
PLOT.1D COND X.START=1.5 X.END=1.5 x.size=0.4 y.size=0.4 SYMBOL=2 COLOR=11 NEG Y.START=0
+Y.END=0.2TITLE="BAND STRUCTURE UNDER 0 BIAS-GaAs_01Channel_04DeltaDoping" OUT.FILE="BAND
STRUCURE_0104_2_0V"
PLOT.1D QFN X.START=1.5 X.END=1.5 x.size=0.4 y.size=0.4 COLOR=5 NEG UNCH
+OUT.FILE="FermiLevel_0104_2_0V"
LABEL LABEL=ALGAAS col=2 x=0.005 y=.5 C.SIZE=0.4
LABEL LABEL=INGAAS col=2 x=.023 y=.5 C.SIZE=0.4
LABEL LABEL=ALGAAS col=2 x=0.04 y=.5 C.SIZE=0.4
LABEL LABEL="FERMI LEVEL" col=2 x=0.07 y=-0.04 C.SIZE=0.4
LABEL LABEL="BUFFER & S.I.GAAS" col=2 x=.06 y=.5 C.SIZE=0.4
CONTACT NAME=Cathode CON.RES=1E-6
CONTACT NAME=Anode CON.RES=1E-6
$ Symbolic factorization, solve, and save the solution at 1.0 V************************************************
SYMB NEWTON CARRIERS=1 ELEC
METHOD ITLIMIT=1000 STACK=10
SOLVE V(Cathode)=0 V(Anode)=1.0 OUT.FILE=MDGUNNGaAs_0104_2_1V
$ band structure plot
Plot.2D FILL Y.MIN=0 Y.MAX=0.2 BOUND x.size=0.4 y.size=0.4 TITLE="CURRENT FLOW_0104_2 AT 1.0V"
+CONTOUR FLOW COLOR=2
FILL REGION=BLANK COLOR=0
LABEL LABEL=ANODE col=2 x=0.1 y=0.04 C.SIZE=0.4
LABEL LABEL=CATHODE col=2 x=1.9 y=0.04 C.SIZE=0.4
LABEL LABEL=ALGAAS col=2 x=1. y=0.015 C.SIZE=0.4
LABEL LABEL=GAAS col=2 x=1. y=0.05 C.SIZE=0.4
LABEL LABEL=ALGAAS col=2 x=1. y=0.085 C.SIZE=0.4
LABEL LABEL=BUFFER col=2 x=1. y=0.125 C.SIZE=0.4
LABEL LABEL=S.I.GAAS col=2 x=1. y=0.175 C.SIZE=0.4
$ Symbolic factorization, solve, and save the solution at 2.0 V************************************************
SYMB NEWTON CARRIERS=1 ELEC
METHOD ITLIMIT=1000 STACK=10
SOLVE V(Cathode)=0 V(Anode)=2.0 OUT.FILE=MDGUNNGaAs_0104_2_2V
$ band structure plot
Plot.2D FILL Y.MIN=0 Y.MAX=0.2 BOUND x.size=0.4 y.size=0.4 TITLE="CURRENT FLOW_0104_2 AT 2.0V"
CONTOUR FLOW COLOR=2
FILL REGION=BLANK COLOR=0
LABEL LABEL=ANODE col=2 x=0.1 y=0.04 C.SIZE=0.4
LABEL LABEL=CATHODE col=2 x=1.9 y=0.04 C.SIZE=0.4
LABEL LABEL=ALGAAS col=2 x=1. y=0.015 C.SIZE=0.4
LABEL LABEL=GAAS col=2 x=1. y=0.05 C.SIZE=0.4
LABEL LABEL=ALGAAS col=2 x=1. y=0.085 C.SIZE=0.4
LABEL LABEL=BUFFER col=2 x=1. y=0.125 C.SIZE=0.4
LABEL LABEL=S.I.GAAS col=2 x=1. y=0.175 C.SIZE=0.4
$ Symbolic factorization, solve, and save the solution at 3.0 V************************************************
SYMB NEWTON CARRIERS=1 ELEC
```

```
METHOD ITLIMIT=1000 STACK=10
SOLVE V(Cathode)=0 V(Anode)=3.0 OUT.FILE=MDGUNNGaAs_0104_2
$ dopings and electrons profile plots
PLOT.1D DOPING Y.START=0 Y.END=0.2 X.START=1.5 X.END=1.5 x.size=0.4 y.size=0.4 SYMBOL=2
+COLOR=11 Y.LOG TITLE="DOPING PROFILE_0104_2" OUT.FILE="Impurity_Profile_0104_2"
PLOT.1D ELECT X.START=1.5 X.END=1.5 x.size=0.4 y.size=0.4 COLOR=11  SYMBOL=4 Y.LOG Y.START=0
+Y.END=0.2 TITLE="ELECTRON DISTRIBUTION IN EACH LAYER" OUT.FILE="ElectronV_Profile_0104_2"
LABEL LABEL=ALGAAS col=2 x=0.005 y=1e10 C.SIZE=0.4
LABEL LABEL=INGAAS col=2 x=.023 y=1e10 C.SIZE=0.4
LABEL LABEL=ALGAAS col=2 x=0.04 y=1e10 C.SIZE=0.4
LABEL LABEL="BUFFER & S.I.GAAS" col=2 x=.06 y=1e10 C.SIZE=0.4
PLOT.1D N.TOTAL Y.START=0.04 Y.END=0.04 x.size=0.4 y.size=0.4 COLOR=2  SYMBOL=4 Y.LOG
+TITLE="IMPURITY DISTRIBUTION IN CHANNEL LAYER" OUT.FILE="ElectronH_Profile_0104_2"
PLOT.1D COND X.START=1.5 X.END=1.5 x.size=0.4 y.size=0.4 SYMBOL=2 COLOR=11 NEG Y.START=0
Y.END=0.2TITLE="GunnBAND STRUCTURE AT 3.0V" OUT.FILE="BAND STRUCURE_0104_2_3.0V"
PLOT.1D QFN X.START=1.5 X.END=1.5 x.size=0.4 y.size=0.4 COLOR=2 NEG UNCH
OUT.FILE="FermiLevel_0104_2_3.0V"
$ Impurity contour plot
PLOT.2D BOUND TITLE="GaAs_01Channel_04DeltaDoping - Impurity Contours" FILL X.MAX=2.3 Y.MIN=0
Y.MAX=0.2
CONTOUR DOPING LOG MIN=10 MAX=20 DEL=.5 COLOR=2
CONTOUR DOPING LOG MIN=-16 MAX=-15 DEL=.5 COLOR=1 LINE=2
$ Plot current flow
Plot.2D FILL Y.MIN=0 Y.MAX=0.2 BOUND x.size=0.4 y.size=0.4 TITLE="CURRENT FLOW_0104_2 AT 3.0V"
CONTOUR FLOW COLOR=2
FILL REGION=BLANK COLOR=0
LABEL LABEL=ANODE col=2 x=0.1 y=0.04 C.SIZE=0.4
LABEL LABEL=CATHODE col=2 x=1.9 y=0.04 C.SIZE=0.4
LABEL LABEL=ALGAAS col=2 x=1. y=0.015 C.SIZE=0.4
LABEL LABEL=GAAS col=2 x=1. y=0.05 C.SIZE=0.4
LABEL LABEL=ALGAAS col=2 x=1. y=0.085 C.SIZE=0.4
LABEL LABEL=BUFFER col=2 x=1. y=0.125 C.SIZE=0.4
LABEL LABEL=S.I.GAAS col=2 x=1. y=0.175 C.SIZE=0.4
PLOT.3D Y.MIN=0 Y.MAX=0.2 ELECTRON LOG TITLE="ELECTRON DISTRIBUTION_0104_2" ^FRAME
PHI=110 3D.SURF COLOR=4
$ Plot to show contact resistance
PLOT.2D Y.MIN=0 Y.MAX=0.2 BOUND LUMPED TITLE="Gunn Lumped Resistance_0104_2" VECTOR J.HOLE
$ Plot 3D Efield
PLOT.3D E.field x.min=0.5 x.max=1.8 y.min=0.023 y.max=0.073 t.size=0.4 x.size=0.4 y.size=0.4
TITLE="MAGNITUDE OF ELECTRIC FIELD_0104_2 3.0V"  phi=150
LOOP STEPS=1
        ASSIGN NAME=VC01042 N.VALUE=(0, -2, -1.5, -0.5, 0)
        $ Use Newtons method for the solution
        SYMB NEWTON CARRIERS=1 ELEC
        METHOD ITLIMIT=1500 STACK=10
        SOLVE V(Cathode)=@VC01042 V(Anode)=0 ELEC=Anode VSTEP=0.1 NSTEP=56
        $ Plot Ia vs. Va
        PLOT.1D Y.AXIS=I(Anode) X.AXIS=V(Anode) x.size=0.4 y.size=0.4 TITLE="IV
CHARACTERISTICS_0104_2" OUT.FILE="IV_01042"@VC01042 UNCH
        LOG CLOSE
L.END
SAVE MESH OUT.FILE=GAAS0104_2
SAVE TIF OUT.FILE=GAAS0104_2.TIF ALL
```

## A.1.3 Two-channel GaAs-based Planar Gunn Diodes with Four δ-doping Layers

```
$ 01/06/2010
$ Version GaAs0204
$ GaAs planar Gunn diodes with 2 channels 4 delta dopings
$ channel thickness=50 nm
$ number of channel=2
$ Delta-doping level 8E11
$ Annealed Ohmic contacts reach the second channel
$ Lac=1.3 um
$Create a mesh**********************************************************************************
$ All distances in microns (WIDTH, DEPTH, L, H1, Y.MIN)
MESH SMOOTH=1
X.MESH WIDTH=0.49 H1=0.07
X.MESH WIDTH=0.01 H1=0.01
X.MESH WIDTH=1.3 H1=0.065
X.MESH WIDTH=0.01 H1=0.01
X.MESH WIDTH=0.49 H1=0.07
Y.MESH DEPTH=0.003 H1=0.003
Y.MESH DEPTH=0.02 H1=0.002
Y.MESH DEPTH=0.05 H1=0.005
Y.MESH DEPTH=0.02 H1=0.002
Y.MESH DEPTH=0.02 H1=0.002
Y.MESH DEPTH=0.05 H1=0.005
Y.MESH DEPTH=0.02 H1=0.002
Y.MESH DEPTH=0.5 H1=0.05
Y.MESH DEPTH=5 H1=0.5
$ Specify regions*******************************************************************************
$ All distances in microns (Y.MIN, Y.MAX)
REGION NAME=BLANK NITRIDE
$ **************Below Channel 1 & Barriers*****************
REGION NAME=AALGAAS1 ALGAAS X.MIN=0.49 X.MAX=0.5 Y.MIN=0.003 Y.MAX=0.023 X.MOLE=0.23
REGION NAME=CALGAAS1 ALGAAS X.MIN=1.8 X.MAX=1.81 Y.MIN=0.003 Y.MAX=0.023 X.MOLE=0.23
REGION NAME=ALGAAS1 ALGAAS X.MIN=0.5 X.MAX=1.8 Y.MIN=0.003 Y.MAX=0.013 X.MOLE=0.23
REGION NAME=ALGAAS2 ALGAAS X.MIN=0.5 X.MAX=1.8 Y.MIN=0.013 Y.MAX=0.023 X.MOLE=0.23
REGION NAME=AGAAS1 GAAS X.MIN=0.49 X.MAX=0.5 Y.MIN=0.023 Y.MAX=0.073
REGION NAME=CGAAS1 GAAS X.MIN=1.8 X.MAX=1.81 Y.MIN=0.023 Y.MAX=0.073
REGION NAME=GAAS1 GAAS X.MIN=0.5 X.MAX=1.8 Y.MIN=0.023 Y.MAX=0.073
REGION NAME=AALGAAS2 ALGAAS X.MIN=0.49 X.MAX=0.5 Y.MIN=0.073 Y.MAX=0.093  X.MOLE=0.23
REGION NAME=CALGAAS2 ALGAAS X.MIN=1.8 X.MAX=1.81 Y.MIN=0.073 Y.MAX=0.093 X.MOLE=0.23
REGION NAME=ALGAAS3 ALGAAS X.MIN=0.5 X.MAX=1.8 Y.MIN=0.073 Y.MAX=0.083 X.MOLE=0.23
REGION NAME=ALGAAS4 ALGAAS X.MIN=0.5 X.MAX=1.8 Y.MIN=0.083 Y.MAX=0.093 X.MOLE=0.23
$***************** Below Channel 2 & Barriers******************
REGION NAME=AALGAAS3 ALGAAS X.MIN=0.49 X.MAX=0.5 Y.MIN=0.093 Y.MAX=0.113  X.MOLE=0.23
REGION NAME=CALGAAS3 ALGAAS X.MIN=1.8 X.MAX=1.81 Y.MIN=0.093 Y.MAX=0.113 X.MOLE=0.23
REGION NAME=ALGAAS5 ALGAAS X.MIN=0.5 X.MAX=1.8 Y.MIN=0.093 Y.MAX=0.103 X.MOLE=0.23
REGION NAME=ALGAAS6 ALGAAS X.MIN=0.5 X.MAX=1.8 Y.MIN=0.103 Y.MAX=0.113 X.MOLE=0.23
REGION NAME=AGAAS2 GAAS X.MIN=0.49 X.MAX=0.5 Y.MIN=0.113 Y.MAX=0.163
REGION NAME=CGAAS2 GAAS X.MIN=1.8 X.MAX=1.81 Y.MIN=0.113 Y.MAX=0.163
REGION NAME=GAAS2 GAAS X.MIN=0.5 X.MAX=1.8 Y.MIN=0.113 Y.MAX=0.163
REGION NAME=AALGAAS4 ALGAAS POLYGON X.POLY=(0,0,0.49,0.49,0.5,0.5)
Y.POLY=(0.167,0.165,0.165,0.163, 0.163,0.167) X.MOLE=0.23
REGION NAME=CALGAAS4 ALGAAS POLYGON X.POLY=(1.8,1.8,1.81,1.81,2.3,2.3)
Y.POLY=(0.167,0.163,0.163,0.165,0.165,0.167) X.MOLE=0.23
REGION NAME=ALGAAS7 ALGAAS POLYGON X.POLY=(0,0,0.5,0.5,1.8,1.8,2.3,2.3)
Y.POLY=(0.173,0.167,0.167,0.163,0.163,0.167,0.167,0.173) X.MOLE=0.23
REGION NAME=ALGAAS8 ALGAAS X.MIN=0.0 X.MAX=2.3 Y.MIN=0.173 Y.MAX=0.183 X.MOLE=0.23
$ **************Below Buffer & S. I. Substrate*******************
REGION NAME=BGAAS GAAS Y.MIN=0.183 Y.MAX=0.683
REGION NAME=SIGAAS GAAS Y.MIN=0.683 Y.MAX=5.683
$ Electrode definition*************************************************************************
$ All distances in microns (X.MIN, X.MAX)
ELECTR NAME=Anode X.MIN=0 X.MAX=0.49 Y.MIN=0 Y.MAX=0.165
ELECTR NAME=Cathode X.MIN=1.81 X.MAX=2.3 Y.MIN=0 Y.MAX=0.165
$ Specify the doping throughout the device*****************************************************
$ All distances in microns (X.MIN, WIDTH, Y.MIN, Y.CHAR, Y.JUNC)
PROFILE REGION=ALGAAS1 N-TYPE CONC=1E2 UNIFORM OUT.FILE=GAASDOPING_0204
PROFILE REGION=ALGAAS2 N-TYPE CONC=1E2 UNIFORM
```

```
PROFILE REGION=GAAS1 N-TYPE CONC=1E2 UNIFORM
PROFILE REGION=GAAS2 N-TYPE CONC=1E2 UNIFORM
PROFILE REGION=ALGAAS3 N-TYPE CONC=1E2 UNIFORM
PROFILE REGION=ALGAAS4 N-TYPE CONC=1E2 UNIFORM
PROFILE REGION=ALGAAS5 N-TYPE CONC=1E2 UNIFORM
PROFILE REGION=ALGAAS6 N-TYPE CONC=1E2 UNIFORM
PROFILE REGION=ALGAAS7 N-TYPE CONC=1E2 UNIFORM
PROFILE REGION=ALGAAS8 N-TYPE CONC=1E2 UNIFORM
PROFILE REGION=AALGAAS1 N-TYPE CONC=2E20 UNIFORM
PROFILE REGION=CALGAAS1 N-TYPE CONC=2E20 UNIFORM
PROFILE REGION=AALGAAS2 N-TYPE CONC=2E20 UNIFORM
PROFILE REGION=CALGAAS2 N-TYPE CONC=2E20 UNIFORM
PROFILE REGION=AALGAAS3 N-TYPE CONC=2E20 UNIFORM
PROFILE REGION=CALGAAS3 N-TYPE CONC=2E20 UNIFORM
PROFILE REGION=AALGAAS4 N-TYPE CONC=2E20 UNIFORM
PROFILE REGION=CALGAAS4 N-TYPE CONC=2E20 UNIFORM
PROFILE REGION=AGAAS1 N-TYPE CONC=2E20 UNIFORM
PROFILE REGION=CGAAS1 N-TYPE CONC=2E20 UNIFORM
PROFILE REGION=AGAAS2 N-TYPE CONC=2E20 UNIFORM
PROFILE REGION=CGAAS2 N-TYPE CONC=2E20 UNIFORM
PROFILE REGION=BGAAS N-TYPE CONC=1E2 UNIFORM
PROFILE REGION=SIGAAS P-TYPE CONC=5E15 UNIFORM
INTERFACE REGION=(ALGAAS1,ALGAAS2) QF=8E11
INTERFACE REGION=(ALGAAS3,ALGAAS4) QF=8E11
INTERFACE REGION=(ALGAAS5,ALGAAS6) QF=8E11
INTERFACE REGION=(ALGAAS7,ALGAAS8) QF=8E11
$ Define materials**********************************************************************************
MATERIAL REGION=BLANK PERMITTI=1
$ GaAs
MATERIAL REGION=(GAAS2,GAAS1,AGAAS1,CGAAS1,AGAAS2,CGAAS2,BGAAS,SIGAAS) PERMITTI=12.9
+EG.MODEL=0 EG300=1.425 EG.X1=0.0 EG.X2=0.0 AFFINITY=4.07 AF.X1=0.0 AF.X2=0.0 NC300=4.7E17
$ AlGaAs (X=0.23) MATERIAL REGION=(AALGAAS1,AALGAAS2,AALGAAS3,AALGAAS4,ALGAAS1,
ALGAAS2, ALGAAS3,ALGAAS4,ALGAAS5,ALGAAS6,ALGAAS7,ALGAAS8,CALGAAS1,CALGAAS2,
CALGAAS3,CALGAAS4) PERMITTI=12.2 EG.MODEL=0 EG300=1.71 AFFINITY=3.82 NC300=5.9E17 AF.X1=0
+AF.X2=0 EG.X1=0 EG.X2=0
$ GaAs
MOBILITY REGION=(GAAS1,GAAS2,AGAAS1,CGAAS1,AGAAS2,CGAAS2,BGAAS,SIGAAS) MUN0=8500
+FLDMOB=2 VSATN=1.0E7 BETAN=1.0
$ AlGaAs (X=0.23)
MOBILITY REGION=(AALGAAS1,AALGAAS2,AALGAAS3,AALGAAS4,ALGAAS1,ALGAAS2,
CALGAAS1,CALGAAS2,CALGAAS3,CALGAAS4,ALGAAS3,ALGAAS4,ALGAAS5,ALGAAS6,ALGAAS7,
ALGAAS8) MUN0=4000 FLDMOB=2 VSATN=0.9E7 BETAN=1.0
$ Plot the mesh*************************************************************************************
PLOT.2D GRID Y.MIN=0 Y.MAX=0.2 TITLE="GaAs_02Channel_04DeltaDoping- Grid" FILL
PLOT.OUT="Grid_GaAs_0204"
$ Select models, numerical methods and initial guess***********************************************
MODELS  CONSRH AUGER FLDMOB=2
SYMB NEWT CARR=0
SOLVE V(Anode)=0 V(Cathode)=0
$ band structure plot
PLOT.1D COND X.START=1.5 X.END=1.5 Y.START=0 Y.END=0.2  x.size=0.4 y.size=0.4 SYMBOL=2  COLOR=11
NEG TITLE="BAND STRUCTURE 0V_0204" OUT.FILE="Conduction Band GaAs_0204_0V"
PLOT.1D QFN X.START=1.5 X.END=1.5 x.size=0.4 y.size=0.4 COLOR=5 NEG UNCH OUT.FILE="Fermi Level
GaAs_0204_0V"
LABEL LABEL=ALGAAS col=2 x=0.005 y=.5 C.SIZE=0.4
LABEL LABEL=INGAAS col=2 x=.023 y=.5 C.SIZE=0.4
LABEL LABEL=ALGAAS col=2 x=0.04 y=.5 C.SIZE=0.4
LABEL LABEL="FERMI LEVEL" col=2 x=0.07 y=-0.04 C.SIZE=0.4
LABEL LABEL="BUFFER & S.I.GAAS" col=2 x=.06 y=.5 C.SIZE=0.4
$ Define specific contact resistance
CONTACT NAME=Cathode CON.RES=1E-6
CONTACT NAME=Anode CON.RES=1E-6
$ Symbolic factorization, solve, and save the solution at 3.0 V*************************************

SYMB NEWTON CARRIERS=1 ELEC
METHOD ITLIMIT=1000 STACK=10
SOLVE V(Cathode)=0 V(Anode)=3.0 OUT.FILE=MDGUNNGaAs_0204
$ dopings and electrons profile plots
```

```
PLOT.1D DOPING X.START=1.5 X.END=1.5 Y.START=0 Y.END=0.2 x.size=0.4 y.size=0.4 SYMBOL=2
COLOR=11 Y.LOG TITLE="DOPING PROFILE_0204" OUT.FILE="Impurity GaAs_Profile_0204"
PLOT.1D ELECT X.START=1.5 X.END=1.5 x.size=0.4 y.size=0.4 COLOR=11 SYMBOL=4 Y.LOG Y.START=0
Y.END=0.2 TITLE="ELECTRON GaAs_0204" OUT.FILE="ElectronV_GaAs_0204"
LABEL LABEL=ALGAAS col=2 x=0.005 y=1e10 C.SIZE=0.4
LABEL LABEL=INGAAS col=2 x=.023 y=1e10 C.SIZE=0.4
LABEL LABEL=ALGAAS col=2 x=0.04 y=1e10 C.SIZE=0.4
LABEL LABEL="BUFFER & S.I.GAAS" col=2 x=.06 y=1e10 C.SIZE=0.4
PLOT.1D N.TOTAL Y.START=0.04 Y.END=0.04 x.size=0.4 y.size=0.4 COLOR=2 SYMBOL=4 Y.LOG
+TITLE="IMPURITY DISTRIBUTION _0204" OUT.FILE="ElectronH_Profile_0204"
 PLOT.1D COND X.START=1.5 X.END=1.5 Y.START=0 Y.END=0.2 x.size=0.4 y.size=0.4 SYMBOL=2 COLOR=11
NEG TITLE="BAND GaAs 0204 @ 3 V" OUT.FILE="ConducBand_GaAs_0204_3V"
PLOT.1D QFN X.START=1.5 X.END=1.5 x.size=0.4 y.size=0.4 COLOR=2 NEG UNCH
OUT.FILE="FermiLevel_GaAs_0204_3V"
$ Impurity contour plot
PLOT.2D BOUND Y.MIN=0 Y.MAX=0.2 TITLE="Impurity Contours GaAs 0204" FILL  X.MAX=2.3
CONTOUR DOPING LOG MIN=10 MAX=20 DEL=.5 COLOR=2
CONTOUR DOPING LOG MIN=-16 MAX=-15 DEL=.5 COLOR=1 LINE=2
$ Plot current flow
Plot.2D Y.MIN=0 Y.MAX=0.2 FILL BOUND x.size=0.4 y.size=0.4 TITLE="CURRENT FLOW GaAs_0204 @ 3.0 V"
CONTOUR FLOW COLOR=2 FILL REGION=BLANK COLOR=0
LABEL LABEL=ANODE col=2 x=0.1 y=0.04 C.SIZE=0.4
LABEL LABEL=CATHODE col=2 x=1.9 y=0.04 C.SIZE=0.4
LABEL LABEL=ALGAAS col=2 x=1. y=0.015 C.SIZE=0.4
LABEL LABEL=GAAS col=2 x=1. y=0.05 C.SIZE=0.4
LABEL LABEL=ALGAAS col=2 x=1. y=0.085 C.SIZE=0.4
LABEL LABEL=BUFFER col=2 x=1. y=0.125 C.SIZE=0.4
LABEL LABEL=S.I.GAAS col=2 x=1. y=0.175 C.SIZE=0.4
PLOT.3D Y.MIN=0 Y.MAX=0.2 ELECTRON LOG TITLE="ELECTRON 3D GaAs_0204" ^FRAME PHI=110
3D.SURF COLOR=4
$ Plot to show contact resistance
PLOT.2D Y.MIN=0 Y.MAX=0.2 BOUND LUMPED TITLE="Gunn Lumped Resistance GaAs 0204"
VECTOR J.HOLE
PLOT.3D E.field  x.min=0.5 x.max=1.8 y.min=0.023 y.max=0.073 t.size=0.4 x.size=0.4 y.size=0.4 TITLE="|E| 3D
GaAs 0204 @3V"  phi=150
LOOP STEPS=1
        ASSIGN NAME=VCGa0204 N.VALUE=(0, -2, -1.5, -0.5, 0)
        $ Use Newtons method for the solution
        SYMB NEWTON CARRIERS=1 ELEC
        METHOD ITLIMIT=1500 STACK=10
        SOLVE V(Cathode)=@VCGa0204 V(Anode)=0 ELEC=Anode VSTEP=0.2 NSTEP=20
        $ Plot Ia vs. Va
        PLOT.1D Y.AXIS=I(Anode) X.AXIS=V(Anode) x.size=0.4 y.size=0.4 TITLE="IV_GaAs_0204"
OUT.FILE="IV_GaAs_0204"@VCGa0204 UNCH
        LOG CLOSE
L.END
$ Save the mesh
SAVE MESH OUT.FILE=GAAS0204
SAVE TIF OUT.FILE=GAAS0204.TIF ALL
```

## A.1.4 Seven-channel GaAs based-Planar Gunn Diodes with Fourteen δ-doping Layers

```
$ 23/03/2010
$ Version GaAs0714
$ channel thickness=50 nm
$ number of channel=7  number of delta-doping=14
$ Delta-doping level 8E11
$ Annealled ohmic contacts reach the second channel
$ Lac=1.3 um
$Create a mesh**********************************************************************************************
$ All distances in microns (WIDTH, DEPTH, L, H1, Y.MIN)
MESH SMOOTH=1
$ Define device width
X.MESH WIDTH=0.49 H1=0.07
X.MESH WIDTH=0.01 H1=0.01
X.MESH WIDTH=1.3 H1=0.065
X.MESH WIDTH=0.01 H1=0.01
X.MESH WIDTH=0.49 H1=0.07
$Define device depth
Y.MESH DEPTH=0.003 H1=0.003
$ *******Channel 1***************
Y.MESH DEPTH=0.009 H1=0.003
Y.MESH DEPTH=0.002 H1=0.001
Y.MESH DEPTH=0.009 H1=0.003
Y.MESH DEPTH=0.05 H1=0.01
Y.MESH DEPTH=0.009 H1=0.003
Y.MESH DEPTH=0.002 H1=0.001
Y.MESH DEPTH=0.009 H1=0.003
$ *******Channel 1***************
$ *******Channel 2***************
Y.MESH DEPTH=0.009 H1=0.003
Y.MESH DEPTH=0.002 H1=0.001
Y.MESH DEPTH=0.009 H1=0.003
Y.MESH DEPTH=0.05 H1=0.01
Y.MESH DEPTH=0.009 H1=0.003
Y.MESH DEPTH=0.002 H1=0.001
Y.MESH DEPTH=0.009 H1=0.003
$ *******Channel 2***************
$ *******Channel 3***************
Y.MESH DEPTH=0.009 H1=0.003
Y.MESH DEPTH=0.002 H1=0.001
Y.MESH DEPTH=0.009 H1=0.003
Y.MESH DEPTH=0.05 H1=0.01
Y.MESH DEPTH=0.009 H1=0.003
Y.MESH DEPTH=0.002 H1=0.001
Y.MESH DEPTH=0.009 H1=0.003
$ *******Channel 3***************
$ *******Channel 4***************
Y.MESH DEPTH=0.009 H1=0.003
Y.MESH DEPTH=0.002 H1=0.001
Y.MESH DEPTH=0.009 H1=0.003
Y.MESH DEPTH=0.05 H1=0.01
Y.MESH DEPTH=0.009 H1=0.003
Y.MESH DEPTH=0.002 H1=0.001
Y.MESH DEPTH=0.009 H1=0.003
$ *******Channel 4***************
$ *******Channel 5***************
Y.MESH DEPTH=0.009 H1=0.003
Y.MESH DEPTH=0.002 H1=0.001
Y.MESH DEPTH=0.009 H1=0.003
Y.MESH DEPTH=0.05 H1=0.01
Y.MESH DEPTH=0.009 H1=0.003
Y.MESH DEPTH=0.002 H1=0.001
Y.MESH DEPTH=0.009 H1=0.003
$ *******Channel 5***************
$ *******Channel 6***************
```

```
Y.MESH DEPTH=0.009 H1=0.003
Y.MESH DEPTH=0.002 H1=0.001
Y.MESH DEPTH=0.009 H1=0.003
Y.MESH DEPTH=0.05 H1=0.01
Y.MESH DEPTH=0.009 H1=0.003
Y.MESH DEPTH=0.002 H1=0.001
Y.MESH DEPTH=0.009 H1=0.003
$ *******Channel 6**************
$ *******Channel 7**************
Y.MESH DEPTH=0.009 H1=0.003
Y.MESH DEPTH=0.002 H1=0.001
Y.MESH DEPTH=0.009 H1=0.003
Y.MESH DEPTH=0.05 H1=0.01
Y.MESH DEPTH=0.008 H1=0.002
Y.MESH DEPTH=0.002 H1=0.001
Y.MESH DEPTH=0.01 H1=0.002
$ *******Channel 7**************
$ *******Buffer&Substrate**************
Y.MESH DEPTH=0.5 H1=0.25
Y.MESH DEPTH=500 H1=250
$ Fine meshing
ELIMINATE ROWS X.MIN=0 X.MAX=0.49 Y.MIN=0 Y.MAX=0.456
ELIMINATE ROWS X.MIN=1.81 X.MAX=2.3 Y.MIN=0 Y.MAX=0.456
$ Specify regions*********************************
$ All distances in microns (Y.MIN, Y.MAX)
REGION NAME=BLANK NITRIDE
$ **************Below Channel 1 & Barriers*********************
REGION NAME=AGAAS1 GAAS POLYGON X.POLY=(0,0,0.49,0.49,0.5,0.5) Y.POLY=(0.617,0.615,0.615,0.003,
+0.003,0.617)
 REGION NAME=CGAAS1 GAAS POLYGON X.POLY=(2.3,2.3,1.81,1.81,1.8,1.8) Y.POLY=(0.617,0.615,0.615,
+0.003,0.003,0.617)
$ *******Channel 1**************
REGION NAME=ALGAAS1 ALGAAS X.MIN=0.5 X.MAX=1.8 Y.MIN=0.003 Y.MAX=0.013 X.MOLE=0.23
REGION NAME=ALGAAS2 ALGAAS X.MIN=0.5 X.MAX=1.8 Y.MIN=0.013 Y.MAX=0.023 X.MOLE=0.23
REGION NAME=GAAS1 GAAS X.MIN=0.5 X.MAX=1.8 Y.MIN=0.023 Y.MAX=0.073
REGION NAME=ALGAAS3 ALGAAS X.MIN=0.5 X.MAX=1.8 Y.MIN=0.073 Y.MAX=0.083 X.MOLE=0.23
REGION NAME=ALGAAS4 ALGAAS X.MIN=0.5 X.MAX=1.8 Y.MIN=0.083 Y.MAX=0.093 X.MOLE=0.23
$ *******Channel 1**************
$ *******Channel 2**************
REGION NAME=ALGAAS5 ALGAAS X.MIN=0.5 X.MAX=1.8 Y.MIN=0.093 Y.MAX=0.103 X.MOLE=0.23
REGION NAME=ALGAAS6 ALGAAS X.MIN=0.5 X.MAX=1.8 Y.MIN=0.103 Y.MAX=0.113 X.MOLE=0.23
REGION NAME=GAAS2 GAAS X.MIN=0.5 X.MAX=1.8 Y.MIN=0.113 Y.MAX=0.163
REGION NAME=ALGAAS7 ALGAAS X.MIN=0.5 X.MAX=1.8 Y.MIN=0.163 Y.MAX=0.173 X.MOLE=0.23
REGION NAME=ALGAAS8 ALGAAS X.MIN=0.5 X.MAX=1.8 Y.MIN=0.173 Y.MAX=0.183 X.MOLE=0.23
 $ *******Channel 2**************
$ *******Channel 3**************
REGION NAME=ALGAAS9 ALGAAS X.MIN=0.5 X.MAX=1.8 Y.MIN=0.183 Y.MAX=0.193 X.MOLE=0.23
REGION NAME=ALGAAS10 ALGAAS X.MIN=0.5 X.MAX=1.8 Y.MIN=0.193 Y.MAX=0.203 X.MOLE=0.23
REGION NAME=GAAS3 GAAS X.MIN=0.5 X.MAX=1.8 Y.MIN=0.203 Y.MAX=0.253
REGION NAME=ALGAAS11 ALGAAS X.MIN=0.5 X.MAX=1.8 Y.MIN=0.253 Y.MAX=0.263 X.MOLE=0.23
REGION NAME=ALGAAS12 ALGAAS X.MIN=0.5 X.MAX=1.8 Y.MIN=0.263 Y.MAX=0.273 X.MOLE=0.23
$ *******Channel 3**************
$ *******Channel 4**************
REGION NAME=ALGAAS13 ALGAAS X.MIN=0.5 X.MAX=1.8 Y.MIN=0.273 Y.MAX=0.283 X.MOLE=0.23
REGION NAME=ALGAAS14 ALGAAS X.MIN=0.5 X.MAX=1.8 Y.MIN=0.283 Y.MAX=0.293 X.MOLE=0.23
REGION NAME=GAAS4 GAAS X.MIN=0.5 X.MAX=1.8 Y.MIN=0.293 Y.MAX=0.343
REGION NAME=ALGAAS15 ALGAAS X.MIN=0.5 X.MAX=1.8 Y.MIN=0.343 Y.MAX=0.353 X.MOLE=0.23
REGION NAME=ALGAAS16 ALGAAS X.MIN=0.5 X.MAX=1.8 Y.MIN=0.353 Y.MAX=0.363 X.MOLE=0.23
$ *******Channel 4**************
$ *******Channel 5**************
REGION NAME=ALGAAS17 ALGAAS X.MIN=0.5 X.MAX=1.8 Y.MIN=0.363 Y.MAX=0.373 X.MOLE=0.23
REGION NAME=ALGAAS18 ALGAAS X.MIN=0.5 X.MAX=1.8 Y.MIN=0.373 Y.MAX=0.383 X.MOLE=0.23
REGION NAME=GAAS5 GAAS X.MIN=0.5 X.MAX=1.8 Y.MIN=0.383 Y.MAX=0.433
REGION NAME=ALGAAS19 ALGAAS X.MIN=0.5 X.MAX=1.8 Y.MIN=0.433 Y.MAX=0.443 X.MOLE=0.23
REGION NAME=ALGAAS20 ALGAAS X.MIN=0.5 X.MAX=1.8 Y.MIN=0.443 Y.MAX=0.453 X.MOLE=0.23
$ *******Channel 5**************
$ *******Channel 6**************
REGION NAME=ALGAAS21 ALGAAS X.MIN=0.5 X.MAX=1.8 Y.MIN=0.453 Y.MAX=0.463 X.MOLE=0.23
REGION NAME=ALGAAS22 ALGAAS X.MIN=0.5 X.MAX=1.8 Y.MIN=0.463 Y.MAX=0.473 X.MOLE=0.23
```

```
REGION NAME=GAAS6 GAAS X.MIN=0.5 X.MAX=1.8 Y.MIN=0.473 Y.MAX=0.523
REGION NAME=ALGAAS23 ALGAAS X.MIN=0.5 X.MAX=1.8 Y.MIN=0.523 Y.MAX=0.533 X.MOLE=0.23
REGION NAME=ALGAAS24 ALGAAS X.MIN=0.5 X.MAX=1.8 Y.MIN=0.533 Y.MAX=0.543 X.MOLE=0.23
$ *******Channel 6**************
$ *******Channel 7**************
REGION NAME=ALGAAS25 ALGAAS X.MIN=0.5 X.MAX=1.8 Y.MIN=0.543 Y.MAX=0.553 X.MOLE=0.23
REGION NAME=ALGAAS26 ALGAAS X.MIN=0.5 X.MAX=1.8 Y.MIN=0.553 Y.MAX=0.563 X.MOLE=0.23
REGION NAME=GAAS7 GAAS X.MIN=0.5 X.MAX=1.8 Y.MIN=0.563 Y.MAX=0.613 X.MOLE=0.23
REGION NAME=ALGAAS27 GAAS POLYGON X.POLY=(0,0,0.5,0.5,1.8,1.8,2.3,2.3)
Y.POLY=(0.623,0.617,0.617,0.613,0.613,0.617,0.617,0.623)
REGION NAME=ALGAAS28 ALGAAS X.MIN=0. X.MAX=2.3 Y.MIN=0.623 Y.MAX=0.633 X.MOLE=0.23
$ **************Below Buffer & S. I. Substrate*********************
REGION NAME=BGAAS GAAS Y.MIN=0.633 Y.MAX=1.133
REGION NAME=SIGAAS GAAS Y.MIN=1.133 Y.MAX=501.133
$ Electrode definition*****************************************************************************************
$ All distances in microns (X.MIN, X.MAX)
ELECTR NAME=Anode X.MIN=0 X.MAX=0.49 Y.MIN=0 Y.MAX=0.615
ELECTR NAME=Cathode X.MIN=1.81 X.MAX=2.3 Y.MIN=0 Y.MAX=0.615
$ Specify the doping throughout the device*************************************************************************
$ Doping quantities in cm-3 (N.PEAK)
$ All distances in microns (X.MIN, WIDTH, Y.MIN, Y.CHAR, Y.JUNC)
PROFILE REGION=ALGAAS1 N-TYPE CONC=1E2 UNIFORM OUT.FILE=GAASDOPING_0714_7ch
PROFILE REGION=ALGAAS2 N-TYPE CONC=1E2 UNIFORM
PROFILE REGION=ALGAAS3 N-TYPE CONC=1E2 UNIFORM
PROFILE REGION=ALGAAS4 N-TYPE CONC=1E2 UNIFORM
PROFILE REGION=ALGAAS5 N-TYPE CONC=1E2 UNIFORM
PROFILE REGION=ALGAAS6 N-TYPE CONC=1E2 UNIFORM
PROFILE REGION=ALGAAS7 N-TYPE CONC=1E2 UNIFORM
PROFILE REGION=ALGAAS8 N-TYPE CONC=1E2 UNIFORM
PROFILE REGION=ALGAAS9 N-TYPE CONC=1E2 UNIFORM
PROFILE REGION=ALGAAS10 N-TYPE CONC=1E2 UNIFORM
PROFILE REGION=ALGAAS11 N-TYPE CONC=1E2 UNIFORM
PROFILE REGION=ALGAAS12 N-TYPE CONC=1E2 UNIFORM
PROFILE REGION=ALGAAS13 N-TYPE CONC=1E2 UNIFORM
PROFILE REGION=ALGAAS14 N-TYPE CONC=1E2 UNIFORM
PROFILE REGION=ALGAAS15 N-TYPE CONC=1E2 UNIFORM
PROFILE REGION=ALGAAS16 N-TYPE CONC=1E2 UNIFORM
PROFILE REGION=ALGAAS17 N-TYPE CONC=1E2 UNIFORM
PROFILE REGION=ALGAAS18 N-TYPE CONC=1E2 UNIFORM
PROFILE REGION=ALGAAS19 N-TYPE CONC=1E2 UNIFORM
PROFILE REGION=ALGAAS20 N-TYPE CONC=1E2 UNIFORM
PROFILE REGION=ALGAAS21 N-TYPE CONC=1E2 UNIFORM
PROFILE REGION=ALGAAS22 N-TYPE CONC=1E2 UNIFORM
PROFILE REGION=ALGAAS23 N-TYPE CONC=1E2 UNIFORM
PROFILE REGION=ALGAAS24 N-TYPE CONC=1E2 UNIFORM
PROFILE REGION=ALGAAS25 N-TYPE CONC=1E2 UNIFORM
PROFILE REGION=ALGAAS26 N-TYPE CONC=1E2 UNIFORM
PROFILE REGION=ALGAAS27 N-TYPE CONC=1E2 UNIFORM
PROFILE REGION=ALGAAS28 N-TYPE CONC=1E2 UNIFORM
PROFILE REGION=AGAAS1 N-TYPE CONC=2E19 UNIFORM
PROFILE REGION=CGAAS1 N-TYPE CONC=2E19 UNIFORM
PROFILE REGION=GAAS1 N-TYPE CONC=1E2 UNIFORM
PROFILE REGION=GAAS2 N-TYPE CONC=1E2 UNIFORM
PROFILE REGION=GAAS3 N-TYPE CONC=1E2 UNIFORM
PROFILE REGION=GAAS4 N-TYPE CONC=1E2 UNIFORM
PROFILE REGION=GAAS5 N-TYPE CONC=1E2 UNIFORM
PROFILE REGION=GAAS6 N-TYPE CONC=1E2 UNIFORM
PROFILE REGION=GAAS7 N-TYPE CONC=1E2 UNIFORM
PROFILE REGION=BGAAS N-TYPE CONC=1E2 UNIFORM
PROFILE REGION=SIGAAS P-TYPE CONC=5E15 UNIFORM
INTERFACE REGION=(ALGAAS1,ALGAAS2) QF=8E11
INTERFACE REGION=(ALGAAS3,ALGAAS4) QF=8E11
INTERFACE REGION=(ALGAAS5,ALGAAS6) QF=8E11
INTERFACE REGION=(ALGAAS7,ALGAAS8) QF=8E11
INTERFACE REGION=(ALGAAS9,ALGAAS10) QF=8E11
INTERFACE REGION=(ALGAAS11,ALGAAS12) QF=8E11
INTERFACE REGION=(ALGAAS13,ALGAAS14) QF=8E11
INTERFACE REGION=(ALGAAS15,ALGAAS16) QF=8E11
INTERFACE REGION=(ALGAAS17,ALGAAS18) QF=8E11
```

```
INTERFACE REGION=(ALGAAS19,ALGAAS20) QF=8E11
INTERFACE REGION=(ALGAAS21,ALGAAS22) QF=8E11
INTERFACE REGION=(ALGAAS23,ALGAAS24) QF=8E11
INTERFACE REGION=(ALGAAS25,ALGAAS26) QF=8E11
INTERFACE REGION=(ALGAAS27,ALGAAS28) QF=8E11
$ Define materials**********************************************************************************
MATERIAL REGION=BLANK PERMITTI=1
$ GaAs
MATERIAL REGION=(AGAAS1,CGAAS1,GAAS1,GAAS2,GAAS3,GAAS4,GAAS5,GAAS6,GAAS7,BGAAS,
SIGAAS) PERMITTI=12.9 EG.MODEL=0 EG300=1.425 EG.X1=0.0EG.X2=0.0 AFFINITY=4.07 AF.X1=0.0
+ AF.X2=0.0 NC300=4.7E17
$ AlGaAs (X=0.23)
MATERIAL  REGION=(ALGAAS1,ALGAAS2,ALGAAS3,ALGAAS4,ALGAAS5,ALGAAS6,ALGAAS7,ALGAAS8,
ALGAAS9,ALGAAS10,ALGAAS11,ALGAAS12,ALGAAS13,ALGAAS14,ALGAAS15,ALGAAS16,ALGAAS17,AL
GAAS18,ALGAAS19,ALGAAS20,ALGAAS21,ALGAAS22,ALGAAS23,ALGAAS24,ALGAAS25,ALGAAS26,ALG
AAS27,ALGAAS28) PERMITTI=12.2 EG.MODEL=0 EG300=1.71 AFFINITY=3.82 NC300=5.9E17 AF.X1=0
+AF.X2=0 EG.X1=0 EG.X2=0
$ GaAs
MOBILITY REGION=(AGAAS1,CGAAS1,GAAS1,GAAS2,GAAS3,GAAS4,GAAS5,GAAS6,GAAS7,BGAAS,
SIGAAS) MUN0=8500 FLDMOB=2 VSATN=1.0E7 BETAN=1.0
$ AlGaAs (X=0.23)
MOBILITY  REGION=(ALGAAS1,ALGAAS2,ALGAAS3,ALGAAS4,ALGAAS5,ALGAAS6,ALGAAS7,ALGAAS8,
ALGAAS9,ALGAAS10,ALGAAS11,ALGAAS12,ALGAAS13,ALGAAS14,ALGAAS15,ALGAAS16,ALGAAS17,AL
GAAS18,ALGAAS19,ALGAAS20,ALGAAS21,ALGAAS22,ALGAAS23,ALGAAS24,ALGAAS25,ALGAAS26,ALG
AAS27,ALGAAS28) MUN0=4000 FLDMOB=2 VSATN=0.8E7 BETAN=1.0
$ Plot the mesh*************************************************************************************
PLOT.2D GRID Y.MIN=0 Y.MAX=0.8 TITLE="GaAs_07Channel_14DeltaDoping- Grid" FILL
PLOT.OUT="Grid_GaAs_0714_7ch"
$ Select models, numerical methods and initial guess*****************************************************
MODELS CONSRH AUGER FLDMOB=2 IMPACT.I
SYMB NEWT CARR=0
SOLVE V(Anode)=0 V(Cathode)=0
$ band structure plot
PLOT.1D COND X.START=1.5 X.END=1.5 Y.START=0.03 Y.END=0.8  x.size=0.4 y.size=0.4 SYMBOL=2
COLOR=11 NEG TITLE="BAND STRUCTURE 0V_0714_7ch" OUT.FILE="ConducBand GaAs_0714_7ch_0V"
PLOT.1D QFN X.START=1.5 X.END=1.5 x.size=0.4 y.size=0.4 COLOR=5 NEG UNCH OUT.FILE="FermiLevel
GaAs_0714_7ch_0V"
$ Symbolic factorization, solve, and save the solution at 0.6 V*************************************************
SYMB NEWTON CARRIERS=2 ELEC
METHOD ITLIMIT=1000 STACK=10
SOLVE V(Cathode)=0 V(Anode)=0.6 IMPACT.I OUT.FILE=MDGUNNGaAs_0714_7ch
$ dopings and electrons profile plots
PLOT.1D DOPING X.START=1.5 X.END=1.5 Y.START=0 Y.END=0.8 x.size=0.4 y.size=0.4 SYMBOL=2
COLOR=11 Y.LOG TITLE="DOPING PROFILE_0714_7ch" OUT.FILE="Impurity GaAs_Profile_0714_7ch"
PLOT.1D ELECT X.START=1.5 X.END=1.5 x.size=0.4 y.size=0.4 COLOR=11  SYMBOL=4 Y.LOG Y.START=0
Y.END=0.2TITLE="ELECTRON GaAs_0714_7ch" OUT.FILE="ElectronV_GaAs_0714_7ch"
PLOT.1D N.TOTAL Y.START=0.04 Y.END=0.04 x.size=0.4 y.size=0.4 COLOR=2  SYMBOL=4 Y.LOG
+TITLE="IMPURITY DISTRIBUTION _0714_7ch" OUT.FILE="ElectronH_Profile_0714_7ch"
 PLOT.1D COND X.START=1.5 X.END=1.5 Y.START=0 Y.END=0.8 x.size=0.4 y.size=0.4 SYMBOL=2 COLOR=11
NEG TITLE="BAND GaAs 0714_7ch @ 3 V" OUT.FILE="ConducBand_GaAs_0714_7ch_0.6V"
PLOT.1D QFN X.START=1.5 X.END=1.5 x.size=0.4 y.size=0.4 COLOR=2 NEG UNCH
OUT.FILE="FermiLevel_GaAs_0714_7ch_3V"
$ Impurity contour plot
PLOT.2D BOUND Y.MIN=0 Y.MAX=0.8 TITLE="Impurity Contours GaAs 0714_7ch" FILL  X.MAX=2.3
CONTOUR DOPING LOG MIN=10 MAX=20 DEL=.5 COLOR=2
CONTOUR DOPING LOG MIN=-16 MAX=-15 DEL=.5 COLOR=1 LINE=2
$ Plot current flow
Plot.2D Y.MIN=0 Y.MAX=0.8 FILL BOUND x.size=0.4 y.size=0.4 TITLE="CURRENT FLOW GaAs_0714_7ch @
0.6 V" CONTOUR FLOW COLOR=2
FILL REGION=BLANK COLOR=0
PLOT.3D Y.MIN=0 Y.MAX=0.8 ELECTRON LOG TITLE="ELECTRON 3D GaAs_0714_7ch" ^FRAME PHI=110
3D.SURF COLOR=4

$ Plot to show contact resistance
PLOT.2D Y.MIN=0 Y.MAX=0.8 BOUND LUMPED TITLE="Gunn Lumped Resistance GaAs 0714_7ch"
VECTOR J.HOLE
PLOT.3D E.field  x.min=0.5 x.max=1.8 y.min=0.023 y.max=0.073 t.size=0.4 x.size=0.4 y.size=0.4 TITLE="|E| 3D
GaAs 0714_7ch @3V"  phi=150
$ Plot ionisation
```

```
PLOT.2D BOUND Y.MIN=0 Y.MAX=0.8 TITLE="IMPACT IONISATION " FILL
CONTOUR II.GENER LOG
LOOP STEPS=1
        ASSIGN NAME=07147 N.VALUE=(0, -2, -1.5, -0.5, 0)
        $ Use Newtons method for the solution
        SYMB NEWTON CARRIERS=2 ELEC
        METHOD ITLIMIT=1500 STACK=10
        SOLVE V(Cathode)=@07147 V(Anode)=0 ELEC=Anode VSTEP=0.1 NSTEP=6
        $ Plot Ia vs. Va
        PLOT.1D Y.AXIS=I(Anode) X.AXIS=V(Anode) x.size=0.4 y.size=0.4 TITLE="IV_GaAs_0714_7ch"
OUT.FILE="IV_GaAs_0714_7ch"@07147 UNCH
        LOG CLOSE
L.END
$ Save the mesh
SAVE MESH OUT.FILE=GAAS0714_7ch
SAVE TIF OUT.FILE=GAAS0714_7ch.TIF ALL
```

## A.1.5 Single-channel $In_{0.23}Ga_{0.77}As$-based Planar Gunn Diodes with Four δ-doping Layers

```
$ 23/02/2010
$ Version InGaAs0104
$ Single In0.23Ga0.77As channel with four delta doping levels
$ channel thickness=12 nm
$Create a mesh*********************************************************************************
$ All distances in microns (WIDTH, DEPTH, L, H1, Y.MIN)
MESH SMOOTH=1
X.MESH WIDTH=0.49 H1=0.07
X.MESH WIDTH=0.01 H1=0.01
X.MESH WIDTH=1.45 H1=0.145
X.MESH WIDTH=0.01 H1=0.01
X.MESH WIDTH=0.49 H1=0.07
Y.MESH DEPTH=0.003 H1=0.003
Y.MESH DEPTH=0.009 H1=0.003
Y.MESH DEPTH=0.006 H1=0.003
Y.MESH DEPTH=0.02 H1=0.002
Y.MESH DEPTH=0.012 H1=0.003
Y.MESH DEPTH=0.006 H1=0.002
Y.MESH DEPTH=0.014 H1=0.002
Y.MESH DEPTH=0.5 H1=0.25
Y.MESH DEPTH=400 H1=200
$ Specify regions*****************************************************************************
$ All distances in microns (Y.MIN, Y.MAX)
REGION NAME=BLANK NITRIDE
REGION NAME=CAP GAAS X.MIN=0.49 X.MAX=1.96 Y.MIN=0.012 Y.MAX=0.018
REGION NAME=AALGAAS1 ALGAAS x.min=0.49 X.MAX=0.5 Y.MIN=0.018 Y.MAX=0.038 X.MOLE=0.23
REGION NAME=CALGAAS1 ALGAAS X.MIN=1.95 X.MAX=1.96 Y.MIN=0.018 Y.MAX=0.038 X.MOLE=0.23
REGION NAME=ALGAAS1 ALGAAS X.MIN=0.5 X.MAX=1.95 Y.MIN=0.018 Y.MAX=0.024 X.MOLE=0.23
REGION NAME=ALGAAS2 ALGAAS X.MIN=0.5 X.MAX=1.95 Y.MIN=0.024 Y.MAX=0.030 X.MOLE=0.23
REGION NAME=ALGAAS3 ALGAAS X.MIN=0.5 X.MAX=1.95 Y.MIN=0.030 Y.MAX=0.038 X.MOLE=0.23
REGION NAME=AINGAAS INGAAS x.min=0.49 X.MAX=0.5 Y.MIN=0.038 Y.MAX=0.050 X.MOLE=0.77
REGION NAME=CINGAAS INGAAS X.MIN=1.95 X.MAX=1.97 Y.MIN=0.038 Y.MAX=0.050 X.MOLE=0.77
REGION NAME=INGAAS INGAAS X.MIN=0.5 X.MAX=1.95 Y.MIN=0.038 Y.MAX=0.050 X.MOLE=0.77
REGION NAME=AALGAAS2 ALGAAS  POLYGON X.POLY=(0,0,0.49,0.49,0.50,0.50)
+Y.POLY=(0.054,0.052,0.052,0.050,0.050,0.054) X.MOLE=0.23
REGION NAME=CALGAAS2 ALGAAS  POLYGON X.POLY=(1.95,1.95,1.96,1.96,2.45,2.45)
+Y.POLY=(0.054,0.050,0.050,0.052,0.052,0.054) X.MOLE=0.23
REGION NAME=ALGAAS4 ALGAAS POLYGON X.POLY=(0,0,0.5,0.5,1.95,1.95,2.45,2.45)
Y.POLY=(0.056,0.054,0.054,0.050,0.050,0.054,0.054,0.056) X.MOLE=0.23
REGION NAME=ALGAAS5 ALGAAS Y.MIN=0.056 Y.MAX=0.064 X.MOLE=0.23
REGION NAME=ALGAAS6 ALGAAS Y.MIN=0.064 Y.MAX=0.070 X.MOLE=0.23
REGION NAME=BGAAS GAAS Y.MIN=0.070 Y.MAX=0.570
REGION NAME=SIGAAS GAAS Y.MIN=0.570 Y.MAX=400.57
$ Electrode definition************************************************************************
$ All distances in microns (X.MIN, X.MAX)
ELECTR NAME=Anode X.MIN=0 X.MAX=0.49 Y.MIN=0.009 Y.MAX=0.052
ELECTR NAME=Cathode X.MIN=1.96 X.MAX=2.45 Y.MIN=0.009 Y.MAX=0.052
$ ELECTR NAME=BOTTOM X.MIN=0.5 X.MAX=1.95 Y.MIN=0.012 Y.MAX=0.012
$ Specify the doping throughout the device*****************************************************
$ Doping quantities in cm-3 (N.PEAK)
$ All distances in microns (X.MIN, WIDTH, Y.MIN, Y.CHAR, Y.JUNC)
PROFILE REGION=CAP N-TYPE CONC=3.5E18 UNIFORM OUT.FILE=MDGUNNDOPING_InGaAs_0104
PROFILE REGION=ALGAAS1 N-TYPE CONC=1E2 UNIFORM
PROFILE REGION=ALGAAS2 N-TYPE CONC=1E2 UNIFORM
PROFILE REGION=INGAAS N-TYPE CONC=1E2 UNIFORM
PROFILE REGION=ALGAAS3 N-TYPE CONC=1E2 UNIFORM
PROFILE REGION=ALGAAS4 N-TYPE CONC=1E2 UNIFORM
PROFILE REGION=ALGAAS5 N-TYPE CONC=1E2 UNIFORM
PROFILE REGION=ALGAAS6 N-TYPE CONC=1E2 UNIFORM
PROFILE REGION=AALGAAS1 N-TYPE CONC=2E19 UNIFORM
PROFILE REGION=CALGAAS1 N-TYPE CONC=2E19 UNIFORM
PROFILE REGION=AALGAAS2 N-TYPE CONC=2E19 UNIFORM
PROFILE REGION=CALGAAS2 N-TYPE CONC=2E19 UNIFORM
PROFILE REGION=AINGAAS N-TYPE CONC=2E19 UNIFORM
```

```
PROFILE REGION=CINGAAS N-TYPE CONC=2E19 UNIFORM
PROFILE REGION=BGAAS N-TYPE CONC=1E2 UNIFORM
PROFILE REGION=SIGAAS P-TYPE CONC=5E15 UNIFORM
INTERFACE REGION=(ALGAAS1,ALGAAS2) QF=8E11
INTERFACE REGION=(ALGAAS3,ALGAAS2) QF=8E11
INTERFACE REGION=(ALGAAS4,ALGAAS5) QF=8E11
INTERFACE REGION=(ALGAAS5,ALGAAS6) QF=8E11
$ Define materials**********************************************************************************
$ GaAs
MATERIAL REGION=(BGAAS,SIGAAS) PERMITTI=12.9 EG.MODEL=0 EG300=1.425 EG.X1=0.0 EG.X2=0.0
+AFFINITY=4.07 AF.X1=0.0 AF.X2=0.0 NC300=4.7E17
MATERIAL REGION=CAP PERMITTI=12.9 EG.MODEL=0 EG300=1.425 EG.X1=0.0EG.X2=0.0 AFFINITY=4.07
+AF.X1=0.0 AF.X2=0.0 NC300=4.7E17
$ AlGaAs (X=0.23)
MATERIAL REGION=(AALGAAS1,AALGAAS2,ALGAAS1,ALGAAS2,ALGAAS3,ALGAAS4,ALGAAS5,
+ALGAAS6,CALGAAS1,CALGAAS2) PERMITTI=12.2 EG.MODEL=0 EG300=1.71 AFFINITY=3.82
+NC300=5.9E17 AF.X1=0 AF.X2=0 EG.X1=0 EG.X2=0
$ InGaAs (X=0.23)
MATERIAL REGION=(AINGAAS,INGAAS,CINGAAS) PERMITTI=13.9 EG.MODEL=0 EG300=1.1EG.X1=0.0
+ EG.X2=0.0 AFFINITY=4.26 AF.X1=0.0 AF.X2=0.0 NC300=2.9E17
$ GaAs
MOBILITY REGION=(CAP,BGAAS,SIGAAS) MUN0=8500 FLDMOB=2 VSATN=1.0E7 BETAN=1.0
$ AlGaAs (X=0.23)
$MOBILITY
REGION=(AALGAAS1,ALGAAS1,ALGAAS2,CALGAAS1,ALGAAS3,ALGAAS4,ALGAAS5,ALGAAS6)
MOBILITY REGION=(AALGAAS1,AALGAAS2,ALGAAS1,ALGAAS2,CALGAAS1,CALGAAS2,ALGAAS3,
+ALGAAS4,ALGAAS5,ALGAAS6) MUN0=4000 FLDMOB=2 VSATN=0.8E7 BETAN=1.0
$ InGaAs (X=0.23)
MOBILITY REGION=(AINGAAS,INGAAS,CINGAAS) MUN0=8000 FLDMOB=2VSATN=1.8E7 BETAN=1.0
$ Plot the mesh*************************************************************************************
PLOT.2D GRID Y.MIN=0 Y.MAX=0.1 TITLE="InGaAs_01Channel_04DeltaDoping- Grid" FILL
PLOT.OUT="Grid_InGaAs_0104"
$ Select models, numerical methods, and initial guess**********************************************
MODELS  CONSRH AUGER FLDMOB=2
SYMB NEWT CARR=0
SOLVE V(Anode)=0 V(Cathode)=0
$ band structure plot
PLOT.1D COND X.START=1.5 X.END=1.5  Y.START=0 Y.END=0.1 x.size=0.4 y.size=0.4 SYMBOL=2  COLOR=11
NEG TITLE="BAND STRUCTURE 0V_InGaAs_0104" OUT.FILE="ConducBand InGaAs_0104_0V"
PLOT.1D QFN X.START=1.5 X.END=1.5 x.size=0.4 y.size=0.4 COLOR=5 NEG UNCH OUT.FILE="FermiLevel
InGaAs_0104_0V"
LABEL LABEL=ALGAAS col=2 x=0.005 y=.5 C.SIZE=0.4
LABEL LABEL=INGAAS col=2 x=.023 y=.5 C.SIZE=0.4
LABEL LABEL=ALGAAS col=2 x=0.04 y=.5 C.SIZE=0.4
LABEL LABEL="FERMI LEVEL" col=2 x=0.07 y=-0.04 C.SIZE=0.4
LABEL LABEL="BUFFER & S.I.GAAS" col=2 x=.06 y=.5 C.SIZE=0.4
$Define contact resistances
CONTACT NAME=Cathode CON.RES=0.7E-6
CONTACT NAME=Anode CON.RES=0.7E-6
$ Symbolic factorization, solve, and save the solution at 1.0V*************************************
SYMB NEWTON CARRIERS=1 ELEC
METHOD ITLIMIT=1000 STACK=10
SOLVE V(Cathode)=0 V(Anode)=1.0 OUT.FILE=MDGUNNInGaAs_0104_1V
$Plot current
Plot.2D Y.MIN=0 Y.MAX=0.1 FILL BOUND x.size=0.4 y.size=0.4 TITLE="CURRENT FLOW InGaAs_0104 @ 1 V"
CONTOUR FLOW COLOR=2
FILL REGION=BLANK COLOR=0
LABEL LABEL=ANODE col=2 x=0.1 y=0.035 C.SIZE=0.4
LABEL LABEL=CATHODE col=2 x=2.0 y=0.035 C.SIZE=0.4
LABEL LABEL=ALGAAS col=2 x=1.1 y=0.03 C.SIZE=0.4
LABEL LABEL=INGAAS col=2 x=1.1 y=0.045 C.SIZE=0.4
LABEL LABEL=ALGAAS col=2 x=1.1 y=0.065 C.SIZE=0.4
LABEL LABEL=BUFFER col=2 x=1.1 y=0.085 C.SIZE=0.4
$ Symbolic factorization, solve, and save the solution at 3.0V*************************************
SYMB NEWTON CARRIERS=1 ELEC
METHOD ITLIMIT=1000 STACK=10
SOLVE V(Cathode)=0 V(Anode)=3 OUT.FILE=MDGUNNInGaAs_0104_3V
$ Dopings and electrons profile plots
```

```
PLOT.1D DOPING X.START=1.5 X.END=1.5 Y.START=0 Y.END=0.1 x.size=0.4 y.size=0.4 SYMBOL=2
COLOR=11 Y.LOG TITLE="DOPING PROFILE InGaAs_0104" OUT.FILE="Impurity_Profile InGaAs_0104"
PLOT.1D ELECT X.START=1.5 X.END=1.5 Y.START=0 Y.END=0.1 x.size=0.4 y.size=0.4 COLOR=11
SYMBOL=4 Y.LOG TITLE="ELECTRON InGaAs 0104" OUT.FILE="ElectronV_Profile InGaAs_0104"
LABEL LABEL=ALGAAS col=2 x=0.005 y=1e10 C.SIZE=0.4
LABEL LABEL=INGAAS col=2 x=.023 y=1e10 C.SIZE=0.4
LABEL LABEL=ALGAAS col=2 x=0.04 y=1e10 C.SIZE=0.4
LABEL LABEL="BUFFER & S.I.GAAS" col=2 x=.06 y=1e10 C.SIZE=0.4
PLOT.1D N.TOTAL Y.START=0.03 Y.END=0.03 x.size=0.4 y.size=0.4 COLOR=2  SYMBOL=4 Y.LOG
+TITLE="IMPURITY @Y=0.03 um " OUT.FILE="ElectronH_0.03 InGaAs_0104"
PLOT.1D COND X.START=1.5 X.END=1.5 Y.START=0 Y.END=0.1 x.size=0.4 y.size=0.4 SYMBOL=2 COLOR=11
NEG TITLE="ConducBand InGaAs 0104 @ 3 V" OUT.FILE="ConducBand InGaAs_0104 3V" NEG UNCH
PLOT.1D QFN X.START=1.5 X.END=1.5  Y.START=0 Y.END=0.1 x.size=0.4 y.size=0.4 COLOR=2 NEG UNCH
OUT.FILE="FermiLevel InGaAs_0104 3V"
$ Impurity contour plot
PLOT.2D BOUND TITLE="Gunn InGaAs_0104 - Impurity Contours" FILL  X.MAX=2.45 Y.MIN=0 Y.MAX=0.1
CONTOUR DOPING LOG MIN=10 MAX=20 DEL=.5 COLOR=2
CONTOUR DOPING LOG MIN=-16 MAX=-15 DEL=.5 COLOR=1 LINE=2
$ Plot current flow
Plot.2D  Y.MIN=0 Y.MAX=0.2 FILL BOUND x.size=0.4 y.size=0.4 TITLE="CURRENT FLOW InGaAs_0104 @ 3 V"
FILL REGION=BLANK COLOR=0
FILL REGION=BGAAS COLOR=4
FILL REGION=Anode COLOR=0
FILL REGION=Cathode COLOR=0
FILL REGION=SIGAAS COLOR=10
CONTOUR FLOW COLOR=1
PLOT.3D ELECTRON LOG TITLE="ELECTRON 3D InGaAs_0104" ^FRAME PHI=110 3D.SURF COLOR=4
$ Plot to show contact resistance
PLOT.2D BOUND LUMPED TITLE="Gunn Lumped Resistance InGaAs 0104" Y.MIN=0 Y.MAX=0.1
VECTOR J.HOLE
LOOP STEPS=1
        ASSIGN NAME=VCIn0104 N.VALUE=(0, -2, -1.5, -0.5, 0)
        $ Use Newtons method for the solution
        SYMB NEWTON CARRIERS=1 ELEC
        METHOD ITLIMIT=1500 STACK=10
        SOLVE V(Cathode)=@VCIn0104 V(Anode)=0 ELEC=Anode VSTEP=0.1 NSTEP=10
        $ Plot Ia vs. Va
        PLOT.1D Y.AXIS=I(Anode) X.AXIS=V(Anode) x.size=0.4 y.size=0.4 TITLE="IV_InGaAs_0104"
OUT.FILE="IV_InGAas 0104"@VCIn0104 UNCH
        LOG CLOSE
L.END
$ Save the mesh
SAVE MESH OUT.FILE=MDGUNNMESH_InGaAs_0104
SAVEFILE TIF OUT.FILE=InGaAs_0104.TIF
```

## A.2 Simulation Results of Passive Components and Circuits (Attached DVD)

### A.2.1 Coplanar Waveguide and Coplanar Striplines

### A.2.2 Radial Line Resonators

### A.2.3 Low Pass Filters

### A.2.4 Interdigital Couplers

### A.2.5 Power Divider/Combiners

# REFERENCES


1. J. B. Gunn, *Microwave oscillation of current in III-V semiconductors.* Solid State Communications, 1963. **1**(4): p. 4.

2. H. Eisele and G.I. Haddad, *Efficient power combining with D-band (110–170 GHz) InP Gunn devices in fundamental-mode operation.* IEEE Microwave and Guided Wave Letters, 1998. **8**(1): p. 3.

3. P. H. Siegel, *Terahertz technology.* IEEE Transactions on Microwave Theory and Techniques, 2002. **50**(3): p. 19.

4. H. Eisele, *InP Gunn devices for 400-425 GHz.* IET Electronics Letters, 2006. **42**(6): p. 2.

5. H. Eisele, *State of the art and future of electronic sources at terahertz frequencies.* IET Electronics Letters, 2010. **46**(26): p. 4.

6. H. Eisele, *480 GHz oscillator with an InP Gunn device.* IET Electronics Letters, 2010. **46**(6): p. 2.

7. E. R. Brown, W. D. Goodhue, and T.C.L.G. Sollner, *Fundamental oscillations up to 200 GHz in resonant tunneling diodes and new estimates of their maximum oscillation frequency from stationarystate tunneling theory.* Journal of Applied Physics, 1988. **64**(3): p. 11.

8. E. R. Brown, et al., *Oscillations up to 420 GHz in GaAs/AlAs resonant tunneling diodes.* Applied Physics Letters, 1989. **55**(17): p. 3.

9. E. R. Brown, et al., *Oscillations up to 712 GHz in InAs/AlSb resonant tunneling diodes.* Applied Physics Letters, 1991. **58**(20): p. 3.

10. M. N. Feiginov and D.R. Chowdhury, *Operation of resonant-tunneling diodes beyond resonant-state-lifetime limit.* Applied Physics Letters 2007. **91**(20): p. 3.

11. M. Asada, S. Suzuki, and N. Kishimoto, *Resonant tunneling diodes for sub-terahertz and terahertz oscillators.* Japanese Journal of Applied Physics, 2008. **47**(6): p. 10.

12. S. Suzuki, et al., *Fundamental oscillation of up to 831 GHz in GaInAs/AlAs resonant tunneling diode.* Applied Physics Express, 2009. **2**(5): p. 3.

13. S. Suzuki, et al., *Fundamental oscillation of resonant tunneling diodes above 1 THz at room temperature.* Applied Physics Letters, 2010. **97**(24): p. 3.

14. M. Ino, T. Ishibashi, and M. Ohmori, *CW oscillation with p+pn+ silicon IMPATT diodes in 200 GHz and 300 GHz bands.* IET Electronics Letters, 1976. **12**(6): p. 2.

15. K. Chang, W. F. Thrower, and G.M. Hayashibara, *Millimeter-wave silicon IMPATT sources and combiners for the 110–260 GHz range.* IEEE Transactions on Microwave Theory and Techniques, 1981. **29**(12): p. 7.

16. E. Ö jefors, B. Heinemann, and U.R. Pfeiffer, *A 325 GHz frequency multiplier chain in a SiGe HBT technology*, in *IEEE Radio Frequency Integrated Circuits Symposium (RFIC-2010)*. 2010: Anaheim USA. p. 4.

17. V. Radisic, et al., *A 50 mW 220 GHz power amplifier module*, in *IEEE MTT-S International Microwave Symposium*. 2010: Anaheim, USA. p. 4.

18. V. Radisic, et al., *A 10-mW submillimetre-wave solid-state power-amplifier module.* IEEE Transactions on Microwave Theory and Techniques, 2010. **58**(7): p. 7.

19. W. R. Deal, *Solid-state amplifiers for terahertz electronics*, in *IEEE MTT-S International Microwave Symposium Digest*. 2010: Anaheim, USA.

20. L. Ajili, et al., *High power quantum cascade lasers operating at λ=87 and 130 mm.* Applied Physics Letters, 2004. **85**(18): p. 3.

21. B. Williams, et al., *Operation of terahertz quantum-cascade lasers at 164 K in pulsed mode and at 117 K in continuous-wave mode.* Optics Express, 2005. **13**(9): p. 9.

22. J. Alton, et al., *Optimum resonant tunnelling injection and influence of doping density on the performance of THz bound-to-continuum cascade lasers.* Proceedings of SPIE, 2005. **5727**: p. 9.

23. S. Kumar, et al., *1.9 THz quantum-cascade lasers with one-well injector.* Applied Physics Letters, 2006. **88**(12): p. 3.

24. G. Scalari, et al., *Electrically switchable, two-color quantum cascade laser emitting at 1.39 and 2.3 THz.* Applied Physics Letters, 2006. **88**(14): p. 3.

25. C. Walther, et al., *Low frequency terahertz quantum cascade laser operating from 1.6 to 1.8 THz.* Applied Physics Letters, 2006. **89**(23): p. 3.

26. Williams, B.S., *Terahertz quantum-cascade lasers.* Nature Photonics, 2007. **1**: p. 9.

27. P. -C. Huang, et al., *A 131 GHz push-push VCO in 90-nm CMOS technology*, in *IEEE Radio Frequency Integrated Circuits Symposium (RFIC-2005)*. 2005: California, USA. p. 4.

28. C. Cao, E. Seok, and K.K. O, *192 GHz push–push VCO in 0.13 um CMOS.* IET Electronics Letters, 2006. **42**(4): p. 2.

29. R. Wanner, et al., *A SiGe monolithically integrated 278 GHz push-push oscillator*, in *IEEE MTT-S International Microwave Symposium*. 2007: Honolulu, USA. p. 4.

30. E. Seok, et al., *A 410 GHz CMOS push-push oscillator with an on-chip patch antenna*, in *IEEE International Solid-State Circuits Conference*. 2008: San Francisco, USA. p. 3.

31. K. W. Kobayashi, et al., *A 108 GHz InP-HBT monolithic push-push VCO with low phase noise and wide tuning bandwidth.* IEEE Journal of Solid-state Circuits, 1999. **34**(9): p. 8.

32. K Uchida, et al., *A series of InGaP/InGaAs HBT oscillators up to D-band.* IEEE Transactions on Microwave Theory and Techniques, 2001. **49**(5): p. 8.

33. Y. Baeyens and Y.K. Chen, *A monolithic integrated 150 GHz SiGe HBT push-push VCO with simultaneous differential V-band output*, in *IEEE MTT-S International Microwave Symposium* 2003: Philadelphia, USA. p. 4.

34. M. C. Kemp, *A review of millimetre-wave and terahertz technology for detection of concealed threats*, in *33rd International Conference on Infrared, Millimeter and Terahertz Waves*. 2008: Pasadena, CA, USA. p. 2.

35. N. Kukutsu and Y. Kado, *Overview of millimeter and terahertz wave application research.* NTT Technical Review, 2009. **7**(3): p. 6.

36. V. N. Sokolov, et al., *Terahertz generation in submicron GaN diodes within the limited space-charge accumulation regime.* Journal of Applied Physics, 2005. **98**(6): p. 7.

37. O. Yilmazoglu, et al., *First observation of bias oscillations in GaN Gunn diodes on GaN substrate* IEEE Transactions on Electron Devices, 2008. **55**(6): p. 5.

38. S. J. J. Teng and R.E. Goldwasser, *High-performance second-harmonics operation w-band GaAs Gunn diode.* IEEE Electron Device Letters, 1989. **10**: p. 3.

39. F. Driouch and C. Dalle, *Investigation of FECTED performance for millimeter-wave applications.* IEEE Transactions on Microwave Theory and Techniques, 2001. **49**(7): p. 9.

40. K. Y. Xu, G. Wang, and A.M. Song, *Gunn oscillations in a self-switching nanodiodes.* Applied Physics Letters, 2008. **93**(23): p. 3.

41. S. Perez, et al., *Terahertz Gunn-like oscillations in InGaAs/InAlAs planar diodes.* Journal of Applied Physics, 2008. **103**(9).

42. A. Khalid, et al., *A planar Gunn diode operating above 100 GHz.* IEEE Electron Device Letters, 2007. **28**(10): p. 3.

43. D. –H. Kim and J.A.d. Alamo, *30-nm InAs PHEMTs with $f_T$=644 GHz and $f_{max}$=681 GHz.* IEEE Electron Device Letters, 2010. **31**(8): p. 3.

44. H. Kromer, *Theory of the Gunn Effect.* Proceedings of the IEEE, 1964. **52**(12): p. 1.

45. C. Hilsum, *Transferred electron amplifiers and oscillators.* Proceedings of the IRE, 1962. **50**(2): p. 5.

46. B. K. Ridley and T. B. Watkins, *The possibility of negative resistance effects in semiconductors.* Proceedings of the Physical Society, 1961. **78**(2): p. 12.

47. P. J. Bulman, G. S. Hobson, and B.C. Taylor, *Transferred electron devices*. 1972, London: Academic Press.

48. W. Shockley and W.P. Mason, *Dissected amplifiers using negative resistance.* Journal of Applied Physics, 1954. **25**(5): p. 1.

49. H. Kromer, *The physical principles of a negative-mass amplifier.* Proceedings of the IRE, 1959. **47**(3): p. 10.

50. J. B. Gunn, *The field-dependence of electron mobility in germanium.* Journal of Electronics and Control, 1956. **2**(1): p. 8.

51. B. K. Ridley, *Specific negative resistance in solids.* Proceedings of Physical Society, 1963. **82**(6): p. 13.

52. J. B. Gunn, in *7th International Conference on the Physics of Semiconductors*. 1964: Paris, France.

53. J. S. Heeks, *Some properties of the moving high-field domain in Gunn effect devices.* IEEE Transactions on Electron Devices, 1966. **13**(1).

54. J. E. Carroll, *Oscillations covering 4 Gc/s to 31 Gc/s from a single Gunn diode.* IET Electronics Letters, 1966. **2**(4): p. 1.

55. J. A. Copeland, *A new mode of operation for bulk negative resistance oscillators.* Proceedings of the IEEE, 1966. **54**(10): p. 2.

56. J. A. Copeland, *LSA oscillator-diode theory.* Journal of Applied Physics, 1967. **38**(8): p. 6.

57. H. -C. Huang and L.A. MacKenzie, *A Gunn diode operated in the hybrid mode.* Proceedings of the IEEE, 1968. **56**(7): p. 2.

58. B. J. Elliott, J. B. Gunn, and J.C. McGroddy, *Bulk negative differential conductivity and traveling domains in n-type germanium.* Applied Physics Letters, 1967. **11**(8): p. 3.

59. A. G. Foyt and A.L. McWhorter, *The Gunn effect in polar semiconductors.* IEEE Transactions on Electron Devices, 1966. **13**(1): p. 9.

60. J. W. Allen, et al., *Microwave oscillations in $GaAs_xP_{1-x}$ alloys.* Applied Physics Letters, 1965. **7**(4): p. 3.

61. J. C. McGroddy, M. R. Lorenz, and T.S. Plaskett, *The gunn effect and conduction band structure in $Ga_xIn_{1-x}Sb$ alloys.* Solid State Communications, 1969. **7**(13): p. 3.

62. K. Segawa, et al., *$Ga_xIn_{1-x}Sb$ Gunn diodes*, in *International Conference on Solid State Devices*. 1976, Japanese Journal of Applied Physics: Tokyo, Japan. p. 4.

63. Y. Takeda, N. Shikagawa, and A. Sasaki, *Transferred-electron oscillation in n-$In_{0.53}Ga_{0.47}As$.* Solid-State Electronics, 1980. **23**(9): p. 2.

64. R. E. Hayes and R.M. Raymond, *Observation of the transferred-electron effect in $Ga_xIn_{1-x}As_yP_{1-y}$.* Applied Physics Letters, 1977. **31**(4): p. 2.

65. W. C. Tsai, F. J. Rosenbaum, and L.A. MacKenzie, *Circuit analysis of waveguide-cavity Gunn-effect oscillator*. IEEE Transactions on Microwave Theory and Techniques, 1970. **18**(11): p. 10.

66. W. R. Curtice, *Quenched-domain mode oscillation in waveguide circuits.* IEEE Transactions on Microwave Theory and Techniques, 1973. **21**(6): p. 6.

67. F. L. Warner and P. Herman, *Miniature X-band Gunn oscillator with a dielectric-tuning system.* IET Electronics Letters, 1966. **2**(12): p. 2.

68. R. B. Smith and P.W. Crane, *Varactor-tuned Gunn-effect oscillator.* IET Electronics Letters, 1970. **6**(5): p. 2.

69. J. A. G. Malherbe and M.C. Wijnbeek, *Gunn diode oscillator constructed in nonradiative dielectric waveguide.* Electronics Letters, 1987. **23**(25): p. 2.

70. C. L. Zhong, et al., *Ka-band substrate integrated waveguide Gunn oscillator.* IEEE Microwave and Wireless Components Letters, 2008. **18**(7): p. 3.

71. A. Mortazawi and T. Itoh, *A periodic plannar Gunn diode power combining oscillator.* IEEE Transactions on Microwave Theory and Techniques, 1990. **38**(1): p. 2.

72. Ch. D. Prasad, S. S. Sarin, and D. Singh, *35 GHz dielectric resonator stabilised gunn oscillator* International Journal of Infrared and Millimeter Waves, 1996. **17**(2): p. 10.

73. N. L. Wang and S.E. Schwarz, *Planar Oscillators for Monolithic Integration.* International Journal of Infrared and Millimeter Waves, 1982. **3**(6): p. 12.

74. S. Montanari, *Fabrication and characterization of planar Gunn diodes for monolithic microwave integrated circuits*, in *Institute ISG1*. 2005, Forschungzentrum Julich: Julich. p. 158.

75. M. P. Shaw, H. L. Grubin, and P.R. Solomon, *The Gunn-Hilsum Effect*. 1979: Academic Press. 250.

76. M. Shur, *GaAs devices and circuits*. Microdevices Physics and Fabrication Technologies, ed. I. Brodie and J.J. Muray. 1987, New York Plenum Press.

77. J. A. Copeland, T. Hayashi, and M. Uenohara, *Logic and memory elements using two-valley semiconductors.* Proceedings of the IEEE, 1967. **55**(4): p. 2.

78. G. White and N.J. Marlboro, *Gunn-diode logic circuits*, U.S. Patent, Editor. 1971, Bell Telephone Laboratories, Incorporated Murray Hill, N. J.: USA. p. 6.

79. H. Hayakawa, et al., *Generation of coherent ultrasonic waves with GaAs Gunn oscillator.* Applied Physics Letters, 1969. **14**(9): p. 2.

80. A. A. Grinberg and A.A. Kastalskii, *The ultrasound generation under the gunn effect in a piezoelectric material.* Physica Status Solidi (b), 1968. **26**(1): p. 6.

81. R. E. Lee and R.M. White, *Elastic wave generation by a Gunn effect oscillator coupled to a piezoelectric.* Applied Physics Letters, 1970. **16**(9): p. 4.

82. M. Cohen, S. Knight, and J. Elward, *Optical modulation in bulk GaAs using the Gunn effect.* Applied Physics Letters, 1966. **8**(11): p. 3.

83. P. Guetin and D. Boccon-Gibod, *Franz-Keldysh effect with Gunn domains in bulk GaAs.* Applied Physics Letters, 1968. **13**(5): p. 3.

84. M. S. Shur, *The effect of the shift of the absorption edge by electrical field in the degenerate semiconductors.* Physics Letters A, 1969. **29**(9): p. 2.

85. S. I. Domrachev and V.I. Naianov, *Electrooptic light modulation in a waveguide by a Gunn domain edge field.* Pis'ma v Zhurnal Tekhnicheskoi Fiziki, 1986. **12**: p. 5.

86. Michael Shur, *GaAs devices and circuits*. Microdevices Physics and Fabrication Technologies, ed. Ivor Brodie and J.J. Muray. 1986, New York: Plenum PRess.

87. D. A. Robertson, et al., *Semi-chaotic pulse effects in self-modulating Gunn oscillators.* International Journal of Infrared and Millimeter Waves, 1994. **15**(3): p. 11.

88. C. G. Diskus, et al., *Gunn effect in MESFET-like strucuctures.* IET Electronics Letters, 1992. **28**(11): p. 2.

89. T. Sugeta, et al., *Characteristics and applications of a Schottky-barrier-gate Gunn-effect digital-device.* IEEE Transactions on Electron Devices, 1974. **21**(8): p. 12.

90. V. A. Posse and B. Jalali, *Gunn effect in heterojunction bipolar transistors.* IET Electronics Letters, 1994. **30**(14): p. 2.

91. J. K. Twynam, et al., *Demostration of a 77-GHz heterojunction bipolar transferred electron devices.* IEEE Electron Device Letters, 2000. **21**(1): p. 3.

92. G. M. Dunn, A. Phillips, and P.J. Topham, *Current instability in power HEMTs.* Semiconductor Science and Technology, 2001. **16**(7): p. 6.

93. R. Kohler, et al., *Terahertz semiconductor-heterostrucurte laser.* Nature, 2002. **417**: p. 4.

94. P. E. Powers, et al., *Terahertz generation with tandem seeded optical parametric generators.* Optics Letters, 2005. **30**(6): p. 3.

95. T. D. Wang, et al., *Forward and backward terahertz-wave difference frequency generations from periodically poled lithium niobate.* Optics Express, 2008. **16**(9): p. 8.

96. A. Maestrini, et al., *A frequency-multiplied source with more than 1 mW of power across the 840-900 GHz band.* IEEE Transactions on Antennas and Propagation, 2010. **58**(7): p. 8.

97. A. Suzuki, et al., *Fundamental oscillation of resonant tunneling diodes above 1 THz at room temperature.* Applied Physics Letters, 2010. **97**(24): p. 3.

98. M. Ino, T. Ishibashi, and M. Ohmori, *C.W. oscillation with P+-P-N+ silicon IMPATT diodes in 200 GHz and 300 GHz.* IET Electronics Letters, 1976. **12**(6): p. 2.

99. M. Mukherjee, et al., *GaN IMPATT diode: a photosensitive high power THz source.* Semiconductor Science and Technology, 2007. **22**(12): p. 10.

100. M.-R. Friscourt, et al., *Theoretical contribution to the design of millimeter-wave TEO's.* IEEE Transactions on Electron Devices, 1983. **30**(3): p. 7.

101. C. Li, et al., *Novel planar Gunn diode operating in fundamental mode up to 158 GHz*, in *16th International Conference on Electron Dynamics in Semiconductors, Optoelectronics and Nanostructures*, L. Varani, C. Palermo, and G. Bastard, Editors. 2009, IOP Publishing: Montpellier, France. p. 4.

102. C. Li, et al., *An $In_{0.23}Ga_{0.77}As$-based pHEMT-like planar Gunn diode operating at 116 GHz*, in *35th International Conference on Infrared, Millimeter and Terahertz Waves*. 2010: Rome, Italy. p. 2.

103. R. F. Adams, *CW operation of GaAs planar Gunn diodes with evaporated contacts.* Proceedings of the IEEE, 1969. **57**(12): p. 2.

104. M. Takeuchi, A. Higashisaka, and K. Sekido, *GaAs planar Gunn diodes for DC-biased operation.* IEEE Transactions on Electron Devices, 1972. **19**(1): p. 3.

105. K. Sekido, et al., *CW oscillations in GaAs planar-type bulk diodes.* Proceedings of the IEEE, 1969. **57**(5): p. 2.

106. Y. Nakamura, A. Shibayama, and T. Ohml, *Domain transit-mode oscillation in planar-type Gunn device of InP.* Proceedings of the IEEE, 1974. **62**(1): p. 2.

107. K. Murayama, et al., *Planar-type Gunn diode of InP.* Japanese Journal of Applied Physics, 1974. **13**(4): p. 5.

108. Y. Y. Zhao, C. J. Wei, and H. Beneking, *Transferred-electron oscillation in In0.53Ga0.47As.* IET Electronics Letters, 1982. **18**(19): p. 2.

109. W. H. Haydl, *Planar Gunn diodes with ideal contact geometry.* Proceedings of the IEEE, 1973. **61**(4): p. 1.

110. B. Jeppsson, I. Marklund, and K. Olsson, *Voltage tuning of concentric planar Gunn diodes.* IET Electronics Letters, 1967. **3**(11): p. 3.

111. G. M. Clarke, A. L. Edridge, and J.C. Bass, *Planar Gunn-effect oscillators with concentric electrodes.* IET Electronics Letters, 1969. **5**(20): p. 2.

112. C. O. Newton and G. Bew, *Frequency measurements on Gunn effect devices with concentric electrodes.* Journal of Physics D: Applied Physics, 1970. **3**(8): p. 11.

113. Z. N. Chigogidze, et al., *Voltage-controlled frequency tuning in Gunn diodes with annular electrode geometry.* Radiotekhnika i Elektronika, 1975. **20**: p. 5.

114. T. Sugeta, H. Yanai, and K. Sekid, *Schottky-gate bulk effect digital devices.* Proceedings of the IEEE, 1971. **58**(11): p. 2.

115. K. Kurumada, T. Mizutani, and M. Fujimoto, *GaAs planar Gunn digital devices with subsidiary anode.* IET Electronics Letters, 1974. **10**(9): p. 3.

116. H. Scheiber, et al., *MIMIC-compatible GaAs and InP field effect controlled transferred electron ( FECTED) oscillators.* IEEE Transactions on Microwave Theory and Techniques, 1989. **37**(12): p. 6.

117. A. L. Springer, et al., *Transferred electron effect in AlGaAs/GaAs multi-quantum-well structures*, in *Proceeding of the 27th European Solid-State Device Research Conference*. 1997: Stuttgart, Gemany. p. 4.

118. A. M. Song, et al., *Unidirectional electron flow in a nanometer-scale semiconductor channel: A self-switching device.* Applied Physics Letters, 2003. **83**(9): p. 3.

119. A. Khalid, et al., *Planar Gunn-type triode oscillator at 83 GHz.* IET Electronics Letters, 2007. **43**(15): p. 2.

120. M. R. Kim, et al., *Design and fabrication of planar GaAs Gunn diodes.* IEICE Transactions on Electronics E Series C, 2008. **91**(5): p. 6.

121. J. Huang, et al., *Design and manufacture of planar GaAs Gunn diode for millimeter wave application.* Chinese Physics B, 2010. **19**(12).

122. M. R. Brozel and G.E. Stillman, eds. *Properties of Gallium Asenide*. 3rd ed. 1996, Instituion of Engineering and Technology. 1010.

123. T. P. Pearsall, *Properties, processing and applications of indium phosphide*. EMIS Datareviews Series, ed. T.P. Pearsall. 2000, UK: INSPEC/IEE. 300.

124. Ioffe Physical Technical Institute. *GaN-Gallium Nitride*. 2011 [cited 2011 December 2011]; Available from: http://www.ioffe.ru/SVA/NSM/Semicond/GaN/index.html.

125. S. M. Sze, *Semiconductor devices physics and technology* 2ed. 2002: John Wiley & Sons, INC. 564.

126. P. D. Southgate, *Recombination processes following impact ionization by high - field domains in Gallium Arsenide.* Journal of Applied Physics, 1967. **38**(12): p. 7.

127. D. M. Pozar, *Microwave engineering*. 2nd ed. 1998, Toronto: John Wiley & Sons

128. G. D. Vendelin, A. M. Pavio, and U.L. Rohde, *Microwave circuit design using linear and nonlinear techniques*. 2nd ed. 2005, Hoboken, New Jersey: John Wiley & Sons, Inc. 1080.

129. L. B. Valdes, *Resistivity measurements on germanium for transistors.* Proceedings of the IRE, 1954. **42**(2): p. 8.

130. L. J. Van Der Pauw, *A method of measuring specific resistivity and Hall effect of discs of arbitrary shape.* Philips Research Reports, 1958. **13**(1): p. 9.

131. W. L. V. Price, *Extension of van der Pauw's theorem for measuring specific resistivity in discs of arbitrary shape to anisotropic media*. Journal of Physics D: Applied Physics, 1972. **5**(6): p. 6.

132. S. V. Lozanova and C.S. Roumenin, *A three-point-probe method for measuring resistivity and the Hall coefficient using Hall devices with minimal design complexity*. Measurement, 2010. **43**(3): p. 7.

133. F. M. Smits, *Measurement of sheet resistivities with the four-point probe.* The Bell System Technical Journal, 1958. **37**(3): p. 8.

134. L. J. Van Der Pauw, *A method of measuring the resistivity and Hall coefficient on lamellae of arbitrary shape.* Philips Technical Review, 1958/1959. **20**(8): p. 5.

135. V. L. Rideout, *A review of the theory and technology for ohmic contacts to group III–V compound semiconductors.* Solid-State Electronics, 1975. **18**: p. 10.

136. J. M. Woodall, et al., *Ohmic contacts to n-GaAs using graded band gap layers of $Ga_{1-x}In_xAs$ grown by molecular beam epitaxy*. Journal of Vaccum Science and Technology, 1981. **19**(3): p. 2.

137. C. P. Lee, B. M. Welch, and W.P. Fleming, *Reliability of AuGe/Pt and AuGe/Ni ohmic contacts on GaAs.* IET Electronics Letters, 1981. **17**(12): p. 2.

138. R. H. Cox and H. Strack, *Ohmic contacts for GaAs devices* Solid-State Electronics, 1967. **10**(12): p. 8.

139. L. E. Terry and R.W. Wilson, *Metallization systems for silicon integrated circuits.* Proceedings of the IEEE, 1969. **57**(9): p. 7.

140. G. K. Reeves and H.B. Harrison, *Obtaining the specific contact resistance from transmission line model measurements.* IEEE Electron Device Letters, 1982. **3**(5): p. 3.

141. A. Goetzberger and R.M. Scarlett, *Research and invesitgation of inverse epitaxial UHF power transistors*. 1964, Wright-Patterson Air Force Base: Ohio, USA. p. 151.

142. G. S. Marlow and M.B. Das, *The effects of contact size and non-zero metal resistance on the determination of specific contact resistance.* Solid-State Electronics, 1982. **25**(2): p. 4.

143. J. H. Klootwijk and C.E. Timmering, *Merits and limitations of circular TLM structures for contact resistance determination for novel III-V HBTs* in *The 17th*

*International Conference on Microelectronics Test Structures*. 2004: Awaji Yumebutai, Japan. p. 247-252.

144. G. K. Reeves, *Specific contact resistance using a circular transmission line model.* Solid-State Electronics, 1980. **23**(5): p. 4.

145. R. A. Witte, *Spectrum and network measurements*. 2006, Raleigh: Scitech

146. R. J. Collier and A.D. Skinner, *Microwave measurements*. 3 ed. IET Electrical Measurement ed. R. J. Collier and A.D. Skinner. 2007: The Institution of Engineering and Technology.

147. M. Hiebel, *Vector network analyzer (VNA) calibration: the basics*, R. Schwarz, Editor. 2008. p. 10.

148. R. A. Hackborn, *An automatic network analyzer system.* Microwave Journal, 1968. **11**: p. 8.

149. S. Rehnmark, *On the calibration process of automatic network analyzer systems.* IEEE Transactions on Microwave Theory and Techniques, 1974. **22**(4): p. 2.

150. H. Van Hamme and M.V. Bossche, *Flexible vector network analyzer calibration with accuracy bounds using an 8-term or a 16-term error correction model.* IEEE Transactions on Microwave Theory and Techniques, 1994. **42**(6): p. 12.

151. A. Ferrero, *Two-port network analyzer calibration using an unknown "thru".* IEEE Microwave and Guided Wave Letters, 1992. **2**(12): p. 3.

152. H. J. Eul and B. Scheik, *Reducing the number of calibration standards for network analyzer calibration.* IEEE Transactions on Instrumentation and Measurement, 1991. **40**(4): p. 4.

153. E. Strid, *Planar impedance standards and accuracy considerations in vector network analysis*, in *27th ARFTG Conference Digest-Spring*. 1986: Baltimore, MD, USA. p. 159-166.

154. K. Jones and E. Strid, *Where are my on-wafer reference planes?*, in *30th ARFTG Conference Digest-Winter*. 1987: Dallas, TX, USA. p. 14.

155. S. Basu and L. Hayden, *An SOLR calibration for accurate measurement of orthogonal on-wafer DUTs*, in *IEEE MTT-S International Microwave Symposium Digest*. 1997: Denver, USA. p. 4.

156. U. Stumper, *Influence of nonideal calibration items on S-parameter uncertainties applying the SOLR calibration method.* IEEE Transactions on Instrumentation and Measurement, 2009. **58**(4): p. 6.

157. W. -K. Deng and T.-H. Chu, *A three-port vector network analyzer - measurement system, calibration and results*, in *2001 IEEE MTT-S International Microwave Symposium Digest*. 2001: Phoenix, AZ , USA p. 1531-1534.

158. G. F. Engen and C.A. Hoer, *Thru-Reflect-Line: an improved technique for clibrating the dual six-port automatic network analyzer*. IEEE Transactions on Microwave Theory and Techniques, 1979. **27**(12): p. 7.

159. H. -J. Eul and B. Schiek, *Thru-Match-Reflect: one result of a rigorous theory for de-embedding and network analyzer calibration*, in *The 18th European Microwave Conference*. 1988: Stockholm, Sweden. p. 909-914.

160. A. Davidson, E. Strid, and K. Jones, *Achieving greater on-wafer S-parameter accuracy with the LRM calibration technique*, in *The 34th ARFTG Conference Digest-Winter*. 1989: Ft. Lauderdale, FL, USA. p. 61-66.

161. F. Purroy and L. Pradell, *New theoretical analysis of the LRRM calibration technique for vector network analyzers.* IEEE Transactions on Instrumentation and Measurement, 2001. **50**(5): p. 8.

162. A. Davidson, K. Jones, and E. Strid, *LRM and LRRM calibrations with automatic determination of load inductance*, in *36th ARFTG Conference Digest-Fall*. 1990: Monterey, CA, USA. p. 57-63.

163. J. Ou and M.F. Caggiano, *Determine two-port S-parameters from one-port measurements using calibration substrate standards*, in *55th Electronic Components and Technology Conference*. 2005: Florida, USA. p. 1765-1768.

164. V. M. Hietala, *Determining two-port S-parameters from a one-port measurmeent using a novel impedance-state test chip*, in *IEEE MTT-S International Microwave Symposium Digest* 1999: Anaheim, CA, USA. p. 1639-1642.

165. Virginia Diodes, *Millimeter-submillimeter power meter operating manual*. 2009: Charlottesville, VA, USA.

166. Agilent Technologies Inc., *Agilent spectrum analysis basics*. 2006, Application Note 150.

167. Agilent Technologies Inc., *Agilent E5071B ENA series RF network analzyers user's guide*. 2007.

168. Agilent Technologies Inc., *Agilent E8257D PSG microwave analog signal generator data sheet*. 2010.

169. Y. K. Chen, et al., *Observation of high-frequency high-field instability in GaAs InGaAs AlGaAs DH-MODFETs at K band.* IEEE Electron Device Letters, 1988. **9**(1): p. 3.

170. S. P. Stapleton, et al., *Experimental study of microwave reflection gain of AlAs/GaAs/AlAs quantum well structures.* IET Electronics Letters, 1990. **26**(2): p. 2.

171. J. Figueiredo, et al., *Resonant tunnelling optoelectronic circuits* in *Advances in optical and photonic devices*, K.Y. Kim, Editor. 2010, InTech. p. 34.

172. I. G. Eddison and D.M. Brookbanks, *Operating modes of millimetre wave transferred electron oscillators.* IET Electronics Letters, 1981. **17**(3): p. 2.

173. C. Li, et al., *Enhancement of power and frequency in HEMT-like planar Gunn diodes by introducing extra delta-doping layers.* Microwave and Optical Component Letters, 2011. **53**(7): p. 3.

174. C. Li, et al., *Design, fabrication and characterization of $In_{0.23}Ga_{0.77}As$-channel planar Gunn diodes for millimeter wave applications.* Solid-State Electronics, 2011. **64**(1): p. 6.

175. N. J. Pilgrim, et al., *Gunn oscillations in planar heterostructure diodes.* Semiconductor Science and Technology, 2008. **23**(7).

176. N. J. Pilgrim, et al., *Vertical scaling of multi-stack planar Gunn diodes*, in *International Semiconductor Conference*. 2010: Sinaia, Romania.

177. N. J. Pilgrim, et al., *Contact shaping in planar Gunn diodes.* Physica Status Solidi (c), 2010. **8**(2): p. 3.

178. A. Khalid, et al., *Novel composite contact design and fabrication for planar Gunn devices for millimeter-wave and terahertz frequencies.* Physica Status Solidi (c), 2011. **8**(3): p. 3.

179. C. A. Mead and W.G. Spitzer, *Fermi level position at metal-semiconductor interfaces.* Physics Review, 1964. **134**(3A): p. 4.

180. R. T. Tung, *Recent advances in Schottky barrier concepts.* Materials Science and Engineering: R: Reports, 2001. **35**(1-3): p. 138.

181. W. T. Anderson, A. Christou, and J.E. Davey, *Development ot ohmic contacts for GaAs devices using epitaxial Ge films.* IEEE Journal of Solid State Circuits, 1978. **13**(4): p. 6.

182. R. Stall, et al., *Ultra low resistance ohmic contacts to n-GaAs.* IET Electronics Letters, 1979. **15**(24): p. 2.

183. E. D. Marshall, et al., *Non-alloyed ohmic contact to n-GaAs by solid phase epitaxy.* Applied Physics Letters, 1985. **47**(3): p. 3.

184. I. Mehdi, et al., *Nonalloyed and alloyed low-resistance ohmic contacts with good morphology for GaAs using a graded InGaAs cap layer.* Journal of Applied Physics, 1989. **65**(2): p. 3.

185. T. Sands, *Compound semiconductor contact metallurgy.* Materials Science and Engineering: B, 1988. **1**(3-4): p. 24.

186. K. Kajiyama, Y. Mizushima, and S. Sakata, *Schottky barrier height of n-$In_xGa_{1-x}As$ diodes.* Applied Physics Letters, 1973. **23**(8): p. 2.

187. I. -K. Kim, *Pd/Si-based ohmic contacts to n-type InGaAs for AlGaAs/GaAs HBTs.* Materials Letters, 2004. **58**(6): p. 6.

188. I. -H. Kim, et al., *A study on Au/Ni/Au/Ge/Pd ohmic contact and its application to AlGaAs/GaAs heterojunction bipolar transistors.* Applied Physics Letters, 1997. **71**(13): p. 3.

189. P. Hendriks, et al., *Modulation doping and delta doping of III-V compound semiconductors*, in *Physical Concepts of Materials for Novel Optoelectronic Device Applications II: Device Physics and Applications*, M. Razeghi, Editor. 1991, Proceedings of SPIE: Aachen, Germany. p. 11.

190. J. R. Dale and R.G. Turner, *Simple ohmic contacts on gallium arsenide.* Solid-State Electronics, 1963. **6**(4): p. 2.

191. J. B. Gunn, *Instabilities of current in III-V semiconductors.* IBM Journal of Research and Development, 1964. **8**(2): p. 19.

192. N. Braslau, J. B. Gunn, and J.L. Staples, *Metal-semiconductor contacts for GaAs bulk effect devices.* Solid-State Electronics, 1967. **10**(5): p. 3.

193. N. Braslau, *Ohmic contacts to GaAs.* Thin Solid Films, 1983. **104**(3-4): p. 7.

194. A. G. Bacaa, et al., *A survey of ohmic contacts to III-V compound semiconductors.* Thin Solid Films, 1997. **308-309**: p. 18.

195. M. Murakami, *Development of Ohmic contact materials for GaAs integrated circuits.* Materials Science Reports 1990. **5**(5): p. 45.

196. N. Takumi, et al., *Extremely low resistance non-alloyed ohmic contacts to n-GaAs using compositionally graded $In_xGa_{1-x}As$ layers.* Japanese Journal of Applied Physics, 1986. **25**(10): p. 3.

197. N. Takumi, et al., *Non-alloyed Ohmic contacts to n-GaAs using compositionally graded $In_xGa_{1-x}As$ layers.* Japanese Journal of Applied Physics, 1988. **27**(9): p. 5.

198. F. A. Amina, A. A. Rezazadeha, and S.W. Bland, *Non-alloyed ohmic contacts using MOCVD grown $n^+$-$In_xGa_{1-x}As$ on n-GaAs.* Materials Science and Engineering: B, 1999. **66**(1-3): p. 5.

199. J. -W. Lim, et al., *Performance of Pd/Ge/Au/Pd/Au ohmic contacts and its application to GaAs metal-semiconductor field-effect transistors* Solid-State Electronics, 1999. **43**(10): p. 8.

200. P. H. Hao, et al., *On the low resistance Au/Ge/Pd ohmic contact to n-GaAs.* Journal of Applied Physics, 1996. **79**(8): p. 5.

201. A. Paccagnella, et al., *GaAs MESFETs with nonalloyed ohmic contacts: technology and performance.* IET Electronics Letters, 1988. **24**(11): p. 2.

202. H. R. Kawata, et al., *NiGe-based ohmic contacts to n-type GaAs. II. Effects of Au addition.* Journal of Applied Physics, 1994. **75**(5): p. 8.

203. L. C. Wang, P. H. Hao, and B.J. Wu, *Low-temperature-processed (150–175 ℃) Ge/Pd-based Ohmic contacts ($\rho_c \sim 1\times10^{-6}\ \Omega\,cm^2$) to n-GaAs.* Applied Physics Letters, 1995. **67**(4): p. 3.

204. A. Wakita, et al., *Design and surface chemistry of non-alloyed ohmic contacts to pseudomorphic InGaAs on $n^+$ GaAs.* Journal of Applied Physics, 1990. **68**(6): p. 6.

205. B. Jeppson and I. Marklund, *Failure mechanisms in Gunn diodes.* IET Electronics Letters, 1967. **3**(5): p. 2.

206. R. J. Tree, M. J. Josh, and C.T. Foxon, *On a failure mechanism in indium phosphide microwave oscillators.* Solid-State Electronics, 1971. **16**(6): p. 2.

207. D. Ullrich, *Observation of recombination radiation in planar Gunn-effect devices.* IET Electronics Letters, 1971. **7**(8): p. 2.

208. W. F. Fallman and H.L. Hartnagel, *Metallic channels formed by high surface fields on GaAs planar devices.* IET Electronics Letters, 1971. **7**(23): p. 2.

209. C. G. Diskus, et al., *Composite anode contact for planar transferred electron devices.* IEEE Microwave and Guided Wave Letters, 1993. **3**(6): p. 2.

210. N. J. Pilgrim, W. Batty, and R.W. Kelsall, *Thermally self-consistent Monte Carlo device simulations* Journal of Computational Eelctronics, 2002. **1**(1-2): p. 4.

211. A. Chambers, *Modern vaccum physics*. 2005: Chapman&Hall/CRC.

212. W. J. Schaff, et al., *Superlattice buffers for GaAs power MESFET's grown by MBE.* Journal of Vaccum Science and Technology B, 1984. **2**(2): p. 4.

213. I. G. Thayne, et al., *Comparison of 80-200 nm gate length $Al_{0.25}GaAs/GaAs/(GaAs:AlAs)$, $Al_{0.3}GaAs/In_{0.15}GaAs/GaAs$, and $In_{0.52}AlAs/In_{0.65}GaAs/InP$ HEMTs* IEEE Transactions on Electron Devices, 1995. **42**(12): p. 9.

214. X. Hue, B. Boudart, and Y. Crosnier, *Gate recessing optimization of $GaAs/Al_{0.22}Ga_{0.78}As$ heterojunction field effect transistor using citric acid/hydrogen peroxide/ammonium hydroxide for power applications.* Journal of Vacuum Science & Technology B: Microelectronics and Nanometer Structures 1998. **16**(5): p. 5.

215. J. -H. Kim, D. H. Lim, and G.M. Yang, *Selective etching of AlGaAs/GaAs structures using the solutions of citric acid/$H_2O_2$ and de-ionized $H_2O$/buffered oxide etch.* Journal of Vaccum Science and Technology B, 1998. **16**(2): p. 3.

216. Synopsys, *Medici user guide*. Version Z-2007.03 ed. 2007.

217. S. Adachi, *GaAs, AlAs, and AlxGa1-xAs@B: material parameters for use in research and device applications.* Journal of Applied Physics, 1985. **58**(3): p. 29.

218. I. S. Vasil'evskiĭ, et al., *Electrical and structural properties of PHEMT heterostructures based on AlGaAs/InGaAs/AlGaAs and δ-doped on two sides.* Semiconductors, 2008. **42**(9): p. 8.

219. H. M. Shieh, W. C. Hsu, and C.L. Wu, *Very high two-dimensional electron gas concentrations with enhanced mobilities in selectively double-δ-doped GaAs/InGaAs pseudomorphic single quantum well heterostructures.* Applied Physics Letters, 1993. **63**(4): p. 3.

220. W. Kowalsky and A. Schlachetzki, *InGaAs Gunn oscillators.* IET Electronics Letters, 1984. **20** (12): p. 2.

221. S. Perez, J. Mateos, and T. Gonzalez, *Submillimeter-wave oscillations in recessed InGaAs/InAlAs heterostructures: origin and tunability*. ACTA PHYSICA POLONICA A, 2011. **119**(2): p. 3.

222. M. R. Friscourt, P. A. Rolland, and R. Fauquembergue, *Theoretical investigation of $n^+$-n-$n^+$ $Ga_{0.47}In_{0.53}As$ TEO's Up to the millimeter-wave range.* IEEE Electron Device Letters, 1984. **5** (11): p. 3.

223. P. Bhattacharya, *Properties of lattice-matched and strained indium gallium arsenide*. 1993, Londo: INSPEC.

224. P. C. Chao, et al., *DC and microwave characteristics of sub-0.1-um gate-length planar-doped pseudomorphic HEMTs.* IEEE Transactions on Electron Devices, 1989. **36**(3): p. 13.

225. K. L.Tan, et al., *High-power V-band pseudomorphic InGaAs HEMT.* IEEE Electron Device Letters, 1991. **12**(5): p. 2.

226. A. Leuther, et al., *DX centres conduction band offsets and Si-dopant segregation in $Al_xGa_{1-x}As$/GaAs heterostructures.* Semiconductor Science and Technology, 1996. **11**(5): p. 6.

227. D. E. McCumber and A.G. Chynoweth, *Theory of negative-conductance amplification and of Gunn instabilities in "two-valley" semiconductors.* IEEE Transactions on Electron Devices, 1966. **13**(1): p. 18.

228. R. Holmstrom, *Small-signal behavior of Gunn diodes.* IEEE Transactions on Electron Devices, 1967. **14**(9): p. 6.

229. G. King and M.P. Wasse, *Frequency modulation of Gunn-effect oscillators.* IEEE Transactions on Electron Devices, 1967. **14**(10): p. 2.

230. A. Forster, et al., *Hot electron injector Gunn diode for advanced driver assistance systems* Applied Physics A: Materials Science & Processing, 2007. **87**(3): p. 14.

231. A. Khalid, et al., *Observation of multiple domains in a planar Gunn diode*, in *European Microwave Integrated Circuits Conference*. 2009: Rome, Italy. p. 3.

232. L. B. Lok, et al., *Demonstration of the self-mixing effect with a planar Gunn diode at millimeter-wave frequency* in *The 35th International Conference on Infrared, Millimeter and THz Waves*. 2010: Rome, Italy. p. 2.

233. K. -I Oshio and H. Yahata, *Non-periodic current oscillations in the Gunn-effect device with the impact-ionization effect.* Journal of the Physical Society of Japan, 1995. **64**(5): p. 14.

234. J. L. Chu, D.J.J. Coleman, and S.M. Sze, *Microwave oscillations in p-n-p and metal-n-p BARITT diodes*, in *International Electron Devices Meeting*. 1971: Washington DC, USA.

235. H. W. Thim and M.R. Barber, *Observation of multiple high-field domains in n-GaAs.* Proceedings of the IEEE, 1968. **56**(1): p. 2.

236. T. Bhattacharya, *Two domain transist in Gunn-effect oscillators.* Physics Letters A, 1968. **27**(9): p. 2.

237. M. Slater and R.I. Harrison, *An investigation of multiple domain Gunn effect oscillators.* IEEE Transactions on Electron Devices, 1976. **23**(6): p. 8.

238. M. J. Lazarus, E. D. Bullimore, and S. Novak, *A sensitive millimeter wave self-oscillating Gunn diode mixer.* Proceedings of the IEEE, 1971. **59**(5): p. 3.

239. J. Krasavin and H. Hinrikus, *Performance and optimization of Gunn self-oscillating mixer.* IEEE Microwave and Guided Wave Letters, 1995. **5**(6): p. 3.

240. P. Albrecht and M. Bechteler, *Noise figure and conversion loss of self-excited Gunn-diode mixers.* IET Electronics Letters, 1970. **6**(11): p. 2.

241. K. R. Freeman and G.S. Gibson, *The $Vf_T$ relation of CW Gunn-effect devices.* IEEE Transactions on Electron Devices, 1972. **19**(1): p. 9.

242. A. L. Edridge, *Frequency stability of Gunn oscillators with variation of ambient temperature.* Solid-State Electronics, 1972. **15**(11): p. 10.

243. F. Hasegawa and Y. Aono, *Thermal limitation for CW output power of a Gunn diode.* Solid-State Electronics, 1973. **16**(3): p. 8.

244. F. A. Myers, J. McStay, and B.C. Taylor, *Variable-length Gunn oscillator.* IET Electronics Letters, 1968. **4**(18): p. 2.

245. W. H. Haydl and R. Solomon, *The effect of illumination on Gunn oscillations in epitaxial GaAs.* IEEE Transactions on Electron Devices, 1968. **15**(11): p. 2.

246. H. Barth and A. Wideband, *A wideband, backshort-tunable second harmonic W-band Gunn-oscillator*, in *IEEE MTT-S Internationa Microwave Symposium Diges*. 1981: Los Angeles, CA, USA. p. 4.

247. C. P. Wen, *Coplanar waveguide: a surface strip transmission line suitable for nonreciprocal gyromagnetic device applications.* IEEE Transactions on Microwave Theory and Techniques, 1969. **17**(12): p. 4.

248. R. N. Simons, *Coplanar waveguide circuits, component and systems*. 1st ed. 2001: Wiley-IEEE Press. 464.

249. J. B. Knorr and K. Kuchler, *Analysis of coupled slots and coplanar strips on dielectric substrate.* IEEE Transactions on Microwave Theory and Techniques, 1975. **23**(7): p. 8.

250. S. B. Cohn, *Slot line on a dielectric substrate.* IEEE Transactions on Microwave Theory and Techniques, 1969. **17**(10): p. 11.

251. K. C. Gupta, et al., *Microstrip lines and slotlines*. Second ed. 1996, Norwood: Artech House.

252. R. M. Barrett and M.H. Barnes, *Microwave printed circuits.* Radio and TV News, 1951. **46**(16): p. 16.

253. H. Howe, *Stripline circuit design*. 1974, Dedham, MA: Artech House.

254. D. D. Grieg and H.F. Engelmann, *Microstrip-a new transmission technique for the klilomegacycle range.* Proceedings of the IRE, 1952. **40**(12): p. 7.

255. H. A. Wheeler, *Transmission-line properties of parallel strips separated by a dielectric sheet.* IEEE Transactions on Microwave Theory and Techniques, 1965. **13**(2): p. 14.

256. J. Chen, *Double-sided parallel-strip line circuit analysis and applications to microwave component designs*, in *Department of Electronic Engineering*. 2008, City University of Hong Kong: Hong Kong.

257. I. McGregor, F. Aghamoradi, and K. Elgaid, *An approximate analytical model for the quasi-static parameters of elevated CPW lines.* IEEE Transactions on Microwave Theory and Techniques, 2010. **58**(12): p. 6.

258. G. Ghione and C.U. Naldi, *Coplanar waveguides for MMIC applications: effect of upper shielding, conductor backing, finite-extent ground planes, and line-to-line coupling.* IEEE Transactions on Microwave Theory and Techniques, 1987. **35**(3): p. 8.

259. G. Ghione and C. Nald, *Analytical formulas for coplanar lines in hybrid and monolithic MICs.* IET Electronics Letters, 1984. **20**(4): p. 3.

260. C. -H. Ho, L. Fan, and K. Chang, *Broad-band uniplanar hybrid-ring and branch-line couplers.* IEEE Transactions on Microwave Theory and Techniques, 1993. **41**(12): p. 10.

261. B. Jokanovic and V. Trifunovic, *Double-Y baluns for MMICs and wireless applications.* Microwave Journal, 1998. **41**(1): p. 23.

262. R. E. DeBrecht, *Coplanar balun circuits for GaAs FET high-power push-pull amplifiers*, in *IEEE G-MTT International Microwave Symposium Digest*. 1973: Boulder, CO, USA. p. 309-311.

263. V. Trifunovic and B. Jokanovic, *Four decade bandwidth uniplanar balun.* IET Electronics Letters, 1992. **28**(6): p. 2.

264. C. -Y. Chang, C. -W. Tang, and D.-C. Niu, *Ultra-broad-band doubly balanced star mixers using planar Mouw's hybrid junction.* IEEE Transactions on Microwave Theory and Techniques, 2001. **49**(6): p. 9.

265. R. B. Mouw, *A broad-band hybrid junction and application to the star modulator.* IEEE Transactions on Microwave Theory and Techniques, 1968. **16**(11): p. 8.

266. C. H. Lane, *Nichrome resistor properties and reliability*. 1973, Rome Air Development Center: New York. p. 73.

267. K. L. Coates, et al., *Development of thin film resistors for use in mulichip modules*, in *International Conference on Multichip Modules and High Density Packaging* 1998. p. 6.

268. H. Shen and R. Ramanathan, *Fabrication and characterization of thin film resistors for GaAs-based power amplifiers.* Microelectronic Engineering, 2006. **83**(2): p. 7.

269. H. Shen, et al., *Fabrication and characterization of thin film resistors for GaAs-based power amplifiers* in *International Conference on Compounde Semiconductor Manufacturing Technology*. 2003: Scottsdale, AZ, USA. p. 4.

270. J. S. Hayden and G.M. Rebeiz, *Very low-loss distributed X-band and Ka-band MEMS phase shifters using metal-air-metal capacitors.* IEEE Transactions on Microwave Theory and Techniques, 2003. **51**(1): p. 6.

271. K. Grenier, et al., *Germanium resistors for RF MEMS based microsystems*, in *Conference Smart Sensors, Actuators and MEMS*. 2008, Microsystem Technologies: Maspalomas, Gran Canaria, Spain. p. 6.

272. R. R. Kola, et al., *Thin film resistors and capacitors for advanced packaging*, in *International Symposium on Advanced Packaging Materials*. 1997: Braselton GA USA. p. 4.

273. K. I. Elgaid, *A Ka-band GaAs MESFET monolithic downconverter*, in *Department of Electronics and Electrical Engineering*. 1998, University of Glasgow: Glasgow. p. 150.

274. R. Sharma, et al., *RF parameter extraction of MMIC nichrome resistors.* Microwave and Optical Technology Letters, 2003. **39**(5): p. 4.

275. Z. Wang, J. Deen, and A. Rahal, *Accurate modelling of thin-film resistor up to 40 GHz*, in *32nd European Solid-State Device Research Conference*. 2002: Bologna, Italy. p. 307-310.

276. R. N. Simons, *Coplanar waveguide circuits, components, and systems*. 2001: Wiley-IEEE Press.

277. N. H. L. Koster, et al., *Investigations on air bridges used for MMICs in CPW technique*, in *19th European Microwave Conference*. 1989: London, UK. p. 6.

278. K. Y. Hur and R.C. Compton, *Airbridged-gate MESFETS fabricated by isotropic reactive ion etching.* IEEE Transactions on Electron Devices, 1993. **40**(10): p. 4.

279. S. Barker and G.M. Rebeiz, *Distributed MEMS true-time delay phase shifters and wide-band switches.* IEEE Transactions on Microwave Theory and Techniques 1998. **46**(11): p. 10.

280. D. Lopez-Diaz, et al., *Monolithic integrated 210 GHz couplers for balanced mixers and image rejection mixers.* Workshop on Integrated Nonlinear Microwave and Millimeter-Wave Circuits (INMMIC), 2010: p. 4.

281. T. Lodhi, *InP based 77 GHz monolithic millimeter wave integrated circuits*, in *Department of Electronics and Electrical Engineering*. 2001, University of Glasgow: Glasgow. p. 160.

282. M. A. Gritz, et al., *Fabrication of air bridges using electron beam lithography.* Journal of Vaccum Science Technology B: Microelectronics and Nanometer Structures, 2003. **21**(1): p. 3.

283. E. Girgis, J. Liu, and M.L. Benkhedar, *Fabrication of metallic air bridges using multiple-dose electron beam lithography.* Applied Physics Letters, 2006. **88**(20): p. 3.

284. R. G. Woodham, et al., *T-gate and airbridge fabrication for MMICs by combining multi-voltage electron-beam lithography and ion-beam lithography.* Microelectronic Engineering, 1992. **17**(1-4): p. 4.

285. S. Gautsch and N.F.d. Rooij, *Pattern transfer and post processing of complex nanostructures formed by e-beam exposure in PMMA.* Microelectronic Engineering, 2011. **88**(8): p. 4.

286. D. M. Pozar, *Microwave engineering* 3rd ed. 2005: John Wiley & Sons, Inc

287. T. Makino and A. Hashima, *A highly stabilized MIC Gunn oscillator using a dielectric resonator.* IEEE Transactions on Microwave Theory and Techniques, 1979. **27**(7): p. 6.

288. M. Takada and T. Yoneyama, *Self-injection locked Gunn oscillator using nonradiative dielectric waveguide.* Electronics and Communications in Japan (Part 2: Electronics) 1989. **72**(11): p. 7.

289. I. Wolff and V.K. Tripathi, *The microstrip open-ring resonator.* IEEE Transactions on Microwave Theory and Techniques, 1984. **32**(1): p. 6.

290. M. Sagawa, K. Takahashi, and M. Makimoto, *Miniaturized hairpin resonator filters and their application to receiver front-end MICs.* IEEE Transactions on Microwave Theory and Techniques, 1989. **37**(12): p. 7.

291. R. N. Simons and S.R. Taub, *Coplanar waveguide radial line stub.* IET Electronics Letters, 1993. **29**(4): p. 3.

292. R. N. Simons and S.R. Taub, *Coplanar waveguide radial line double stub and application to filter circuits.* IET Electronics Letters, 1993. **29**(17): p. 3.

293. M. Naghed and I. Wolff, *Equivalent capacitance of coplanar waveguide discontinuities and interdigital capacitors using a three-dimensional finite difference method.* IEEE Transactions on Microwave Theory and Techniques 1990. **38**(12): p. 8.

294. L. Li, et al., *Slow-wave line coupler with interdigital capacitor loading.* IEEE Transactions on Microwave Theory and Techniques 2007. **55**(11): p. 7.

295. E. Wilkinson, *An n-way hybrid power divider.* IEEE Transactions on Microwave Theory and Techniques, 1960. **8**(1): p. 3.

296. X. Lan, et al., *Ultra-wideband power divider using multi-wafer packaging technology.* IEEE Microwave and Wireless Components Letters, 2011. **21**(1): p. 3.

297. K. Kim, J. Byun, and H.-Y. Lee, *Substrate integraged waveguide Wilkinson power divider with improved isolation performance.* Progress In Electromagnetics Research Letters, 2010. **19**: p. 8.

298. L. Chiu and Q. Xue, *A parallel-strip ring power divider with high isolation and arbitrary power-dividing ratio.* IEEE Transactions on Microwave Theory and Techniques, 2007. **55**(11): p. 8.

299. L. Chiu and Q. Xue. *A new parallel-strip power divider with enhanced isolation performance*. in *Asia-Pacific Microwave Conference* 2006. Yokohama, Japan.

300. M. A. Antoniades and G.V. Eleftheriades, *A broadband Wilkinson balun using microstrip metamaterial lines.* IEEE Antennas and Wireless Propagation Letters, 2005. **4**(1): p. 4.

301. Y. Sun and A.P. Freundorfer, *Broadband folded Wilkinson power combiner/splitter.* IEEE Microwave and Wireless Components Letters, 2004. **14**(6): p. 3.

302. A. M. Pelaez, J. I. Alonso, and P. Almorox-Gonzalez, *Ultra-broadband mmwave Wilkinson power divider.* Microwave Journal, 2009. **52**(11).

303. C. Li, et al., *Coplanar ring divider with wideband high isolation performance.* Progress In Electromagnetics Research Letters, 2011. **25**: p. 10.

304. C. Li, et al., *A broadband circular combiner/divider for planar Gunn oscillators,* in *2nd Annual Seminar on Passive RF and Microwave Components*. 2011, IET: Glasgow, UK. p. 2.

305. K. W. Wong, L. Chiu, and Q. Xue, *Uniplanar power dividers using asymmetric coplanar striplines and slotlines,* in *38th European Microwave Conference*. 2008, Proceedings of 38th European Microwave Conference: Amsterdam, The Netherlands. p. 337-340.

306. N. Yang, C. Caloz, and K. Wu, *Wideband phase-reversal antenna using a novel bandwidth enhancement technique.* IEEE Transactions on Antennas Propagation, 2010. **58**(9): p. 8.

307. T. Hirota, Y. Tarusawa, and H. Ogawa, *Uniplanar MMIC hybrids – a proposed new MMIC structure.* IEEE Transactions on Microwave Theory and Techniques, 1987. **35**(6): p. 6.

308. L. H. Chua, et al., *Design and analysis of coplanar Lange coupler for millimetre-wave applications up to 90 GHz,* in *Asia-Pacific Microwave Conference*. 2000: Sydney, NSW , Australia p. 4.